TECHNISCHE UNIVERSITÄT WIEN

Improved Methods for Ultra-High Field Magnetic Susceptibility Imaging

Dissertation

zur Erlangung des akademischen Grades

Doktor der Technischen Wissenschaften

an der Fakultät für Physik der Technischen Universität Wien

eingereicht von

Dipl.-Ing. Korbinian Eckstein
Matrikelnummer: 01328705

ausgeführt am
Atominstitut – E141
unter Anleitung von **Univ. Prof. Dipl.-Ing. Dr.techn. Gerald Badurek**

in Zusammenarbeit mit **Assoc. Prof. Dr. Simon Robinson**
Universitätsklinik für Radiologie und Nuklearmedizin
Medizinische Universität Wien

Ort, Datum

(Unterschrift Verfasser) (Unterschrift Betreuer)

Die approbierte gedruckte Originalversion dieser Dissertation ist an der TU Wien Bibliothek verfügbar.
The approved original version of this doctoral thesis is available in print at TU Wien Bibliothek.
TU Bibliothek Your knowledge hub WIEN

Die approbierte gedruckte Originalversion dieser Dissertation ist an der TU Wien Bibliothek verfügbar.
The approved original version of this doctoral thesis is available in print at TU Wien Bibliothek.

Abstract

Introduction The magnetic resonance signal is complex in nature, comprising both magnitude and phase constituents. The magnitude, which is the basis for most Magnetic Resonance Imaging (MRI) methods, reflects tissue parameters such as proton density and the characteristic relaxation times T_1, T_2 and T_2^*. The phase is not used in conventional imaging, but contains useful information: in gradient echo imaging it is proportional to the local magnetic field which is generated by the presence of tissues with different magnetic susceptibilities. These reflect the presence of calcium and iron, providing a contrast mechanism which can be used to explore the vasculature and changes in susceptibility which accompany neurodegenerative processes such as demyelination and iron accumulation in multiple sclerosis. Increasing the field strength generally leads to increased resolution and signal-to-noise ratio (SNR), but phase imaging benefits particularly from ultra-high fields (7 T and higher), as the size of phase effects is proportional to the field. However, ultra-high field imaging poses several challenges due to phase artefacts and signal drop-outs which result from more rapid phase variations and image inhomogeneities caused by the shorter wavelength of the magnetic resonance signal.

Methods Three challenges in ultra-high field phase imaging were addressed in this PhD project: I) The combination of complex-valued signals from an array of radio-frequency receive coils, with special consideration to the phase part of the complex signal. II) Correctly identifying phase ambiguities, or wraps, especially in the context of multi-echo or multi-timepoint data from high-resolution three dimensional datasets. III) Eliminating artefacts arising due to high field strengths in clinically used Susceptibility Weighted Imaging (SWI) sequences.

Results I) The coil combination methods developed were free of common high field phase artefacts in brain images and also in datasets acquired in other, more problematic regions of the body, such as the knee. II) A new phase unwrapping method was developed which achieved higher accuracy, temporal stability, and a reduced runtime compared to the predominantly used methods at three field strengths (3 T, 7 T, 9.4 T). III) A reworked acquisition and processing pipeline for SWI was devised that completely avoided the main artefacts corrupting standard SWI, which arise from an inhomogeneous static magnetic field B_0 and coil sensitivities B_1. Additionally, the severity of signal dropouts was reduced, the SNR increased, and the visibility of small structures such as veins improved while keeping the same total measurement time.

Die approbierte gedruckte Originalversion dieser Dissertation ist an der TU Wien Bibliothek verfügbar.
The approved original version of this doctoral thesis is available in print at TU Wien Bibliothek.
TU Bibliothek Your knowledge hub WIEN

Conclusion Three challenges in ultra-high field phase imaging were investigated and new solutions proposed: an improved framework for coil combination with the two methods ASPIRE and MCPC-3D-S, a new phase unwrapping approach, ROMEO, and a reworked pipeline for susceptibility weighted imaging, CLEAR-SWI. These new methods target the most severe problems of magnetic susceptibility imaging at high and ultra-high field strengths. They have already been adopted by large parts of the research community and are being transitioned to clinical application.

Die approbierte gedruckte Originalversion dieser Dissertation ist an der TU Wien Bibliothek verfügbar.
The approved original version of this doctoral thesis is available in print at TU Wien Bibliothek.
TU Bibliothek Your knowledge hub WIEN

Kurzfassung

Einleitung Das Magnetresonanzsignal ist eine komplexe Größe und kann in Magnitude und Phase zerlegt werden. Die Magnitude findet in den meisten Methoden der Magnetresonanztomographie (MRT) Anwendung und spiegelt Gewebeparameter wie die Protonendichte und die charakteristischen Relaxationszeiten T_1, T_2 and T_2^* wider. Die Phase wird in der konventionellen Bildgebung nicht verwendet, enthält jedoch nützliche Informationen: Bei Gradientenechosequenzen ist sie proportional zum lokalen Magnetfeld, welches durch unterschiedliche magnetische Suszeptibilitäten im Gewebe erzeugt wird. Das lokale Magnetfeld spiegelt Kalzium und Eisen im Gewebe wider und untersützt die Untersuchung des Gefäßsystems und die Erkennung von Suszeptibilitätsveränderungen, welche mit neurodegenerativen Prozessen wie der Demyelinisierung und Eisenakkumulation bei Multipler Sklerose einhergehen. Eine Erhöhung der Feldstärke führt im Allgemeinen zu einer höheren Auflösung und einem besseren Signal-Rausch-Verhältnis. Phasenbasierte Methoden profitieren zusätzlich von ultrahohen Feldern (7 T und höher), da die Größe der Phaseneffekte proportional zum Feld ist. Die Bildgebung bei ultrahohen Feldern ist jedoch aufgrund von Phasenartefakten und Signalausfällen, die sich aus schnelleren Phasenänderungen und Bildinhomogenitäten aufgrund der kürzeren Wellenlänge des Magnetresonanzsignals ergeben, mit einigen Herausforderungen verbunden.

Methoden Drei Problematiken der Ultrahochfeld-Phasenbildgebung wurden in dieser Doktorarbeit behandelt: I) Die Kombination von komplexwertigen Signalen aus einem Array von Hochfrequenz-Empfangsspulen unter besonderer Berücksichtigung des Phasenanteils des komplexen Signals. II) Die korrekte Identifizierung von Phasenmehrdeutigkeiten auch Wraps genannt, insbesondere im Zusammenhang mit Multi-Echo oder Multi-Timepoint-Daten aus hochauflösenden dreidimensionalen Datensätzen. III) Die Eliminierung von Artefakten, die durch hohe Feldstärken in klinisch verwendeten suszeptibilitätsgewichteten Bildgebungssequenzen (SWI) entstehen.

Ergebnisse I) Die entwickelten Spulenkombinationsmethoden waren nicht von den üblicherweise auftretenden Hochfeld-Phasenartefakten betroffen, was anhand von Datensätzen aus Gehirnaufnahmen und von Datensätzen aus problematischeren Körperregionen, wie z. B. dem Knie, bestätigt wurde. II) Es wurde eine neue Phasen-"Unwrapping"-Methode entwickelt, die bei drei Feldstärken (3 T, 7 T, 9,4 T) eine höhere Genauigkeit, zeitliche Stabilität und eine geringere Laufzeit im Vergleich zu den standardmäßig verwendeten Methoden erreichte. III) Es wurde ein überarbeitetes Schema zu Aufnahme und Verarbeitung für SWI entwickelt, das

Die approbierte gedruckte Originalversion dieser Dissertation ist an der TU Wien Bibliothek verfügbar.
The approved original version of this doctoral thesis is available in print at TU Wien Bibliothek.
TU Bibliothek Your knowledge hub WIEN

die schwerwiegenden Artefakte, die bei SWI durch ein inhomogenes statisches Magnetfeld B_0 und die Spulenempfindlichkeiten B_1 entstehen, vollständig vermeidet. Darüber hinaus konnten Signalausfälle reduziert, das Signal-Rausch-Verhältnis erhöht und die Sichtbarkeit kleiner Strukturen wie Venen verbessert werden – bei unveränderter Gesamtmesszeit.

Zusammenfassung Drei Problempunkte der Ultrahochfeld-Phasenbildgebung wurden untersucht und neue Lösungen vorgeschlagen: ein verbessertes Konzept für die Spulenkombination mit zwei Methoden (ASPIRE und MCPC-3D-S), ein neuer Ansatz für das Phasen-unwrapping (ROMEO) und ein überarbeitetes Schema für die suszeptibilitätsgewichtete Bildgebung (CLEAR-SWI). Diese neuen Methoden setzen an den gravierendsten Problemen der Bildgebung magnetischer Suszeptibilität bei hohen Feldstärken an. Sie wurden bereits von großen Teilen der Forschungsgemeinschaft übernommen und werden derzeit in die klinische Anwendung überführt.

Die approbierte gedruckte Originalversion dieser Dissertation ist an der TU Wien Bibliothek verfügbar.
The approved original version of this doctoral thesis is available in print at TU Wien Bibliothek.
TU Bibliothek Your knowledge hub WIEN

Acknowledgements

Firstly, I want to thank Simon Robinson, my PhD advisor, who supported me through the entire process, starting by encouraging me to do a PhD, pointing out interesting problems to solve during my PhD, and finally providing guidance for writing the thesis. Furthermore, he ensured extensions of my funding to avoid cutting short the interesting scientific projects that had developed over time.

I am also grateful to Gerald Badurek for serving as my supervisor at the Vienna University of Technology and for helping me with scientific and organizational matters throughout the years. Siegfried Trattnig provided financial support for me to attend several workshops and conferences that played a big role in shaping my scientific career, and he was incredibly supportive and enthusiastic about the methods we developed.

I also want to thank my fantastic coworkers for the cheerful atmosphere at work, the help with measurements, and the many interesting discussions, specifically Barbara Dymerska, Pedro Cardoso, Beata Bachrata, Chad Guthrie, and David Bancelin. I especially enjoyed the joint projects at the "Holzhaus" with Gilbert Hangel, Esau Rodriguez, Wolfgang Bogner, and Philipp Moser, and interacting with all the other amazing people there for climbing sessions and coffee room talks. I also enjoyed the scientific exchange of the external collaborations with Gisela Hagberg, Ashley Stewart, Markus Barth, and Steffen Bollmann, and I'm deeply grateful that I could be part of those projects.

Cosima Barbarino supported me through my entire PhD, both emotionally and scientifically. She helped me when I was stuck, motivated me when I was discouraged, and helped me sort my thoughts on many occasions. And of course, our Japanese green tea Saturdays, shared hobbies, and trips around the world provided a wonderful counterweight to both of our scientific endeavors. It was also through Cosima that I got aware of the magnetic resonance group at the Holzhaus when I was in search of a topic for my master's thesis.

I thank my family for always believing in me, especially my sister, Maria Eckstein, for many interesting conversations and for being a role model to join science, and my parents and grandparents for all their encouragement and support.

I want to thank my friends for many enjoyable evenings that balanced out many long hours in front of my computer. Marcel Obermaier even read parts of my thesis and seeing his positive response was a great encouragement.

I gratefully acknowledge the financial support by the Austrian Federal Ministry for Digital and Economic Affairs and the National Foundation for Research, Technology and Development (FWF 31452).

Die approbierte gedruckte Originalversion dieser Dissertation ist an der TU Wien Bibliothek verfügbar.
The approved original version of this doctoral thesis is available in print at TU Wien Bibliothek.
TU Bibliothek WIEN Your knowledge hub

Die approbierte gedruckte Originalversion dieser Dissertation ist an der TU Wien Bibliothek verfügbar.
The approved original version of this doctoral thesis is available in print at TU Wien Bibliothek.

List of Publications

During the work on this thesis the following parts have been published as articles in peer-reviewed journals:

I ASPIRE

Eckstein, K., Dymerska, B., Bachrata, B., Bogner, W., Poljanc, K., Trattnig, S., Robinson, S.D., Computationally Efficient Combination of Multi-channel Phase Data From Multi-echo Acquisitions (ASPIRE). *Magnetic Resonance in Medicine* 79, 2996–3006 (2018)

The author was the main author of the manuscript. The author was the main actor in development and implementation of the method, designed and conducted all MRI measurements, performed the data-analysis and wrote the manuscript.

II ROMEO

Dymerska, B., Eckstein, K., Bachrata, B., Siow, B., Trattnig, S., Shmueli, K., Robinson, S.D., Phase unwrapping with a rapid opensource minimum spanning tree algorithm (ROMEO). *Magnetic Resonance in Medicine* 85, 2294–2308 (2021)

The author is one of two shared first authors. The author was the main actor in development and implementation of the method, and contributed to the data-analysis and writing of the manuscript.

III CLEAR-SWI

Eckstein, K., Bachrata, B., Hangel, G., Widhalm, G., Enzinger, C., Barth, M., Trattnig, S., Robinson, S.D., Improved susceptibility weighted imaging at ultra-high field using bipolar multi-echo acquisition and optimized image processing: CLEAR-SWI. *NeuroImage* 118175 (2021)

The author was the main author of the manuscript. The author was the main actor in development and implementation of the method, designed the MRI measurements and conducted parts of them, performed the data-analysis and wrote the manuscript.

Die approbierte gedruckte Originalversion dieser Dissertation ist an der TU Wien Bibliothek verfügbar.
The approved original version of this doctoral thesis is available in print at TU Wien Bibliothek.
TU Bibliothek Your knowledge hub WIEN

Further publications

Hagberg G., Eckstein K., Tuzzi E., Zhou J., Robinson S., Scheffler K., Phase-based masking for quantitative susceptibility mapping of the human brain at 9.4T. Submitted to *Magnetic Resanance in Medicine* (2021)

Stewart, A. W., Robinson, S. D., O'Brien, K., Jin, J., Widhalm, G., Hangel, G., Walls, A., Goodwin, J., Eckstein, K., Tourell, M., Morgan, C., Narayanan, A., Barth, M., Bollmann, S., QSMxT: Robust Masking and Artefact Reduction for Quantitative Susceptibility Mapping Preprint on *bioRxiv* (2021)

Kořínek, R., Pfleger, L., Eckstein, K., Beiglböck, H., Robinson, S. D., Krebs, M., Trattnig, S., Starčuk, Z., Krššák, M., Feasibility of Hepatic Fat Quantification Using Proton Density Fat Fraction by Multi-Echo Chemical-Shift-Encoded MRI at 7T. *Frontiers in Physics*, 9, 197 (2021)

Voelker, M. N., Kraff, O., Goerke, S., Laun, F. B., Hanspach, J., Pine, K. J., Ehses, P., Zaiss, M., Liebert, A., Straub, S., Eckstein, K., Robinson, S., Nagel, A. N., . . . Quick, H. H., The traveling heads 2.0: Multicenter reproducibility of quantitative imaging methods at 7 Tesla. *NeuroImage*, 232 (2021)

Rodriguez, E. P., Moser, P., Auno, S., Eckstein, K., Dymerska, B., Kouwe, A. van der, Gruber, S., Trattnig, S., Bogner, W., Real-time motion and retrospective coil sensitivity correction for CEST using volumetric navigators (vNavs) at 7T. *Magnetic Resonance in Medicine*, 85(4), 1909–1923 (2020)

Moser, P., Eckstein, K., Hingerl, L., Weber, M., Motyka, S., Strasser, B., van der Kouwe, A., Robinson, S., Trattnig, S., Bogner, W., Intra-session and inter-subject variability of 3D-FID-MRSI using single-echo volumetric EPI navigators at 3T. *Magnetic Resonance in Medicine*, 83(6), 1920–1929 (2019)

Motyka, S., Moser, P., Hingerl, L., Hangel, G., Heckova, E., Strasser, B., Eckstein, K., Daniel Robinson, S., Poser, B. A., Gruber, S., Trattnig, S., Bogner, W., The influence of spatial resolution on the spectral quality and quantification accuracy of whole-brain MRSI at 1.5T, 3T, 7T, and 9.4T. *Magnetic Resonance in Medicine*, 82(2), 551–565 (2019)

Dymerska, B., Poser, B. A., Bogner, W., Visser, E., Eckstein, K., Cardoso, P., Barth, M., Trattnig, S., Robinson, S. D., Correcting dynamic distortions in 7T echo planar imaging using a jittered echo time sequence. *Magnetic Resonance in Medicine*, 76(5), 1388–1399 (2016)

Eckstein, K., Trattnig, S., Robinson, S. D., A Simple Homogeneity Correction for Neuroimaging at 7T. *Proceedings of the 27th Annual Meeting ISMRM*, #2716. (2019)

Eckstein, K., Trattnig, S., Robinson, S. D., Correction for Geometric Distortion in Bipolar Gradient Echo Images from B0 Field Variations. *Proceedings of the 27th Annual Meeting ISMRM*, #4510 (2019)

Eckstein, K., Trattnig, S., Robinson, S. D., High resolution frequency difference mapping using ASPIRE phase combination. *Proceedings of the 26th Annual Meeting ISMRM*, #4991 (2018)

Die approbierte gedruckte Originalversion dieser Dissertation ist an der TU Wien Bibliothek verfügbar.
The approved original version of this doctoral thesis is available in print at TU Wien Bibliothek.
TU Bibliothek Your knowledge hub WIEN

Eckstein, K., Trattnig, S., and Robinson, S. D., An assessment of the 'Prescan-Normalize Adaptive Combine' approach to combining phase images from multi-channel coils at 3T. *Proceedings of the 26th Annual Meeting ISMRM*, #4992 (2018)

Eckstein, K., Trattnig, S., and Robinson, S. D., A Simple Phase Imaging REconstruction method (ASPIRE). *Proceedings of the 25th Annual Meeting ISMRM*, #1966 (2017)

Die approbierte gedruckte Originalversion dieser Dissertation ist an der TU Wien Bibliothek verfügbar.
The approved original version of this doctoral thesis is available in print at TU Wien Bibliothek.
TU WIEN Bibliothek Your knowledge hub

TU WIEN Bibliothek Your knowledge hub
Die approbierte gedruckte Originalversion dieser Dissertation ist an der TU Wien Bibliothek verfügbar.
The approved original version of this doctoral thesis is available in print at TU Wien Bibliothek.

List of Figures

2.1 MRI magnet design 6
2.2 Solution to the Bloch equation 19
2.3 Sampling strategies for a 2D section of k-space 22
2.4 Relative SNR of the phase for a range of echo times 29
2.5 Signal separation with different coil combinations 32
2.6 Combination of phase images according to MCPC-3D 37
2.7 Laplacian unwrapping of a simulated topology 40
2.8 Common phase artefacts 42

3.1 Visualization of the ROMEO weights 59
3.2 Order in which unwrapping is performed 61
3.3 Proposed SWI processing pipeline 66
3.4 Visualization of different phase masking approaches 68
3.5 MRI background noise 71
3.6 Comparison of vendor homogeneity corrections tested on a spherical water phantom 72
3.7 Visualization of the Simple Segmentation 74
3.8 Estimated sensitivity 75
3.9 Smoothing effects at a simulated sharp edge 78

5.1 Evaluation of different coil combination schemes 97
5.2 Challenging coil combination of a knee dataset 98
5.3 ASPIRE applied to a bipolar phantom acquisition 99
5.4 Images from the acquisition Bipolar Brain combined using ASPIRE 100
5.5 Unwrapping of a simulated topography 101
5.6 Selected unwrapped slices for GRE and EPI scans at 3 T 103
5.7 Unwrapping evaluation with the temporal reference 104
5.8 Phase unwrapping error histograms 106
5.9 Noise comparison between single-echo and SNR-combined monopolar and bipolar magnitude 107

Die approbierte gedruckte Originalversion dieser Dissertation ist an der TU Wien Bibliothek verfügbar.
The approved original version of this doctoral thesis is available in print at TU Wien Bibliothek.
TU Bibliothek Your knowledge hub WIEN

5.10 Qualitative comparison between homogeneity corrected single-echo and a bipolar multi-echo magnitude . . . 108
5.11 Magnitude images from single-echo and SNR-weighted combination of multi-echo . . . 109
5.12 Contrast comparison of different multi-echo magnitude combination methods . . . 111
5.13 High-pass filtered phase from Standard SWI and CLEAR-SWI . . . 112
5.14 Comparison of phase masks obtained with standard SWI and CLEAR-SWI . . . 113
5.15 Filtered and scaled phase for CLEAR-SWI . . . 114
5.16 Comparison of standard SWI and CLEAR-SWI . . . 115
5.17 Comparison of minimum intensity projections of Standard SWI and CLEAR-SWI . . . 116
5.18 Comparison of standard SWI with CLEAR-SWI in a small region . 117
5.19 Phase artefact appearing as microbleeding in standard SWI . . . 117
5.20 Comparison between standard SWI and CLEAR-SWI in a multiple sclerosis patient . . . 119
5.21 CLEAR-SWI versus simulated single-echo SWI from the same dataset 120
5.22 Comparison of standard SWI and CLEAR-SWI at \unit[3]{T} . . . 121
5.23 Automatic masks for 14 different acquisitions . . . 123
5.24 Sensitivity estimation and homogeneity correction . . . 124
5.25 Homogeneity correction in 3D view . . . 125
5.26 Impulse response of the estimated Gaussian smoothing . . . 126
5.27 Average deviation per voxel from perfect Gaussian smoothing . . . 127
5.28 Complex smoothing of phase images at 3 different echo times . . . 128
5.29 Complex smoothing of phase images of a lower slice . . . 129
5.30 Smoothing with a different number of iterations . . . 130
5.31 Comparison of division smoothing with nangaussian smoothing . . . 131
5.32 Comparison of SNR efficiency for single-echo, monopolar, and bipolar multi-echo scans . . . 133
5.33 Comparison of CNR efficiency for single-echo, monopolar, and bipolar multi-echo scans . . . 134
5.34 Comparison of phase SNR efficiency for single-echo, monopolar, and bipolar multi-echo scans . . . 135
5.35 Simulated SNR for the performed SWI measurements in comparison with ideal settings . . . 137
5.36 Relative SNR estimated from a total of 150 regions in 3 volunteers . 138
5.37 Simulated single-echo data from an acquired multi-echo scan . . . 139
5.38 Comparison of B_0 maps . . . 140
5.39 Comparison of B_0 maps in triplanar view . . . 141

Die approbierte gedruckte Originalversion dieser Dissertation ist an der TU Wien Bibliothek verfügbar.
The approved original version of this doctoral thesis is available in print at TU Wien Bibliothek.
TU Bibliothek Your knowledge hub WIEN

List of Tables

2.1 Magnetic susceptibility of different materials 45

4.1 Acquisition parameters for the scans presented in the coil combination study 86
4.2 Acquisition parameters for results presented in the unwrapping study 87
4.3 Acquisition parameters for measurements performed for the SWI study 89

5.1 Percentage of voxels inside the mask that differed between the unwrapped result and the temporal reference 105

6.1 Availability of Code 157

Die approbierte gedruckte Originalversion dieser Dissertation ist an der TU Wien Bibliothek verfügbar.
The approved original version of this doctoral thesis is available in print at TU Wien Bibliothek.
TU WIEN Bibliothek Your knowledge hub

Abbreviations

BOLD - Blood Oxygen Level Dependent
CNR - Contrast-to-Noise-Ratio
CT - Computer Tomography
EPI - Echo Planar Imaging
FOV - Field of View
GM - Grey Matter
GRE - Gradient Echo
HiP - Hermitian inner Product
mIP - minimum Intensity Projection
MR - Magnetic Resonance
MRI - Magnetic Resonance Imaging
NMR - Nuclear Magnetic Resonance
PET - Positron Emission Tomography
QSM - Quantitative Susceptibility Mapping
RF - Radiofrequency
ROI - Region of Interest
RSOS - Root-Sum-of-Squares
SD - Standard Deviation
SNR - Signal-to-Noise-Ratio
SWI - Susceptibility Weighted Imaging
TE - Echo Time
TR - Repetition Time
VRC - Virtual Reference Coil
WM - White Matter

Die approbierte gedruckte Originalversion dieser Dissertation ist an der TU Wien Bibliothek verfügbar.
The approved original version of this doctoral thesis is available in print at TU Wien Bibliothek.
TU Bibliothek Your knowledge hub WIEN

Contents

1 Introduction **1**

2 Theory **5**

2.1 MRI - Hardware . . . 5
2.1.1 Main Magnet . . . 5
2.1.2 Electromagnetic Shielding . . . 6
2.1.3 Radiofrequency Coils . . . 7
2.1.3.1 Coil sensitivity . . . 7
2.1.3.2 Coil types . . . 8
2.1.4 Gradient Coil . . . 8
2.1.4.1 Eddy currents . . . 9
2.1.4.2 Gradient timing mismatch . . . 9
2.1.5 Active Shim Coils . . . 9
2.1.6 Signal Amplifier and Digitization . . . 10
2.1.7 Control and Reconstruction Computer . . . 10
2.2 (N)MR - Signal Formation . . . 10
2.2.1 Single Spin in Magnetic Field . . . 11
2.2.1.1 Quantum mechanical description . . . 11
2.2.1.2 Energy eigenstates . . . 11
2.2.2 An Ensemble of Spins . . . 13
2.2.2.1 Boltzmann distribution . . . 13
2.2.2.2 Rotating frame of reference . . . 14
2.2.3 Excitation . . . 15
2.2.3.1 Bloch equation without relaxation . . . 15
2.2.3.2 Radiofrequency pulse . . . 16
2.2.4 Relaxation Processes . . . 16
2.2.4.1 T_1 relaxation . . . 16
2.2.4.2 T_2 relaxation . . . 17
2.2.4.3 T_2^* and T_2' relaxation . . . 17
2.2.4.4 Bloch equation with relaxation . . . 18
2.3 MRI - From Acquired Signal to Image . . . 18

Die approbierte gedruckte Originalversion dieser Dissertation ist an der TU Wien Bibliothek verfügbar.
The approved original version of this doctoral thesis is available in print at TU Wien Bibliothek.
TU WIEN Bibliothek Your knowledge hub

2.3.1 K-space Imaging . . . 20
2.3.1.1 Gradient echo imaging . . . 21
2.3.1.2 2D GRE slice selective excitation . . . 23
2.3.1.3 3D GRE k-space imaging . . . 23
2.3.1.4 Multi echo imaging . . . 23
2.3.2 Bandwidth, Flip Angle and Repetition Time . . . 24
2.3.3 Signal-to-Noise-Ratio in MRI . . . 25
2.3.3.1 Magnitude SNR . . . 26
2.3.3.2 Phase SNR . . . 27
2.3.4 Measurement of Magnitude and Phase . . . 28
2.4 MRI Reconstruction and Preprocessing . . . 30
2.4.1 Magnitude . . . 30
2.4.1.1 Coil combination . . . 30
2.4.1.2 Multi echo combination . . . 33
2.4.1.3 Common magnitude artefacts . . . 33
2.4.1.4 T_2^* and M_0 calculation . . . 34
2.4.2 Phase . . . 34
2.4.2.1 Coil combination . . . 34
2.4.2.2 Phase unwrapping . . . 38
2.4.2.3 Common phase artefacts . . . 41
2.4.2.4 Multi-echo combination . . . 42
2.5 Magnetic Susceptibility in MRI . . . 44
2.5.1 Definition and Properties . . . 44
2.5.2 Interaction in MRI . . . 45
2.5.3 Blood, Iron and Ferritin . . . 45
2.5.3.1 Hemoglobin . . . 46
2.5.3.2 Hematoma: the role of ferritin and hemosiderin . . . 46
2.5.4 Susceptibility Weighted Imaging . . . 46
2.5.5 Quantitative Susceptibility Mapping . . . 47

3 Methods **49**
3.1 Combination of Complex Data from Array Coils . . . 49
3.1.1 MCPC-3D-S . . . 49
3.1.2 ASPIRE . . . 51
3.1.3 Bipolar Corrections . . . 53
3.1.3.1 Calculation of the bipolar artefact . . . 53
3.1.3.2 Calculation of a correction term . . . 55
3.1.3.3 Additional considerations . . . 56
3.2 ROMEO . . . 58
3.2.1 Edge Weights . . . 58
3.2.2 Region Growing . . . 60

Die approbierte gedruckte Originalversion dieser Dissertation ist an der TU Wien Bibliothek verfügbar.
The approved original version of this doctoral thesis is available in print at TU Wien Bibliothek.
TU Bibliothek Your knowledge hub WIEN

3.2.3 Seed Determination and Offset Correction 60
3.2.4 Template Unwrapping 61
3.2.5 Performance Considerations and Algorithm Complexity . . . 62
3.3 CLEAR-SWI 63
3.3.1 Sequence 63
3.3.2 Preprocessing 64
3.3.2.1 Coil combination 64
3.3.2.2 Noise mask 65
3.3.3 CLEAR-SWI Steps 65
3.3.3.1 Phase processing 65
3.3.3.2 Sigmoidal phase masking 67
3.3.3.3 Multi echo magnitude combination 69
3.3.3.4 Non-linear magnitude scaling 69
3.3.3.5 SWI calculation 70
3.3.3.6 T_2^* and M_0 calculation 70
3.4 Supporting Methods 70
3.4.1 Automatic Masking 70
3.4.2 Sensitivity Estimation and Homogeneity Correction 72
3.4.2.1 Simple segmentation 73
3.4.2.2 Smoothing with missing values 73
3.4.2.3 Homogeneity correction 74
3.4.3 Fast Gaussian 3D Smoothing 75
3.4.3.1 Optimizing the runtime 76
3.4.3.2 Application for smoothing phase 76
3.4.3.3 Image border effects 77
3.4.3.4 Weighted smoothing 77
3.4.3.5 Application with missing values 78
3.4.4 B_0 Calculation 79
3.4.5 SNR Simulation 80
3.4.5.1 Gradient timing calculation 80
3.4.5.2 Magnitude SNR 82
3.4.5.3 Magnitude CNR 82
3.4.5.4 Phase SNR 83
3.4.6 Simulated Single-Echo 83
3.4.6.1 Magnitude 84
3.4.6.2 Phase 84

4 Analysis **85**
4.1 Measurements 85
4.1.1 Coil Combination 85
4.1.2 Phase Unwrapping 86

Die approbierte gedruckte Originalversion dieser Dissertation ist an der TU Wien Bibliothek verfügbar.
The approved original version of this doctoral thesis is available in print at TU Wien Bibliothek.
TU WIEN Bibliothek Your knowledge hub

4.1.3 SWI . . . 87
4.2 Evaluations . . . 88
4.2.1 Smoothing Evaluation . . . 88
4.2.2 Simulation settings of the SNR Evaluation . . . 90
4.2.3 Coil Combination . . . 90
4.2.4 Phase Unwrapping . . . 91
4.3 Measurement of Signal-to-Noise-Ratio in MRI . . . 91
4.3.1 SNR Estimation Approach . . . 92
4.3.1.1 Automatic definition of regions of interest . . . 92
4.3.1.2 Sequence comparison . . . 93

5 Results **95**
5.1 Combination of Complex Data from Array Coils . . . 95
5.1.1 Bipolar Acquisitions . . . 99
5.2 ROMEO . . . 101
5.3 CLEAR-SWI . . . 107
5.3.1 Magnitude Comparison . . . 107
5.3.2 Phase Comparison . . . 110
5.3.3 Comparison of Standard SWI and CLEAR-SWI . . . 110
5.4 Supporting Methods . . . 122
5.4.1 Automatic Masking . . . 122
5.4.2 Sensitivity Estimation and Homogeneity Correction . . . 122
5.4.3 Fast Gaussian 3D Smoothing . . . 125
5.4.4 SNR Simulation . . . 132
5.4.5 Simulated Single Echo . . . 136
5.4.6 B_0 Calculation . . . 140

6 Discussion **143**
6.1 Coil Combination . . . 144
6.2 Phase Unwrapping . . . 146
6.3 Susceptibility Weighted Imaging . . . 148
6.4 Supporting Methods . . . 152
6.5 Impact and Code Availability . . . 155

7 Conclusion **159**

Bibliography **161**

Die approbierte gedruckte Originalversion dieser Dissertation ist an der TU Wien Bibliothek verfügbar.
The approved original version of this doctoral thesis is available in print at TU Wien Bibliothek.
TU Bibliothek Your knowledge hub WIEN

Die approbierte gedruckte Originalversion dieser Dissertation ist an der TU Wien Bibliothek verfügbar.
The approved original version of this doctoral thesis is available in print at TU Wien Bibliothek.

Die approbierte gedruckte Originalversion dieser Dissertation ist an der TU Wien Bibliothek verfügbar.
The approved original version of this doctoral thesis is available in print at TU Wien Bibliothek.

Chapter 1

Introduction

Magnetic Resonance Imaging (MRI) is a clinically relevant technique in radiology for anatomical and physiological imaging of the body. The alternatives are CT (computer tomography) or PET (positron emission tomography) scans, which have poor soft tissue contrast and use ionizing radiation with harmful stochastic effects or biopsy, which can severely damage neighboring tissue. Ultrasound is another alternative that does not involve harmful radiation, but has limited use in certain situations, such as when the volume to be imaged is obstructed by bones.

MRI has the potential to measure several different tissue parameters, including T_1 relaxation, T_2 relaxation, magnetic susceptibility, proton density, flow, elasticity and connectivity. Additionally, by comparison with a baseline the activation can be measured indirectly with the BOLD (blood oxygen level dependent) effect. By using special coils, spectroscopic MR measures the concentrations of different elements, like neurotransmitters or metabolites. A contrast agent can be used as well with MRI to either visualize blood flow or enhance the visibility of internal structures.

As MRI is sensitive to many different underlying tissue parameters this creates the challenge to disentangle those, which is the main reason that many MRI methods are not quantitative, but only shows meaningful contrast between different tissue types. The weighting of different tissue parameters depends on the specific execution steps and timings of the experiment, called the MRI sequence, and a number of different sequences exist that are adapted to best visualize a specific phenomenon.

The underlying principle of MRI is the behavior of proton spins inside the measured object when subjected to a strong magnetic field. Coherent resonance signals from the proton spins are measured after certain perturbations were applied to the system. These signals are complex in nature and can be reconstructed into 3D volumes, with the magnitude and the phase of the complex signal containing different information about tissue properties. This complex nature of MRI signals

Die approbierte gedruckte Originalversion dieser Dissertation ist an der TU Wien Bibliothek verfügbar.
The approved original version of this doctoral thesis is available in print at TU Wien Bibliothek.
TU Bibliothek Your knowledge hub WIEN

is of special importance in this work.

Benefits and Challenges of Ultra-High Field in MRI Clinical MRI scanners have mostly static magnetic field strengths of $0.5 - 3\,\mathrm{T}$ and recently $7\,\mathrm{T}$ scanners have been certified for clinical use as well. Research scanners for human MRI range up to $10.5\,\mathrm{T}$ [1] and $21.1\,\mathrm{T}$ for smaller bore machines [2]. NMR (nuclear magnetic resonance) magnets range up to $45\,\mathrm{T}$ in continuous operation, however with a small bore size and no imaging capability.

The benefits of higher field strengths are a stronger resonance signal, and for imaging a higher possible resolution and faster acquisition, but higher field strengths also introduce new difficulties, like a shorter transceive wavelength that leads to inhomogeneities in the image, severe distortion effects from not an inhomogeneous static magnetic field, or spatially depending offsets impeding many processing steps that involve the phase of the MR signal.

Solutions to all three problems are developed and discussed within this work.

Multi Echo Acquisition MRI acquisitions require a large number of acquired resonance signals, each being shifted by a different phase component, to reconstruct the 3D appearance of the inserted object. After an excitation, a resonance signal is created by applying a gradient in the magnetic field and before the next excitation can occur, a relaxation period is required to allow the pool of magnetic spins to recover. In commonly applied single echo acquisitions, only one resonance is acquired after each excitation and therefore only fractions of the time between excitations are utilized for signal acquisition. In multi echo acquisitions, the gradient is reversed after the acquisition of a resonance and the same resonance is scanned again with a different echo time – the time between excitation and center of the resonance or echo. This way the waiting time between two excitations can be completely filled with multiple acquisition at different echo times, which results in one 3D volume for each echo time.

Methods to combine the information from multiple volumes from different echo times are presented and new approaches are developed within this work.

Coil Combination To increase signal to noise ratio, provide coverage over an extended body region and allow time-consuming Fourier encoding to be replaced by sensitivity encoding, modern MRI machines employ multi-channel array coils with currently up to 128 coil elements, each acquiring a full 3D volume. The essential information is identical for each coil element, however, with different spatially varying sensitivities and offset values. For further processing and analyzing the acquired data, the individual volumes have to be combined, removing the coil dependent aspects and only retrieving the common information. The combination

Die approbierte gedruckte Originalversion dieser Dissertation ist an der TU Wien Bibliothek verfügbar.
The approved original version of this doctoral thesis is available in print at TU Wien Bibliothek.
TU Bibliothek Your knowledge hub WIEN

of the magnitude of the complex signal can be performed without major challenges but the phase combination is complicated by spatially varying phase offsets that are different for each coil element and depend on the geometry of the coil as well as on the magnetic susceptibility properties of the object inside the scanner.

Coil combination methods with a focus on phase combination that are based on multi echo acquisitions are discussed and new developments are presented in this work.

Phase Unwrapping The phase in MRI is calculated as the angle of the reconstructed complex image and is therefore inherently limited to a 2π range (commonly $[-\pi;\pi)$ or $[0;2\pi)$). The underlying physical quantity, the strength of the local magnetic field, however, is not restricted to this range, which results in aliasing effects. In images, these aliasing effects are seen as sharp borders, where the phase value transitions from $-\pi$ to π, and are accordingly called wraps. At high field strengths and longer echo times, it is common that several wraps arise in the phase, impeding further processing without resolving, or unwrapping, the aliasing effects first.

A new technique is presented in this work, which is based on both spatial unwrapping, where phase behavior of neighboring voxels is used for unwrapping, as well as temporal unwrapping, i.e. using the information of one voxel at several echo times.

Susceptibility Weighted Imaging Susceptibility weighted imaging (SWI) is an imaging technique that utilizes MR phase information to enhance certain features in the magnitude image, such as veins or iron deposits, which exhibit strong susceptibility effects. SWI is routinely employed for a range of neurological diagnoses and is also a promising candidate as an early imaging biomarker, for example for multiple sclerosis.

SWI benefits from high field strengths due to increased phase contrast and stronger weighting of susceptibility effects, however, suffers from a range of artefacts especially pronounced at high field strengths. The challenges for SWI include all previously mentioned challenges that occur at high fields and multi echo acquisitions as well as those that have to be addressed in coil combination and unwrapping and additionally include SWI specific challenges like phase filtering and weighting.

The goal of this work was to address all before mentioned issues and to find solutions with a focus on robustness, computational efficiency and the avoidance of severe artefacts occurring due to the high field strength. While also generally applicable, all presented new methods find application in an improved SWI acquisition and processing pipeline.

Die approbierte gedruckte Originalversion dieser Dissertation ist an der TU Wien Bibliothek verfügbar.
The approved original version of this doctoral thesis is available in print at TU Wien Bibliothek.
TU Bibliothek Your knowledge hub WIEN

Die approbierte gedruckte Originalversion dieser Dissertation ist an der TU Wien Bibliothek verfügbar.
The approved original version of this doctoral thesis is available in print at TU Wien Bibliothek.

Chapter 2

Theory

The theory section provides a brief overview of the physics involved in MR, and should also create a foundation that is sufficient to understand the newly developed methods presented in later chapters. This section is split into several subparts, describing the important hardware parts of MRI scanners, explaining the basic physical principles governing the MR phenomenon, deriving the k-space notation, introducing common acquisition and reconstruction schemes, and lastly focusing on the role of magnetic susceptibility in MR.

2.1 MRI - Hardware

The important electric components of an MRI machine are its main magnet producing a strong and homogeneous magnetic field, the radiofrequency (RF) coils that excite the spins and measure the resonance signal, and the gradient coils that apply spatially varying magnetic fields for signal encoding. Further required parts are electromagnetic shielding, shim coils that correct deviations in the main magnetic field, the specifically designed signal amplification and digitization pipeline and the control and reconstruction computer. Each mentioned part will be briefly discussed to provide a basic understanding of its operation and the associated challenges that might arise and lead to non-ideal behavior.

2.1.1 Main Magnet

The function of the main magnet is to produce a static magnetic field inside a given volume, called B_0 field. This can be achieved with different types and designs of magnets such as open c-shaped magnets – either as permanent magnets or electromagnets – or in a closed-bore cylindrical design using solenoid type electromagnets around the bore. To achieve high magnetic fields (3 T or higher)

Die approbierte gedruckte Originalversion dieser Dissertation ist an der TU Wien Bibliothek verfügbar.
The approved original version of this doctoral thesis is available in print at TU Wien Bibliothek.
TU Bibliothek Your knowledge hub WIEN

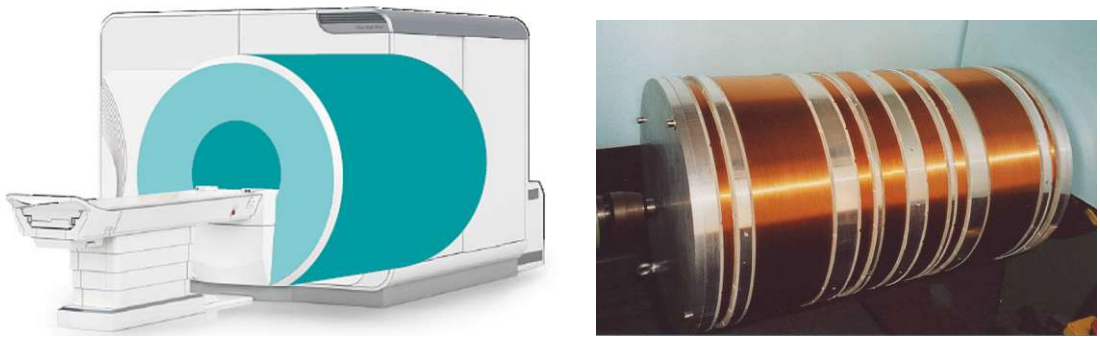

Figure 2.1: MRI magnet design; the left image shows the design of a 7 T MR scanner (Copyright of Siemens Healthineers), where the patient table is inserted into the bore of the turquoise cylinder that includes a similar magnet to that on the right image. The right image (Courtesy of Allen D. Elster, MRIquestions.com) shows a superconducting magnet in production with multiple coil segments to produce a homogeneous magnetic field.

inside a large volume human scanners only exist as solenoid type. The creation of such high fields requires the electromagnets to be operated in superconducting mode with a temperature of about 4 K (−269 °C), achieved by a combination of liquid helium cooling, cold shielding and active cryocoolers. Figure 2.1 shows an model of a 7 T MR scanner with the turquoise cylinder containing the main magnet. An open main magnet in production is shown on the right side of the image. It is divided into several coil segments, which increases the homogeneity of the generated magnetic field. The direction of the main magnetic field is along the bore, usually referred to as the $\vec{z}$-direction.

2.1.2 Electromagnetic Shielding

Different types of shielding are required for MR scanners. The field lines of a solenoid magnet close on the outside of the bore to form a loop, which would cause a large static magnetic field surrounding the MR machine. This is partly avoided by passive iron shielding that guides the field lines closer to the solenoid magnet and, in some newer models, is further reduced with active shielding coils at the edges of the bore. As an additional measure, MR rooms usually contain passive magnetic shielding in the walls, made from copper or iron to limit the static fringe fields that reach outside the MR room. Another function of the shielding in the walls of the MR room is radiofrequency shielding, to avoid interference from RF fields emanating from outside sources, for example an electromagnetic signal created by a passing vehicle.

Die approbierte gedruckte Originalversion dieser Dissertation ist an der TU Wien Bibliothek verfügbar.
The approved original version of this doctoral thesis is available in print at TU Wien Bibliothek.
TU Bibliothek Your knowledge hub WIEN

2.1.3 Radiofrequency Coils

The radiofrequency coils perform two major tasks when performing an MR measurement; the excitation of magnetic spins and the acquisition of the resonance signal. In principle, both tasks could be achieved by the same RF coil. However, to increase homogeneity and signal-to-noise ratio (SNR) excitation and acquisition is commonly split between specialized coils. The RF coils are tuned to the Larmor frequency of the magnetic spins to be excited, which is in the radiofrequency range for common field strengths of a few Tesla, thereby giving them their name. The physical concepts regarding the excitation of magnetic spins using RF fields are further discussed in Subsection 2.2.3. The working principles of RF coils are divided into two different types, linearly polarized and circularly polarized [3], where the first type can detect or emit a linear projection of the complex signal (rotating spins) and the second type two orthogonal projections, the real and imaginary part of the complex signal. Linear polarized coils have a $\sqrt{2}$ loss of sensitivity, requiring more power for excitation and receiving a signal with lowered amplitude. The sizes and shapes of RF coils can vary strongly, ranging from whole body coils to few-centimeters small single-loop surface coils.

2.1.3.1 Coil sensitivity

The field generated by an RF coil is called the B_1 field and its sensitivity is not uniform due to the hardware setup and propagation and attenuation effects of the electromagnetic wave inside the measured object. The shape of the B_1 field in vacuum can be calculated from the currents that are applied in the RF coils using the Biot-Savart law. However, the interaction of the B_1 field with the measured tissue plays an important role, creating local currents that mainly attenuate the B_1 field, and is characterized by the permittivity and conductivity of the tissue. At an higher frequency of the B_1 field (which is given by the strength of the main magnetic field B_0), the permittivity and thus penetration depth is lower.

This can be understood by viewing the main contributions to the currents induced in tissue, which are translational motion of ions and rotational motion of electric dipoles (water molecules). With a static or low frequency field, the motion of ions is stopped at boundaries and the rotational motion of dipoles stops in their aligned state, resulting in low induced current. When increasing the frequency of the B_1 field, fewer ions and dipoles reach their end state in a single cycle resulting in a higher induced current [4].

The RF wavelength at high B_0 fields is only several centimeters long, and causes the B_1 field to have a strong spatial dependency. This has a severe effect on the phase part of the measured signal and is referred to as phase offsets. It can be thought of as a phase change (or spin rotation) that occurs during the time that

Die approbierte gedruckte Originalversion dieser Dissertation ist an der TU Wien Bibliothek verfügbar.
The approved original version of this doctoral thesis is available in print at TU Wien Bibliothek.
TU Bibliothek Your knowledge hub WIEN

the electromagnetic signal requires to travel the distance from the voxel location to the coil it is measured at. As the propagation speed of electromagnetic waves depends on the matter it passes through, these spatial phase variations not only depend on the geometry of the setup, but also on the electromagnetic properties of the measured object. A last and setup specific contribution is an arbitrary global phase offset added by the readout chain, which has no spatial dependence but varies for each coil.

At low field strengths, the transmit field B_1^+ and the receive field B_1^- are very similar, although at higher field strengths, significant asymmetries arise between the two [5]. The sensitivity is given as a complex field containing both magnitude and phase. If it is known, the induced inhomogeneity and phase offset can be corrected.

2.1.3.2 Coil types

A plethora of different coil types exist for MR measurements. The most common are cylindrical birdcage coils that consist of two conductive loops connected with long rungs. These are circularly polarized volume coils and are used as whole body coils or head coils for both transmitting and receiving. The advantage of this type is a mostly homogeneous coil sensitivity at lower field strengths. The disadvantages are a low signal yield and severe central signal attenuation especially for the shorter wavelengths encountered at higher field strengths.

Surface coils are small coils (often only a single loop) that have high sensitivity in close proximity to the coil, but a steep drop-off and very low signal in regions further away. Also the phase component of their B_1 field tends to be highly inhomogeneous. The problem of low sensitivity in distant regions can be mitigated by connecting a number of surface coils in an array. When designed in an overlapping fashion, such that the inductance of neighboring coils vanishes, it is called a phased array, with the advantage of avoiding unwanted crosstalk between coils. These phased array coils can be in the shape of a flexible blanket for torso measurements, but also as a helmet for head measurements and are usually only used for receiving the signal.

2.1.4 Gradient Coil

The generation of spatial information in MRI is based on acquiring multiple resonance signals with a set of different gradients applied to the magnetic field, and those gradients are generated by dedicated gradient coils. There is an individual set of gradient coils for each spatial direction, $\vec{x}$, $\vec{y}$ and $\vec{z}$. A gradient in a certain direction corresponds to a linear change of the amplitude of the main magnetic field in that direction.

Die approbierte gedruckte Originalversion dieser Dissertation ist an der TU Wien Bibliothek verfügbar.
The approved original version of this doctoral thesis is available in print at TU Wien Bibliothek.
TU Bibliothek Your knowledge hub WIEN

By applying magnetic field gradients, the direction of the main magnetic field B_0 is only marginally influenced and still points in the $\vec{z}$ direction, as the magnetic field produced by the gradient coil is considerably smaller than the main magnetic field. In 7 T scanners, gradient coils can usually produce a maximum gradient strength of about 40 mT/m. The gradient coils are placed inside the bore one layer closer to the central axis than the main magnetic field coil.

2.1.4.1 Eddy currents

Most sequences require the gradients to rapidly change or oscillate, effectively producing a time varying magnetic field, and which according to the Maxwell equations induces an electric current in conductive materials. This causes heating of biological tissue as well as peripheral nerve stimulation and therefore, to ensure a safe operation, the MR hardware enforces strict limitations on fast changing gradients to stay within safety limits.

Further eddy current related effects occur from currents that are induced in other coil elements, which leads to temporary inhomogeneities or imperfections in the magnetic field due to both current induced in other coils, as well as a lower effective field produced from the original coil. A common manifestation of an eddy current artefact is the appearance of additional ghost images of the original object that are shifted and overlayed on the reconstructed image.

2.1.4.2 Gradient timing mismatch

Due to eddy currents and other system imperfections a gradient timing mismatch can occur, which is when the effective center of the gradient does not correspond to the timing that is expected by the sequence. In the reconstructed image, this leads to phase shift that changes linearly in readout direction, the direction of the fast switching gradient that causes the eddy currents. Especially bipolar multi-echo acquisitions, which are efficient imaging schemes introduced in Section 2.3.1.4, suffer from this gradient timing mismatch, which can lead to severe artefacts. Solutions to remove these artefacts in post-processing are presented in Section 3.1.3.

2.1.5 Active Shim Coils

Even if the main magnetic field would be perfectly homogeneous, introducing an object causes the field to change due to an interaction of the main magnetic field with the magnetic susceptibility distribution inside the object. Active shimming tries to reduce the inhomogeneity of the magnetic field by applying a combination of currents to multiple shim coils, effectively producing a non-linear field with the opposite direction of the field distortions. Usually a fast phase imaging scan

Die approbierte gedruckte Originalversion dieser Dissertation ist an der TU Wien Bibliothek verfügbar.
The approved original version of this doctoral thesis is available in print at TU Wien Bibliothek.
TU Bibliothek Your knowledge hub WIEN

is performed to measure the field distortions (ΔB_0) and then currents are estimated by theoretical models and applied to the shim coils. This procedure is often performed iteratively to obtain an optimally shimmed volume for measurement.

2.1.6 Signal Amplifier and Digitization

When a magnetic resonance signal induces a current in a receive coil, it has to be amplified first to be able to perform a measurement. The preamplifiers are usually placed close to the coils directly inside the bore of the MR scanner to prevent contamination of the signal with noise. The next stage is amplification and digitization of the signal, which is usually performed outside of the scanner but increasingly placed closer to the coils in newer models. The biggest frequency component of the induced signal is the frequency of the main magnetic field, which, however, is not of interest in the measurement. Therefore, the digitization is performed in the rotating frame of reference with the frequency of the main magnetic field removed, which is either achieved by analog signal manipulation or in the digitization process. Two different cases of signals have to be distinguished here, signals from circularly polarized coils with real and imaginary parts and from linearly polarized ones with only a real part. Signals in the first case can be directly converted into the complex signals required for further signal processing, while the latter need an imaginary part to be added, which is commonly performed by applying a phase shift of 90° to the real part.

2.1.7 Control and Reconstruction Computer

The sequence execution with controlling the transmission coils, the gradients and the active shims is performed by the specially designated control computer, which is optimized for realtime control. The digital preprocessing of the large amount of acquired data is performed in a reconstruction pipeline on the reconstruction hardware, designed for high data throughput and computation power, often with graphic processing units in newer models for high performance of parallel execution and possibly with a view to machine learning applications directly on the hardware of the scanner. A third computer is the access terminal, which is used by the operator to select the sequences to be run and receive the images after reconstruction.

2.2 (N)MR - Signal Formation

This chapter discusses the theoretical background of nuclear magnetic resonance, the physical principles involved in MR measurements. The signal that is measured

Die approbierte gedruckte Originalversion dieser Dissertation ist an der TU Wien Bibliothek verfügbar.
The approved original version of this doctoral thesis is available in print at TU Wien Bibliothek.
TU Bibliothek Your knowledge hub WIEN

in magnetic resonance originates in the magnetic moment created by an ensemble of nuclear spins after excitation with a radiofrequency pulse. To disassemble this complex process, first a single spin in a magnetic field is considered.

2.2.1 Single Spin in Magnetic Field

A single magnetic spin in a magnetic field can be thought of as a vector rotating around the magnetic field direction, where its origin is the same as the origin of the magnetic field vector, a motion called precession. This simple visualization of a precessing spin as a classical system, however, is only valid if the quantum mechanical spin system has two 2 eigenstates, which is the case for a single proton. This subsection, however, discusses the quantum mechanical view of a single spin in a magnetic field.

2.2.1.1 Quantum mechanical description

The nuclear magnetic moment of an element arises from the spins of its constituents – the neutrons and protons. In the simplest case of the hydrogen atom H, the nucleus consists of only one proton. The nuclear magnetic moment arises from the spin of the proton, which is $S = \frac{1}{2}$. Magnetic resonance imaging is mainly performed with hydrogen due to its abundance and only in niche cases other elements are considered. Therefore, this description only concerns itself with the proton, the nucleus of the hydrogen atom.

For a spin $\frac{1}{2}$ system, as is the magnetic moment of the proton, there are two possible spin states $m \in \left[\frac{1}{2}, -\frac{1}{2}\right]$, which are commonly called up ($\uparrow$) and down ($\downarrow$). m is related to the z-component of the spin vector $\boldsymbol{S}$ via $S_z = m\hbar$, where $\hbar$ is the reduced Planck constant. The spin vector $\boldsymbol{S}$ translates further to the magnetic dipole moment $\boldsymbol{\mu}$ via the gyromagnetic ratio γ with the relation

$$\boldsymbol{\mu} = \gamma \boldsymbol{S}. \tag{2.1}$$

The gyromagnetic ratio γ is a factor that describes the strength of the produced magnetic moment and depends on the internal structures of the observed particle, for example in the case of a proton, the dynamic of quarks inside the nucleon leads to the magnetic moment.

2.2.1.2 Energy eigenstates

The magnetic dipole moment $\boldsymbol{\mu}$ interacts with the magnetic field, causing the two spin state system to split into two states with different energy when measured, the eigenstates of the system. This effect is called the Zeeman effect. The energy

Die approbierte gedruckte Originalversion dieser Dissertation ist an der TU Wien Bibliothek verfügbar.
The approved original version of this doctoral thesis is available in print at TU Wien Bibliothek.
TU Bibliothek Your knowledge hub WIEN

difference between the states ΔE depends on the strength of the magnetic field and the gyromagnetic ratio of the particle that is observed. It is given by

$$\Delta E = \gamma \hbar B_0 \tag{2.2}$$

and the energies $E_\uparrow$ and $E_\downarrow$ for the two eigenstates are given by

$$E_\uparrow = -\frac{1}{2}\gamma \hbar B_0. \tag{2.3}$$

$$E_\downarrow = +\frac{1}{2}\gamma \hbar B_0 \tag{2.4}$$

Due to the conservation of energy, the transition from $E_\uparrow$ to $E_\downarrow$ requires the energy ΔE, which can be provided by the absorption of a photon with matching energy ΔE, and the opposite transition from $E_\downarrow$ to $E_\uparrow$ leads to the transmission of a photon with energy ΔE. The frequency ν_0 of the photon in relation to its energy ΔE is given by

$$\Delta E = h\nu_0 \tag{2.5}$$

$$= \hbar 2\pi \nu_0, \tag{2.6}$$

with the Planck constant $h = \hbar 2\pi$. The Larmor frequency ω_0 is the corresponding frequency of the magnetic spin of the proton, which is

$$\omega_0 = 2\pi\nu_0, \tag{2.7}$$

where the factor 2π stems from the conversion between angular frequency used for precession (ω_0) and ordinary frequency used for photons (ν_0). By combining the equations 2.2, 2.6 and 2.7, the angular frequency of the precession of the magnetic spin can be determined as

$$\omega_0 = \gamma B_0. \tag{2.8}$$

In the classical view, the precession frequency ω_0 is the number of revolutions of the magnetic moment per time, and for a magnetic field strength of 7 T it is about 298 MHz.

Die approbierte gedruckte Originalversion dieser Dissertation ist an der TU Wien Bibliothek verfügbar.
The approved original version of this doctoral thesis is available in print at TU Wien Bibliothek.
TU Bibliothek Your knowledge hub WIEN

2.2.2 An Ensemble of Spins

If there are multiple spins inside the measured volume, all those spins need to be considered together as an ensemble, which creates a net magnetization vector that gives rise to the signal that is measured. The consideration as an ensemble means that no collapse of the wave function of individual spins occurs during the measurement (see [6] for details) and the individual spins are not forced to take the eigenstates of the system, but are weighted combinations of the eigenstates.

In the absence of an external magnetic field, all states are equally likely, which leads to a spherical distribution of the spins and results in zero net magnetization of the ensemble. In a magnetic field, each spin individually precesses around the magnetic field vector and additionally there is a slight tendency toward the lower energy state. This creates a non vanishing net magnetization vector pointing in the opposite direction of the magnetic field, with its size depending on the skewness of the spin distribution. The thermal energy is still orders of magnitude larger than the influence of the magnetic field and the distribution of spins is only slightly shifted away from a symmetrical distribution. The distribution of states in system can be calculated with the Boltzmann distribution and, in thermal equilibrium, only depends on the energies of the states and the temperature.

2.2.2.1 Boltzmann distribution

The magnetic moment of an ensemble of spins in its thermal equilibrium can be either calculated classically via the integral over the angular Boltzmann distribution of spins [6] or in the quantum mechanical view using the projection onto the two eigenstates. In the quantum mechanical view, the Boltzmann distribution of the eigenstates at the temperature T is given with the probability $P_{\uparrow,\downarrow}$ by

$$P_{\uparrow,\downarrow} = \frac{\exp\left(-E_{\uparrow,\downarrow}/kT\right)}{\exp\left(-E_{\uparrow}/kT\right) + \exp\left(-E_{\downarrow}/kT\right)} \tag{2.9}$$

and when inserting the energy levels of the eigenstates in relation to the magnetic field B_0 (equations 2.3 and 2.4) it translates to

$$P_{\uparrow,\downarrow} = \frac{\exp\left(\pm\hbar\gamma B_0/2kT\right)}{\exp\left(\hbar\gamma B_0/2kT\right) + \exp\left(-\hbar\gamma B_0/2kT\right)}. \tag{2.10}$$

Die approbierte gedruckte Originalversion dieser Dissertation ist an der TU Wien Bibliothek verfügbar.
The approved original version of this doctoral thesis is available in print at TU Wien Bibliothek.
TU Bibliothek WIEN Your knowledge hub

The net longitudinal magnetization per spin is

$$\begin{aligned}
\langle \mu_z \rangle &= \mu \left(P_\uparrow - P_\downarrow \right) && (2.11)\\
&= \mu \frac{\exp\left(-E_\uparrow/kT\right) - \exp\left(-E_\downarrow/kT\right)}{\exp\left(-E_\uparrow/kT\right) + \exp\left(-E_\downarrow/kT\right)} && (2.12)\\
&= \mu \frac{\exp\left(E_\downarrow/kT\right) - \exp\left(-E_\downarrow/kT\right)}{\exp\left(E_\downarrow/kT\right) + \exp\left(-E_\downarrow/kT\right)} && (2.13)\\
&\approx \mu E_\downarrow/kT && (2.14)\\
&= \frac{\mu \hbar \gamma B_0}{2kT}, && (2.15)
\end{aligned}$$

where the approximation comes from the Taylor expansion around $a = 0$ as

$$\frac{\exp(a) - \exp(-a)}{\exp(a) + \exp(-a)} = a - \frac{a^3}{3} + \frac{2a^5}{15} + O\left(a^6\right), \tag{2.16}$$

where all terms except a can be dropped for very small $a = E_\downarrow/kT$, as is the case. The resulting net magnetization in z-direction, M_z, is the product of the net longitudinal magnetization per spin $\langle \mu_z \rangle$ and the number of the spins N:

$$M_z = N \langle \mu_z \rangle = \frac{N \mu \hbar \gamma B_0}{2kT} \tag{2.17}$$

Due to the symmetry of the system, all contributions other than in the z-direction cancel out, leaving only the M_z component in thermal equilibrium.

2.2.2.2 Rotating frame of reference

If the net magnetization vector $\boldsymbol{M}$ is not in equilibrium but contains transverse components in the x- or y-direction, it starts precessing around the main magnetic field B_0 – as a linear combination of individually precessing proton spins – with identical frequency ω_0. The mathematical description of the system in the rotating frame of reference with the frequency ω_0 leads to a simpler notation and helps understanding the effects of applying a radio frequency excitation pulse (Section 2.2.3).

The magnetic field is not completely homogeneous inside the volume of interest, with $B(\boldsymbol{r}) = B_0 + \Delta B_0(\boldsymbol{r})$ and therefore, the precession frequency $\omega(\boldsymbol{r})$ is spatially dependent as well. Analogous to Equation 2.8, the precession frequency is given by

$$\omega(\boldsymbol{r}) = \gamma B(\boldsymbol{r}) = \gamma \left(B_0 + \Delta B_0(\boldsymbol{r}) \right) = \overbrace{\gamma B_0}^{\omega_0} + \overbrace{\gamma \, \Delta B_0(\boldsymbol{r})}^{\Delta\omega(\boldsymbol{r})}. \tag{2.18}$$

Die approbierte gedruckte Originalversion dieser Dissertation ist an der TU Wien Bibliothek verfügbar.
The approved original version of this doctoral thesis is available in print at TU Wien Bibliothek.
TU Bibliothek Your knowledge hub WIEN

In the rotating frame of reference, ω (r) is substituted by $\omega'(\boldsymbol{r}) = \omega(\boldsymbol{r}) - \omega_0$, and the equation simplifies to

$$\omega'(\boldsymbol{r}) = \gamma \Delta B_0(\boldsymbol{r}) = \Delta\omega(\boldsymbol{r}). \tag{2.19}$$

Formally, the transformation between the axes is given by [7]

$$x = x' \cos(\omega_0 t) - y' \sin(\omega_0 t) \tag{2.20}$$
$$y = x' \sin(\omega_0 t) - y' \cos(\omega_0 t) \tag{2.21}$$
$$z = z'. \tag{2.22}$$

2.2.3 Excitation

The excitation of an ensemble of spins has to be distinguished from the excitation of a single spin. The excitation of a single spin from the lower energy state into a higher energy state via a photon of the exact energy $\Delta E = \gamma \hbar B_0$ requires a collapse of the wave function into the eigenstate with the higher energy $E_{\downarrow}$. The excitation of the ensemble of spins on the other hand does not lead to a collapse of the wave function, as there is no possibility to infer the state of the individual spins from the measurement. The excitation of an ensemble of spins via an RF pulse can be seen as the application of the RF pulse on the net magnetization vector [6].

2.2.3.1 Bloch equation without relaxation

The effect of a magnetic field $\boldsymbol{B}$ on a magnetic moment $\boldsymbol{M}$ is given by the differential equation

$$\frac{d\boldsymbol{M}(t)}{dt} = \gamma \boldsymbol{M}(t) \times \boldsymbol{B}(t). \tag{2.23}$$
$$= \gamma \begin{pmatrix} 0 & B_z & -B_y \\ -B_z & 0 & B_x \\ B_y & -B_x & 0 \end{pmatrix} \begin{pmatrix} M_x \\ M_y \\ M_z \end{pmatrix} \tag{2.24}$$

The individual components of $\boldsymbol{B}(t)$ and $\boldsymbol{M}(t)$ are also time dependent. To avoid cluttering the formulation, the time dependence of the components is omitted in Equation 2.24 and the following subsection. In the case of a static magnetic field, Equation 2.24 describes the previously mentioned precessing motion of $\boldsymbol{M}(t)$ around $\boldsymbol{B}_0$.

Die approbierte gedruckte Originalversion dieser Dissertation ist an der TU Wien Bibliothek verfügbar.
The approved original version of this doctoral thesis is available in print at TU Wien Bibliothek.
TU Bibliothek Your knowledge hub WIEN

2.2.3.2 Radiofrequency pulse

We start by considering an excitation that is performed on the net magnetization vector in its equilibrium position, with the only non-zero component M_z pointing in the direction of the main magnetic field. The frequency of the RF pulse has to be matched to the precession frequency ω_0 of the magnetization, which, in the rotational frame of reference, simplifies the notation of B_1, the magnetic component of the RF field, to have B_{1x} as only non-zero component. The application of the RF pulse on the magnetization vector in the rotating frame can be written using Equation 2.23 as the differential equation

$$\frac{d\boldsymbol{M}}{dt} = \gamma \begin{pmatrix} 0 & 0 & 0 \\ 0 & 0 & B_{1x} \\ 0 & -B_{1x} & 0 \end{pmatrix} \begin{pmatrix} M_x \\ M_y \\ M_z \end{pmatrix} \tag{2.25}$$

with the solution

$$\boldsymbol{M}(t) = \begin{pmatrix} 1 & 0 & 0 \\ 0 & \cos(\omega_1 t) & \sin(\omega_1 t) \\ 0 & -\sin(\omega_1 t) & \cos(\omega_1 t) \end{pmatrix} \begin{pmatrix} M_x(0) \\ M_y(0) \\ M_z(0) \end{pmatrix} = \boldsymbol{R}(t) \cdot \boldsymbol{M}_0, \tag{2.26}$$

where $\omega_1 = \gamma B_{1x}$ and $\boldsymbol{R}$ is a rotation matrix in the yz-plane [7]. The flip angle α is the angle by which the magnetization vector is rotated about the x'-axis, the substituted axis in the rotating frame of reference. It can be calculated as the rotation performed by $\boldsymbol{R}$ to be $\alpha = \omega_1 t_{\mathrm{RF}}$, or in terms of the RF pulse B_1 as

$$\alpha = \gamma B_{1x} t_{\mathrm{RF}}, \tag{2.27}$$

with t_{RF} being the time for which the RF pulse is applied. Thus, by adjusting the amplitude or the duration of the RF pulse, a desired value for α can be selected.

2.2.4 Relaxation Processes

After flipping the net magnetization into the xy-plane by RF excitation of the spin ensemble, the planar projection of precessing net magnetization can be measured. The planar projection of the net magnetization vector slowly diminishes by different mechanisms, which are called relaxation processes. These relaxation processes strongly depend on the tissue as well as the magnetic field strength and return the system into its thermal equilibrium.

2.2.4.1 T_1 relaxation

Longitudinal, or spin-lattice relaxation with relaxation constant T_1 is caused by the interactions of the spins with their neighboring atomic environment. The

Die approbierte gedruckte Originalversion dieser Dissertation ist an der TU Wien Bibliothek verfügbar.
The approved original version of this doctoral thesis is available in print at TU Wien Bibliothek.
TU Bibliothek Your knowledge hub WIEN

relaxation is formulated as an exponential regrowth of the z-component of the net magnetization while it returns to its equilibrium state aligned with B_0. Assuming a 90° flip of the magnetization into the xy-plane, the z-magnetization slowly recovers over time as

$$M_z(t) = M_0\left(1 - e^{-t/T_1}\right). \tag{2.28}$$

The signal recovery is important for consecutive excitations, as only the recovered signal part can be flipped. Waiting a longer time between excitations leads to larger signal excitations but more unused time between measurements, and a trade-off has to be determined matched to the specific sequence settings. The T_1 time constant for signal recovery is in a macroscopic range of $1-2\,\mathrm{s}$ at $7\,\mathrm{T}$ field strength in brain tissue. The same phenomenon can also be expressed as decay in the xy-plane as

$$M_{xy}(t) = M_0 e^{-t/T_1}, \tag{2.29}$$

where $M_{xy} = \sqrt{M_x^2 + M_y^2}$.

2.2.4.2 T_2 relaxation

The transverse relaxation with the relaxation constant T_2 occurs due to spin dephasing in the transverse (xy-)plane caused by variations in the local Larmor frequencies. The variation in Larmor frequencies leads to a loss of phase coherence, which in turn leads to an exponential decay of the transverse component of the magnetization M_{xy}:

$$M_{xy}(t) = M_0 e^{-t/T_2} \tag{2.30}$$

Usually, T_2-decay has a shorter time constant than T_1-decay with relaxation times in the range of $30-50\,\mathrm{ms}$ at $7\,\mathrm{T}$ field strength in brain tissue. Therefore, when considering the decay after an excitation, the T_1-decay is often neglected, as T_2-decay is the dominant effect.

2.2.4.3 T_2^* and T_2' relaxation

T_2^*-decay includes the effects discussed under T_2-decay and additional contributions that depend not only on the tissue but also on the measurement, called T_2'-decay. Although it is referred to as T_2'-decay, it is not a true decrease in magnetization, but an effect caused by the nature of the measurement. This additional effect is caused by inhomogeneities in the local B_0 field, which can cause signal reduction in a measurement if the phase change within a voxel is too large to cause destructive interference. The inhomogeneities arise from the microscopic heterogeneity of the tissue with a different range of susceptibilities. The measured effect is similar to T_2-decay in that it leads to varying precession frequencies within voxels and thus signal decay. However, due to its systematic nature, it can be recovered, which

Die approbierte gedruckte Originalversion dieser Dissertation ist an der TU Wien Bibliothek verfügbar.
The approved original version of this doctoral thesis is available in print at TU Wien Bibliothek.
TU Bibliothek Your knowledge hub WIEN

is performed in spin echo imaging but is not discussed in detail in this work. If not recovered, this T_2'-decay is combined with the T_2-decay resulting in the faster effective decay of the transverse magnetization, T_2^*-decay, which is described as

$$\frac{1}{T_2^*} = \frac{1}{T_2} + \frac{1}{T_2'}. \tag{2.31}$$

Analogously to T_2-decay, it can be formulated as exponential decay

$$M_{xy}(t) = M_0 e^{-t/T_2^*} \tag{2.32}$$

and replaces T_2-decay. Commonly encountered T_2^*-decay values are $25 - 35\,\mathrm{ms}$ for brain tissue and $5 - 10\,\mathrm{ms}$ for veins at $7\,\mathrm{T}$.

2.2.4.4 Bloch equation with relaxation

The complete Bloch equation contains the relaxation terms for T_1 and T_2 described above. T_2^* is not included, as it is an effect related to the measurement and not only the magnetic moment and tissue constants. The Bloch equation in matrix notation is given by

$$\frac{d\boldsymbol{M}(t)}{dt} = \gamma \boldsymbol{M}(t) \times \boldsymbol{B}(t) - \begin{pmatrix} \frac{M_x(t)}{T_2} \\ \frac{M_y(t)}{T_2} \\ \frac{M_z(t) - M_0}{T_1} \end{pmatrix}, \tag{2.33}$$

where M_0 is the amplitude of the magnetization in equilibrium. The solution of the Bloch equation is shown in Figure 2.2, starting in the most common condition where the equilibrium magnetization is flipped into the horizontal plane by a 90° RF pulse.

2.3 MRI - From Acquired Signal to Image

The first step in understanding the formation of an image from the measured signal is a simplified formulation of the signal over time. The relaxation is disregarded here as the time for signal acquisition is short compared to the decay time and commonly assumed to happen at a specific time after excitation, the echo time. The precessing magnetization is measured as a projection onto the xy-plane and, disregarding relaxation, it can be represented in complex notation as

$$M(\boldsymbol{r}, t) = M(\boldsymbol{r}) \exp(i\varphi(t)), \tag{2.34}$$

where $M(\boldsymbol{r})$ is the magnitude of the magnetization vector at location $\boldsymbol{r}$, and $\varphi(\boldsymbol{r}, t)$ is the phase at location $\boldsymbol{r}$ and time t after excitation. Since time dependent

Die approbierte gedruckte Originalversion dieser Dissertation ist an der TU Wien Bibliothek verfügbar.
The approved original version of this doctoral thesis is available in print at TU Wien Bibliothek.
TU Bibliothek Your knowledge hub WIEN

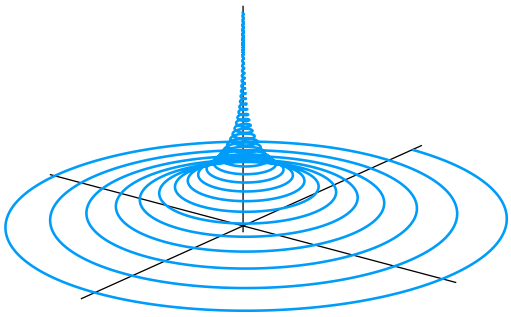

Figure 2.2: Solution to the Bloch equation where the starting point is a 90° flip of the equilibrium magnetization from the z-direction to the y-direction. In the beginning, the dominating effect besides precession is T_2^*-decay, leading to a reduction in signal. Later on, the T_1-relaxation becomes essential in recovering the signal in z-direction towards the equilibrium.

T_1- and T_2-relaxation effects are not important for spatial encoding, they are not considered here and $M(\boldsymbol{r})$ is regarded a constant in time and its values could be calculated from equations 2.29 and 2.32 with the mean of the time of signal acquisition. The induced signal in the receive coil comprises the integration over the whole measured volume

$$S(t) = \int M(\boldsymbol{r}) B_1(\boldsymbol{r}) \exp(i\varphi(\boldsymbol{r}, t))\, d\boldsymbol{r}, \tag{2.35}$$

where $B_1(\boldsymbol{r})$ is the sensitivity of the coil, which, in general, is complex. The phase of the magnetization accumulates as a result of precession with the frequency $\omega(\boldsymbol{r}, t)$ as

$$\varphi(\boldsymbol{r}, t) = -\int_0^t \omega(\boldsymbol{r}, t')\, dt'. \tag{2.36}$$

To simplify the notation, the following description will be in the rotating frame of reference, where the frequency component of interest is $\Delta\omega(\boldsymbol{r}, t) = \gamma \Delta B_0(\boldsymbol{r}, t)$ and the precession of the main magnetic field ω_0 is subtracted (see Equation 2.18), leading to

$$\varphi(\boldsymbol{r}, t)_{\text{rot}} = -\int_0^t \Delta\omega(\boldsymbol{r}, t')\, dt' \tag{2.37}$$

Die approbierte gedruckte Originalversion dieser Dissertation ist an der TU Wien Bibliothek verfügbar.
The approved original version of this doctoral thesis is available in print at TU Wien Bibliothek.
TU Bibliothek Your knowledge hub WIEN

and the complete signal formulation is given as

$$S(t)_{\text{rot}} = \int \rho(\boldsymbol{r}) \exp\left(-i \int_0^t \Delta\omega(\boldsymbol{r}, t')\, dt'\right) d\boldsymbol{r}, \tag{2.38}$$

where the product of $M(\boldsymbol{r})$ and $B_1(\boldsymbol{r})$ has been merged into $\rho(\boldsymbol{r})$. Future considerations will be in the rotating frame of reference and the explicit subscript will be dropped.

2.3.1 K-space Imaging

The basic method of spatial encoding is to perform multiple acquisitions with the application of stepwise varying magnetic field gradients. The application of a gradient $\boldsymbol{G}(t)$ leads to the frequency shift $\gamma\, \boldsymbol{r} \cdot \boldsymbol{G}(t)$ and, together with the magnetic field variations $\Delta B_0(\boldsymbol{r})$ from local susceptibility effects, leads to the precession frequency of $\Delta\omega(\boldsymbol{r}, t) = \gamma \Delta B_0(\boldsymbol{r}) + \gamma\, \boldsymbol{r} \cdot \boldsymbol{G}(t)$. Inserted into Equation 2.38 this leads to the signal formulation

$$S(t) = \int \rho(\boldsymbol{r}) \exp\left(-i \int_0^t \gamma \Delta B_0(\boldsymbol{r}) + \gamma \boldsymbol{r} \cdot \boldsymbol{G}(t')\, dt'\right) d\boldsymbol{r}. \tag{2.39}$$

The accumulated gradient over time can now be isolated and defined as

$$\boldsymbol{k}(t) = \gamma \int_0^t \boldsymbol{G}(t')\, dt' \tag{2.40}$$

and further the phase of interest $\varphi(\boldsymbol{r}, t)$, defined as $\gamma \Delta B_0(\boldsymbol{r})\, t = \varphi(\boldsymbol{r}, t)$, can be found as

$$\int_0^t \gamma \Delta B_0(\boldsymbol{r})\, dt' = \gamma \Delta B_0(\boldsymbol{r})\, t \tag{2.41}$$

$$= \varphi(\boldsymbol{r}, t) \tag{2.42}$$

This phase part does not contain the artificially added gradient but only the magnetic field variation $\Delta B_0(\boldsymbol{r})$ due to the susceptibility distribution of inserted object and system imperfections. Inserted into Equation 2.39 this leads to the signal formulation as

$$S(t) = \int \rho(\boldsymbol{r})\, e^{i\varphi(\boldsymbol{r},t)} e^{-i\boldsymbol{r}\cdot\boldsymbol{k}(t)} d\boldsymbol{r}. \tag{2.43}$$

Next, the complex quantity

$$\Phi(\boldsymbol{r}, t) = \rho(\boldsymbol{r})\, e^{i\varphi(\boldsymbol{r},t)} \tag{2.44}$$

Die approbierte gedruckte Originalversion dieser Dissertation ist an der TU Wien Bibliothek verfügbar.
The approved original version of this doctoral thesis is available in print at TU Wien Bibliothek.
TU Bibliothek WIEN Your knowledge hub

is defined that represents both the magnitude (ρ) and phase (φ) information. Substituting it in Equation 2.43, and making the signal dependence on $\boldsymbol{k}$ explicit, leads to the k-space formulation of signal encoding

$$S(\boldsymbol{k}, t) = \int \Phi(\boldsymbol{r}, t)\, e^{-i\boldsymbol{r}\cdot k} d\boldsymbol{r}. \tag{2.45}$$

The appealing property of this formulation is that $S(\boldsymbol{k}, t)$ resembles the Fourier transform of $\Phi(\boldsymbol{r}, t)$. To obtain the complex signal $\Phi(\boldsymbol{r}, t)$ in image space from the acquired signal $S(\boldsymbol{k}, t)$, the inverse Fourier transform can be applied as

$$\Phi(\boldsymbol{r}, t) = \int S(\boldsymbol{k}, t)\, e^{i2\pi\boldsymbol{r}\cdot\boldsymbol{k}}. \tag{2.46}$$

The practical reconstruction of an image is performed on a grid of values for $\Phi(\boldsymbol{r}, t)$, for which the signal $S(\boldsymbol{k}, t)$ is measured for a matching grid of $\boldsymbol{k}$ values at time t. Ideally t is kept constant for the measurement to obtain $\Phi(\boldsymbol{r}, t = T_E)$ but in real measurements t is usually confined to a small range around the echo time T_E. To measure $S(\boldsymbol{k}, t = T_E)$ for specific value of $\boldsymbol{k}$, the image gradients $\boldsymbol{G}(t')$ are applied in the time from excitation to measurement so that $\boldsymbol{k}(t) = \gamma \int_0^t \boldsymbol{G}(t')\, dt'$, as described by Equation 2.40. Most common sequences measure a number of $\boldsymbol{k}$ points after one excitation over a small range of changing t values. The path that connects the measured $\boldsymbol{k}$ values is called the k-space trajectory. The acquisition of a full k-space constitutes an MRI sequence and the sequences of interest for this thesis are presented in the following sections. This description of sequences in k-space leads to trajectories that can be understood and visualized in k-space and the computational efficient Fourier transform for image reconstruction. Possible trajectories to sample the k-space are illustrated in Figure 2.3.

2.3.1.1 Gradient echo imaging

In gradient echo imaging (GRE), after each excitation one line in k-space is measured, the direction of which is called the readout direction. Directly after the excitation, the position in k-space is in the center and has to be brought to the beginning of the line to be measured. This is done by applying a strong negative (or prewinder) gradient in readout direction, moving the k-space position in the negative readout direction. At the same time, the application of a short gradient in the orthogonal direction, called the phase encode direction, moves the current position orthogonally to a specific line.

After this preparation, the measurement of a k-space line is performed by applying a gradient in the readout direction that moves the position from the left to right through k-space. The sampling of the signal is divided into discrete steps constituting the sampled k-space points. This sampling pattern is illustrated in

Die approbierte gedruckte Originalversion dieser Dissertation ist an der TU Wien Bibliothek verfügbar.
The approved original version of this doctoral thesis is available in print at TU Wien Bibliothek.
TU Bibliothek Your knowledge hub WIEN

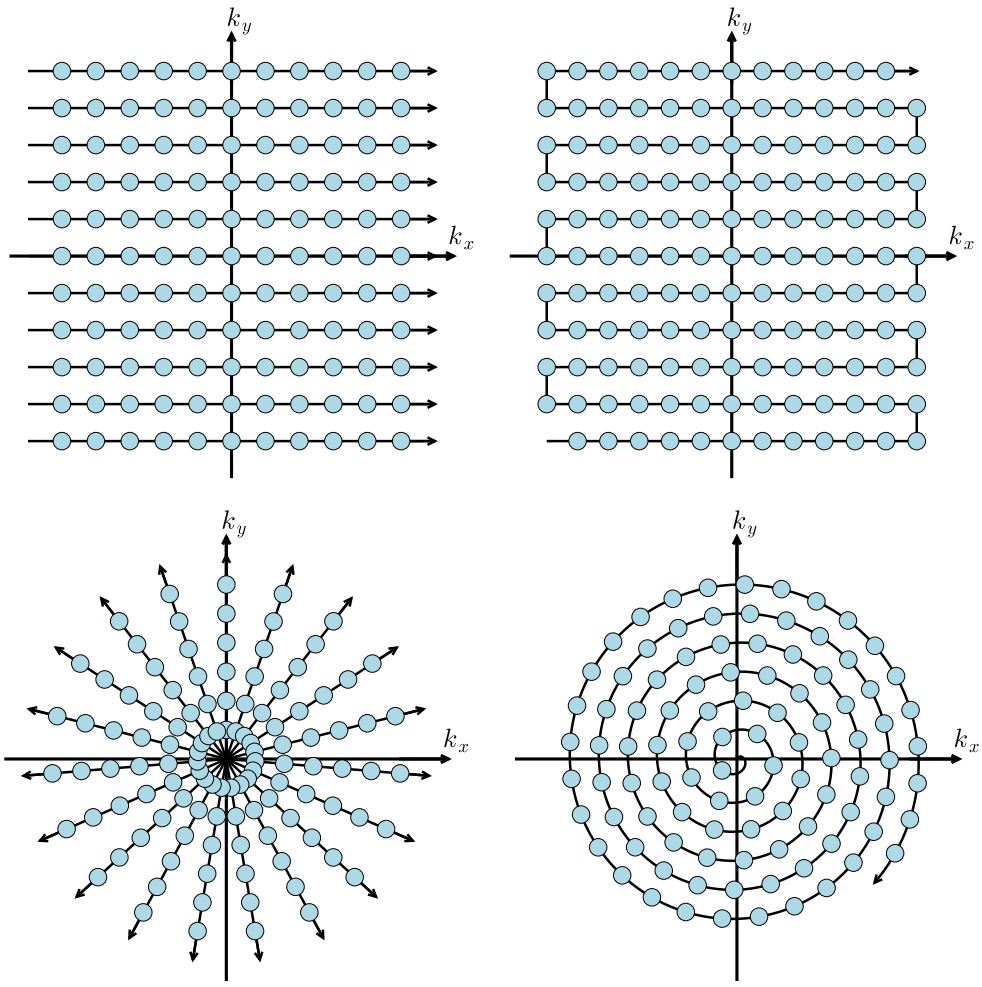

Figure 2.3: Different sampling strategies for a 2D section of k-space. Gradient echo imaging, echo planar imaging, radial imaging and spiral imaging. (Visual presentation based on [8])

Die approbierte gedruckte Originalversion dieser Dissertation ist an der TU Wien Bibliothek verfügbar.
The approved original version of this doctoral thesis is available in print at TU Wien Bibliothek.
TU Bibliothek Your knowledge hub WIEN

Figure 2.3. Since the signal is higher in the central k-space region, the measured signal grows toward the center and shrinks again after passing, which is why the acquisition of a line is called an echo.

2.3.1.2 2D GRE slice selective excitation

The previous section, Gradient Echo Imaging, described the measurement of a 2D grid of k-space points, which translates via Fourier transform into a 2D image. Spins are excited only if the RF frequency precisely matches the precession frequency, which can be exploited to perform subsequent excitations of slices. For this purpose, a slice selective gradient is applied, resulting in precession frequencies that change in the slice direction. Further, an RF pulse is designed to contain a frequency band that excites all spins whose precession frequencies are in the given range, representing an excited slice in the physical object.

After a single k-space line is measured, only a small fraction of the magnetization has returned to its equilibrium position, and therefore k-space lines are typically acquired interleaved over slices to ensure the longest possible time before the next excitation of the same slice to T_1 relaxation.

2.3.1.3 3D GRE k-space imaging

Equation 2.46 describes the relationship between k-space and image space independent of the number of dimensions and identically leads to a 3D image after Fourier transform when applied on a three-dimensional k-space grid. 3D Gradient Echo Imaging is one way of systematically acquiring the 3D k-space and is again based on iteratively acquiring lines. The only differences compared to 2D acquisitions are an excitation of the whole volume and the use of z-gradient blips for reaching the z-coordinate of the k-space line to be measured.

On the one hand, 3D acquisition increases the signal strength due to the excitation of a whole volume instead of only one slice, on the other hand, in 3D acquisitions the time between successive excitations of the same volume is usually very short compared to T_1, so that only a small portion of the magnetic moment is available for the next excitation.

2.3.1.4 Multi echo imaging

An advanced acquisition scheme for 2D and 3D gradient echo imaging is the acquisition of multiple echoes after one excitation. The notion of multiple echoes translates to multiple acquisitions of the same k-space line with increasing echo time – the time at which the center of the line is measured after excitation. The echo time corresponds to the time for signal evolution, and due to tissue dependent decay constants, the image appearance changes with echo time. Typically,

Die approbierte gedruckte Originalversion dieser Dissertation ist an der TU Wien Bibliothek verfügbar.
The approved original version of this doctoral thesis is available in print at TU Wien Bibliothek.
TU Bibliothek Your knowledge hub WIEN

images with short echo times are referred to as T_1-weighted and those with long echo times are referred to as T_2-weighted because the respective constant has the greatest influence on visible contrast.

There are two methods for multi-echo acquisition, monopolar and bipolar, corresponding to the polarity of the gradient during signal sampling. In bipolar multi-echo imaging, after sampling the k-space line, the polarity of the readout gradient is reversed and the same line is sampled again in opposite direction. Monopolar acquisitions first rewind the k-space position to the beginning of the line before the same line is sampled again so that all echoes are sampled in the same direction or with the same polarity.

The additional k-space rewinding required in monopolar acquisitions results in reduced time for signal sampling and thus lower SNR compared to bipolar acquisition. Bipolar acquisitions, however, are subject to certain inconsistencies between echoes due to the change in direction in which lines are acquired.

2.3.2 Bandwidth, Flip Angle and Repetition Time

The flip angle α, introduced in Section 2.2.3.2, describes the rotation of the net magnetization $\boldsymbol{M}(t)$ from the pure alignment in the z-direction into the xy-plane. Due to the long relaxation time T_1 on the order of seconds, it is not efficient to wait several seconds for the signal to fully recover before the next excitation. Therefore, let us consider the excitation of a magnetization that has not yet fully recovered. The only requirement for excitation is the pure alignment of $\boldsymbol{M}(t)$ into the z-direction, which can be easily satisfied by applying so called "crusher" gradients, leading to strong T_2'-decay (see Section 2.2.4.3) to remove signal coherence in the xy-plane.

Considering equally spaced excitations, where the time between excitations is the repetition time T_R, the first excitation flips the whole magnetic moment M_0 by the angle α and subsequent excitation flip only the recovered parts of the magnetization. Usually α is chosen to be smaller than 90°, which means that $\boldsymbol{M}(t)$ has contributions both in the z-direction ($M_0 \cos(\alpha)$) and in the xy-plane ($M_0 \sin(\alpha)$) after applying the RF pulse. For the next excitation, the available magnetization in z-direction is the sum of the previous z-component and the recovered part of the component in the xy-plane:

$$M_z(t = T_R) = M_0 \cos(\alpha) + M_0 \sin(\alpha) \left(1 - e^{-\frac{T_R}{T_1}}\right) \tag{2.47}$$

This system has a dynamic behavior and the available M_z changes from one RF pulse to the next, but after several excitations a steady state is reached where the recovered excitation equals the excitation that is flipped into the xy-plane.

Die approbierte gedruckte Originalversion dieser Dissertation ist an der TU Wien Bibliothek verfügbar.
The approved original version of this doctoral thesis is available in print at TU Wien Bibliothek.
TU Bibliothek Your knowledge hub WIEN

After reaching the steady state, the magnetization in the z-direction available for excitation is given by

$$M_z = \frac{M_0 \left(1 - e^{-\frac{T_R}{T_1}}\right)}{1 - e^{-\frac{T_R}{T_1}} \cos(\alpha)}. \tag{2.48}$$

In the steady state, the excited proportion of M_0 depends on the flip angle and is given by (from Equation 2.48 and flipping by α into the xy-plane)

$$f_\alpha(T_R, T_1, \alpha) = \frac{\left(1 - e^{-\frac{T_R}{T_1}}\right) \sin(\alpha)}{1 - e^{-\frac{T_R}{T_1}} \cos(\alpha)}. \tag{2.49}$$

The flip angle that gives the highest signal is obtained when f_α reaches a maximum and can be determined as

$$\arg\max_\alpha f_\alpha(T_R, T_1, \alpha) = \arccos e^{-\frac{T_R}{T_1}}. \tag{2.50}$$

This optimum flip angle depends on the tissue constant T_1 and the repetition time T_R of the sequence and is called the Ernst angle.

2.3.3 Signal-to-Noise-Ratio in MRI

So far, we have learned that the measured signal of a gradient echo scan decays after excitation with the decay constants T_1 (Equation 2.29) and T_2^* (Equation 2.32). In addition, we have described the proportion of M_0 that is flipped into the xy-plane and available for measurement when a steady state is reached (Equation 2.49). These lead to the signal formulation

$$S = M_0 f_\alpha(T_R, T_1, \alpha) f_{\mathrm{T}_1}(T_1, T_E) f_{T_2^*}(T_2^*, T_E), \tag{2.51}$$

where the terms f_{T_1} and $f_{T_2^*}$ are the respective T_1 and T_2^* decay terms, defined as

$$f_{T_2^*}(T_2^*, T_E) = e^{-\frac{T_E}{T_2^*}} \tag{2.52}$$

$$f_{T_1}(T_1, T_E) = e^{-\frac{T_E}{T_1}}. \tag{2.53}$$

To obtain a realistic formulation of the reconstructed signal in an MRI measurement, an additional sampling factor must be considered that deals with the time spent sampling, T_{acq}, and also includes attenuation effects from the varying echo time of individual k-space points around T_E. The acquisition of one echo does not happen perfectly synchronized at the specified echo time T_E but one echo (or

Die approbierte gedruckte Originalversion dieser Dissertation ist an der TU Wien Bibliothek verfügbar.
The approved original version of this doctoral thesis is available in print at TU Wien Bibliothek.
TU Bibliothek Your knowledge hub WIEN

k-space line) is acquired over the duration T_{acq} (the acquisition time) and is centered at the specified echo time. With a fixed number of k-space points acquired in one echo, a longer acquisition time leads to a longer "dwell" time, which is the time spent at each individual k-space point for signal sampling.

Thus, a longer T_{acq} leads to a higher signal that is obtained, however, a second effect reduces the signal for long T_{acq}, which is when the signals acquired at different times start to dephase. A formulation of signal behavior due to this phenomenon can be found in [9], where it is derived from the formulation for a similarly constructed spin-echo sequence [10]:

$$f_{\text{BW}}\left(T_2^*, T_{\text{acq}}\right) = 2T_2^*\left(1 - e^{-\frac{T_{\text{acq}}}{2T_2^*}}\right) \tag{2.54}$$

This term grows linearly for small acquisition windows T_{acq} compared to T_2^* and saturates for larger acquisition windows. The full formulation of the signal strength at a specific echo time T_E, when acquired over a time T_{acq}, with a repetition time T_R, and the flip angle α for the tissue parameters T_1, T_2^*, and ρ is

$$S\left(T_E, T_{\text{acq}}, T_R, \alpha, T_1, T_2^*, \rho\right) \propto \rho f_\alpha\left(T_R, T_1, \alpha\right) f_{\text{BW}}\left(T_2^*, T_{\text{acq}}\right) f_{\text{T}_1}\left(T_1, T_E\right) f_{T_2^*}\left(T_2^*, T_E\right), \tag{2.55}$$

where M_0 has been additionally replaced with the proportional value of ρ, which is the proton density of the given tissue. The full dependence on the parameters is only shown here for completeness and is left out in following considerations. This signal formulation is the basis of SNR calculations performed in the following subsections and for the contrast-to-noise (CNR) calculation in Section 3.4.5.3.

2.3.3.1 Magnitude SNR

The SNR of the magnitude is difficult to estimate in absolute terms, but the relative SNR when changing the sequence parameters is easier to calculate. The noise in MRI measurements is identical for all echoes and is affected only by the amount of time spent sampling the signal and increases with $\sqrt{T_{\text{acq}}}$, assuming independent noise over the sampling time. Together with the signal from Equation 2.55 the SNR can be written as the proportionality

$$\text{SNR} \propto \frac{S}{\sqrt{T_{\text{acq}}}}. \tag{2.56}$$

As the magnitude signal S grows linearly with T_{acq} for small values of T_{acq}, the SNR increases with $\sqrt{T_{\text{acq}}}$ for small values. Equation 2.56 is later used for simulations of the SNR of different acquisition schemes. When multiple echoes are acquired the resulting SNR depends on the type of combination that is performed, and for the case of SNR-weighted combination is given as

Die approbierte gedruckte Originalversion dieser Dissertation ist an der TU Wien Bibliothek verfügbar.
The approved original version of this doctoral thesis is available in print at TU Wien Bibliothek.
TU Bibliothek Your knowledge hub WIEN

$$\mathrm{SNR}_{\mathrm{ME}} = \sqrt{\sum_i \mathrm{SNR}_i^2}. \tag{2.57}$$

This is also validated for the root-sum-of-squares combination of echoes [9] (more details in Section 2.4.1.1 and Section 2.4.1.2). Often, the SNR efficiency is given, as it allows the fair comparison of sequences with different repetition times. When T_R is doubled, the acquisition takes twice the time and the SNR increase from measuring twice as long is usually $\sqrt{2}$. This leads to the formulation of SNR efficiency as

$$\mathrm{SNRe} = \frac{\mathrm{SNR}}{\sqrt{T_R}}. \tag{2.58}$$

2.3.3.2 Phase SNR

The noise of the phase can be inferred from the magnitude, and a detailed derivation is performed to obtain the relationship. The noise is usually considered to be Gaussian distributed and independent between the real and imaginary part, but with the same standard deviation σ. From geometrical considerations, one can assume that if the magnitude is doubled, the variation of the phase or angle is halved. To confirm this intuitive understanding the noise dependence of the phase is derived here. We begin by formulating the complex number $z = x_1 + i\,x_2$, where x_1 is the real and x_2 the imaginary part. The phase or angle of a complex number is

$$\varphi\left(x_1, x_2\right) = \tan^{-1}\left(\frac{x_2}{x_1}\right). \tag{2.59}$$

Assuming that both x_1 and x_2 have the same noise standard deviation σ, the noise of the phase is given by

$$\sigma_\varphi = \sqrt{\sum_{i=1}^{2}\left(\sigma\frac{\partial\varphi}{\partial x_i}\right)^2}, \tag{2.60}$$

using error propagation. With the derivative $\frac{d\tan^{-1}(x)}{dx} = \frac{1}{x^2+1}$ and the chain rule, the partial derivatives are calculated as

$$\frac{\partial\varphi}{\partial x_1} = \frac{1}{\frac{x_2^2}{x_1^2}+1}\left(-\frac{x_2}{x_1^2}\right) = -\frac{x_2}{x_1^2+x_2^2} \tag{2.61}$$

$$\frac{\partial\varphi}{\partial x_2} = \frac{1}{\frac{x_2^2}{x_1^2}+1}\frac{1}{x_1} = \frac{x_1}{x_1^2+x_2^2}. \tag{2.62}$$

Die approbierte gedruckte Originalversion dieser Dissertation ist an der TU Wien Bibliothek verfügbar.
The approved original version of this doctoral thesis is available in print at TU Wien Bibliothek.
TU Bibliothek Your knowledge hub WIEN

Substituting the results of the partial derivatives into Equation 2.60, we obtain the noise standard deviation of the phase as

$$\sigma_\varphi = \sigma\sqrt{\left(-\frac{x_2}{x_1^2+x_2^2}\right)^2 + \left(\frac{x_1}{x_1^2+x_2^2}\right)^2} \tag{2.63}$$

$$= \sigma\sqrt{\frac{x_1^2+x_2^2}{\left(x_1^2+x_2^2\right)^2}} \tag{2.64}$$

$$= \sigma\frac{1}{\sqrt{x_1^2+x_2^2}} \tag{2.65}$$

$$= \sigma\frac{1}{|z|}, \tag{2.66}$$

using the identity of the magnitude as $|z| = \sqrt{x_1^2+x_2^2}$ in the last step. Equation 2.66 confirms that the standard deviation of the noise of the phase is inversely proportional to the magnitude of a complex number.

For the calculation of SNR values, a signal of interest must be defined in the phase image. This can be a tissue interface, a vein contrast or large effects several centimeters apart due to slow field changes. The size of all these effects depends only on the echo time and grows linearly. Therefore, the SNR can be written as

$$\mathrm{SNR}_{\mathrm{phase}} \propto \frac{T_E}{\frac{1}{M}} = T_E \cdot M, \tag{2.67}$$

where M is the magnitude of the measured signal. According to the signal formulation (Equation 2.55), the magnitude itself depends on the echo time with the two factors f_{T_1} and $f_{T_2^*}$. Usually, only T_2^*-decay is considered, since it is the dominant effect, yielding

$$\mathrm{SNR}_{\mathrm{phase}} \propto T_E \cdot e^{-\frac{T_E}{T_2^*}}. \tag{2.68}$$

The relative phase SNR in dependence of the echo time (Equation 2.68) is shown graphically in Figure 2.4.l

2.3.4 Measurement of Magnitude and Phase

The two-dimensional projection of the magnetization vector into the xy-plane is measured and is commonly expressed as a complex number. This complex character transfers from the measured signal to the reconstructed image $\rho(\boldsymbol{r})$ after the Fourier transform (Equation 2.46). In most applications only the magnitude of the complex signal $M(\boldsymbol{r}) = |\rho(\boldsymbol{r})|$ is considered, since it shows the tissue contrast as

Die approbierte gedruckte Originalversion dieser Dissertation ist an der TU Wien Bibliothek verfügbar.
The approved original version of this doctoral thesis is available in print at TU Wien Bibliothek.
TU Bibliothek Your knowledge hub WIEN

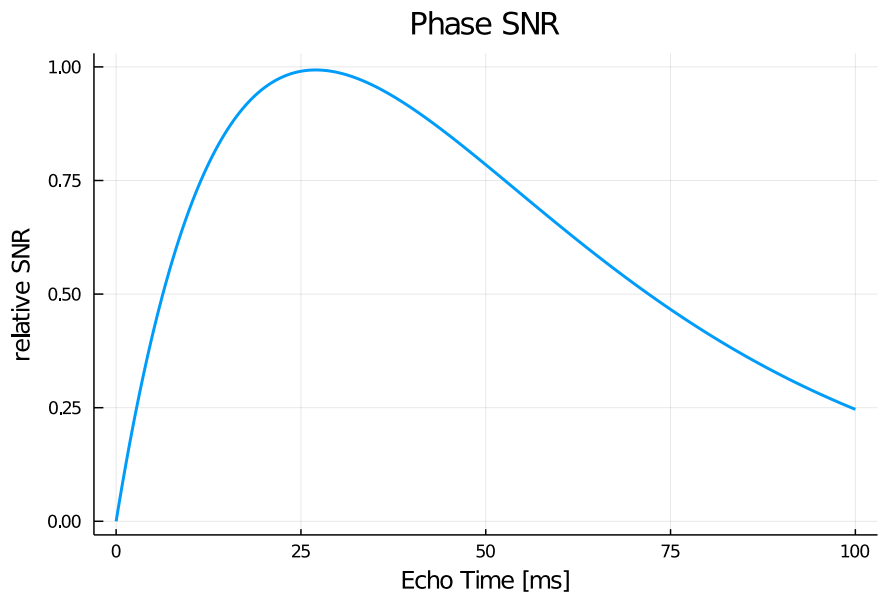

Figure 2.4: Relative SNR of the phase for a range of echo times. $T_2^* = 27\,\text{ms}$ for white matter at 7 T field strength was used. The maximum phase SNR is obtained when the echo time matches T_2^*.

a function of proton density, T_1 and T_2^* values. Other influences on the magnitude are the transmit $(B_1^+(\boldsymbol{r}))$ and receive $(B_1^-(\boldsymbol{r}))$ fields. Due to the absorption of RF-fields in tissue, the intensity of the B_1^+-field decreases after traveling through tissue into regions further away from the excitation coil, effectively resulting in higher flip angles near the coil and lower flip angles further away. This effect is particularly pronounced at high field strengths due to the shorter wavelength and thus faster absorption. The receive field B_1^- (also called sensitivity) similarly depends on the coil geometry and the measured object. It describes the amount of signal received at each coil element, depending on where it was emitted from.

The phase of the complex signal $\varphi(\boldsymbol{r}) = \angle\rho(\boldsymbol{r})$ has several contributions that make it difficult to present as a meaningful image. Since the measurement is performed in the rotating frame of reference (Section 2.1.6 and Section 2.2.2.2), the magnetization vector rotates over time with the difference of the local magnetic field to the main magnetic field, ΔB_0. The interesting contributions to ΔB_0 come from the different susceptibilities of the tissue, which are mostly local and lead to different phase evolutions and thus tissue contrasts. Other contributions to ΔB_0 include a non-uniform B_0 field, non-ideal shimming, or objects inside or outside the measurement volume causing strong susceptibility effects. While ΔB_0 leads to a linear change of the phase over time, there are also constant contributions that depend on the complex aspects of the $B_1^\pm$ fields as well as measurement delays, e.g.

Die approbierte gedruckte Originalversion dieser Dissertation ist an der TU Wien Bibliothek verfügbar.
The approved original version of this doctoral thesis is available in print at TU Wien Bibliothek.
TU Bibliothek Your knowledge hub WIEN

due to cable lengths. All the effects that are constant in time can be summarized into one phase offset term $\varphi_0^c(\boldsymbol{r})$, that depends on the position $\boldsymbol{r}$ and the coil c. An important feature of the phase offsets is that they are spatially smooth, since all contributions produce spatially smooth changes.

2.4 MRI Reconstruction and Preprocessing

Raw data from MRI machines consists of a full 3D volume for each coil. The reconstruction is usually pipelined and requires several steps for reconstruction to the final image, including artefact correction steps, Fourier transform, coil combination, and other preprocessing steps. The steps that are specifically relevant to the topic of this thesis are described in more detail. The following description assumes that Fourier reconstruction has been performed for all coils and that the complex data is split into a magnitude and a phase image.

2.4.1 Magnitude

The magnitude provides information about the proton density ρ and the relaxation constants of the tissue, and after Fourier reconstruction an image is formed for each coil containing one magnitude value per voxel. The influence of the proton density and the relaxation constants can be adapted by selecting specific sequence settings (see Equation 2.55). As each acquisition coil produces one 3D image with essentially the same information but different sensitivity profiles, these need to be combined into one high quality image.

2.4.1.1 Coil combination

The individual magnitude images can be described as the true object O altered by a multiplicative sensitivity field S_i for each coil i and the additive noise term ϵ with a Rician noise distribution and are given as

$$M_i = S_i O + \epsilon, \tag{2.69}$$

where the description is for a single voxel. The objective of coil combination is to add the information from multiple individual coil elements to obtain the true object O with highest possible SNR.

Sensitivity-weighted coil combination With the sensitivities S_i known, a sensitivity-weighted combination can both lead to optimal SNR and remove the false intensity variations due to inhomogeneous sensitivities. The combined magnitude is given as

Die approbierte gedruckte Originalversion dieser Dissertation ist an der TU Wien Bibliothek verfügbar.
The approved original version of this doctoral thesis is available in print at TU Wien Bibliothek.
TU Bibliothek Your knowledge hub WIEN

$$M_{\mathrm{sw}} = \frac{\sum_i M_i S_i}{\sum_i S_i^2} = O + f_{\mathrm{SW}}(\epsilon)\,, \tag{2.70}$$

where f_{sw} is a function of the initial noise. In high SNR regions, this results in both the true object O and the highest possible SNR. In low SNR regions, however, the Rician noise distribution leads to a bias towards larger intensities, which is shown in Figure 2.5. In the left column, the blue histogram contains only noise with the signal set to 0, where the blue histogram in the second image in that column, corresponding to sensitivity-weighted combination, shows a bias of about 1.8 on the x-axis. In all three columns, the contrast between the two regions of interest (ROIs) is kept constant, but the SNR in the individual ROIs is higher towards the right direction. The distributions of the voxels of the two regions are better separated at higher SNR, which is also seen by the calculated CNR values shown in the figure.

However the sensitivities of the individual coils depend not only on the static hardware setup but also on the object inside and are therefore usually not available and the sensitivity-weighted combination is not applied in practice.

Root sum of squares coil combination Root sum of squares (RSOS) is a simple method that does not require measured sensitivities and has high SNR. It computes the voxelwise signal combination via

$$M_{\mathrm{RSOS}} = \sqrt{\sum_i M_i^2} = \sqrt{\sum_i S_i^2} \cdot O + f_{\mathrm{RSOS}}(\epsilon)\,. \tag{2.71}$$

A disadvantage of RSOS is again the bias due to the summation of the Rician noise profile, which is slightly worse than for the sensitivity-weighted combination (Figure 2.5). However, in high SNR regions (right column), the different methods for magnitude combination converge to the same CNR. Another and often larger problem is the presence of sensitivity variations $\sqrt{\sum_i S_i^2}$ after combination, which vary more rapidly in space at higher field strengths.

Adaptive coil combination The "adaptive combine" method [11] performs weighted averaging of the complex signals from the individual coils. Both the signal and noise are modeled as separate stochastic processes and the aim is to maximize the ratio between the two. The theoretical formulation is a stochastic process in time and requires multiple repeated measurements to acquire the noise and signal correlation matrices to perform a voxelwise combination. However, to avoid repeated measurements, adaptive combine takes the approach of computing the signal correlation locally in the image by using the voxels inside a region, and the noise correlation is obtained globally with a fast prescan and is often already

Die approbierte gedruckte Originalversion dieser Dissertation ist an der TU Wien Bibliothek verfügbar.
The approved original version of this doctoral thesis is available in print at TU Wien Bibliothek.
TU Bibliothek Your knowledge hub WIEN

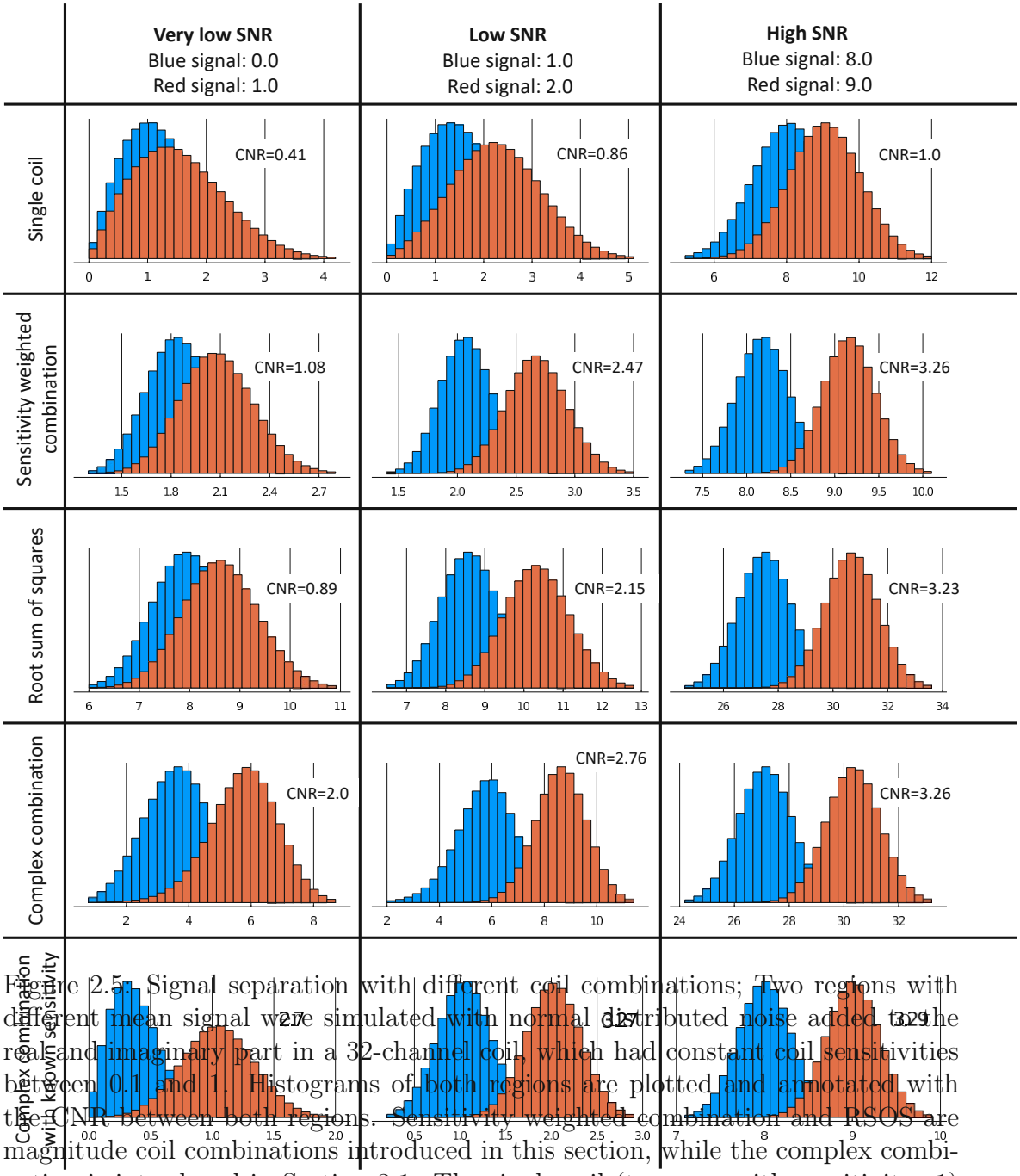

Figure 2.5: Signal separation with different coil combinations; Two regions with different mean signal were simulated with normal distributed noise added to the real and imaginary part in a 32-channel coil, which had constant coil sensitivities between 0.1 and 1. Histograms of both regions are plotted and annotated with the CNR between both regions. Sensitivity weighted combination and RSOS are magnitude coil combinations introduced in this section, while the complex combination is introduced in Section 3.1. The single coil (top row, with sensitivity=1) shows a strong bias effect at lower SNR due to the projection of a complex distribution onto the magnitude. All coil combinations increase the CNR compared to single coil, but still suffer from the bias effect, which is strongest in the very low SNR regime, resulting in low CNR between the regions. In the lower SNR regime, the complex coil combination has higher CNR values than both magnitude coil combinations. Note that in the high SNR regime (right column), there is minimal difference in CNR between the coil combinations.

Die approbierte gedruckte Originalversion dieser Dissertation ist an der TU Wien Bibliothek verfügbar.
The approved original version of this doctoral thesis is available in print at TU Wien Bibliothek.
TU Bibliothek Your knowledge hub WIEN

available on the system. When the coil sensitivities vary slowly in space, this calculation provides near-optimal SNR and removes the high noise floor that is seen in Figure 2.5 for sensitivity-weighted and RSOS magnitude combination. Adaptive combine is discussed again in relation to phase outcomes in Section 2.4.2.1.

2.4.1.2 Multi echo combination

In a multi-echo acquisition, each echo can be viewed separately and the information contained varies over the echo time, with the largest echo-dependent effect due to the T_2^*-decay (see signal formulation in Equation 2.55). However, viewing images from individual echoes is not practical and the simplest way to obtain a single image is to average the individual echoes in a voxelwise approach [12]. The same RSOS combination as previously discussed for combining the magnitude from multiple coil elements can be also applied for combining the magnitude of multiple echoes [9]. The RSOS method is close to optimal in terms of SNR [13], but the contrast of the combined image is usually weak as it is more strongly influenced by earlier echoes and these have often little contrast between neighboring tissues because they have little T_2^* weighting. A new method to optimize the CNR between two tissues is developed in Section 3.3.3.3 and methods to increase the contrast without influencing SNR are presented in Section 3.3.3.4.

2.4.1.3 Common magnitude artefacts

One type of artefacts in the magnitude images is signal dropouts in areas where T_2^* is short compared to the echo time. This occurs not only due to tissue properties, but also due to inhomogeneities with strong local gradients in the magnetic field when the phase change over the length of one voxel is close to 2π. Since this effect already takes place at the level of signal formation, the same signal dropout effect is measured at every coil element. However, it can be partly remedied in echo combination by using the information from earlier echoes instead of later ones for the affected region. Strategies to retain contrast of later echoes while reducing signal dropouts are discussed in sections 3.3.3.3 and 3.3.3.4. In addition, sequence settings can limit signal dropouts by either trying to reduce inhomogeneities with active shimming, reducing voxel size, or reducing echo times.

Another common artefact is intensity variations in the magnitude caused by the varying sensitivity of the individual coils. If the sensitivity profiles are known, the variation can be removed during coil combination, but this is usually not the case or only crude estimations are available. A new post-processing method for homogeneity correction is developed in Section 3.4.2.

Both artefact types, signal dropouts and sensitivity variations, tend to be more pronounced at higher field strengths as the inhomogeneities of the magnetic field

Die approbierte gedruckte Originalversion dieser Dissertation ist an der TU Wien Bibliothek verfügbar.
The approved original version of this doctoral thesis is available in print at TU Wien Bibliothek.
TU Bibliothek Your knowledge hub WIEN

increase and the shorter wavelength leads to more spatially varying sensitivities of the individual coils.

2.4.1.4 T_2^* and M_0 calculation

By analyzing the signal evolution over the echo time in a multi-echo scan, the relaxation time T_2^* can be determined. The signal model from Equation 2.55 can be reduced to contain only parts that depend on the echo time and a constant called M_0. The two remaining parts are T_2^*-decay and T_1-decay, but since the relaxation constant for T_1-decay is larger by a factor of ~ 50 it can be neglected and added into the constant term M_0. The simple signal equation

$$S\left(T_E\right) = M_0 e^{\frac{T_E}{T_2^*}} \tag{2.72}$$

can be fitted to the multi-echo data to obtain maps of both M_0 and T_2^*. All echoes have the same noise distribution and fitting in a least-squares sense yields an optimal solution, but this is rather time consuming. Other approaches first apply the logarithm to the data and perform regression to now fit the linear data, which is fast but weights later echoes too heavily and leads to increased noise at low T_2^* values. The method NumART2* [14] uses a numerical approach and yields T_2^* maps with similar accuracy to least-squares fitting, but requires only simple operations and runs in a fraction of the time.

2.4.2 Phase

The measured phase φ has two main contributions; the local magnetic field that the proton spins are subjected to, ΔB_0, and a spatially varying offset term ϕ_0 caused by the time the signal needs to travel from its origin to the receive coil, cable lengths and measurement imperfections. The two components can be distinguished by their dependence on the echo time according to the formula

$$\varphi\left(T_E\right) = 2\pi\gamma\Delta B_0 \cdot T_E + \phi_0. \tag{2.73}$$

However, the measured phase θ is the angle of the complex measurement, which is limited to a range of 2π and therefore the underlying phase φ is measured only up to an unknown multiple n of 2π:

$$\theta\left(T_E\right) = \varphi\left(T_E\right) + n \cdot 2\pi, \qquad n \in \mathbb{Z} \tag{2.74}$$

2.4.2.1 Coil combination

Unlike magnitude images, combining the measured phase from an array of coils into a single volume cannot be performed by weighted summation without introducing

Die approbierte gedruckte Originalversion dieser Dissertation ist an der TU Wien Bibliothek verfügbar.
The approved original version of this doctoral thesis is available in print at TU Wien Bibliothek.
TU Bibliothek Your knowledge hub WIEN

various phase artefacts, because coil dependent offsets and phase ambiguities. A multitude of different phase combination techniques have been published, all trying to avoid these artefacts and produce combined phase images with the highest possible SNR. The most common phase combination methods and those relevant to this thesis are presented here.

Adaptive Combine Adaptive Combine has been described in Section 2.4.1.1 focusing on the magnitude, but it performs the combination in complex and additionally produces a combined phase output. The measured complex values for different coils point in different directions due to coil-dependent phase offsets (see explanation in Section 2.3.4) and need to be aligned prior to averaging to avoid signal cancellation. This alignment (or phase matching) is implicitly performed by using complex correlation matrices, where the signal correlation matrices are estimated from local regions. However, at high field strengths, the pronounced inhomogeneities in the phase lead to strong phase variations inside even small local regions and the estimated correlation values can lead to signal cancellations.

Homodyne Filtering In its original application, homodyne filtering was used to remove low-frequency phase variation from an image acquired with a single coil [15]. Three paths are described to obtain a low-frequency phase reference, which is then used to demodulate the phase component and resembles a high-pass filter. The reference is either measured as a separate low-resolution scan or is obtained using low-pass filtering of the acquired complex signal in k-space or after Fourier reconstruction in image space.

A second use of homodyne filtering is as a preprocessing step for coil-combination. The removal of the slowly varying phase also removes the phase offsets and thus performs phase matching, after which the complex images of separate coils can be combined using a simple weighted combination. Current methods for susceptibility weighted imaging rely on homodyne filtering for both phase combination and to obtain an filtered phase image that can be readily applied for generating a phase weighting mask [16]. A common method of obtaining the low-frequency reference is the application in 2D using a Hann window (raised cosine) for filtering.

Homodyne filtering is only suggested to be applied for slowly varying phase [15], which is often violated for high field applications and leads to common phase artefacts as shown in Figure 2.8.

Hermitian inner Product The Hermitian inner product for coil combination [17] is defined as the dot product between the complex data from the k-th echo and the complex conjugate of the j-th echo, where $j < k$, written as

Die approbierte gedruckte Originalversion dieser Dissertation ist an der TU Wien Bibliothek verfügbar.
The approved original version of this doctoral thesis is available in print at TU Wien Bibliothek.
TU Bibliothek WIEN Your knowledge hub

$$\Delta\theta = \angle \sum_c S_k^c \mathrm{conj}\left(S_j^c\right) \tag{2.75}$$

$$= \angle \sum_c M_k^c M_j^c e^{i\left(\theta_k^c - \theta_j^c\right)}, \tag{2.76}$$

where S_i^c is the complex image for coil c and echo time $T_{E,i}$ for echo i. The method combines all channels from exactly two echoes and yields one phase image with the difference of the echo times as the effective time for phase evolution. The advantages of this method are a simple application for a dual-echo scan without requiring reference scans or coils, and a phase combination without remaining phase offsets or combination artefacts. The downside is, however, the low SNR in the combined phase image due to the phase difference operation involved.

MCPC-3D The method MCPC-3D [18] was specifically designed for applications at high and ultra-high field strengths. During coil combination, a strong spatial dependence of the phase offsets is taken into account. In order to combine individual phase images, the phase offsets are removed from the measured phase, leading to matched phases (shown in Figure 2.6), and after phase matching, the individual phase images can be combined into one high SNR phase image by calculating the angle of the complex sum of the individual phase matched signals. With the magnitude of the complex signal M^c, the phase θ^c, and the phase offset ϕ_0^c for the coil element c, the combination is formulated as

$$\phi = \angle \sum_c M^c e^{i\left(\theta^c - \phi_0^c\right)}. \tag{2.77}$$

The remaining problem is to obtain good estimates for the phase offsets. In MCPC-3D, the first step is to formulate Equation 2.73 depending on the different coils and timepoints (echoes) as

$$\varphi_i^c = 2\pi\gamma\Delta B_0 \cdot T_{E,i} + \phi_0^c. \tag{2.78}$$

By considering two different time points, this equation is solved for the phase offset

$$\phi_0^c = \frac{T_{E,j}\varphi_k^c - T_{E,k}\varphi_j^c}{T_{E,j} - T_{E,k}}. \tag{2.79}$$

The phase offsets are known to vary slowly in space. This can be exploited by applying low-pass filtering to the calculated phase offsets before applying them in

Die approbierte gedruckte Originalversion dieser Dissertation ist an der TU Wien Bibliothek verfügbar.
The approved original version of this doctoral thesis is available in print at TU Wien Bibliothek.
TU Bibliothek Your knowledge hub WIEN

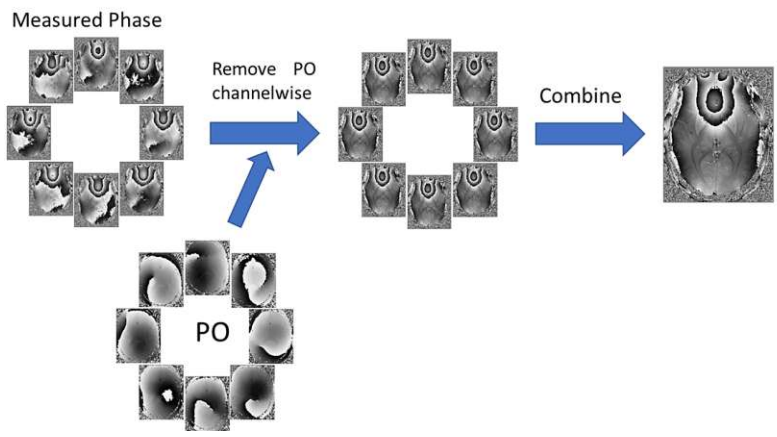

Figure 2.6: Combination of phase images according to MCPC-3D; individual phase offsets (PO) are removed from the measured phase individually for each coil element. The resulting phase images are visually very similar and differ only in noise distribution. As a last step, these individual phase images are combined to obtain a high SNR phase image.

Equation 2.77 for coil combination, avoiding noise contributions from the phase offsets. The only difficulty with this approach is that the underlying phase φ_i^c is not measured but the wrapped version θ_i^c. Thus, in order to estimate the phase offsets, all measured phase images θ_i^c have to be unwrapped as a first step. However, phase unwrapping, which will be introduced in the next section, is performed for each individual coil image and two echo times, which amounts to 64 individual, whole volume unwrapping applications for a commonly used setup of 32 coil elements.

In summary, the method MCPC-3D requires a multi-echo scan with at least two echoes for estimating the phase offsets, from which it produces one high SNR combined phase image for each echo. The unwrapping of the all individual phase images, however, is a huge computational burden, and unwrapping of noisy single-channel images is also error prone leading to occasionally unresolved wraps and corrupted combined phase images. Improvements to MCPC-3D are developed within this work and are presented in Section 3.1.2 as MCPC-3D-S and ASPIRE.

Volume coil reference This method requires, as its name suggests, a reference phase image from a volume coil. The relative phase offsets $\phi_0^{c,\mathrm{rel}}$ between the array coils and the volume coil are calculated in order to substitute the array coil offsets

Die approbierte gedruckte Originalversion dieser Dissertation ist an der TU Wien Bibliothek verfügbar.
The approved original version of this doctoral thesis is available in print at TU Wien Bibliothek.
TU WIEN Bibliothek Your knowledge hub

ϕ_0^c with the phase offsets from the volume coil ϕ_0^V as

$$\phi_0^{c,\mathrm{rel}} = \theta^c - \theta^V \tag{2.80}$$
$$= (2\pi\gamma\Delta B_0 \cdot T_E + \phi_0^c) - \left(2\pi\gamma\Delta B_0 \cdot T_E + \phi_0^V\right) \tag{2.81}$$
$$= \phi_0^c - \phi_0^V . \tag{2.82}$$

The remaining steps are performed analogously to MCPC-3D, where $\phi_0^{c,\mathrm{rel}}$ is smoothed and used for phase matching of the measured multi-channel phase images. The volume coil reference method works well for low field strengths (it was first introduced in 1990 and applied at 1.5 T [19]), where the volume coil produces a homogeneous image and has low phase offset itself. At higher field strengths, however, volume coils become increasingly affected by spatial variation in the phase offsets and sensitivities due to shorter wavelengths of the RF signal, which leads to inhomogeneous phase images from volume coils and even signal dropouts in the central region. Due to this poor performance and the additional space requirement inside the restricted volume, many ultra-high field scanners don't even provide volume coils for measurements.

2.4.2.2 Phase unwrapping

The measurement of the phase (or angle) of a complex signal is restricted to a range of 2π and is represented here as $[-\pi;\pi)$. The underlying physical quantity, the local magnetic field ΔB, causing the phase angle to rotate is not restricted and thus a measured phase value can be shifted by an unknown number of full rotations, i.e. multiples of 2π. Phase unwrapping is the process of resolving these ambiguities and reconstruct the "true" phase. It is an ill-posed problem with a surjective and non-injective connection of true phase to wrapped phase, as multiple true phase values yield the same wrapped phase value. Therefore, common phase unwrapping solutions include additional spatial or temporal information to estimate the true phase.

Examples for wrapped phase images can be seen in Figure 2.7 and Figure 2.8 for a phantom and a brain image respectively. Sharp boundaries exist in wrapped phase images, where the phase values jump from $-\pi$ to π. Especially in noisy regions or at tissue interfaces, correct unwrapping is challenging.

Laplacian unwrapping The phase can be formulated as

$$\varphi(\boldsymbol{r}) = \theta(\boldsymbol{r}) + 2\pi n(\boldsymbol{r}), \tag{2.83}$$

where $\varphi(\boldsymbol{r})$ is the unwrapped (or true) phase, $\theta(\boldsymbol{r})$ is the wrapped phase, $n(\boldsymbol{r})$ is an integer and $\boldsymbol{r}$ refers to the pixel position. One idea of unwrapping is to take

Die approbierte gedruckte Originalversion dieser Dissertation ist an der TU Wien Bibliothek verfügbar.
The approved original version of this doctoral thesis is available in print at TU Wien Bibliothek.
TU Bibliothek Your knowledge hub WIEN

the partial derivative in one direction, and assuming the phase change between neighboring voxels is less than π, all wraps can be resolved in the partial derivative. A partial derivative without wraps can be calculated as the angle difference in complex representation. The integration of the derivative would ideally lead back to the original image (up to a constant) with the wraps removed, however, noise and tissue interfaces severely corrupt this process, ultimately leading to poor performance. The idea in Laplacian unwrapping is to integrate the information from both partial derivatives in x- and y-direction. The first step is applying the two-dimensional Laplacian operator $\nabla_\perp^2$ to Equation 2.83 [20], yielding

$$\nabla_\perp^2 \varphi(\boldsymbol{r}) = \nabla_\perp^2 \theta(\boldsymbol{r}) + \nabla_\perp^2 2\pi n(\boldsymbol{r}), \tag{2.84}$$

which can be solved for $n(\boldsymbol{r})$ to obtain a formulation of the integer number of wraps, which is depending on the Laplacian of the wrapped and unwrapped phase as

$$n(\boldsymbol{r}) = \frac{1}{2\pi} \nabla_\perp^{-2} \left[\nabla_\perp^2 \varphi(\boldsymbol{r}) - \nabla_\perp^2 \theta(\boldsymbol{r}) \right], \tag{2.85}$$

where $\nabla_\perp^{-2}$ is the inverse two-dimensional Laplacian operator. The problematic part is the calculation of $\nabla_\perp^2 \varphi(\boldsymbol{r})$, as $\varphi(\boldsymbol{r})$ is the unknown unwrapped phase, but by using the complex representation of the phase,

$$\begin{aligned} P(\boldsymbol{r}) &= \exp(i\varphi(\boldsymbol{r})) && (2.86)\\ &= \exp(i\theta(\boldsymbol{r}) + 2\pi n(\boldsymbol{r})) && (2.87)\\ &= \exp(i\theta(\boldsymbol{r})), && (2.88) \end{aligned}$$

the Laplacian $\nabla_\perp^2 \varphi(\boldsymbol{r})$ can be calculated using $P(\boldsymbol{r})$ obtained from the wrapped phase $\theta(\boldsymbol{r})$. The concept is similar to the above mentioned one-dimensional version of removing the wraps in the partial derivative by calculating phase differences in complex notation. Applying the Laplacian to $P(\boldsymbol{r})$ yields

$$\nabla_\perp^2 P(\boldsymbol{r}) = -e^{i\varphi(\boldsymbol{r})} \left(\left(\frac{\partial \varphi(\boldsymbol{r})}{\partial \boldsymbol{r}} \right)^2 - i \overbrace{\frac{\partial^2 \varphi(\boldsymbol{r})}{\partial \boldsymbol{r}}}^{\nabla_\perp^2 \varphi(\boldsymbol{r})} \right), \tag{2.89}$$

from which $\nabla_\perp^2 \varphi(\boldsymbol{r})$ can be identified leading to

$$\nabla_\perp^2 \varphi = \Im \left(\frac{1}{P} \nabla_\perp^2 P \right), \tag{2.90}$$

where $\Im(z)$ is the imaginary part of the complex number z. The right part of Equation 2.90 can be reformulated to obtain the relation

$$\nabla_\perp^2 \varphi = \cos\theta \nabla_\perp^2 \sin\theta - \sin\theta \nabla_\perp^2 \cos\theta \tag{2.91}$$

Die approbierte gedruckte Originalversion dieser Dissertation ist an der TU Wien Bibliothek verfügbar.
The approved original version of this doctoral thesis is available in print at TU Wien Bibliothek.
TU Bibliothek Your knowledge hub WIEN

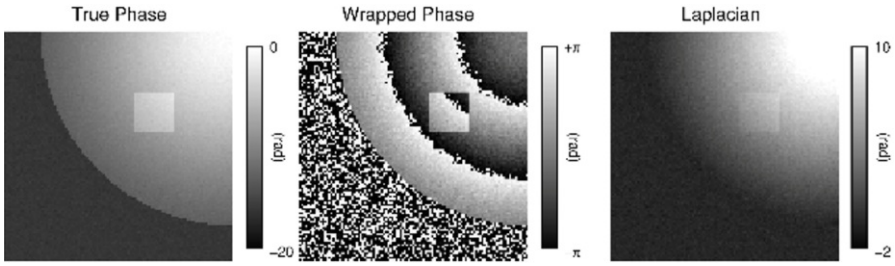

Figure 2.7: Laplacian unwrapping of a simulated topology with 10% noise. The wraps are fully removed in Laplacian unwrapping, however, the true phase could not be reconstructed. Additionally, the noise in the Laplacian unwrapped image is increased compared to the true phase. Reproduced from Supplementary Material of [21]

allowing the calculation of $\nabla_{\perp}^{2}\varphi$ by only knowing the wrapped phase θ. With equations 2.91 and 2.85, $n\left(r\right)$ can be calculated, where both the Laplacian and inverse Laplacian operator can be efficiently calculated using Fast Fourier techniques. With $n\left(\boldsymbol{r}\right)$, the unwrapped phase $\varphi\left(\boldsymbol{r}\right)$ is simply obtained by Equation 2.83.

The explanation of Laplacian unwrapping was kept to two dimensions but the same applies to 3D unwrapping.

However, the calculated $n\left(\boldsymbol{r}\right)$ is not a true integer field and the resulting unwrapped phase has arbitrary background field contributions. Additionally, the Laplacian unwrapping process increases the noise and tends to reduce the value of absolute phase jumps between regions, which is demonstrated in Figure 2.7.

Region growing methods Region growing methods start with a wrap free region and add further regions by resolving the wraps between them. The assumption for resolving wraps is that more than π phase difference between neighboring voxels corresponds to a wrap, which is removed by adding or removing multiples of 2π to reach a phase difference smaller than π.

The unwrapping method PRELUDE [22] first cuts the volume into wrap-less region by thresholding to a small part of the 2π range and then merges the regions. PRELUDE is relatively robust and is considered the gold standard for phase unwrapping [23]. The unwrapping process, however, is relatively slow, taking hours for large datasets and even days for complicated cases or at late echo times.

Another region growing method is best-path [24], which starts with single voxels as individual regions and merges regions by only considering the voxel with the best connection between both regions, trying to avoid traversing noisy voxels in the process. Best-path is computationally highly efficient, usually finishing in a few minutes for large datasets and its runtime is independent of the complexity of

Die approbierte gedruckte Originalversion dieser Dissertation ist an der TU Wien Bibliothek verfügbar.
The approved original version of this doctoral thesis is available in print at TU Wien Bibliothek.
TU Bibliothek Your knowledge hub WIEN

the unwrapping task but only depends on the datasize. The unwrapping accuracy tends to be slightly lower than PRELUDE and similarly to PRELUDE, late echoes are very challenging for best-path.

Temporal unwrapping Temporal unwrapping methods can be applied to multi-echo scans, where the phase information is measured at multiple time points. The simplest way is to assume a linear evolution of the phase over time and perform voxelwise unwrapping of later echoes using information from earlier echoes, but the wraps that already occur in the first echo are not unwrapped in this scheme.

The method STAGE [25] specifically acquires one pair of echoes with a short echo spacing and uses the difference between those two echoes as a template for unwrapping, assuming the absolute phase evolution is less than π. This does not work at ultra-high field strength, as the minimal time between echoes would have to be less than 1 ms to avoid wraps [23], and such short echo spacings are not possible for reasonable imaging resolutions.

UMPIRE [26] requires at least three echoes and calculates a difference of phase differences as a template to solve this problem. By choosing the echo times e.g. 5 ms, 10 ms and 16 ms, the phase differences contain 5 ms and 6 ms respectively and the difference of differences contains only 1 ms phase evolution. Using this approach, the phase difference can be chosen arbitrarily small, however, there is a trade-off between noise and phase artefacts corrupting the template image and a phase evolution that is short enough to not contain any wraps.

Another approach again is to fit the phase data to a model, which is performed by GEPCI [27] but can lead to fitting instabilities that depend on the specific acquisition parameters and voxelwise fitting is computationally highly demanding.

2.4.2.3 Common phase artefacts

Figure 2.8 presents common artefacts encountered in phase images. The left image is highly wrapped, which needs to be resolved to restore the relationship between phase and B_0 and to make it usable as input for phase-based methods. The image contains a strong gradient in the anterior to posterior direction (causing many wraps in that direction), which is an uncompensated background field. The background field is defined as the low frequency phase components that are not related to susceptibilities found inside the measured volume. It can have many sources, including large susceptibilities outside the measured volume, incorrect parameter estimation in active shimming or introduced bias in coil-combination.

The right image shows an (unrelated) homodyne filtered phase image, containing unresolved wraps. Many of the unresolved wraps present as open-ended fringe lines, terminating in a point and leading to unrecoverable image corruption. Due to the "nonphysical" structure of these homodyne wraps, there is no method to

Die approbierte gedruckte Originalversion dieser Dissertation ist an der TU Wien Bibliothek verfügbar.
The approved original version of this doctoral thesis is available in print at TU Wien Bibliothek.
TU Bibliothek Your knowledge hub WIEN

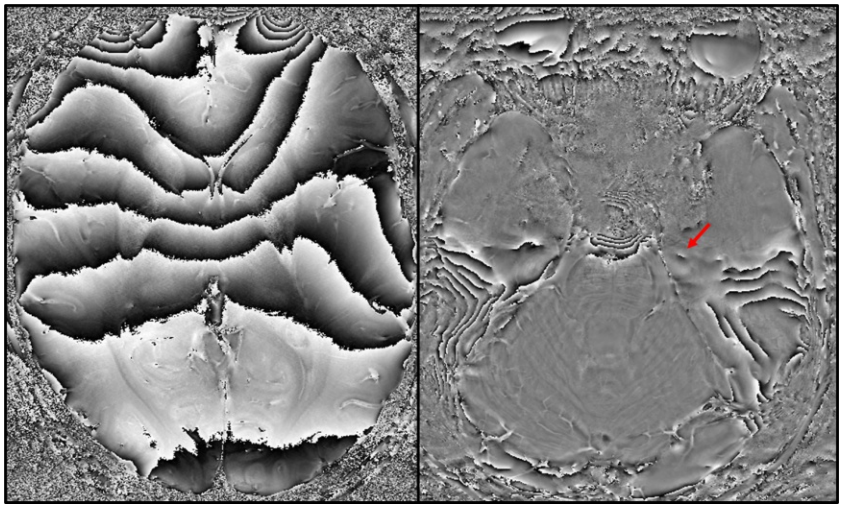

Figure 2.8: Common phase artefacts; the left side shows a wrapped phase image with a strong background field gradient from anterior to posterior. The right image is an homodyne filtered phase, where some wraps have been only partly removed. The arrow points to a location where the homodyne artefact is far away from obvious wraps. Note that the image on the left and right are not related and were chosen to demonstrate different common phase artefacts.

further unwrap them. Some homodyne artefacts might also occur with a displacement of several centimeters from obvious wraps artefacts, potentially leading to misdiagnosis if not recognized as an artefact (red arrow). Examples are also shown later in the comparison of SWI methods in figures 5.18 and 5.19.

A further phase artefact (not shown here) is a linear phase variation in readout direction in a bipolar acquisition. A linear phase change occurs, when the center of k-space is shifted, and for bipolar acquisitions, there is often a slight mismatch in timing between even and odd echoes, leading to a shift in k-space center between even and odd echoes. This artefact will be addressed in the bipolar corrections section of the coil combination methods (Section 3.1.3).

2.4.2.4 Multi-echo combination

In general, the phase has less signal loss from dephasing in earlier echoes and higher SNR in later echoes. Therefore, it is advantageous to combine all phase images from different echoes to increase SNR and still having low signal dropouts. In principle, the information in each echo phase is identical and only the noise levels differ, however, the difficulties in combining multi-echo phase are phase wraps and phase offsets. In principle, wrapped phase images from different echoes can be directly combined by performing complex multiplication, however, it would cause

Die approbierte gedruckte Originalversion dieser Dissertation ist an der TU Wien Bibliothek verfügbar.
The approved original version of this doctoral thesis is available in print at TU Wien Bibliothek.
TU Bibliothek Your knowledge hub WIEN

the individual wraps to accumulate, since the phase would effectively correspond to a phase with both echo times added. It would still be possible to unwrap the combined image but it would increase the difficulty of unwrapping, making unwrapping prior to echo combination preferable.

The phase offset $\phi_0 = \varphi_i - 2\pi\gamma\Delta B_0 \cdot T_{E,i}$, which is identical for each echo (see Equation 2.73), is a spatially smooth measurement artefact which is usually removed during echo combination. Weighted least squares fitting of phase [28] uses unwrapped data and first estimates the phase offset term ϕ_0 from Equation 2.73 and uses polynomial fitting to remove the noise. Subsequently, in a second round of fitting, ΔB_0 is estimated using the fitted term of ϕ_0 . In GEPCI [27], the complex mono-exponential signal decay equation

$$S\left(T_E\right) = S_0^2 e^{-\frac{T_E + T_{E,1}}{T_2^*}} e^{i2\pi f\left(T_E - T_{E,1}\right)}, \tag{2.92}$$

with S_0^2, the squared magnitude without decay, the T_2^* decay constant, and the frequency $f = \gamma B_0$, is fitted to the complex data in a voxelwise fashion. In a special coil combination preprocessing step, the phase offset is removed by performing a voxelwise complex conjugated multiplication of each echo with the first one, effectively removing the phase offset and enabling simple coil combination. The conjugated complex multiplication (or phase difference operation) increases the noise level of each individual echo but it does not severely influence the noise of the fit, as for each voxel, all echoes are shifted by the same value. This avoids the need for unwrapping, but the fitting problem is of higher complexity with multiple potential local minima.

The following two methods, which were developed for applications in which only the high frequency phase content is of interest, take a different approach. The first performs homodyne filtering for each echo and divides them by the echo time to yield B_0 maps with only high frequency information. The resulting B_0 maps are combined by simple averaging [12]. The other method uses a similar approach but replaces the averaging with an inverse-variance-weighted combination of homodyne filtered B_0-like maps [16]. Assuming a constant noise distribution over the complex image, the weighting factors are

$$w_i = M_i^2 \cdot T_{E,i}^2, \tag{2.93}$$

where M_i is the magnitude and $T_{E,i}$ the echo time of the i-th echo. This result stems from the calculated phase standard deviation in Section 2.3.3.2, which is inversely proportional to the magnitude and inversely proportional to the echo time due to the division by the echo time to yield B_0 maps.

Die approbierte gedruckte Originalversion dieser Dissertation ist an der TU Wien Bibliothek verfügbar.
The approved original version of this doctoral thesis is available in print at TU Wien Bibliothek.
TU Bibliothek Your knowledge hub WIEN

2.5 Magnetic Susceptibility in MRI

The magnetic susceptibility of the tissue causes changes in the local magnetic field and therefore changes in proton precession speeds. This effect links the measured MR phase to the magnetic susceptibility.

2.5.1 Definition and Properties

Every material has a magnetic susceptibility, meaning there is some kind of interaction with the external magnetic field. The magnetic susceptibility χ is a dimensionless proportionality constant characterizing the degree of magnetization $\boldsymbol{M}$ of a material in response to an applied magnetic field $\boldsymbol{H}$. Under conditions present in usual MRI experiments, the relation can be described as linear with

$$\boldsymbol{M} = \chi \boldsymbol{H}. \tag{2.94}$$

On an atomic level, magnetism is a quantum effect and electrons produce a magnetic field because of their spin and angular momentum quantum numbers. A full orbital with two electrons produces zero net magnetic field, as the electrons cancel each other and when subject to an external magnetic field, electrons that are paired in their orbital act as diamagnetic, in other words, they expel the external magnetic field. The unpaired electrons, on the other hand, tend to align their own magnetic field parallel to an external magnetic field and act paramagnetically, increasing the field strength. As diamagnetism is very weak in comparison, an atom with an unpaired electron is paramagnetic no matter how many paired electrons it has. On the macroscopic level, there are 4 different classifications, with the following characteristic ranges of χ:

Diamagnetism: χ is negative and of the order of 10^{-6}

Paramagnetism: χ is positive and typically in the range 10^{-5}-10^{-3}

Ferromagnetism and Superparamagnetism: χ is positive and typically greater than 100

Diamagnetism and paramagnetism directly translate from the atomic level to a macroscopic level, whereas ferromagnetism and superparamagnetism contain additional effects. In ferromagnetism, through an exchange interaction between unpaired electrons, neighboring spins align and form magnetic domains of the size of a few μm, each producing a net magnetic field. The domains themselves are not aligned in any particular direction and the magnetic field averages to zero, but in an external magnetic field the preferred alignment is parallel, which results in

Die approbierte gedruckte Originalversion dieser Dissertation ist an der TU Wien Bibliothek verfügbar.
The approved original version of this doctoral thesis is available in print at TU Wien Bibliothek.
TU Bibliothek Your knowledge hub WIEN

Table 2.1: Magnetic susceptibility of different materials; obtained from [29, 30, 31] and mriquestion.com.

Material	Iron	Air	Aluminum	Water
Susceptibility	$> 10^5$	$3.6 \cdot 10^{-7}$	$2.2 \cdot 10^{-5}$	$-9.0 \cdot 10^{-6}$
Material	Blood (deoxygenated)		Cortical Bone	Ferritin
Susceptibility	$-7.9 \cdot 10^{-6}$		$-8.9 \cdot 10^{-6}$	$5.2 \cdot 10^{-4}$

large values of χ. Realignment of magnetic domains has an energy cost, and once magnetized, ferromagnetic materials retain their magnetization.

Superparamagnetism appears in small ferromagnetic nanoparticles, where each nanoparticle is its own domain. Their magnetic susceptibility is much larger than that of paramagnets and is in a similar range to that of ferromagnets. Their magnetization is not permanent, as the nanoparticles can freely rearrange themselves when the external magnetic field is switched off.

Susceptibility values of different elements and important tissues is shown in Table 2.1.

2.5.2 Interaction in MRI

The magnetic susceptibility changes the strength of the magnetic field $\boldsymbol{B}$ inside a material with susceptibility χ according to

$$\boldsymbol{B} = \mu_0 \left(1 + \chi\right) \boldsymbol{H}. \tag{2.95}$$

Where multiple tissues are present, the resulting magnetic field is calculated as the convolution of the susceptibility distribution $\boldsymbol{\chi}$ with the dipole kernel $\boldsymbol{d}$ and leads to non-local magnetic field changes caused by susceptibility effects from other regions. Thus, the distribution of the susceptibility determines ΔB_0, which is the deviation of the local magnetic field from the applied main magnetic field strength in z-direction.

The measurement of the phase in MRI is a measurement of the precession frequencies of the spins, which are proportional to the experienced magnetic field, which in turn is given by the distribution of the susceptibility $\boldsymbol{\chi}$. Therefore, the MR phase is an indirect measurement of the magnetic susceptibility distribution.

2.5.3 Blood, Iron and Ferritin

Blood and its breakdown products have a strong influence of the susceptibility.

Die approbierte gedruckte Originalversion dieser Dissertation ist an der TU Wien Bibliothek verfügbar.
The approved original version of this doctoral thesis is available in print at TU Wien Bibliothek.
TU Bibliothek Your knowledge hub WIEN

2.5.3.1 Hemoglobin

Hemoglobin is the macromolecule responsible for oxygen transport in blood and contains iron. When transporting oxygen, as oxyhemoglobin, no unpaired electrons are present and it is weakly diamagnetic. When the oxygen is removed to form deoxyhemoglobin, it contains 4 unpaired electrons and is paramagnetic. Due to the presence of deoxyhemoglobin, the local magnetic field experiences strong changes, leading to intravoxel dephasing effects, resulting in significantly lower T_2 and T_2^* values in blood. This susceptibility change is strong enough that it causes substantial differences in oxygenated and deoxygenated blood, leading to the blood oxygen level dependent (BOLD) effect. It is the basis of functional MRI, because of the correlation of the BOLD contrast to brain activity, as there is a physiological response that delivers fresh and oxygenated blood to active brain regions.

2.5.3.2 Hematoma: the role of ferritin and hemosiderin

Pathological brain areas or injuries are often accompanied with hematomas, which are collections of clotted blood. In several steps the hemoglobin of clotted blood degrades into methemoglobin, hemichromes and finally ferritin and hemosiderin. As each stage has a different magnetic susceptibility, the appearance of hematomas in MRI changes over time and is used to indicate the current stage of the hematoma. In the final stage, ferritin and hemosiderin, which are superparamagnetic with very high susceptibility values, are deposited at the boundaries of the hematoma wall. This leads to strong susceptibility effects in these areas.

2.5.4 Susceptibility Weighted Imaging

While most clinical MRI methods only use the magnitude image, SWI [32, 33] employs high-pass filtered phase information to generate additional contrast that is related to the susceptibility distribution and attenuates the magnitude with the positive part of the high-pass filtered phase, which shows effects of the paramagnetic susceptibility. This results in a darker appearance of veins and strongly paramagnetic blood products. Thus, SWI is used for venography and detection and analysis of pathologies. A more detailed explanation of the standard SWI processing steps, recent literature approaches as well as own contributions are detailed in Section 3.3 CLEAR-SWI.

A central critique of SWI is that it visualizes phase effects, which are not directly related to local tissue properties but are dipole convolutions of the underlying susceptibility distribution of the tissue. This leads to an appearance that is orientation dependent with regard to the main magnetic field. Also, the obtained values lack a foundation to be converted into quantitative measurements and are

Die approbierte gedruckte Originalversion dieser Dissertation ist an der TU Wien Bibliothek verfügbar.
The approved original version of this doctoral thesis is available in print at TU Wien Bibliothek.
TU Bibliothek Your knowledge hub WIEN

only viewed in relation to surrounding tissue, as qualitative contrasts.

2.5.5 Quantitative Susceptibility Mapping

Quantitative Susceptibility Mapping (QSM) [34, 35] represents an attempt to solve the shortcomings of SWI by attempting to reconstruct the underlying susceptibility distribution from the measured phase. Multiple methods exist that try to solve the field-to-source inverse problem, which is complicated by the underdetermined nature of the inversion. The gold standard method COSMOS [36] uses acquisitions in multiple orientations of the object in regard to the B_0 field, which is not practical for clinical application. A simple method is to set the underdetermined values to predetermined non-zero values, and perform the inversion in k-space, called thresholded k-space division [37, 38], which, however, leads to underestimated susceptibility values and streaking artefacts. MEDI [39] applies regularization (l_1 norm), which, in order to further reduce streaking, utilizes the magnitude information for detecting tissue borders, as tissue borders often correspond to susceptibility changes. As there are no straightforward mathematical solutions, newer methods present deep learning algorithms as promising solutions [40]. As soon as QSM reconstruction can be performed using a fast algorithm that is proven to be robust even when encountering pathologies, it could replace the high-pass filtered phase in SWI [41] to produce an improved imaging modality for clinical application.

Die approbierte gedruckte Originalversion dieser Dissertation ist an der TU Wien Bibliothek verfügbar.
The approved original version of this doctoral thesis is available in print at TU Wien Bibliothek.
TU Bibliothek Your knowledge hub WIEN

Die approbierte gedruckte Originalversion dieser Dissertation ist an der TU Wien Bibliothek verfügbar.
The approved original version of this doctoral thesis is available in print at TU Wien Bibliothek.

Chapter 3

Methods

This chapter presents the new developments that were made for this thesis and is split into four subsections. The first three subsections present the main methods, starting with an improved coil combination approach, named MCPC-3D-S, and its more robust variant, ASPIRE. The second method is a new unwrapping algorithm, named ROMEO, and the third method integrates most of the new developments and recent methods from literature into a framework for susceptibility weighted imaging for multi-echo acquisitions, named CLEAR-SWI. All methods were developed for application at ultra-high field but also provide improvements over existing methods at lower field strengths. In the fourth subsection, supporting methods are presented; a collection of smaller tools and processing steps that were developed as building blocks and for the development of the three main methods.

3.1 Combination of Complex Data from Array Coils

Both presented methods, ASPIRE and MCPC-3D-S, have been published in *Magnetic Resonance in Medicine* as an original research article [42]. This section contains parts of the research article but with more detail and with a focus on the bipolar application, including improvements since the publication and the new development of a bipolar correction scheme for MCPC-3D-S.

3.1.1 MCPC-3D-S

MCPC-3D-S is a simplified and improved version of MCPC-3D [18] (see Section 2.4.2.1) that requires only one unwrapping step instead of $2N+1$ unwrapping steps, where N is the number of channels, resulting in a more robust and faster phase offset estimation.

The starting point of combining the data from multiple receiver coils is the

Die approbierte gedruckte Originalversion dieser Dissertation ist an der TU Wien Bibliothek verfügbar.
The approved original version of this doctoral thesis is available in print at TU Wien Bibliothek.
TU Bibliothek Your knowledge hub WIEN

phase offset formulation described in MCPC-3D, Equation 2.79. To compute the phase offset φ_0^c between the echoes k and j, the unwrapping of the raw phase images ϕ_k^c and ϕ_j^c is required for each coil c. The unwrapping process is even further complicated by the fact that single-channel phase data from array coils contains signal dropouts which result in points of singularity in the phase. Those singularities present as open-ended fringe lines and cannot be removed by unwrapping, thus often leading to unwrapping artefacts. To remedy this situation, Equation 2.79 can be rewritten as

$$\varphi_0^c = \frac{T_{E,j}\varphi_k^c - T_{E,k}\varphi_j^c}{T_{E,j} - T_{E,k}} \tag{3.1}$$

$$\varphi_0^c = \frac{T_{E,j}\left(\varphi_k^c - \varphi_j^c\right) - \left(T_{E,k} - T_{E,j}\right)\varphi_j^c}{T_{E,j} - T_{E,k}} \tag{3.2}$$

$$\varphi_0^c = \varphi_j^c - \frac{T_{E,j}}{T_{E,k} - T_{E,j}}\left(\varphi_k^c - \varphi_j^c\right). \tag{3.3}$$

To calculate the phase difference $\varphi_k^c - \varphi_j^c$, instead of calculating the phase difference coil-wise, it can be calculated by the Hermitian inner product of the complex data of the two echo times. This is possible due to the underlying property of the phase that the phase evolution is identical in each coil and only the phase offset ϕ_0 varies (see Equation 2.73). With the magnitude M_k^c for echo k and coil c, the Hermitian inner product is calculated as

$$\mathrm{HiP}_{kj} = \sum_c M_k^c M_j^c e^{i\left(\phi_k^c - \phi_j^c\right)} \tag{3.4}$$

and the combined phase difference $\Delta\phi_{kj}$ is given by calculating the angle

$$\Delta\phi_{kj} = \angle\left(\mathrm{HiP}_{kj}\right). \tag{3.5}$$

This corresponds essentially to a magnitude-weighted combination of the phase differences and results in a combined phase difference image with high SNR. $\Delta\phi_{kj}$ still needs to be unwrapped to yield the true phase difference $\Delta\varphi_{kj}$, as the phase evolution between echoes k and j can exceed the range $[-\pi;\pi]$. This allows the reformulation of Equation 3.3 to

$$\varphi_0^c = \varphi_j^c - \frac{T_{E,j}}{T_{E,k} - T_{E,j}}\Delta\varphi_{kj}. \tag{3.6}$$

The next realization is that the phase offset does not need to be unwrapped when the phase combination is performed in complex and in fact it often contains singularities that cannot be fully unwrapped. However, unwrapping $\Delta\varphi_{kj}$ is still

Die approbierte gedruckte Originalversion dieser Dissertation ist an der TU Wien Bibliothek verfügbar.
The approved original version of this doctoral thesis is available in print at TU Wien Bibliothek.
TU Bibliothek Your knowledge hub WIEN

required, for which any true phase unwrapping method (i.e. one which only adds $n \cdot 2\pi$) can be applied and in this case ROMEO (Section 3.2) was used. This changes Equation 3.6 to

$$\phi_0^c = \phi_j^c - \frac{T_{E,j}}{T_{E,k} - T_{E,j}} \Delta\varphi_{kj} \tag{3.7}$$

in order to calculate the wrapped phase offset ϕ_0^c. Next, smoothing of ϕ_0^c is performed as in MCPC-3D (Section 2.4.2.1 and Application for Smoothing Phase, Section 3.4.3.2) and to avoid edge effects, a mask that removes areas with no object (see Section 3.4.1) can be applied beforehand (Section 3.4.3.5 Fast Gaussian 3D Smoothing, Application with Missing Values). The last step is combination of the complex uncombined data with phase offset removal to yield the combined magnitude M_i and phase φ_i for echo i:

$$S_i = \sum_c (M_i^c)^2 \, e^{i\left(\phi_i^c - \phi_0^c\right)} \tag{3.8}$$

$$\varphi_i = \angle S_i \tag{3.9}$$

$$M_i = \sqrt{|S_i|} \tag{3.10}$$

The combined magnitude is similar to the RSOS method with the difference that RSOS contains a bias at low intensities from combining individual magnitude images with a Rician noise distribution (see demonstration of this effect in Figure 2.5), which is improved by the complex sum in Equation 3.8.

ROMEO for MCPC-3D-S Unwrapping is a crucial step in MCPC-3D-S and can be in principal performed by any method that performs exact unwrapping, i.e. only changing the input by addition and subtraction of multiples of 2π, which excludes Laplacian unwrapping. The unwrapping method ROMEO that is developed in Section 3.2 is proposed as the most robust and computationally efficient solution. As the robustness of ROMEO can be increased using multi-echo information in form of a "temporal coherence" weight, the Hermitian inner product between echoes 2 and 3 can be used as additional information in ROMEO.

3.1.2 ASPIRE

ASPIRE takes a step further and avoids unwrapping completely if certain acquisition parameters are met. The main realization is that unwrapping is only necessary if the phase evolution scaling term $\frac{T_{E,j}}{T_{E,k}-T_{E,j}}$ in Equation 3.7 is not a whole number, resulting immediately in the possibility to avoid unwrapping by enforcing $\frac{T_{E,j}}{T_{E,k}-T_{E,j}}$ to be a whole number.

Die approbierte gedruckte Originalversion dieser Dissertation ist an der TU Wien Bibliothek verfügbar.
The approved original version of this doctoral thesis is available in print at TU Wien Bibliothek.
TU Bibliothek Your knowledge hub WIEN

The reason why unwrapping is necessary when scaling phase by a non-integer number can be understood in two ways. The first explanation is related to the ambiguity of the root of complex numbers, as scaling a phase value by the factor f corresponds to taking the complex number to the power of f. (Note that scaling wrapped phase values should result in phase values again, i.e. values restricted to the range $[-\pi;\pi)$). The power of a complex number has multiple solutions with the number being the denominator of the power f in its reduced rational form, while it has only one solution, if f is a whole number. To resolve this issue, the phase has to be unwrapped prior to scaling, which removes the restriction to the range $[-\pi;\pi)$ as the underlying quantity is reconstructed from the phase.

The second explanation shows that errors of 2π in $\Delta\varphi_{kj}$ don't affect the outcome of the calculated ϕ_0^c given that the scaling term $\frac{T_{E,j}}{T_{E,k}-T_{E,j}}$ is a whole number, here called m. Considering only one voxel and a wrap error of $2\pi n$, Equation 3.7 can be written as

$$\phi_0^c = \phi_j^c - m\left(\Delta\varphi_{kj} + 2\pi n\right) \tag{3.11}$$

$$\phi_0^c + 2\pi mn = \phi_j^c - m\Delta\varphi_{kj} \tag{3.12}$$

and due to ϕ_0^c being used in the exponent in Equation 3.8, multiples of 2π don't affect the resulting combined image. Therefore, in ASPIRE, the wrapped scaled phase evolution $\Delta\phi_{kj}$ (see Equation 3.5) can be used instead:

$$\phi_0^c = \phi_j^c - \frac{T_{E,j}}{T_{E,k} - T_{E,j}}\Delta\phi_{kj} \tag{3.13}$$

The only remaining step is enforcing that in a multi-echo acquisition the scaling factor is a whole number, with the implication

$$\frac{T_{E,j}}{T_{E,k} - T_{E,j}} = m, \qquad m \in \mathbb{N} \tag{3.14}$$

$$T_{E,j} = \left(T_{E,k} - T_{E,j}\right) m, \qquad m \in \mathbb{N} \tag{3.15}$$

$$\left(m+1\right) T_{E,j} = mT_{E,k}, \qquad m \in \mathbb{N}. \tag{3.16}$$

This echo time restriction can be in principle satisfied in multiple ways, by having any two of the given echoes of the multi-echo train exhibit this exact relationship. However, large factors of m are not advised due to the multiplication of possible artefacts (e.g. echo-dependent flow effects) in the phase evolution $\Delta\phi_{kj}$. The simplest form of the ASPIRE echo-time restriction, Equation 3.16, is $m = 1$ applied on the first two echoes, resulting in $2T_{E,1} = T_{E,2}$, which is the default setting for many sequences, as often echo trains with all echoes being multiples of the

Die approbierte gedruckte Originalversion dieser Dissertation ist an der TU Wien Bibliothek verfügbar.
The approved original version of this doctoral thesis is available in print at TU Wien Bibliothek.
TU Bibliothek Your knowledge hub WIEN

first one are employed (e.g. $T_{E,i} = 5, 10, 15, 20\,\text{ms}$). For acquisitions with a long excitation phase, $m = 2$ might be better suited, with example echo times being $T_{E,i} = 6, 9, 12, 15\,\text{ms}$ and the first two echoes used for phase offset estimation.

3.1.3 Bipolar Corrections

This subsection contains a new and improved method of bipolar offset correction, which is related to the published version [42], but uses a different and more robust calculation.

3.1.3.1 Calculation of the bipolar artefact

In bipolar multi-echo acquisitions, the phase offset is, in general, different for even and odd echoes, as explained in Phase Artefacts, Section 2.4.2.3. The difference can be described as a linear phase change in phase encode direction, with only small non-linear contributions. This spatial linear phase change, or bipolar artefact is not coil dependent and can be estimated and corrected after MCPC-3D-S/ASPIRE coil combination has been performed.

Considering the case that the phase evolution is calculated from the first two echoes ($\Delta\phi_{2,1}$) and assuming that even and odd echoes have additional non coil dependent contributions to the phase offsets, G_{even} and respectively G_{odd}, the bipolar artefact in the combined images can be calculated by following along each step of MCPC-3D-S. Disregarding noise, the measured phase at one echo is written as

$$\phi_k^c = \text{PE}_k + \phi_0^c + \begin{cases} G_{\text{even}} & \text{if } k \in 2\mathbb{N} \\ G_{\text{odd}} & \text{otherwise} \end{cases}, \tag{3.17}$$

where $\text{PE}_k = 2\pi\gamma T_{E,k} \cdot \Delta B_0$ is the phase evolution of echo k, which is not depending on the coil element it is measured with. The phase formulation for one echo (Equation 2.73) is here extended for a bipolar multi-echo acquisition, introducing the additional gradient terms of G_{even} and G_{odd}. Note that for single-echo and monopolar acquisitions, in principle the same additional gradient terms are present but can be included in the phase offset term ϕ_0^c, as they do not contain echo dependent effects.

From equations 3.4, 3.5 and 3.17 the following formulation can be obtained for $\Delta\phi_{2,1}$:

Die approbierte gedruckte Originalversion dieser Dissertation ist an der TU Wien Bibliothek verfügbar.
The approved original version of this doctoral thesis is available in print at TU Wien Bibliothek.
TU Bibliothek Your knowledge hub WIEN

$$\begin{aligned}
\mathrm{HiP}_{2,1} &= \sum_c M_2^c M_1^c e^{i\left(\phi_2^c - \phi_1^c\right)} && (3.18)\\
&= \sum_c M_2^c M_1^c e^{i\left(\mathrm{PE}_2 + \phi_0^c + G_{\mathrm{even}} - \mathrm{PE}_1 - \phi_0^c - G_{\mathrm{odd}}\right)} && (3.19)\\
&= e^{i(\mathrm{PE}_2 - \mathrm{PE}_1 + G_{\mathrm{even}} - G_{\mathrm{odd}})} \sum_c M_2^c M_1^c \overbrace{e^{i\left(\phi_0^c - \phi_0^c\right)}}^{1} && (3.20)\\
\Rightarrow \Delta\phi_{2,1} &= \angle\left(\mathrm{HiP}_{2,1}\right) && (3.21)\\
&= \mathrm{PE}_2 - \mathrm{PE}_1 + \overbrace{G_{\mathrm{even}} - G_{\mathrm{odd}}}^{G} && (3.22)\\
&= \mathrm{PE}_2 - \mathrm{PE}_1 + G && (3.23)
\end{aligned}$$

In the following step, the unwrapping of $\Delta\phi_{2,1}$ to yield $\Delta\varphi_{2,1}$ does not change the calculation and is disregarded to simplify the notation. With Equation 3.7, the calculated phase offset is given as

$$\begin{aligned}
\phi_{0,\mathrm{calc}}^c &= \phi_1^c - \overbrace{\frac{T_{E,1}}{T_{E,2} - T_{E,1}}}^{m} \Delta\phi_{2,1} && (3.24)\\
&= \mathrm{PE}_1 + \phi_0^c + G_{\mathrm{odd}} - m\left(\mathrm{PE}_2 - \mathrm{PE}_1 + G\right) && (3.25)\\
&= \overbrace{\mathrm{PE}_1 - m\left(\mathrm{PE}_2 - \mathrm{PE}_1\right)}^{0} + \phi_0^c + G_{\mathrm{odd}} - mG && (3.26)\\
&= \phi_0^c + G_{\mathrm{odd}} - mG. && (3.27)
\end{aligned}$$

Die approbierte gedruckte Originalversion dieser Dissertation ist an der TU Wien Bibliothek verfügbar.
The approved original version of this doctoral thesis is available in print at TU Wien Bibliothek.
TU Bibliothek Your knowledge hub WIEN

Inserting the result in equations 3.9 and 3.8 gives the combined echoes as

$$\varphi_i = \angle S_i \tag{3.28}$$

$$= \angle \sum_c \left(M_i^c\right)^2 e^{i\left(\phi_i^c - \phi_{0,\mathrm{calc}}^c\right)} \tag{3.29}$$

$$= \angle \sum_c \left(M_i^c\right)^2 e^{i\left(\mathrm{PE}_i + \phi_0^c + G_{\mathrm{even/odd}} - \phi_0^c - G_{\mathrm{odd}} + mG\right)} \tag{3.30}$$

$$= \angle \sum_c \left(M_i^c\right)^2 e^{i\left(\mathrm{PE}_i + G_{\mathrm{even/odd}} - G_{\mathrm{odd}} + mG\right)} \tag{3.31}$$

$$= \mathrm{PE}_i + G_{\mathrm{even/odd}} - G_{\mathrm{odd}} + mG \tag{3.32}$$

$$= \mathrm{PE}_i + \begin{cases} G_{\mathrm{even}} - G_{\mathrm{odd}} + mG & \text{if } i \in 2\mathbb{N} \\ G_{\mathrm{odd}} - G_{\mathrm{odd}} + mG & \text{otherwise} \end{cases} \tag{3.33}$$

$$\varphi_i = \mathrm{PE}_i + \begin{cases} (m+1)\,G & \text{if } i \in 2\mathbb{N} \\ mG & \text{otherwise} \end{cases}. \tag{3.34}$$

3.1.3.2 Calculation of a correction term

As m is known (and is a real number for MCPC-3D-S, a whole number for ASPIRE), only G needs to be determined to calculate and remove the bipolar artefact. From the phase images at the first three echoes that were previously combined with MCPC-3D-S or ASPIRE, the following term proportional to G can be calculated:

$$\varphi_1 + \varphi_3 - \overbrace{\frac{T_{E,1} + T_{E,3}}{T_{E,2}}}^{k} \varphi_2 = \mathrm{PE}_1 + mG + \mathrm{PE}_3 + mG - k\left(\mathrm{PE}_2 + (m+1)\,G\right) \tag{3.35}$$

$$= \overbrace{\mathrm{PE}_1 + \mathrm{PE}_3 - k\mathrm{PE}_2}^{0} + 2mG - kmG - kG \tag{3.36}$$

$$= \overbrace{\left((2-k)\,m - k\right)}^{f} G \tag{3.37}$$

$$= fG \tag{3.38}$$

There are multiple ways to combine the first three phase images to yield a term proportional to G. The variant presented above was chosen, since the scaling factor $k = \frac{T_{E,1}+T_{E,3}}{T_{E,2}}$ equals 2 in most acquisitions (equidistant first three echoes) and unwrapping φ_2 can be avoided. Similarly to the phase offset, G might contain remaining small structure artefacts that can be removed in a first smoothing step, as the bipolar artefact G is assumed to be spatially smooth. In general fG might

Die approbierte gedruckte Originalversion dieser Dissertation ist an der TU Wien Bibliothek verfügbar.
The approved original version of this doctoral thesis is available in print at TU Wien Bibliothek.
TU Bibliothek Your knowledge hub WIEN

be wrapped and in MCPC-3D-S, it needs to be unwrapped before scaling to mG or $(m+1)\,G$ can be applied. With $(fG)^u$ being the unwrapped version of fG, the final artefact removal step is given as

$$\varphi_{\text{corrected}} = \varphi_i - \begin{cases} \frac{(m+1)}{f}\,(fG)^u & \text{if } i \in 2\mathbb{N} \\ \frac{m}{f}\,(fG)^u & \text{otherwise} \end{cases}, \tag{3.39}$$

which in ASPIRE with $m = 1$ and equidistant echoes ($f = k = 2$) simplifies to

$$\varphi_{\text{corrected}} = \varphi_i - \begin{cases} (2G)^u & \text{if } i \in 2\mathbb{N} \\ \frac{1}{2}\,(2G)^u & \text{otherwise} \end{cases}. \tag{3.40}$$

3.1.3.3 Additional considerations

The published version of the bipolar correction [42] details a method that avoids unwrapping of fG by estimating it up to a linear term by calculating and averaging the image gradient in the phase encode direction. This is especially beneficial for ASPIRE, as unwrapping could compromise both runtime and robustness, however, the bipolar artefact might contain higher order contributions that remain uncorrected. To have both benefits, the following simple and fast unwrapping scheme can be applied. The first part details the calculation of the artefact up to a linear term, and the second part the unwrapping scheme that is a simple modulo operation after removing the large linear and constant contributions. The bipolar artefact can be divided into a constant term c, a linear term g in phase encode direction and all other linear and higher order terms H, resulting in

$$fG = c + g\,(\hat{\boldsymbol{x}}_{\text{pe}} \cdot \boldsymbol{x}) + H, \tag{3.41}$$

where $\hat{\boldsymbol{x}}_{\text{pe}}$ is the unit vector in the phase encode direction and $\boldsymbol{x}$ the position of the voxel. The gradient g can be estimated by shifting the phase image by a number of voxels n in phase encode direction and subtracting it, where n needs to be small enough that less than π phase evolution occurs in-between the shift. To avoid large contributions from noisy voxels, the sum should be performed weighted, which is achieved in this case by performing the calculation in complex, yielding

$$g = \frac{\angle \sum_{\boldsymbol{x}} M M_n \exp\left\{i\left[fG - (fG)_n\right]\right\}}{n}, \tag{3.42}$$

where M is the magnitude of the first echo, M_n the shifted magnitude and $(fG)_n$ the shifted version of bipolar artefact fG. As the next step, to avoid cancellation in the complex sum, the constant part can be estimated from $fG - g\,(\hat{\boldsymbol{x}}_{\text{pe}} \cdot \boldsymbol{x})$ with

$$c = \angle \sum_{\boldsymbol{x}} M \exp\left\{i\left[fG - g\,(\hat{\boldsymbol{x}}_{\text{pe}} \cdot \boldsymbol{x})\right]\right\}. \tag{3.43}$$

Die approbierte gedruckte Originalversion dieser Dissertation ist an der TU Wien Bibliothek verfügbar.
The approved original version of this doctoral thesis is available in print at TU Wien Bibliothek.
TU Bibliothek Your knowledge hub WIEN

After removing the linear and constant contribution from the bipolar artefact, the remaining true phase values can be assumed to be in the range $[-\pi;\pi)$ and the removal of phase wraps can be simply performed by the γ operation that folds the phase into the range $[-\pi;\pi)$, giving

$$H^u = \gamma\left(fG - c - g\left(\hat{\boldsymbol{x}}_{\mathrm{pe}} \cdot \boldsymbol{x}\right)\right) \tag{3.44}$$

and finally by combining equations 3.41 to 3.44

$$(fg)^u = c + g\left(\hat{\boldsymbol{x}}_{\mathrm{pe}} \cdot \boldsymbol{x}\right) + H^u. \tag{3.45}$$

Although the calculation seems excessive, all steps are simple arithmetic operations and the computational expense is negligible in comparison to the multi-channel smoothing operation that is required for the phase offset.

For completeness, it is shown that the term $f = (2-k)\,m - k$ from Equation 3.37 does not vanish for possible echo time choices. First the echo times are parameterized relative to $T_{E,1}$ as

$$T_{E,2} = aT_{E,1} \qquad a > 1 \tag{3.46}$$

$$T_{E,3} = bT_{E,1} \qquad b > 1, \tag{3.47}$$

which simplifies the terms k and m to

$$k = \frac{T_{E,1} + T_{E,3}}{T_{E,2}} = \frac{T_{E,1} + bT_{E,1}}{aT_{E,1}} = \frac{1+b}{a} \tag{3.48}$$

$$m = \frac{T_{E,1}}{T_{E,2} - T_{E,1}} = \frac{T_{E,1}}{aT_{E,1} - T_{E,1}} = \frac{1}{a-1} \tag{3.49}$$

leading to the condition

$$f = 0 \tag{3.50}$$

$$(2-k)\,m - k = 0 \tag{3.51}$$

$$\left(2 - \frac{1+b}{a}\right)\frac{1}{a-1} - \frac{1+b}{a} = 0 \tag{3.52}$$

$$\frac{2a-1-b}{a\,(a-1)} - \frac{(1+b)\,(a-1)}{a\,(a-1)} = 0 \tag{3.53}$$

$$2a - 1 - b - (1+b)\,(a-1) = 0 \tag{3.54}$$

$$2a - 1 - b - a - ab + 1 + b = 0 \tag{3.55}$$

$$a - ab = 0 \tag{3.56}$$

$$b = 1, \tag{3.57}$$

which can never be fulfilled, as it corresponds to the first and third echo having identical echo time. Thus, f never vanishes for real echo times.

Die approbierte gedruckte Originalversion dieser Dissertation ist an der TU Wien Bibliothek verfügbar.
The approved original version of this doctoral thesis is available in print at TU Wien Bibliothek.
TU Bibliothek Your knowledge hub WIEN

3.2 ROMEO

The new unwrapping method ROMEO [21] published in *Magnetic Resonance in Medicine* was developed in a collaborative effort and resulted in a shared co-first authorship. The most part of the development of ROMEO was performed by the author of this thesis, while the most part of the analysis and manuscript preparation was performed by Dr. Barbara Dymerska of University College London, the other co-first author.

3.2.1 Edge Weights

The central idea in ROMEO is to grow an unwrapping region by always adding and unwrapping the next neighboring voxel that is easiest to unwrap, which is a form of quality-guided unwrapping. The specification of how easy a neighboring voxel is to unwrap is precalculated in a weight matrix with one quality entry for each connection (or edge) between neighboring voxels. Voxels are regarded as neighbors if one face is touching, which results in a total number of $3N$ edges in a 3D volume of N voxels (disregarding border effects). The weight for each edge is calculated by multiplying up to 4 weights, where each individual weight is in the range 0 to 1 and corresponds to a specific quality criterium. This process is shown in Figure 3.1 for two slices. To increase the robustness of the weights multiplication, it has been changed from a simple multiplication in the publication to a multiplication with an offset, specifically

$$w = \prod_k \left(0.1 + 0.9 w^k\right), \quad k \in \{\mathrm{pc}, \mathrm{mc}, \mathrm{tpc}, \mathrm{pl}\}, \tag{3.58}$$

with the corresponding weights defined here:

Phase Coherence This weight is a measure of how close the phase value between neighboring voxels is. If the phase values are far apart, it is considered difficult to unwrap, which is calculated by the expression

$$w_{i,j}^{\mathrm{pc}} = 1 - \frac{|\gamma(\varphi_i - \varphi_j)|}{\pi}, \tag{3.59}$$

where $\gamma(x)$ is the wrapping function, that wraps values into the range $[-\pi, \pi)$.

Magnitude Coherence Tissue interfaces are difficult to unwrap, as a sudden phase change (possibly larger than π) can occur. Particularly, when there is one layer of noise between the different tissues, a noise voxel might assume a phase value that creates a path across the tissue interface, however, with a

Die approbierte gedruckte Originalversion dieser Dissertation ist an der TU Wien Bibliothek verfügbar.
The approved original version of this doctoral thesis is available in print at TU Wien Bibliothek.
TU Bibliothek Your knowledge hub WIEN

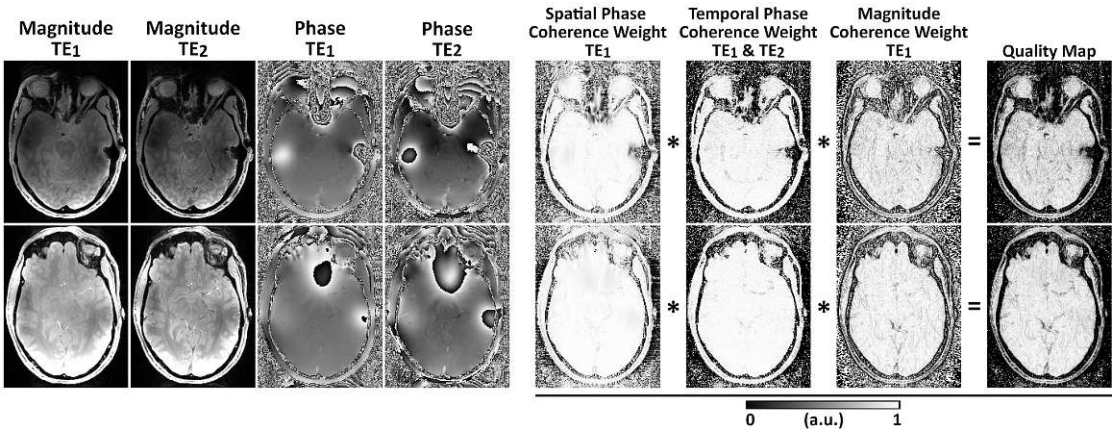

Figure 3.1: Visualization of the ROMEO weights *Phase Coherence*, *Temporal Phase Coherence* and *Magnitude Coherence* in x-direction (left-right). Two slices are presented (top row and bottom row) with the measured magnitude and phase from the first two echoes on the left, the calculated weights in the middle and the resulting quality map on the right. The quality map accumulates the information from the individual weights.

possibly unwanted unwrapping outcome. To avoid these problems, a weight created from the magnitude detects sudden intensity changes using

$$w_{i,j}^{\mathrm{mc}} = \left(\frac{\min\left(M_i, M_j\right)}{\max\left(M_i, M_j\right)} \right)^2 . \tag{3.60}$$

Temporal_Phase Coherence If available, multi-echo information can be utilized to create a further weight. The phase change between two adjacent voxels should scale with the echo time, i.e.

$$\gamma\left(\varphi_{i,t_m} - \varphi_{j,t_m}\right)/T_{E,m} \approx \gamma\left(\varphi_{i,t_n} - \varphi_{j,t_n}\right)/T_{E,n}. \tag{3.61}$$

Expressed as a weight between 0 and 1 this turns into

$$\hat{w}_{i,j,t_1,t_2}^{\mathrm{tpc}} = 1 - \left| \gamma\left(\varphi_{i,t_1} - \varphi_{j,t_1}\right) - \frac{T_{E,t_1}}{T_{E,t_2}} \gamma\left(\varphi_{i,t_2} - \varphi_{j,t_2}\right) \right| \tag{3.62}$$

$$w_{i,j,t_1,t_2}^{\mathrm{tpc}} = \begin{cases} 0 & \text{if } \hat{w}_{i,j,t_1,t_2}^{\mathrm{tpc}} < 0 \\ \hat{w}_{i,j,t_1,t_2}^{\mathrm{tpc}} & \text{otherwise} \end{cases} . \tag{3.63}$$

Phase Linearity Especially if no magnitude and no multi-echo data is available, the Phase Coherence weight alone does not provide sufficient weight information. The phase linearity weight estimates how well the phase values of

Die approbierte gedruckte Originalversion dieser Dissertation ist an der TU Wien Bibliothek verfügbar.
The approved original version of this doctoral thesis is available in print at TU Wien Bibliothek.
TU Bibliothek Your knowledge hub WIEN

four voxels in a row lie on a line. The calculated value is attached to the middle edge and helps to penalize tissue interfaces, noisy voxels and other hard to unwrap regions. The weight $w_{i,j}^{\mathbf{pl}}$ is given by

$$\hat{w}_{i,j,k}^{\mathrm{pl}} = 1 - \frac{|\gamma\,(\varphi_i - 2\varphi_j + \varphi_k)|}{2} \tag{3.64}$$

$$w_{i,j,k}^{\mathrm{pl}} = \begin{cases} 0 & \text{if } \hat{w}_{i,j,k}^{\mathrm{pl}} < 0 \\ \hat{w}_{i,j,k}^{\mathrm{pl}} & \text{otherwise} \end{cases} \tag{3.65}$$

$$w_{i,j}^{\mathrm{pl}} = w_{i,j,j+1}^{\mathrm{pl}} w_{i-1,i,j}^{\mathrm{pl}}. \tag{3.66}$$

The Phase Coherence and Phase Linearity can be always used, the Magnitude Coherence weight if a magnitude is provided and the Phase Gradient Coherence if a multi-echo scan is provided. The weights can be individually deactivated if required or additional weights can be defined (the ROMEO program is specifically written to facilitate easy integration and experimentation of new weights).

3.2.2 Region Growing

The region growing unwrapping process utilizes certain data structures and algorithms to perform region growing efficiently. The unwrapping process starts with the region being a single voxel or seed voxel, then considers all neighbors of the region and unwraps the neighbor with the lowest cost (highest quality) and adds it to the region. This step is iteratively performed until all voxels have been unwrapped. This process is illustrated in Figure 3.2 for a small 2D grid, but is identically performed for 3D volumes with 6 neighbors instead of 4. Out of the roughly $6n$ total edges in a 3D volume with n voxels, the algorithm only uses $n-1$ edges for unwrapping, each having the lowest cost of reaching a certain voxel. Effectively, this creates a minimum spanning tree of edges connecting all voxels to one region according to the Prim–Jarník algorithm [43]. The determination of all neighbors is performed using a priority queue, in which for an encountered new voxel all edges to voxels not yet part of the region are enqueued. When drawing the next edge from the queue (the one with the lowest associated cost currently inside the queue), it is first confirmed that the voxel it connects to is not yet part of the region, otherwise this edge is skipped.

3.2.3 Seed Determination and Offset Correction

The shape of the minimum spanning tree does not depend on the seed voxel that was used, but the unwrapped image might have a global offset of $n2\pi$, depending on the choice of seed voxel. This can be either corrected by ensuring the seed

Die approbierte gedruckte Originalversion dieser Dissertation ist an der TU Wien Bibliothek verfügbar.
The approved original version of this doctoral thesis is available in print at TU Wien Bibliothek.
TU Bibliothek Your knowledge hub WIEN

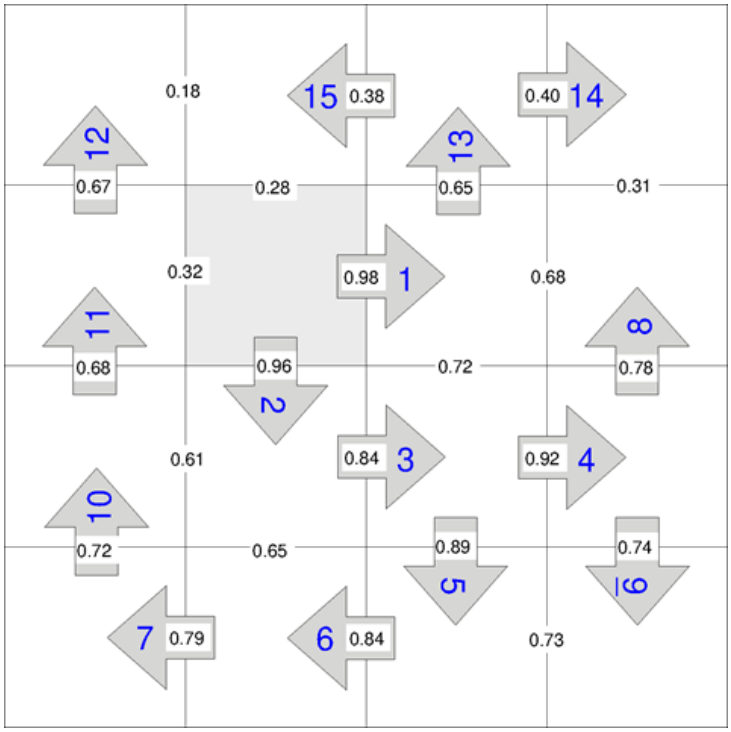

Figure 3.2: Order in which unwrapping is performed, illustrated in 2D on a small grid. The gray voxel is the seed voxel and the values on the edges are the weights. The blue number on the arrows is the order in which new voxels are added to the region. This figure was first presented in Supplementary Material of [21].

voxel does not contain an offset of $n2\pi$, or by performing a global $n2\pi$ correction after unwrapping, each option having its use case. If multi-echo data is available, the proposed method is to choose a high quality seed voxel and perform offset correction using multi-echo information. A high quality seed voxel is chosen by using the voxel with the lowest sum of its 6 edges. For the high-quality seed voxel, a maximum number of 2 wraps is assumed for the two echoes that are used for offset correction of the seed voxel. All different wrap options are tested and the one for which the linearity between both echoes is best matched is used. An additional regularization term is added to avoid the estimation of larger wrap counts when the echo times are multiples of each other. The number of wraps is estimated as

$$n_{\min} = \arg\min_{n,m} \left(\left| \frac{\varphi_i + n \cdot 2\pi}{T_{E,i}} - \frac{\varphi_j + m \cdot 2\pi}{T_{E,j}} \right| + \left| \frac{n+m}{100} \right| \right), \quad n, m \in -2:2, \tag{3.67}$$

where n is the number of wraps for the echo i and m the number of wraps for the echo j.

3.2.4 Template Unwrapping

For data with multiple volumes (e.g. echoes in multi-echo acquisitions or time-points in functional MRI), spatial unwrapping is performed only on one volume,

Die approbierte gedruckte Originalversion dieser Dissertation ist an der TU Wien Bibliothek verfügbar.
The approved original version of this doctoral thesis is available in print at TU Wien Bibliothek.
TU Bibliothek Your knowledge hub WIEN

which is then used in a template-based approach for unwrapping the adjacent volumes. The assumption for template unwrapping in the multi-echo case is that the phase evolves linearly with time and has negligible phase offset. The assumption for multiple timepoints is that phase changes between neighboring volumes are small in comparison to π.

After one template has been unwrapped, it is linearly scaled to estimate the phase of the neighboring volume (in the case of multiple timepoint the scaling factor is 1). The neighboring volume is then unwrapped in relation to the scaled template by adding or subtracting $n2\pi$ so that the difference between both images is less than π. This is performed iteratively by always using the unwrapped neighboring volume as a template until all volumes have been unwrapped. An additional option, when non-ideal behavior is encountered, like local non-linear phase evolution or movement between timepoints, is the detection of temporally unstable voxels and using spatial unwrapping only for those. Voxels are assumed to be unstable if the difference between the voxel value and the template after template unwrapping is larger than $\pi/2$.

If multi-echo acquisitions are linear in time but contain an additional phase offset, MCPC-3D-S can be performed for both monopolar and bipolar sequences as a first phase correction step to remove the phase offset.

3.2.5 Performance Considerations and Algorithm Complexity

For performance considerations, the weights have been converted to integer cost values between 1 and 255, where 1 is the lowest cost (highest weight) and 255 is the highest cost. 0 corresponds to a non-existing edge at image borders and in the application with masked voxels. With integer cost values a bucket priority is used, which ensures a constant runtime per operation. A further benefit of this integer range is the efficient storage as unsigned 8-bit integers ($2^8 = 256$).

The determination of the runtime for ROMEO on one 3D volume is shown to be $O(n)$, where n is the number of voxels and where each subpart of the algorithm is $O(n)$ or less in itself. The determination of the weights is performed in $O(n)$, as each individual weight requires 3-6 data accesses with no loops per voxel. The seed determination requires one maximum search through all weights, which is $O(n)$ as well. The region growing is the most complex part and can be divided into a maximum of $6n$ computations, performed iteratively for each edge drawn from the queue. The first operation of drawing a new edge is constant, as is the determination of the connecting voxel and if it has already been visited. The unwrapping of the new voxel and the determination of up to 6 new neighbors together with the enqueuing of the new values is constant as well, which results in

Die approbierte gedruckte Originalversion dieser Dissertation ist an der TU Wien Bibliothek verfügbar.
The approved original version of this doctoral thesis is available in print at TU Wien Bibliothek.
TU Bibliothek Your knowledge hub WIEN

up to $6n$ computations of constant runtime, which results in $O(n)$.

The template unwrapping aspect of ROMEO also considerably reduces the runtime, as only one volume is unwrapped spatially and the remaining volumes are unwrapped by a simple voxelwise scaling and modulo operation.

3.3 CLEAR-SWI

CLEAR-SWI was published in NeuroImage as a research article [44]. This section contains parts of the research article but in a more comprehensive form with additional considerations.

CLEAR-SWI is a comprehensive reconsideration of SWI which introduces several recently published advancements and own new developments. The main goal is to avoid artefacts present in standard SWI at ultra-high field. Other improvements are higher SNR, more homogeneous appearance, a better visibility of small veins, and additional availability of quantitative information (T_2^* and M_0 maps).

3.3.1 Sequence

Standard SWI is acquired with a single-echo sequence using a late echo for high magnitude contrast [32], which sacrifices SNR by not measuring during the early time of the TR (repetition time). Multi-echo sequences can utilize the whole TR and not only the late part, thus increasing the SNR and obtaining additional echo-time dependent information. There are monopolar and bipolar multi-echo acquisitions, monopolar acquisitions sample the signal for each echo under the same polarity of the readout gradient, which translates to the same measurement direction in k-space. This requires an additional "flyback" or rewind gradient after measuring one k-space line to move back to the beginning of that line. Bipolar acquisitions sample the signal under gradients with both readout polarities, and thus don't require a rewinder gradient, as they sample the echoes in an alternating fashion in positive and negative direction, sampling on the forward and backward pass in k-space. Although most steps of CLEAR-SWI can be performed with single-echo, monopolar or bipolar acquisitions, bipolar has advantages due to the increased SNR and additional multi-echo information. The results of a simulated SNR comparison are presented in Section 5.4.4.

Additional considerations for setting up the bipolar multi-echo sequence are the echo times and the bandwidth. Due to the alternating readout direction between consecutive echoes, bipolar sequences suffer from two types of artefacts; an alternating gradient in phase direction that is caused by timing imperfections and an alternating direction of geometric distortions caused by magnetic field inhomogeneities. The first artefact is removed in coil combination (Subsection 3.3.2.1), the

Die approbierte gedruckte Originalversion dieser Dissertation ist an der TU Wien Bibliothek verfügbar.
The approved original version of this doctoral thesis is available in print at TU Wien Bibliothek.
TU Bibliothek Your knowledge hub WIEN

second artefact can be avoided by adjusting the sequence accordingly. By setting the receiver bandwidth to at least twice the expected B_0 inhomogeneities (both in Hz), the distortions are limited to a shift of 1 voxel (equation in [45]). In case the sequence cannot be adjusted, an additional bipolar distortion correction step can be applied by calculating the inherent B_0 map (Section 3.4.4) and estimating and correcting the geometrical distortion [45].

The optimal TR for SNR efficiency and the optimal number of echoes for a given TR can be obtained from Figure 5.32, where the generally best settings can be found at the bends of the bipolar curves. This is not required, but if the echoes are set to multiples of the first echo time, ASPIRE coil combination (which is faster and more robust than MCPC-3D-S) and the fast NumART* [14] method for T_2^* estimation can be used.

3.3.2 Preprocessing

The acquired data consists of one 3D volume for each coil and each echo. An important preprocessing step is coil combination, which extracts information common to all coils and avoids coil-dependent offsets while significantly reducing the amount of data. The data after preprocessing can be used for estimating B_0 (Section 3.4.4), QSM [35], fitting tissue models [46, 47, 48], or other multi-echo MRI analyses.

3.3.2.1 Coil combination

The choice of the coil combination algorithm is not only crucial in order to avoid artefacts such as open-ended fringe lines, but also to achieve high magnitude SNR and phase CNR [23]. Several methods exist which avoid phase artefacts, although many are subject to particular restrictions. The coil combination method used for the standard single-echo SWI [32] (and as implemented by the manufacturer) is homodyne filtering, which removes all low frequency phase information and then sums the signal of the coils, which leads to severe phase artefacts, however, at fields strengths of 3 T or higher [49]. The Roemer/ SENSE [19] approach requires a reference coil, which limits its applicability at ultra-high field strengths. The phase difference method (also called Hermitian inner product) works for all multi-echo sequences but suffers from markedly reduced phase CNR. The VRC approach [50] would be applicable in general and works for single echo data, however, it needs to detect a valid center for the phase correction, which is a fragile, image-dependent step, and – dependent on the coil geometry – can generate artefacts above 7 T, or at 7 T for objects larger than the head [23]. For multi-echo data, the ASPIRE method of coil combination [42] meets all the criteria imposed by CLEAR-SWI; it does not require a reference coil, making it suitable for all field

Die approbierte gedruckte Originalversion dieser Dissertation ist an der TU Wien Bibliothek verfügbar.
The approved original version of this doctoral thesis is available in print at TU Wien Bibliothek.
TU Bibliothek Your knowledge hub WIEN

strengths, it is not dependent on image-derived parameters and the CNR is higher than in phase difference methods. The only limitation of ASPIRE is that two echoes satisfy $mT_{E,2} = (m+1)T_{E,1} | m \in \mathbb{N}$ for monopolar acquisitions and, for bipolar acquisitions, that three echoes satisfy $T_{E,2} = 2T_{E,1}$ and $T_{E,3} = 3T_{E,1}$. Instead of ASPIRE, MCPC-3D-S might be considered as an alternative in cases, where the echo time restrictions cannot be fulfilled or when the ASPIRE patent for commercial use is too restrictive. The additional required unwrapping step imposes challenges in robustness and speed, however, with the most promising method for unwrapping on the scanner being ROMEO, as it has been proven more robust and faster than other unwrapping methods [21].

The effect of the coil combination method on the magnitude images is less crucial, although, due to the Rician noise distribution in magnitude images, the classical root-sum-of-squares combination incurs a bias (see simulation in Figure 2.5), which is stronger for areas with low intensity (e.g. veins). ASPIRE reduces this effect by performing magnitude weighted combination of the complex data after the removal of coil specific phase offsets. This might improve the accuracy of calculated T_2^* values, especially in areas with low T_2^* such as veins.

3.3.2.2 Noise mask

A brain mask was required for high-pass filtering the phase to avoid image background affecting the values in voxels at the border of the brain. A conservative mask (only removing noise but not the skull) was created by applying the automatic masking, which is described in Section 3.4.1.

3.3.3 CLEAR-SWI Steps

The specific CLEAR-SWI steps are performed in two separate paths for the phase and magnitude. An overview of the steps is illustrated in Figure 3.3.

3.3.3.1 Phase processing

The first step is unwrapping of the multi-echo phase data. From the multitude of existing phase unwrapping methods, two have been chosen as viable for CLEAR-SWI; Laplacian unwrapping [20] and ROMEO [21] for being robust and fast enough for realtime calculation of SWI on the scanner hardware. The advantage of ROMEO is a shorter runtime for multi-echo datasets and that the resulting phase can be used for B_0 calculation or QSM. However, if phase corruptions exist already in early echoes (places where unwrapping is ambiguous, in rare cases in veins), ROMEO unwrapping might produce visible artefacts. The advantage of Laplacian unwrapping in this case is that is resolves these remaining ambiguities

Die approbierte gedruckte Originalversion dieser Dissertation ist an der TU Wien Bibliothek verfügbar.
The approved original version of this doctoral thesis is available in print at TU Wien Bibliothek.
TU Bibliothek Your knowledge hub WIEN

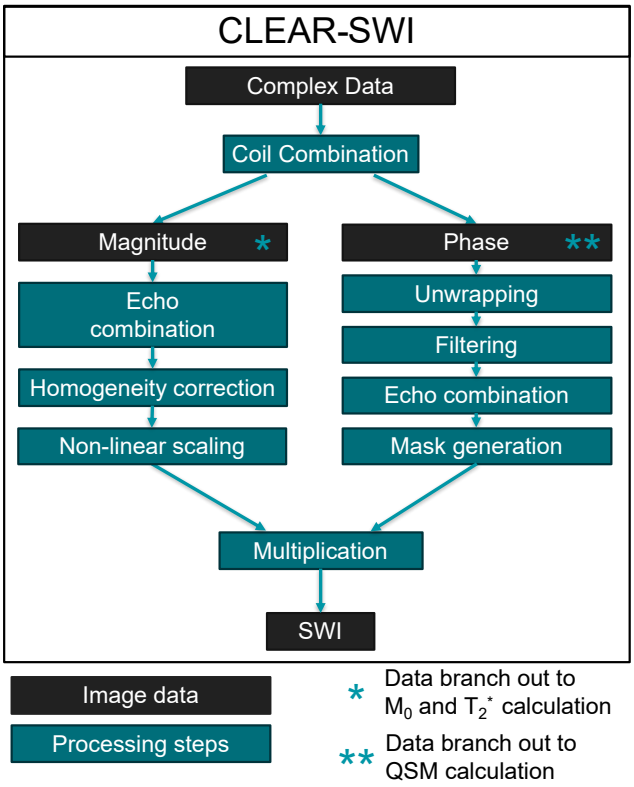

Figure 3.3: Proposed SWI processing pipeline; after coil combination, the magnitude and phase processing is performed separately and joined again in the final multiplication step to generate the SWI.

in a continuous manner, thus making it the more robust choice for the application of CLEAR-SWI. For Laplacian unwrapping and ROMEO, two slightly different phase processing paths are described here.

A) Laplacian Unwrapping After Laplacian unwrapping, the phase contains arbitrary background field variations, which need to be removed by the high-pass filtering step before the echo-combination of the phase can be applied. This is due to bias effects of the noise that would otherwise lead to poor SNR in the combined phase.

For high-pass filtering, a masked, Gaussian low-pass filter with a sigma of 4 pixels was applied to the unwrapped phase and subtracted to achieve high-pass filtering (see Gaussian smoothing with missing values Section 3.4.3). The noise mask calculated above was used to avoid the inclusion of noise voxels. The filtering was applied slice-wise, which provides a satisfactory result in terms of CNR for SWI data, which typically have an aspect ratio of 2 or more [51]. For the more isotropic voxels commonly acquired for QSM, 3D high-pass filtering might yield higher phase CNR.

The multi-echo combination was afterwards performed using inverse-variance-weighting [16] according to Section 2.4.2.4.

Die approbierte gedruckte Originalversion dieser Dissertation ist an der TU Wien Bibliothek verfügbar.
The approved original version of this doctoral thesis is available in print at TU Wien Bibliothek.
TU Bibliothek Your knowledge hub WIEN

B) ROMEO Unwrapping An alternative to Laplacian unwrapping is to apply ROMEO [21] presented in Section 3.2 for unwrapping. While standard spatial unwrapping methods perform poorly for late echoes and temporal unwrapping methods depend on the exact echo timings, ROMEO achieves high accuracy and coherence between all echoes, since it includes temporal information in the spatial unwrapping process and afterwards performs template based unwrapping for later echoes. There are two advantages of ROMEO over Laplacian unwrapping. The first is the avoidance of background fields, which results in a true estimation of B_0, which is not possible with Laplacian unwrapping. The second is a poor performance of Laplacian unwrapping that is observed for some veins, where Laplacian unwrapping tends to smooth fast phase changes. Although ROMEO has these advantages, Laplacian unwrapping is still more robust, as it produces smooth results even in places where integerized unwrapping methods are unable to resolve wraps, e.g. due to open ended fringe lines that are inherently impossible to unwrap.

After ROMEO unwrapping, the phase images are combined according to the B_0 calculation in Section 3.4.4. In this approach, a similar high-pass filtering step is applied as for Laplacian unwrapping, but after the multi-echo combination instead of for each echo individually. Both the template-based unwrapping and the filtering is performed only once, which leads to a reduced runtime of the ROMEO phase processing compared to the Laplacian approach. The B_0 map that is calculated as intermediate step is an additional useful output in this variant.

3.3.3.2 Sigmoidal phase masking

A phase mask is created from the combined and high-pass filtered phase that shows vein and iron contrast. This is used to augment the magnitude image and contains grayscale values in the range [0;1]. The function to obtain the mask which is most commonly described in the literature for SWI [52, 51, 32] is

$$f(x) = \begin{cases} 1 & x < 0 \\ 1 - x & 0 \leq x \leq 1 \\ 0 & x > 1 \end{cases}$$

and is applied voxelwise. Usually, to yield stronger weighting, the magnitude is multiplied several times by the mask, which corresponds to one multiplication by a phase mask that was created with the power function

$$f(x) = \begin{cases} 1 & x < 0 \\ (1 - x)^k & 0 \leq x \leq 1 \\ 0 & x > 1 \end{cases} .$$

Die approbierte gedruckte Originalversion dieser Dissertation ist an der TU Wien Bibliothek verfügbar.
The approved original version of this doctoral thesis is available in print at TU Wien Bibliothek.
TU Bibliothek WIEN Your knowledge hub

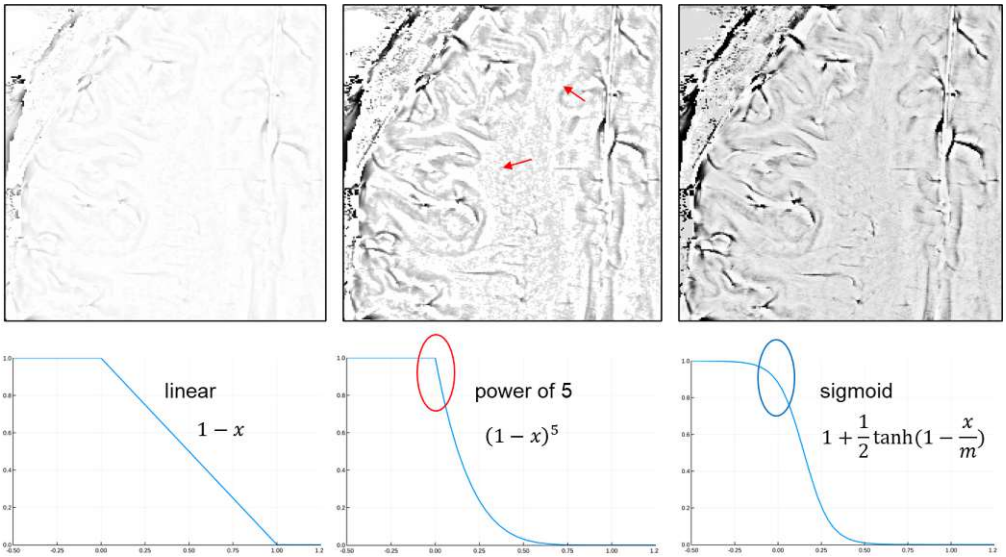

Figure 3.4: Visualization of different phase masking approaches; the first mask is created using linear scaling of the high-pass filtered positive phase part. The second mask is with a power of 5, which creates a steep bend (red ellipse) around the value of 0, leading to increased noise (red arrows) The sigmoidal phase mask is less steep around 0 (blue ellipse).

The power function, however, has a steep incline at 0, which increases the contrast around 0, where most noise is encountered. Figure 3.4 demonstrates this with the red ellipse and the red arrows. The approach taken in CLEAR-SWI is to apply a sigmoidal function that has no steep incline at 0, but can be arbitrarily steep in the middle to enhance contrast. The scaled and shifted tanh function

$$f(x) = \frac{1}{2} + \frac{1}{2}\tanh\left(1 - \frac{x}{m}\right), \tag{3.68}$$

where the parameter m was calculated as

$$m = \text{median}_{>0}(\varphi) \cdot k, \tag{3.69}$$

where the median of the positive phase values was used to obtain a stable scaling value and k is an additional level parameter to adjust the strength.

Figure 3.4 shows the appearance of linear, power of 5 and sigmoidal masking. The lower half of the figure shows how the applied function transforms the phase values. The steep bend at 0 with the power masking leads to noise amplification, since the phase values slightly above 0 are primarily noise voxels.

Die approbierte gedruckte Originalversion dieser Dissertation ist an der TU Wien Bibliothek verfügbar.
The approved original version of this doctoral thesis is available in print at TU Wien Bibliothek.
TU Bibliothek Your knowledge hub WIEN

3.3.3.3 Multi echo magnitude combination

Near optimum SNR in the combined magnitude image can be achieved by root-sum-of-squares weighting over echoes [13], as described in Section 2.4.1.2. This lessens the impact of signal dropouts by weighting early echoes in regions with rapid T_2^* decay. Of primary interest in SWI, however, is the clearest visualization of image features, reflected in the CNR between tissues of interest. The weighting factors which optimize CNR can be calculated given the corresponding T_1, T_2^* and ρ values. We take the example of white matter (WM) and gray matter (GM), but note that other choices may be desirable (e.g. the contrast between veins and white matter, or between lesions and surrounding tissue). Optimum CNR in combined images is achieved by weighting each echo by the CNR for that echo, or (given that noise is constant across echoes), the contrast for each echo, C_i. The combination and weighting factors are given by

$$M = \sum w_i M_i \tag{3.70}$$

$$w_i = C_i = S\left(\mathrm{gm}, T_{E,i}\right) - S\left(\mathrm{wm}, T_{E,i}\right), \tag{3.71}$$

where S is the signal formulation (Equation 2.55) with the tissue parameters for the given tissue type. If the flip angle α varies strongly in space, a flip angle map can be used instead of a scalar value in the calculation of S.

3.3.3.4 Non-linear magnitude scaling

The results of SNR-weighted combination and CNR-weighted combination have both reduced contrast compared to a single-echo acquisition of a late echo time, although being superior in SNR and CNR. Since it is not practical to individually window all areas to obtain good contrast values, a non-linear function was applied to obtain a similar magnitude contrast to single-echo acquisitions without changing local SNR values. From the observation that most interesting contrast is in the upper half of the brightness scale, a function can be defined that removes the lower half of the scale. To avoid making hard cuts, which would lead to unnatural appearance and completely remove low intensity contrast, the following function called softplus was used:

$$f\left(x\right) = \frac{\log\left(1 + e^{a(x-b)}\right)}{a} \tag{3.72}$$

The softness parameter $\alpha = 2$ was used and the cutoff parameter b was set to half the 0.8-quantile, which was around half the mean, but more stable.

Die approbierte gedruckte Originalversion dieser Dissertation ist an der TU Wien Bibliothek verfügbar.
The approved original version of this doctoral thesis is available in print at TU Wien Bibliothek.
TU Bibliothek WIEN Your knowledge hub

3.3.3.5 SWI calculation

The final calculation of the complete SWI is a simple multiplication of the combined magnitude with the phase mask.

Often, a minimum intensity projection (mIP) is performed to better visualize the structure of the veins. This projection uses a stack of several slices and produces one slice as output, where each resulting pixel is set to the lowest value that is assumed for the same pixel in all slices of the stack. A mIP is usually calculated from a stack of 7 or 8 slices and the same process is performed for the whole image, shifting the stack by one slice and leads to 3D mIP volume.

3.3.3.6 T_2^* and M_0 calculation

The additional parameter maps T_2^* and M_0 (where M_0 is the magnitude without decay) can be obtained by fitting from the multi-echo sequence and the steps are detailed in Section 2.4.1.4 in Theory.

3.4 Supporting Methods

Here, a collection of supporting methods is presented, which are developed as parts of the main methods. The general goal is that each method can be applied without user intervention in an automatic, robust and computationally efficient way. To this end, automatic masking, sensitivity estimation, fast and flexible smoothing and B_0 calculation were developed and are presented. Two additional tools were developed, an SNR simulation that helps setting up efficient multi-echo sequences and a method to simulate a single-echo acquisition from a multi-echo scan, which is used in evaluation of the multi-echo SWI approach and can additionally be applied for backwards compatibility of multi-echo acquisitions, e.g. if in a clinical protocol a single-echo acquisition is replaced by a more efficient multi-echo acquisition, output images resembling the single-echo acquisition can still be simulated.

3.4.1 Automatic Masking

Certain methods require the background with no signal to be masked prior to calculation. This is the case for sensitivity estimation presented in Section 3.4.2 and for phase unwrapping with ROMEO (Section 3.2), where prior masking leads to a reduced runtime.

Background noise estimation The first step for masking is estimation of the background noise in the magnitude image. In gradient echo imaging, the noise has a Rician distribution that is spatially independent and has the same properties

Die approbierte gedruckte Originalversion dieser Dissertation ist an der TU Wien Bibliothek verfügbar.
The approved original version of this doctoral thesis is available in print at TU Wien Bibliothek.
TU Bibliothek Your knowledge hub WIEN

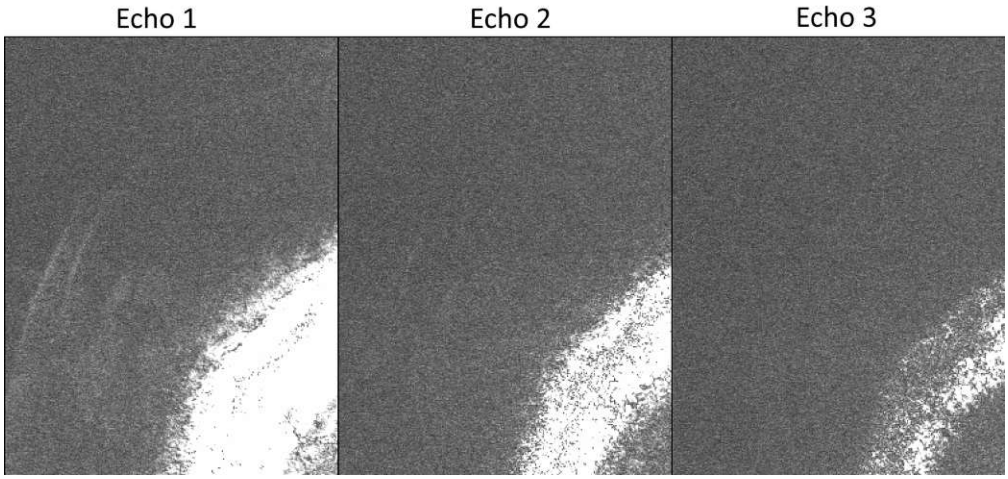

Figure 3.5: MRI background noise; The noise is very homogeneous over the image and identical in amplitude for each echo. In Echo 1, a fold-in artefact is visible from the opposite side of the field of view.

for each echo (see Figure 3.5). The image noise follows the Rayleigh distribution, which the special case of the Rician distribution in regions without signal.

In the automatic masking scheme, it is assumed that at least one of the corners of the image contains only noise, which is a reasonable assumption for brain images. The mean μ and standard deviation σ are calculated for each corner (10x10x10 voxels) and the corner with the lowest mean is chosen.

Removal of background noise Since the noise is not varying across the image, the calculation of a simple threshold is sufficient for masking. The cumulative distribution function of a Rayleigh distribution for the value of $\mu + 3\sigma$ is 0.994, which is a good threshold, as it removes 99.4% of the noise values.

Removal of artefacts in background On the one hand the threshold should be as low as possible to avoid valid signal to be removed and on the other hand it should be as high as possible to remove artefacts in the background that are often present due to certain non-ideal signal behaviors and have larger magnitude than noise. By using a threshold approach, only artefacts that are lower than the lowest meaningful signal can be removed. A value of $m/5$ was found to be a good estimation of the lowest signal, where m is the mean of the image after removing the noise using the previously established threshold of $\mu + 3\sigma$.

Threshold for masking As a final threshold that removes noise and most background artefacts, but avoids removing meaningful signal, the maximum of the both

Die approbierte gedruckte Originalversion dieser Dissertation ist an der TU Wien Bibliothek verfügbar.
The approved original version of this doctoral thesis is available in print at TU Wien Bibliothek.
TU Bibliothek Your knowledge hub WIEN

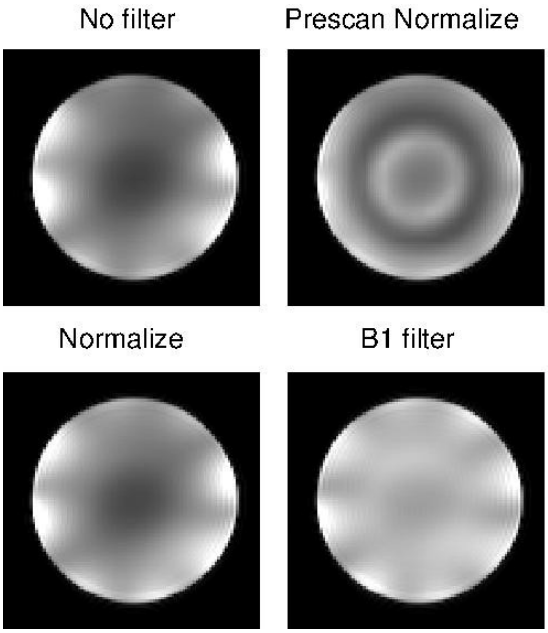

Figure 3.6: Comparison of vendor homogeneity corrections tested on a spherical water phantom. The ideal appearance would be uniform intensity. The system is a 7T TERRA scanner.

the noise threshold and the threshold for background artefact removal was chosen:

$$\text{threshold} = \max\left(\mu + 3\sigma, m/5\right) \tag{3.73}$$

Optional Morphological Filtering If individual noise voxels remaining in the background after applying the threshold are detrimental to the method for which the mask is required, they can be removed using the morphological erosion or opening operations, however, this wasn't required for the methods presented within this thesis.

3.4.2 Sensitivity Estimation and Homogeneity Correction

Figure 3.6 shows various homogeneity correction schemes present in currently existing clinical ultra-high field scanners, all of which are unable to reduce the inhomogeneity to tolerable levels.

The sensitivity is spatially varying and a sensitivity map can be created for each coil individually. However, for homogeneity correction, the sensitivity map of the

Die approbierte gedruckte Originalversion dieser Dissertation ist an der TU Wien Bibliothek verfügbar.
The approved original version of this doctoral thesis is available in print at TU Wien Bibliothek.
TU Bibliothek Your knowledge hub WIEN

combined magnitude suffices and can be estimated more robustly. The sensitivity estimation presented here is split into two parts, a simple segmentation step to isolate a single tissue class, which already represents the sensitivity as there are no tissue dependent effects remaining, and a smoothing step that interpolates and extrapolates the regions where this tissue class is not present.

3.4.2.1 Simple segmentation

Since tissue segmentation itself is a very complicated and not completely solved topic, the aim here is to develop a simple method that achieves the task of segmenting white matter in gradient echo or MPRAGE scans. The segmentation does not need to be perfect, as a small number of wrongly classified voxels only leads to minor difference in the estimated sensitivity map, but no abrupt artefacts, due to the smoothing operation. The sensitivity is identical for each echo in the multi-echo scan and the first echo was chosen for sensitivity estimation, as the tissue contrast caused by T_2^* decay is smaller and wrongly classified voxels have reduced less impact.

The segmentation is performed in a box-wise threshold approach with a default of 15 overlapping boxes per dimension. Inside each box, the slowly varying sensitivity is assumed to be constant and a lower and upper threshold is calculated for tissue segmentation. The "main tissue" inside the box is kept, but tissue types that have significantly lower or higher intensity values are removed. The brightness value of the "main tissue" is estimated as the 90% quantile of the signal inside the box, which is working robustly if less than 10% brighter tissue is present inside each box. This is the case for white matter in MPRAGE and gradient echo imaging, as only vascularity or small artefacts are brighter than white matter. Tissue that is lower than 90% or higher than 110% of the brightness of the "main tissue" is removed. The boxes overlap by half their length in each dimension, leading to 8 classification values for each voxel. To achieve a robust application, a voxel was considered white matter, if it was located inside the automatic mask (see Automatic Masking, Section 3.4.1) and if it was classified as "white matter" in at least 2 out of the 8 boxes it is located in. Examples of resulting segmented images are shown in Figure 3.7 for MPRAGE and gradient echo scans.

3.4.2.2 Smoothing with missing values

The final smoothing step solves two problems; it interpolates and extrapolates the missing values from segmentation and it smooths the sensitivity to remove small structural features, since the sensitivity is known to be spatially smooth. The smoothing is performed in two steps. The first step is smoothing with a modified Gaussian smoothing algorithm which handles interpolation and extrapolation and

Die approbierte gedruckte Originalversion dieser Dissertation ist an der TU Wien Bibliothek verfügbar.
The approved original version of this doctoral thesis is available in print at TU Wien Bibliothek.
TU Bibliothek WIEN Your knowledge hub

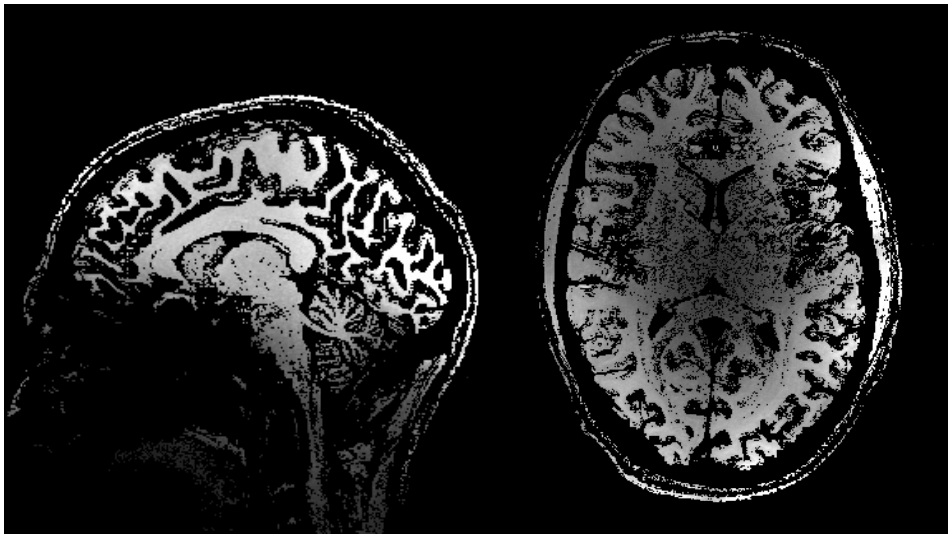

Figure 3.7: Visualization of the Simple Segmentation; The left side shows a sagittal slice of an MPRAGE image, the right side an axial slice of a gradient echo image. Very dark and very bright regions are cut away and mainly white matter remains. The remaining skull does not hinder sensitivity estimation.

is described in Section 3.4.3. The extrapolation range is about 3σ and to fill the parts of the image without signal and not reached by the extrapolation with meaningful sensitivity values, the triple of the average sensitivity inside the image (automatic mask) is taken and a final smoothing step is applied that blurs the boundary. The higher sensitivity values outside the brain reduce the background noise. The effective σ that is applied can be calculated as $\sqrt{\sigma_1^2 + \sigma_2^2}$, where σ_1 and σ_2 result from the first and second smoothing steps respectively. Figure 3.8 presents the obtained sensitivity after each of the two smoothing steps.

3.4.2.3 Homogeneity correction

Once the sensitivity is calculated, a homogeneity correction can be performed by dividing the magnitude image by the smooth sensitivity profile. The calculation does not change local SNR, as both signal intensity and noise are scaled equally and due to the smoothing operation the sensitivity does not contribute significantly to noise. The application of homogeneity correction to inhomogeneous magnitude images can be seen in the results chapter and especially Figure 5.25 might be interesting as it presents different views of one high-resolution dataset.

Die approbierte gedruckte Originalversion dieser Dissertation ist an der TU Wien Bibliothek verfügbar.
The approved original version of this doctoral thesis is available in print at TU Wien Bibliothek.
TU WIEN Bibliothek Your knowledge hub

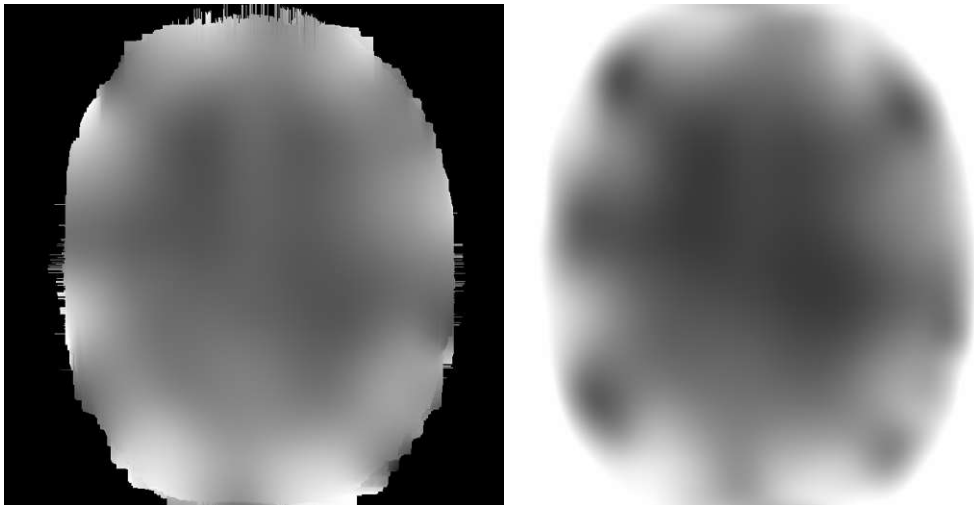

Figure 3.8: Estimated sensitivity; The image on the left shows the estimated sensitivity after the first smoothing with extrapolation and interpolation. The image on the right is after application of the second smoothing, where the remaining missing values have been filled.

3.4.3 Fast Gaussian 3D Smoothing

Gaussian smoothing is an important image processing tool. It is used for creating low-pass and high-pass filters, and especially in the context of MR for removing noise and structural artefacts from maps calculated for image correction steps that are known to be smooth, e.g. sensitivity maps or phase offset maps. A further capability of the Gaussian filter presented here is estimation of missing values, both for inter- and extrapolation. This section about fast Gaussian 3D smoothing is a bit more technical and contains implementation details that were necessary for computationally efficiency.

The canonical approach to creating a Gaussian filter with the standard deviation σ is to convolve a 3D Gaussian kernel with the image volume. The Gaussian kernel has to be as big as possible to be mathematically precise, where a common choice for the kernel size is 4σ (This is used in the Julia toolbox for image filtering[1]). The 3D Gaussian that describes the kernel is

$$G_{3D}\left(x, y, z; \sigma\right) = \frac{1}{\left(\sqrt{2\pi}\sigma\right)^3} e^{-\frac{x^2+y^2+z^2}{2\sigma^2}}. \tag{3.74}$$

It is quite inefficient to evaluate this function for each voxel and kernel point during the convolution, and there are multiple approaches to efficiently calculate

[1] https://github.com/JuliaImages/ImageFiltering.jl

Die approbierte gedruckte Originalversion dieser Dissertation ist an der TU Wien Bibliothek verfügbar.
The approved original version of this doctoral thesis is available in print at TU Wien Bibliothek.
TU Bibliothek Your knowledge hub WIEN

the convolution. The method favored by many image processing toolboxes is to transform both the kernel and the volume into the frequency domain, where the convolution turns into a simple multiplication. However, to allow for more flexible modifications of the smoothing process a spatial method for runtime optimization was chosen here.

3.4.3.1 Optimizing the runtime

The runtime of the canonical application is $O\left((4\sigma)^3 n\right) = O\left(\sigma^3 n\right)$, where n is the number of voxels of the image and the kernel size is 4σ in voxels. The Gaussian filter is a separable filter and can be divided into separate applications for each dimension, which greatly reduces the number of calculation steps to $O\left(3\left(4\sigma\right)n\right) = O\left(\sigma n\right)$. Additionally, the central limit theorem can be utilized, which states the application of multiple convolutions (or filters) converges toward a Gaussian. The computationally most efficient filter is the running average filter with a runtime of $O(n)$, independent of σ or the size of the kernel. With 3 applications of average filtering to estimate Gaussian filtering, an average error of 0.04% per pixel was estimated [53] and the total runtime is reduced to $O\left(9n\right) = O\left(n\right)$. To calculate the standard deviation of the estimated Gaussian filter, we start with the standard deviation of the average filter, which is

$$\sigma_{\text{ave}} = \frac{w}{\sqrt{12}}, \tag{3.75}$$

where w is the length of the filter. The σ of the estimated Gaussian filter is then given by

$$\sigma = \sqrt{\sum_i \sigma_{\text{ave},i}} \tag{3.76}$$

$$= \sqrt{\frac{1}{12}\sum_i w_i^2}, \tag{3.77}$$

where $\sigma_{\text{ave},i}$ is the standard deviation and w_i the filter length of the i-th average filter.

3.4.3.2 Application for smoothing phase

Directly smoothing phase values leads to huge problems around phase wraps, as phase images are only defined in the $[-\pi;\pi)$ range. These problems can be avoided by smoothing phase values in the complex domain with a uniform magnitude of 1. In principle the magnitude values correspond to weighting factors in the smoothing

Die approbierte gedruckte Originalversion dieser Dissertation ist an der TU Wien Bibliothek verfügbar.
The approved original version of this doctoral thesis is available in print at TU Wien Bibliothek.
TU Bibliothek Your knowledge hub WIEN

process and a measured magnitude image could be used instead of uniformly 1, however, this would bias the phase values towards higher magnitude regions.

To perform Gaussian smoothing in complex, some programming languages (e.g. Julia) allow the same function to be applied to different data types, and no modification to the algorithm is required. However, other languages (e.g. C++) would require enormous modifications and it is easier to separate the complex image into the real and imaginary parts and to smooth them separately, as there is no interchange between real and imaginary parts.

3.4.3.3 Image border effects

Smoothing close to borders can lead to different edge effects, depending on the type of border handling that is chosen. Common methods are setting voxels outside the border to a constant value, e.g. 0; using nearest neighbor extrapolation to enlarge the image before smoothing; wrapping the image around the borders; ignoring the borders and smoothing only the image center; or reducing the kernel-size when approaching the border. As mostly brain images from magnetic resonance imaging are considered in this work, usual images encountered have large borders without any signal and edge effects have minor influence. The exact method chosen for border handling differs in the implementations used in this study, in the C++ implementation, the kernel-size is reduced when approaching the border, in MATLAB the image is padded with zeros and in the Julia implementation, the voxels close to the border are not smoothed (refer to the available code; Table 6.1). As border problems are not encountered with brain MR datasets, this topic was not further evaluated.

3.4.3.4 Weighted smoothing

Smoothing images with sharp signal drops at the edges of the object, as is common in MRI, results in mostly unwanted signal alterations close the objects edges. These effects can be mitigated (although not completely avoided) by using a weighted smoothing approach. Undesired effects of weighted smoothing are, however, shifts of the center of mass of the smoothing kernel, which might be unwanted as they lead to effective shifts of voxels. Figure 3.9 illustrates the application of weighted smoothing for a simulated sharp signal drop.

There are multiple ways to obtain weighted smoothing:

1. Using a modified average filter that performs a weighted average and also smooths the weights for each iteration.

2. Scaling the image to a range that is significantly smaller than π, and using the scaled image as phase and the weight as magnitude and performing

Die approbierte gedruckte Originalversion dieser Dissertation ist an der TU Wien Bibliothek verfügbar.
The approved original version of this doctoral thesis is available in print at TU Wien Bibliothek.
TU Bibliothek WIEN Your knowledge hub

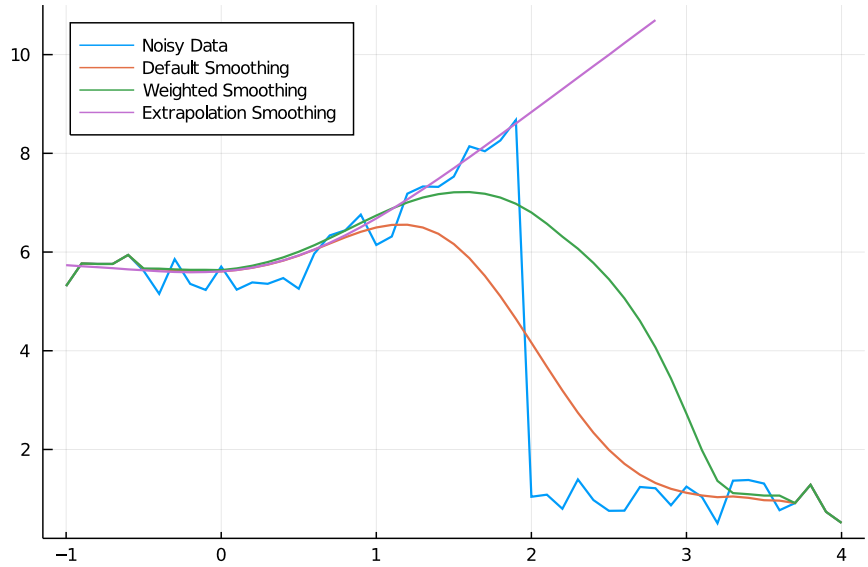

Figure 3.9: Smoothing effects at a simulated sharp edge: the blue curve shows simulated data, the red curve default Gaussian smoothing, the green curve weighted Gaussian smoothing and the purple curve Gaussian smoothing with extrapolation of missing values, where values below 2.5 were set as missing.

complex smoothing.

3. Multiplying the image with the weight and performing smoothing, then dividing the result by a smoothed version of the weight.

All three approaches produce identical results (in the limit of scaling the image to an infinitesimal small range in the second approach) and have similar runtimes. The first approach was chosen for all implementations applied in this study.

3.4.3.5 Application with missing values

Smoothing images after segmentation or other steps leaving holes with missing values is an often performed task in MR image processing. A commonly used and simple approach is Division Smoothing, but this is associated with negative effects, so a second new approach, Extrapolation Smoothing, is presented here as well.

Division Smoothing A simple scheme for smoothing an image with a binary mask or missing values is to set masked values to 0, perform regular smoothing, and afterwards divide the smoothed image by a smoothed version of the binary mask. This approach is effectively identical to weighted smoothing, where the

Die approbierte gedruckte Originalversion dieser Dissertation ist an der TU Wien Bibliothek verfügbar.
The approved original version of this doctoral thesis is available in print at TU Wien Bibliothek.
TU Bibliothek Your knowledge hub WIEN

weight of 0 is chosen for masked voxels (see Weighted Smoothing, Point 3) and has the same downside as weighted smoothing, which is an effective voxel shift in the smoothed image that depends on the mask.

Extrapolation Smoothing The ideal application of smoothing with missing values closely corresponds to interpolation and extrapolation tasks and can completely avoid negative effects at object edges when a good mask is provided. This is illustrated in Figure 3.9 as "Extrapolation Smoothing", and the preferred way of handling sharp signal drops can be selected for a given problem.

The running average approach used above was adjusted to perform extrapolation for small ranges when missing values are encountered, which results in both interpolation and extrapolation when applied iteratively in different directions. The filter can be in one of 3 states, which are normal-mode, where it behaves as a standard running average filter; extrapolation-mode, where encountered missing values are extrapolated and smoothing is performed; and nan-mode, where neither smoothing nor extrapolation can be performed, as too many missing values were encountered. During performing the smoothing of a line, the filter switches between all three states, depending on the pattern of missing values encountered. The extra steps that are performed in comparison to default smoothing result in only a small computational increase. Similarly to the application without missing values, this filter is applied iteratively and separately for each dimension. As the direction of the filter is crucial for extrapolation, the direction is alternated between each consecutive iteration.

3.4.4 B_0 Calculation

The optimal way to calculate a B_0 map from a multi-echo scan is by including the information of all echoes and thereby obtaining the highest possible SNR. The goal is to produce high resolution B_0 maps and therefore, spatial smoothing or spatial regularization, often applied in the literature [54, 55], should be avoided. Since the standard deviation σ of the noise of individual phase voxels can be calculated from the magnitude (see Phase SNR, Section 2.3.3.2) the individual B_0 maps can be combined using the weighting factors $w_i = M_i^2 \cdot T_{E,i}^2$ (multi-echo combination, Section 2.4.2.4). This process has been performed on high-pass filtered phase images to produce high-pass filtered B_0 maps [16], however, we want to obtain the true B_0 field that contains low and high frequency components. This requires the phase offsets to be removed, otherwise the combination would lead to considerable phase offsets in the final B_0 map.

The difficult steps are the removal of phase offsets and the robust unwrapping of the phase at each echo time. In this work, the coil-combination is performed by

Die approbierte gedruckte Originalversion dieser Dissertation ist an der TU Wien Bibliothek verfügbar.
The approved original version of this doctoral thesis is available in print at TU Wien Bibliothek.
TU Bibliothek Your knowledge hub WIEN

ASPIRE (see Section 3.1.2 and [42]), which removes the phase offsets during coil combination for multi-echo scans. The unwrapping of the phase images of each echo is performed using ROMEO (see Section 3.2 and [21]), which is especially suited for multi-echo phase unwrapping.

3.4.5 SNR Simulation

The goal is to simulate and compare the SNR achievable with different acquisition settings, which are number of echoes (single-echo and multi-echo), polarity (monopolar and bipolar) and repetition time. The results shown in Section 5.4.4 can be used to set up sequences with optimal SNR. As a first step, the optimal sequence timings are calculated and then the resulting SNR and CNR values are obtained.

3.4.5.1 Gradient timing calculation

The bandwidth and echo time settings with the best SNR for a given number of echoes and sequence type are calculated in a table of repetition time T_R, echo times $T_{E,i}$, and sampling time per echo T_{acq}. The table is created by using a range of values for T_{acq} and number of echoes to calculate the gradient timings and the resulting echo times $T_{E,i}$ with the T_R that is obtained when the echoes are played directly after each other without dead time in-between. This maximizes the sampling time per T_R to obtain the optimum SNR configuration. The excitation time, T_{exc}, and time for gradient spoiling, T_{spoil}, were considered constant, with the values $T_{\text{exc}} = 2.1\,\text{ms}$ and $T_{\text{spoil}} = 3.3\,\text{ms}$. The detailed calculation of the timings for single-echo, monopolar and bipolar acquisitions to create the Tables with (T_R, T_E, T_{acq}) is presented here and correspond to the code available online[2]. This discussion is analogous to the supplementary material presented together with the publication of CLEAR-SWI.

Single-Echo calculation The echo time for a single echo was calculated as

$$T_{E,\text{SE}} = \frac{T_{\text{EL}}}{2} + T_{\text{Exc}}, \tag{3.78}$$

where $T_{\text{EL}} = T_{\text{acq}} + 2T_{\text{ramp}}$ is the time required for one echo, including the ramps (EL stands for echo length); T_{acq} is the sampling time for one echo and T_{ramp} the time required to ramp the gradient from 0 to G, which is the gradient strength

[2]https://github.com/korbinian90/MriResearchTools.jl/tree/clearswi_publication/src/snr.jl

Die approbierte gedruckte Originalversion dieser Dissertation ist an der TU Wien Bibliothek verfügbar.
The approved original version of this doctoral thesis is available in print at TU Wien Bibliothek.
TU Bibliothek Your knowledge hub WIEN

during sampling. The corresponding T_R for single echo was calculated as

$$T_{R,\mathrm{SE}} = T_{\mathrm{exc}} + T_{\mathrm{EL}} + T_{\mathrm{spoil}} \tag{3.79}$$

$$= T_{E,\mathrm{SE}} + \frac{T_{\mathrm{EL}}}{2} + T_{\mathrm{spoil}}. \tag{3.80}$$

Multi-Echo calculation For each number of echoes N_E, one table (T_R, T_E, T_{acq}) was generated. The bandwidth was kept constant for all echoes and the echo times were restricted to be multiples of the first echo time. The echo spacing ΔT_E needs to include the echo length and prewind time, and to fulfill the echo time restriction, ΔT_E has to be at least as large as the first echo in a single echo acquisition with the same T_{acq}, leading to

$$\Delta T_E = \max\left(T_{E,\mathrm{SE}}, T_{\mathrm{EL}} + T_{\mathrm{prewind}}\right). \tag{3.81}$$

The individual echo times were set to be integer multiples of the echo spacing

$$T_{E,i} = i\Delta T_E, \tag{3.82}$$

which yielded a repetition time of

$$T_R = N_E \Delta T_E + \frac{T_{\mathrm{EL}}}{2} + T_{\mathrm{spoil}}. \tag{3.83}$$

For bipolar acquisitions, no prewinding is performed ($T_{\mathrm{prewind}} = 0$) and the table can was created using the calculations above. For monopolar acquisitions, T_{prewind} is calculated in the next part, where the gradient moment GM that needs to be reversed is calculated according to

$$\mathrm{GM} = T_{\mathrm{ramp}} \cdot G + \frac{N_x}{\gamma \cdot \mathrm{FOV}}, \tag{3.84}$$

where G is the gradient strength during sampling, N_x the matrix size in the readout direction, γ the gyromagnetic ratio, and FOV (field of view) in readout direction. If the ramps played for rewinding do not reach the hardware limit (i.e. the gradient curve is triangular without a flat top), the maximum gradient strength and the associated time for prewinding is

$$G_{\mathrm{max}} = \sqrt{\mathrm{GM} \cdot R_{\mathrm{slew}}} \tag{3.85}$$

$$T_{\mathrm{prewind}} = 2\sqrt{\frac{\mathrm{GM}}{R_{\mathrm{slew}}}}, \tag{3.86}$$

where R_{slew} is the slew rate of the gradient. If G_{max} is bigger than the hardware gradient limit G_{limit}, the following calculation with a flat region on top was used

Die approbierte gedruckte Originalversion dieser Dissertation ist an der TU Wien Bibliothek verfügbar.
The approved original version of this doctoral thesis is available in print at TU Wien Bibliothek.
TU Bibliothek Your knowledge hub WIEN

for T_{prewind}:

$$T_{\text{ramp}} = \frac{G_{\text{limit}}}{R_{\text{slew}}} \tag{3.87}$$

$$\text{GM}_{\text{ramp}} = T_{\text{ramp}} \cdot G_{\text{limit}} \tag{3.88}$$

$$\text{GM}_{\text{box}} = \text{GM} - \text{GM}_{\text{ramp}} \tag{3.89}$$

$$T_{\text{box}} = \frac{\text{GM}_{\text{box}}}{G_{\text{limit}}} \tag{3.90}$$

$$T_{\text{prewind}} = 2T_{\text{ramp}} + T_{\text{box}} \tag{3.91}$$

3.4.5.2 Magnitude SNR

The theoretical framework is covered in Section 2.3 and the equations 2.55-2.58. For a given tissue type and for given echo timings, the image SNR of one echo is calculated by substituting all tissue parameters with the literature values (details in Section 4.2.2). To compare the SNR of single-echo and multi-echo sequences, an optimal echo-combination for SNR is assumed for the multi-echo scan. The image SNR after SNR-weighted (RSOS) combination of a multi-echo scan is given by Equation 2.57 as the root-sum-of-squares of the SNR of the individual echoes. To be comparable across different repetition times, the SNR efficiency (Equation 2.58) is used, which is the SNR divided by the root of the repetition time. The calculation of SNR and SNR efficiency was only in relative terms, i.e. up to a factor that is identical for all simulated sequences.

3.4.5.3 Magnitude CNR

For the same simulated sequences, the CNR between two tissues was calculated. The CNR is a special case of the SNR, where the signal is defined as the difference of the mean of two ROIs. Identical to the case for SNR, the CNR of individual echoes is optimally combined, for a CNR-weighted combination and the CNR of the combined image is given by Equation 2.57 as well, as is the CNR efficiency by Equation 2.58.

In the ideal case, the calculation of the contrast between two tissues in individual echoes could be performed by inserting the literature values for two tissue types into the signal equation (Equations 2.55) and taking the difference to obtain the contrast, however, the literature values fluctuate between different subjects and ways to measure them, which has a strong influence in the difference operation for calculating the contrast. To obtain valid CNR simulations for the given application, the simplified contrast model

$$\text{contrast} = S\left(T_E, T^*_{2,1}, T_{1,1}\right) - hS\left(T_E, T^*_{2,2}, T_{1,2}\right) \tag{3.92}$$

Die approbierte gedruckte Originalversion dieser Dissertation ist an der TU Wien Bibliothek verfügbar.
The approved original version of this doctoral thesis is available in print at TU Wien Bibliothek.
TU Bibliothek Your knowledge hub WIEN

was used, where $T^*_{2,i}$ and $T_{1,i}$ are the tissue constants for tissue i from literature values and the factor h is fitted from acquired data. The fitted factors and literature values are detailed in Section 4.2.2.

3.4.5.4 Phase SNR

The signal of interest in phase images corresponds to a quantitative measurement of the B_0 field, which can be assumed to be constant in the context of SNR estimation, and it increases linearly with echo time T_E. According to the derivation in Section 2.3.3.2, the noise of the phase is given as σ/M, where σ is the standard deviation of the underlying complex noise and M is the magnitude. The term σ/M is the inverse of the magnitude SNR, leading to the simple derivation of phase SNR as

$$\mathrm{SNR}_{\mathrm{phase}} = \mathrm{SNR}_{\mathrm{mag}} \cdot T_E. \tag{3.93}$$

Again, Equation 2.57 is used to calculate the echo-combined SNR, assuming a combination that is optimal in terms of SNR, which is fulfilled by inverse-variance-weighted multi-echo phase combination detailed in Section 2.4.2.4 and applied for B_0 calculation (Section 3.4.4).

3.4.6 Simulated Single-Echo

Simulating the appearance of a single-echo scan from an acquired multi-echo scan can be useful for comparing artefacts of single- and multi-echo acquisitions while only requiring the acquisition of one multi-echo acquisition. This can be useful when the measurement time is limited, as is often the case for studies with patients and was applied for the tumor evaluation in CLEAR-SWI (see Section 5.3.3). Another use case is for longitudinal studies, where a single-echo sequence is replaced by a multi-echo sequence, however, the analysis of single-echo data is still required.

In both single- and multi-echo gradient echo imaging, the signal after the excitation is encoded by gradients to receive spatial information. In single-echo, the spatial encoding is performed once, while in multi-echo the spatial encoding is repeated a number of times after the excitation and usually the sampling for each echo is performed faster so that the repetition time might be comparable between single-echo and multi-echo. Therefore, multi-echo has multiple data points for each voxel with differing echo time, while single-echo has only one data point. If the repetition time and the acquisition window for both scans is identical, the single-echo scan corresponds to averaging the multi-echo scan (disregarding the T^*_2-dependency in the SNR Equation 2.54).

Die approbierte gedruckte Originalversion dieser Dissertation ist an der TU Wien Bibliothek verfügbar.
The approved original version of this doctoral thesis is available in print at TU Wien Bibliothek.
TU Bibliothek Your knowledge hub WIEN

3.4.6.1 Magnitude

When simulating a single-echo magnitude from a multi-echo scan, the resulting single-echo magnitude will have identical repetition time and an acquisition window T_{acq} lying inside the acquisition window of the multi-echo scan. The simulated magnitude M_S is a weighted combination of the multi-echo magnitude M_i using echo-dependent weighting factors w_i that are equal to the fraction of the i-th echo that lies inside T_{acq}:

$$M_S = \sum_i w_i M_i \tag{3.94}$$

3.4.6.2 Phase

To simulate the single-echo phase, scaling of the angle of complex numbers is required, which however is ambiguous. Thus, as a first step, the multi-echo phase has to be unwrapped and the newly developed unwrapping method ROMEO (Section 3.2) can be used, as it is especially suited for multi-echo data. After unwrapping the combined single echo phase, φ_S is calculated from the multi-echo phase φ_i as

$$\varphi_S = \frac{T_{E,S} \sum_i \varphi_i w_i}{\sum_i T_{E,i} w_i}, \tag{3.95}$$

where $T_{E,S}$ is the echo time of the single echo scan and $T_{E,i}$ are the multi-echo echo times. This multi-echo phase combination is not optimal regarding SNR, but should be an estimation of the phase that would be obtained by a single-echo acquisition. The final step is wrapping the phase back into the range $[-\pi; \pi)$ using the modulo operation.

Die approbierte gedruckte Originalversion dieser Dissertation ist an der TU Wien Bibliothek verfügbar.
The approved original version of this doctoral thesis is available in print at TU Wien Bibliothek.
TU Bibliothek Your knowledge hub WIEN

Chapter 4

Analysis

4.1 Measurements

The measurements that were performed are split into 3 sections, as the data was specifically acquired to address relevant aspects of each of the three major methods.

4.1.1 Coil Combination

In the coil combination study, four healthy volunteers participated (three brain datasets and one knee dataset) and were scanned with a Siemens MAGNETOM (Siemens Healthcare, Erlangen, Germany) 7T whole-body MR scanner. The data was acquired with phased array coils with an included birdcage transmit coil for

1. the head with 32 receive elements (Nova Medical, Wilmington, Massachusetts, USA)

2. the knee with 28 receive elements (QED, Mayfield Village, Ohio, USA)

All participants provided written informed consent and the study was approved by the Ethics Committee of the Medical University of Vienna. General considerations are explained in the next paragraphs and the scan parameters can be found in detail in Table 4.1.

Monopolar measurements The first echo was flow compensated and the echo times met the ASPIRE condition of $mT_{E,k} = (m-1)\,T_{E,j}$ with $m = 1, j = 1, k = 2$ and $T_E = [6.3, 12.6\,]ms$. The data collected for MCPC-3D-I and MCPC-3D-S used $T_E = [6.3, 11.7\,]ms$ and intentionally did not meet the ASPIRE condition because these methods would not be affected by unwrapping errors if the ASPIRE echo condition were met. The Roemer method required two reference scans, one was performed with the Birdcage coil and

Die approbierte gedruckte Originalversion dieser Dissertation ist an der TU Wien Bibliothek verfügbar.
The approved original version of this doctoral thesis is available in print at TU Wien Bibliothek.
TU Bibliothek Your knowledge hub WIEN

Table 4.1: Acquisition parameters for the scans presented in the coil combination study, 5.1.

Scan	TR [ms]	Field	FA [°]	BW [Hz/px]	Matrix	Res [mm³]	FOV [cm³]	GRAPPA	Time
Brain	26	7 T	10	385	448x364x112	0.49x0.49x1.1	210x160x125	2	10 min
ASPIRE	TE = [6.3, 12.6] ms								58 s
Brain	26	7 T	10	385	448x364x112	0.49x0.49x1.1	210x160x125	2	10 min
MCPC-3D-S	TE = [6.3, 11.7] ms								58 s
Knee	33	7 T	18	263	528x462x104	0.30x0.30x1.1	160x140x115	2	10 min
ASPIRE	TE = [7.0, 14.0, 22.0] ms								40 s
Knee	33	7 T	18	263	528x462x104	0.30x0.30x1.1	160x140x115	2	10 min
MCPC-3D-S	TE = [7.0, 15.0, 22.0] ms								40 s
Phantom	84	3 T	10	260	128x128x5	1.5x1.5x6.0	190x190x30	1	1 min
	TE = [10.0, 20.0, 30.0, 40.0, 50.0, 60.0, 70.0, 80.0] ms								47 s
Bipolar	26	7 T	10	385	464x406x112	0.49x0.49x1.1	230x200x125	2	10 min
Brain	TE = [6.3, 12.6, 18.9] ms								58 s

one with 32 receiver elements. Both were 2D single-echo gradient echo scans with $T_E = 4.6$ ms, a flip angle of 40°, a matrix size of 128x104x34 and same field of view as the target scan with an total acquisition time of 23 s.

Bipolar measurements A bipolar sequence was acquired at a 3T PRISMA scanner with a 20-channel head/neck coil (Siemens Healthcare) for which 16 channels were activated for a phantom. The acquisition was performed once with monopolar and once with bipolar readout gradients and was an axial 2D gradient echo scan. At 7 T, a bipolar high-resolution brain scan was acquired with similar parameters as the monopolar brain scan with an additional third echo at 18.9 ms to fulfill the ASPIRE requirement for bipolar coil combination, which is $T_{E,2} = 2T_{E,1}$ and $T_{E,3} = 3T_{E,1}$.

4.1.2 Phase Unwrapping

The unwrapping study was performed on simulated data and a number of datasets with different field strengths and imaging parameters to span large parts of possible domains for the application of unwrapping. The simulation was performed to provide a ground truth phase for a complicated pattern of phase wraps. The complex topography was simulated as in references [22] and [56]. One slice of the magnitude and phase of this topography is shown in Figure 5.5 for the echo time of 10 ms. In vivo human head acquisitions were performed at 3 T and 7 T (Siemens MAGNETOM, Siemens Healthineers, Erlangen, Germany) and ex vivo rat head

Die approbierte gedruckte Originalversion dieser Dissertation ist an der TU Wien Bibliothek verfügbar.
The approved original version of this doctoral thesis is available in print at TU Wien Bibliothek.
TU Bibliothek Your knowledge hub WIEN

Table 4.2: Acquisition parameters for results presented in the unwrapping study.

Scan	TR [ms]	Field	FA [°]	BW [Hz/px]	Matrix	Res [mm³]	FOV [cm³]	No. of scans
Simulation	-	-	-	-	256x256x256	-	-	-
	TE = [4, 8, 10] ms							
2D GRE	4370	3 T	90	270	144x144x84	1.5x1.5x1.5	216x216x126	1
	TE = [5, 10, 16, 21, 26, 31] ms							
2D EPI	8680	3 T	90	1655	144x144x84	1.5x1.5x1.5	216x216x126	3
	TE = 31, 35, 40 ms (3 scans)							
3D GRE	80	7 T	15	859	208x208x96	1.0x1.0x1.0	208x208x96	1
	$TE_1/dTE/TE_{31}$ = 2.5/2.5/77.5 ms							
3D GRE 9.4T	22	9.4 T	8.7	1333	150x125x175	0.2x0.2x0.2	30x25x35	1
	$TE_1/dTE/TE_{12}$ = 1.4/1.4/16.8 ms							

images were acquired at 9.4 T (Bruker BioSpec 94/20 USR, Ettlingen, Germany). The details of the individual scans are presented in Table 4.2.

Human measurements were approved by the Ethics Committee of the Medical University of Vienna and all participants provided written informed consent. All human data sets were acquired from healthy volunteers except for five 7 T EPI (echo planar imaging) time series (57 volumes) from a prior study [57], which were collected from four patients with brain tumors and one patient with a developmental venous anomaly.

4.1.3 SWI

Measurements with 5 healthy subjects (1F, 4M, 28.7 ± 4.2 years old) and 14 patients with suspected brain tumors (7F, 7M, 52.6 ± 15.2 years old) were performed using a 7 T MRI Siemens MAGNETOM scanner (Siemens Healthineers, Erlangen, DE) with a 32-channel Nova Medical head coil (Wilmington, Massachusetts, USA). The diagnoses of the patients with brain tumors included astrocytoma WHO grade II/III, glioblastoma multiforme WHO grade IV, meningioma WHO grade I, and brain metastasis of an adenocarcinoma. One patient was diagnosed with CLIPPERS and removed from the cohort. The measurements were approved by the Ethics Committee of the Medical University of Vienna and all participants provided written informed consent.

The same resolution, repetition time, parallel imaging (GRAPPA) acceleration factor and flip angle were used for all 7 T volunteer scans, but with different bandwidths and numbers of echoes. The sequence timings of the 7 T protocols were based on recent clinically applied 7 T SWI studies [58, 59] with increased resolution. The single-echo volunteer scan (see Table 4.3; NE1) was acquired with

Die approbierte gedruckte Originalversion dieser Dissertation ist an der TU Wien Bibliothek verfügbar.
The approved original version of this doctoral thesis is available in print at TU Wien Bibliothek.
TU Bibliothek Your knowledge hub WIEN

a bandwidth of 60 Hz/pixel and TE = 19.3 ms. To ensure a fair comparison with the multi-echo acquisition, the single-echo scan was acquired using all of the available repetition time for sampling, which resulted in a bandwidth of 60 Hz/px and a TE of 19.3 ms. To correspond to a more typical clinical acquisition, a second single-echo scan with a higher bandwidth of 100 Hz/pixel has been additionally acquired (see Table 4.3; NE1 100BW). For the visual comparisons with multi-echo acquisitions, the single-echo scan NE1 with the lowered bandwidth was used, as it had significantly higher SNR than the clinically used version with bandwidth (see Results, Figure 5.35).

Parameters in the multi-echo acquisition (NE6 in Table 4.3) were selected to efficiently use the same TR as the single-echo scan while enabling phase data to be combined over channels using ASPIRE, for which there is the requirement, for bipolar acquisitions, that $2T_{E,1} = T_{E,2}$ and $3T_{E,1} = T_{E,3}$. The results in Section 5.4.4 were used as a guideline for choosing the number of echoes in the bipolar acquisition. A large number of echoes allows sampling of the early part of the signal to avoid signal loss in regions of short T_2^*, and uses a higher bandwidth, which reduces geometric distortions and T_2^* blurring. Time wasted for gradient ramping increases with the number of echoes, however, as do eddy-current-related effects, the possibility of peripheral nerve stimulation and gradient heating. Here, the number of echoes was chosen to maximize SNR for the given repetition time, avoiding values of too high or too low bandwidth.

One volunteer was measured at 3 T to assess the performance of CLEAR-SWI at that field strength. To yield sufficient susceptibility contrast, the TR was increased to 46 msto allow longer echo sampling and the voxel volume was increased by a factor of 6.4 and the single-echo acquisition used the whole TR for sampling (using a bandwidth of 30 Hz/px).

4.2 Evaluations

This section provides detailed explanations of the non-trivial comparisons and evaluations shown in Results.

4.2.1 Smoothing Evaluation

The exact settings required for reproducing the evaluation of the different smoothing approaches presented in Results are listed in this subsection.

Impulse response The 1-dimensional average filter was applied in each dimension and the process is repeated with given number of iterations with the filter size approximated to obtain $\sigma = 7$ px (Equation 3.77). This example was in 2

Die approbierte gedruckte Originalversion dieser Dissertation ist an der TU Wien Bibliothek verfügbar.
The approved original version of this doctoral thesis is available in print at TU Wien Bibliothek.
TU Bibliothek Your knowledge hub WIEN

Table 4.3: Acquisition parameters for measurements performed for the SWI study.

Scan	TR [ms]	NE	FA [°]	BW [Hz/px]	Matrix	Res [mm³]	FOV	GRAPPA	Time
NE1	30	1	15	60	800x600x104	0.26x0.26x1.2	210x158x125	2	9 min
	TE = 19.3 ms								35 s
NE1	30	1	15	100	800x600x104	0.26x0.26x1.2	210x158x125	2	9 min
BW100	TE = 22.5 ms								35 s
NE 4	30	4	15	329	800x600x104	0.26x0.26x1.2	210x158x125	2	9 min
Monopolar	TE = [6.50, 13.00, 19.50, 26.00] ms								35 s
NE6	30	6	15	260	800x600x104	0.26x0.26x1.2	210x158x125	2	9 min
	TE = [4.30, 8.60, 12.90, 17.20, 21.50, 25.80] ms								35 s
Tumor	31	10	10	523	736x552x80	0.30x0.30x1.2	220x164x96	3	5 min
	TE = [3.31, 6.62, 9.93, 12.49, 15.05, 17.61, 20.17, 22.73, 25.29, 27.85] ms								10 s
MS	30	8	10	372	640x520x96	0.32x0.32x1.2	200x139x115	2	7 min
	TE = [3.40, 6.80, 10.20, 13.33, 16.46, 19.59, 22.72, 25.85] ms								30 s
3 T	46	1	15	30	384x336x88	0.57x0.57x1.6	220x193x140	3	5 min
Single-echo	TE = 26 ms								3 s
3 T	46	8	15	210	384x336x88	0.57x0.57x1.6	220x193x140	3	5 min
Multi-echo	TE = [5.02, 10.04, 15.06, 20.08, 25.10, 30.12, 35.14, 40.16] ms								3 s

dimensions where all pixels are 0 except the central pixel in a grid of $51x51$ px. The default Gaussian Smoothing used the standard implementation of the Julia toolbox ImageFiltering.jl[1] with a Gaussian kernel of $\sigma = 7x7$ px with a kernel size of $41x41$ px.

Average deviation per voxel A sample 7 T gradient echo brain image of matrix size 448x448x112 was used for calculating the deviation between the box smoothing for each number of boxes and size of σ with the default Julia implementation. The intensity range of the image was $[0; 1]$ with a mean intensity of 0.34 (inside the mask used for evaluation). The default Julia implementation used an extra large kernel size of $6\,\sigma$ to be close to "perfect" Gaussian smoothing. To avoid different behavior at image borders to influence the result, the image was padded with a large border of zeros before smoothing, which was chosen to be the maximum of $6\,\sigma$ (the range of influence of standard smoothing) and the sum of the box sizes (the range of influence of box smoothing). The deviation per voxel was calculated inside an automatically created magnitude mask (see Section 3.4.1) and averaged.

[1] https://juliaimages.org/ImageFiltering.jl

Die approbierte gedruckte Originalversion dieser Dissertation ist an der TU Wien Bibliothek verfügbar.
The approved original version of this doctoral thesis is available in print at TU Wien Bibliothek.
TU Bibliothek Your knowledge hub WIEN

Comparison with Division Smoothing The division smoothing used for the comparison in Results, Figure 5.31 was implemented using the standard Julia filter on the masked magnitude (same image as in the paragraph above) and dividing the result by the smoothed mask. The kernel size was chosen to be isotropic with 41 voxels. The segmented image was produced using the simple segmentation approach with default setting of 15 overlapping boxes in each dimension.

4.2.2 Simulation settings of the SNR Evaluation

The number of voxels in readout direction were 800 for a FOV of 210 mm in readout direction. The magnetic field was set to 7 T with a gyromagnetic ratio of 42.25756 MHz/T for hydrogen atoms. The gradient system settings were taken from sequence simulations of the Siemens tool POET for the SC72 gradient system (same as equipped in the 7 T MAGNETOM system, where the measurements were acquired), which had a maximum slew rate of 200 (T/m)/s and a maximum gradient strength of 42 mT/m. The time for signal excitation was set to 2.1 ms and the time for spoiling the signal after acquisition was set to 3.0 ms, which were both estimated from POET to correspond realistic values. T_2^* values for different tissue types were obtained from Reference [60] with gray matter as 33.2 ms, white matter as 26.8 ms, and veins as 7.4 ms. The T_1 values were obtained from Reference [61] with gray matter as 1939 ms, gray matter as 1126 ms, and veins were estimated as 2000 ms. The proton density values (normalized to the proton density of cerebrospinal fluid) were obtained from Reference [62] with gray matter as 0.71, white matter as 0.61, and veins were estimated as 0.68.

4.2.3 Coil Combination

A quality measure for the combination of complex coil signals is the quality factor Q, which is calculated by dividing the magnitude after the combination by the magnitude obtained via RSOS. If the phase is perfectly matched after removing phase offsets, the phase of all individual channels points in the same direction and the magnitude of the combination is identical to RSOS. Due to noise, the phase matching is not supposed to perfect and in fact in veins and and low SNR regions the RSOS combination has a bias towards higher values. However, a deviation in the quality factor points to problems in the phase offset estimation (see Results, Figure 5.2). For evaluating the performance of coil combination additional measures are required to estimate how well the true phase offsets have been estimated and removed. A simple way to obtain the true phase evolution, however very noisy, is with a phase difference operation using the Hermitian inner product. If the phase offset has been removed correctly the combined phase should be similar

Die approbierte gedruckte Originalversion dieser Dissertation ist an der TU Wien Bibliothek verfügbar.
The approved original version of this doctoral thesis is available in print at TU Wien Bibliothek.
TU Bibliothek Your knowledge hub WIEN

to the phase evolution. Only at later echo times, the results can deviate significantly due to non-linear phase evolution of tissues with multiple compartments [46].

4.2.4 Phase Unwrapping

Since there is no inherently available ground truth for in vivo measurements, a reliable estimate of the true phase was obtained using the temporal reference method. As a starting point, the unwrapped first echo phase was used, where the unwrapping was performed by all three methods and only the consensus region was chosen. This temporal reference can be obtained for multi-echo data if the first echo time is short and the echo time difference between successive echoes is small, ensuring a small and approximately linear phase evolution between echoes. These requirements were fulfilled for the GRE multiple echo data at 3 T, 7 T, and 9.4 T. The consensus regions contained 99%, 98%, and 89% of the voxels within the brain mask for the 3 T, 7 T, and 9.4 T datasets, respectively. The temporal reference for subsequent echoes was calculated assuming approximately linear phase evolution over time and the expected phase evolution was added to propagate unwrapping from one already unwrapped echo to the next.

The phase unwrapping errors were calculated as the difference between the temporal reference and the unwrapped phase from each method for a given echo time. For the three methods in the comparison, the number of voxels with an error of $2\pi n$ for a range of values for n is presented in logarithmic histograms and the total percentage of voxels that differ from the temporal reference within the mask is presented in a table.

For EPI at 3 T and 7 T, the same calculation of a temporal reference as described above was not possible due to the inherently long minimum echo times of the EPI acquisitions and these images were only visually assessed with MRIcro [63] and FSLeyes [64]. For the 7 T single-echo EPI time-series data, time-averaged images and standard deviations (SD) were calculated across the entire brain mask to examine the regions where unwrapping errors were different at different time points. The SD of the estimated field map was calculated for the 9.4 T GRE data set with 12 echoes.

4.3 Measurement of Signal-to-Noise-Ratio in MRI

A comparison of SNR between MRIs cannot be easily performed. Standard methods use manually drawn regions in the background to estimate the noise [65] but this does not generalize to the whole image after coil combination, multi-echo combination or other processing steps like homogeneity correction [66], or require two

Die approbierte gedruckte Originalversion dieser Dissertation ist an der TU Wien Bibliothek verfügbar.
The approved original version of this doctoral thesis is available in print at TU Wien Bibliothek.
TU Bibliothek Your knowledge hub WIEN

or more repeated acquisitions and manually drawn ROIs from which the SNR is estimated [67, 68]. These methods were not practical for a relative comparison of SNR between two subsequent acquisitions with identical resolution but different sequence parameters and the following SNR estimation approach was applied to produce SNR comparison in Section 5.4.4.

4.3.1 SNR Estimation Approach

To avoid differences in the homogeneity correction to influence the SNR comparison, an identical sensitivity map was applied to all images. This is justified, as the sensitivity is identical for all scans, and the best sensitivity estimation can be performed on the first echo of the multi-echo scan, as it has least signal dropouts.

4.3.1.1 Automatic definition of regions of interest

The objective is a relative comparison between acquisitions of the same object, where multiple regions are taken into account to produce one relative SNR value that is representative for the whole image. The method for comparing the SNR of two or more images has to be symmetric, meaning that no image is specially treated, for example for the determination of ROIs. Additionally, slight spatial shifts between scans have to be expected and shouldn't influence the calculated SNR.

ROIs that were used for the SNR estimation were automatically chosen to contain only one tissue type with minimal noise arising from the tissue substructure. This was ensured by iteratively selecting regions of a given size with the least standard deviation inside a mask and with a required distance between regions. To avoid a bias effect towards the image from which the ROI was selected, the same ROI selection process was performed for each image and the evaluation was afterwards performed on all ROIs. Slight spatial shifts between have been taken into account by discarding the border (one layer of voxels) of each ROI. The masking was performed on each image individually (using the automatic mask described in Section 3.4.1) and voxels were discarded if they were discarded in any mask. The shape of the chosen ROIs was cubic with 23x23x7 voxels, where the central 21x21x5 voxels were used for SNR calculation. Multiple ROIs without overlap were defined on each image by iteratively by selecting the ROI with lowest standard deviation then removing all voxels inside this ROI and searching for the next one.

Die approbierte gedruckte Originalversion dieser Dissertation ist an der TU Wien Bibliothek verfügbar.
The approved original version of this doctoral thesis is available in print at TU Wien Bibliothek.
TU Bibliothek Your knowledge hub WIEN

4.3.1.2 Sequence comparison

Since individual acquisitions can contain additional noise from motion, the SNR comparison was performed on measurements from 3 volunteers. 10 ROIs were defined in each image from a different acquisition, which resulted in 50 ROIs per volunteer, because of the comparison between 5 different acquisitions. The relative SNR was calculated for each ROI individually by normalizing the SNR values by the mean of the 5 methods for this ROI. These relative SNR values for all 150 ROIs are presented in Section 5.4.4 in a boxplot.

Die approbierte gedruckte Originalversion dieser Dissertation ist an der TU Wien Bibliothek verfügbar.
The approved original version of this doctoral thesis is available in print at TU Wien Bibliothek.
TU Bibliothek Your knowledge hub WIEN

Die approbierte gedruckte Originalversion dieser Dissertation ist an der TU Wien Bibliothek verfügbar.
The approved original version of this doctoral thesis is available in print at TU Wien Bibliothek.

Chapter 5

Results

The results are split into several sections; the results are presented for each of the three main topics – complex coil combination, phase unwrapping and an improved pipeline for SWI, then the validation of the supporting methods that are applied as steps inside the main methods.

The results for the three main methods are partly reproduced from the corresponding publications, while the presentation of some additional results and most results of the supporting methods were specifically produced for this thesis.

5.1 Combination of Complex Data from Array Coils

Preliminary results of applying ASPIRE and MCPC-3D-S were already presented in the authors' Diplomarbeit "Development of a Method for Combining MRI Data from Multiple Receiver Coils" [69]. After further development, especially for bipolar corrections and robustness, both methods were published in Reference [42] and evaluated against the other coil combination methods Roemer, VRC and MCPC-3D-I.

Figure 5.1 shows a qualitative comparison of different coil combination methods on equally spaced monopolar multi-echo data. The combination of the first echo is shown in the left column. The Roemer approach replaces the individual coil offsets with the offset of a volume coil. This leads to high quality factors for coil combination but introduces large phase offsets, especially at higher field strength, as seen by the many wraps in the combined phase image and in the difference to the Hermitian inner product (Figure 5.1). If the phase offsets are removed, the difference to the Hermitian inner product is close to 0, since the time for phase evolution is identical to the phase evolution of the first echo time. The method VRC is similar to Roemer but instead of acquiring the reference image using a

Die approbierte gedruckte Originalversion dieser Dissertation ist an der TU Wien Bibliothek verfügbar.
The approved original version of this doctoral thesis is available in print at TU Wien Bibliothek.
TU Bibliothek Your knowledge hub WIEN

reference coil, it calculates a virtual reference image from the multi-channel data itself. As seen by the lower number of wraps, this reduces the strength of the remaining phase offsets, however, they are still in the range of π (VRC difference to Hermitian inner product, Figure 5.1).

The method MCPC-3D-I calculates the phase offsets from the multi-echo information and requires single-channel phase unwrapping. The resulting combined phase image resembles the phase of the Hermitian inner product, showing the generally correct estimation and removal of the phase offset. Note that the phase of the Hermitian inner product has reduced SNR due to the difference operation. The main problem of MCPC-3D-I is, however, the unstable single-channel phase unwrapping, which leads to problems in lower slices and the skull (arrows in Figure 5.1). The improved version, MCPC-3D-S, requires only the unwrapping of one combined image, which has higher SNR than single-coil images, significantly reducing the unwrapping errors. The quality factor achieved with MCPC-3D-S is very high over the whole brain and even in the skull. As seen in the difference to the Hermitian inner product, there are still wraps occurring in the skull (bright and dark areas in the skull). The last method, ASPIRE, is a special case of MCPC-3D-S and completely avoids unwrapping if the ASPIRE relation between echo times is fulfilled. The result shows a very low difference to the Hermitian inner product, even in the skull.

Figure 5.2 shows an evaluation of the application of coil combination in the knee, which is a difficult environment due to multiple tissue interfaces, fat and bone, which can be seen in the magnitude image. The Roemer coil combination was not possible for the knee dataset, as no volume coil was available. The method MCPC-3D-I produced many phase errors (red arrows) and had large regions with a low quality factor. The improved method MCPC-3D-S reduced the phase problems and had mostly very high quality factors but still two severe phase problems could be identified (red arrows). ASPIRE was able to combine the images without visible problems and with overall very high quality factors.

The difference between all three methods is the application of unwrapping, and they would yield identical results if the unwrapping would be without errors. In MCPC-3D-I, unwrapping is performed for each single-channel image for two echoes, and unwrapping errors accumulate (Figure 5.1 in the skull and Figure 5.2). The unwrapping of single-channel images is especially challenging, as they have low SNR, and suffer from phase singularities due to the coil geometry, which are not possible to unwrap by definition. MCPC-3D-S reduces the amount to only one application of unwrapping on the Hermitian inner product, which has higher SNR than individual channels and no phase singularities. This yield results without error in the brain (Figure 5.1) but in complicated areas unwrapping errors occur (Figure 5.2, red and black arrows). ASPIRE completely avoids unwrapping by

Die approbierte gedruckte Originalversion dieser Dissertation ist an der TU Wien Bibliothek verfügbar.
The approved original version of this doctoral thesis is available in print at TU Wien Bibliothek.
TU Bibliothek Your knowledge hub WIEN

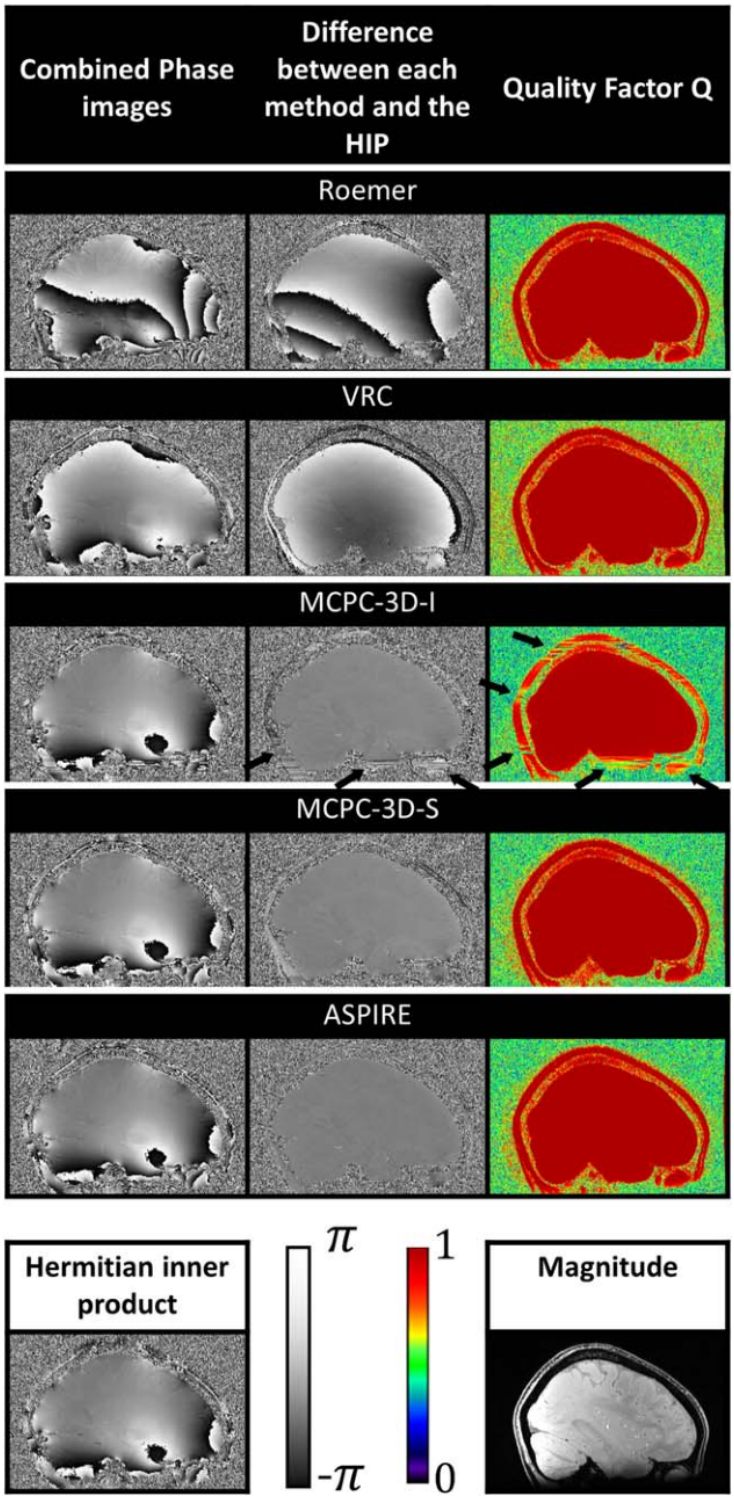

Figure 5.1: Evaluation of different coil combination schemes; The combined phase image is shown in the left column. The difference of the combined first echo and the Hermitian inner product (with identical echo time difference) is shown in the middle column and visualizes the remaining phase offset. The quality factor is shown in the right column and presents the level of coherence that was achieved between the phase of different channels after phase offset subtraction. The Hermitian inner product and the magnitude of the first echo are shown below for reference. This figure was modified from [42].

Die approbierte gedruckte Originalversion dieser Dissertation ist an der TU Wien Bibliothek verfügbar.
The approved original version of this doctoral thesis is available in print at TU Wien Bibliothek.
TU Bibliothek Your knowledge hub WIEN

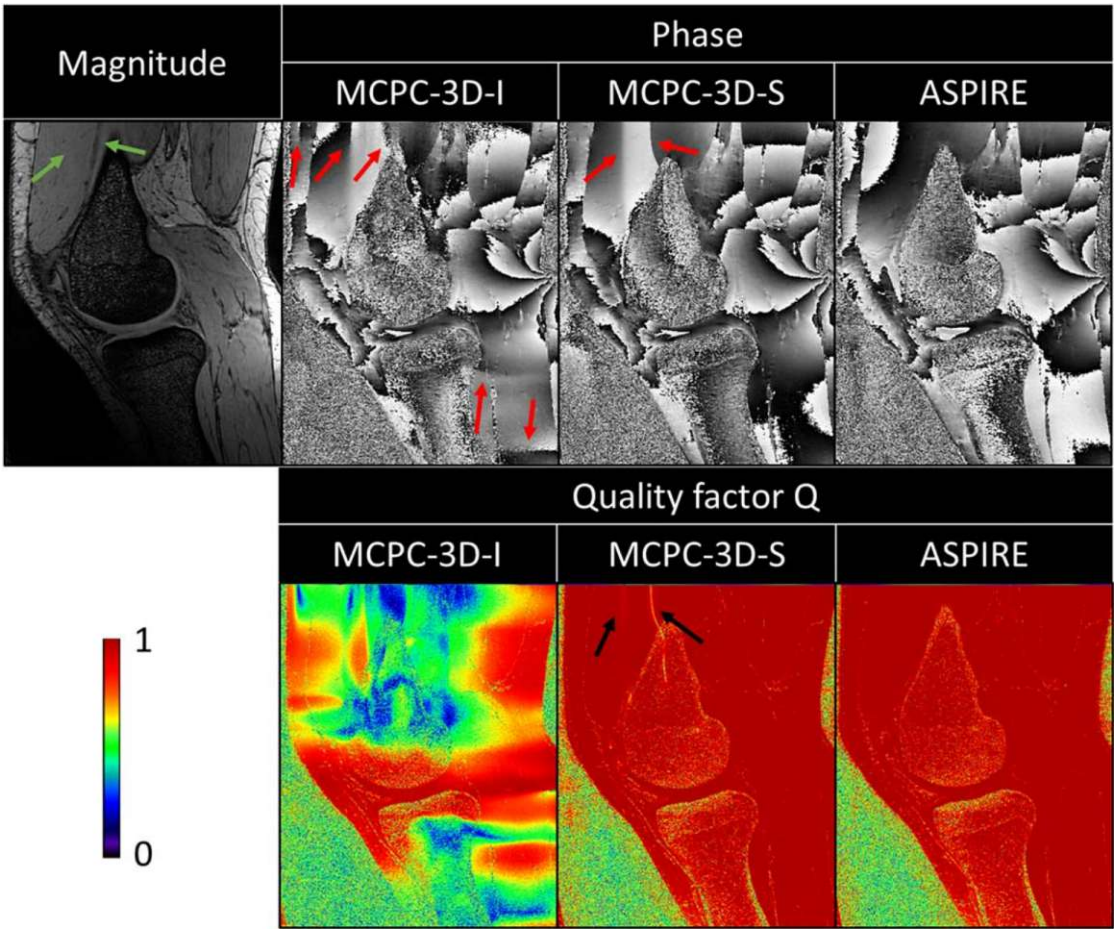

Figure 5.2: Challenging coil combination of a knee dataset; MCPC-3D-I has generally very low quality factors, pointing to incoherent phase offset subtraction, which leads to spurious phase changes (red arrows). The MCPC-3D-S quality factors have two phase changes not corresponding to tissue interfaces in the magnitude (arrows). In ASPIRE, no phase artefacts are visible. This figure was modified from [42].

Die approbierte gedruckte Originalversion dieser Dissertation ist an der TU Wien Bibliothek verfügbar.
The approved original version of this doctoral thesis is available in print at TU Wien Bibliothek.
TU Bibliothek Your knowledge hub WIEN

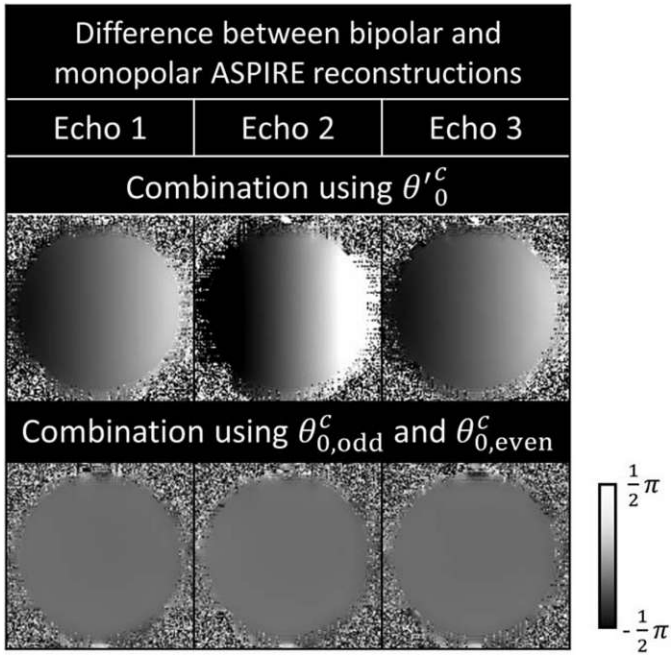

Figure 5.3: ASPIRE applied to a bipolar phantom acquisition; The top row shows the naive application of ASPIRE and the bottom row the application with consideration of bipolar phase gradient effects. This figure was modified from [42].

restricting the possible echo times and thus the combination is robust for spatially complicated regions as well (no phase spurious phase jumps in Figure 5.2).

5.1.1 Bipolar Acquisitions

Figure 5.3 illustrates the necessity of correction for bipolar phase gradients in coil combination. The top row presents the combination of the bipolar dataset using the monopolar ASPIRE approach and yields combined phase with a strong left-right phase gradient artefact. This is demonstrated with a phantom dataset, as the phantom is known to have homogeneous susceptibility and the phase should be flat across the whole phantom. The second row in Figure 5.3 shows the combined phase after applying the bipolar correction approach for ASPIRE combination, and results in highly homogeneous phase without a remaining left-right gradient.

A similar result is achieved for brain images in Figure 5.4, which shows combined phase without artefacts and no readout gradient is visible. The phase is presented for the first three echoes and an approximately linear evolution can be seen from the first echo to the second and third echo.

Die approbierte gedruckte Originalversion dieser Dissertation ist an der TU Wien Bibliothek verfügbar.
The approved original version of this doctoral thesis is available in print at TU Wien Bibliothek.
TU Bibliothek Your knowledge hub WIEN

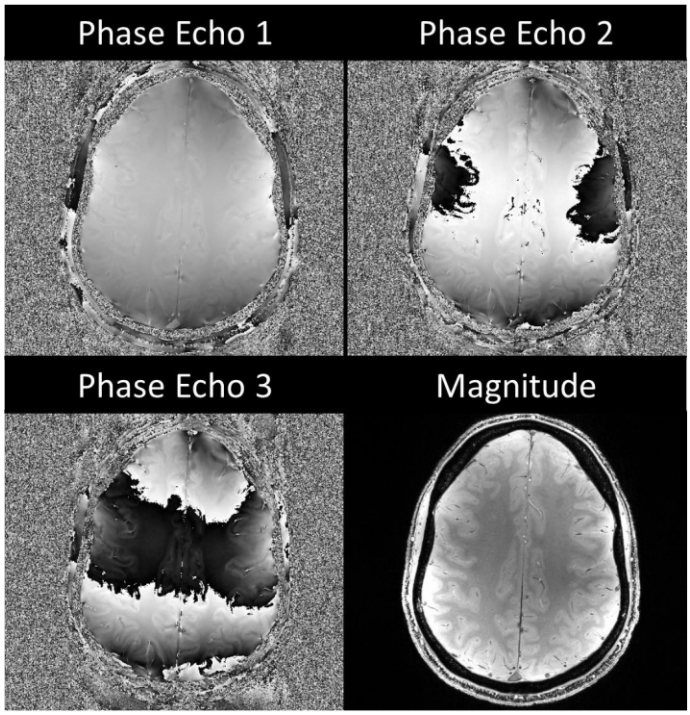

Supporting Figure S1: Images combined using ASPIRE from a bipolar acquisition at 7 T. Note that phase wraps are quite symmetrical about the interhemispheric fissure, indicating no significant phase gradient in the readout direction (left-right) after channel combination. There are only a small number of wraps, as the B_1 field is removed.

Figure 5.4: Images from the acquisition *Bipolar Brain* combined using ASPIRE. Phase wraps are present in the combined images but no significant phase gradient in the readout direction is visible (left-right). This figure is reproduced from the Supplementary Material of [42].

Die approbierte gedruckte Originalversion dieser Dissertation ist an der TU Wien Bibliothek verfügbar.
The approved original version of this doctoral thesis is available in print at TU Wien Bibliothek.
TU Bibliothek Your knowledge hub WIEN

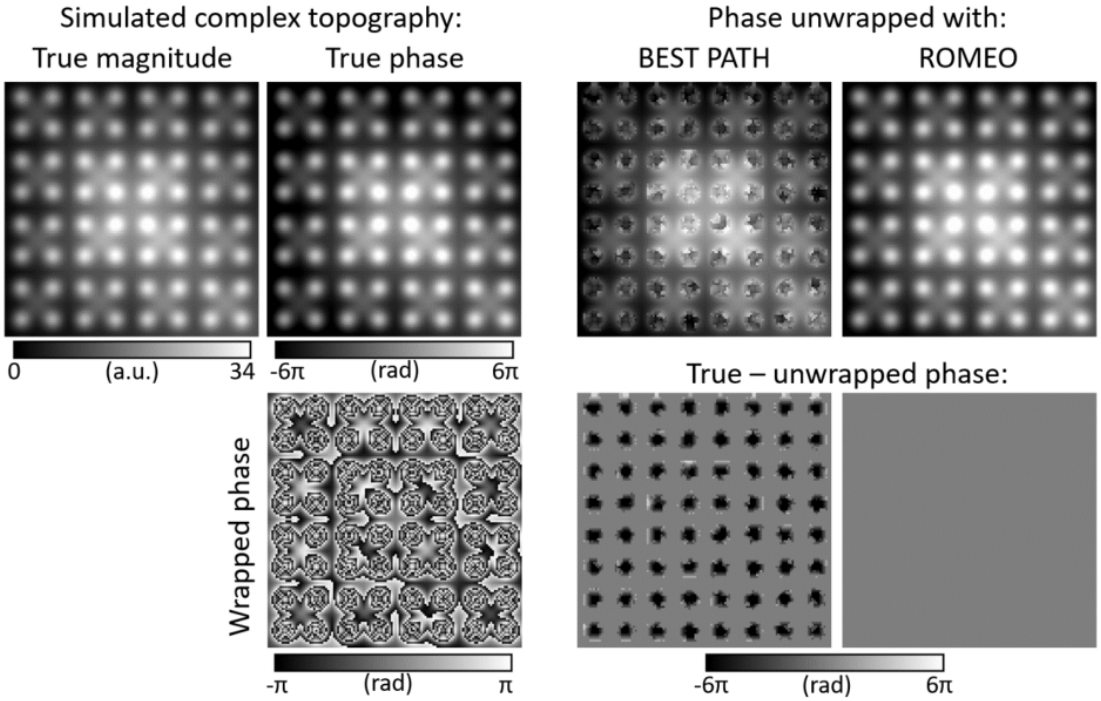

Figure 5.5: Unwrapping of a simulated topography; The echo with 10 ms is shown from the echoes 4, 8 and 10 ms. BEST PATH shows many unwrapping errors, while PRELUDE was unable to obtain a result within 38 days. This figure was published in [21].

5.2 ROMEO

Quantitative comparison in simulated data To compare with a ground truth, simulated phase data were unwrapped using BEST PATH and ROMEO. PRELUDE did not finish the computation in 38 days. The first echo at 4 ms could be unwrapped with both methods without errors. At 8 ms, BEST PATH had 216 incorrectly unwrapped voxels (0.001% of all voxels) and at 10 ms 7.524% (Figure 5.5). ROMEO had an accurate outcome for all echo times, attributable to the use of multi-echo information and temporal unwrapping.

Qualitative comparison at 3T For GRE and EPI scans at 3 T, two slices are shown that contain visible differences in unwrapping between PRELUDE, BEST PATH, and ROMEO (Figure 5.6). The areas near the sinuses (red arrows) are heavily wrapped and show the most unwrapping problems with BEST PATH and the least problems with ROMEO. The blue arrows point to open-ended fringe lines near the ear canal that are artefacts due to the coil geometry or coil combination

Die approbierte gedruckte Originalversion dieser Dissertation ist an der TU Wien Bibliothek verfügbar.
The approved original version of this doctoral thesis is available in print at TU Wien Bibliothek.
TU Bibliothek Your knowledge hub WIEN

method and cannot be unwrapped completely. Both PRELUDE and BEST PATH produced a region around these areas where many noisy wraps remained, while the size of the affected area increased with echo time. The affected region was small with ROMEO, which produced a clear remaining phase wrap emanating from the singularity. Vessels (yellow arrows) have fast phase variations at their edges where large phase changes occur over a small region. In BEST PATH, the unwrapped veins often show non-physiological phase jumps (vein of Galen in GRE, Figure 5.6), whereas in PRELUDE and ROMEO they mostly look correct. To summarize the 3 T findings, ROMEO had the fewest residual wraps and the smallest area affected by unwrapping problems.

Qualitative comparison against quasi-ground truth at 7T Figure 5.7 evaluates the unwrapping performance of PRELUDE, BEST PATH and ROMEO by comparing them to a temporal reference ground truth image (see Analysis, Section 4.2.4). The comparison was performed at 7 T field strength with 31 echoes and echo times up to 77.5 ms, with a large number of wraps at longer echo times. Due to a short first echo time and short echo spacing, an unwrapped temporal reference image could be generated, which is used as ground truth for the comparison. For echo times below 15 ms, all three methods have only minor differences to the temporal reference (not shown). At 15 ms, the first major errors occur in PRELUDE and BEST PATH in large veins. At 30 ms, the regions with strong phase deviation (red arrow) become difficult to unwrap and cause a large number of errors in PRELUDE and BEST PATH, while ROMEO still unwraps the images correctly. With longer echo times, the area of incorrectly unwrapped voxels grows, rendering the results of PRELUDE and BEST PATH unusable. ROMEO, on the other hand, unwraps these heavily wrapped regions without any extended regions of errors and only single voxels with different phase were observed.

Quantitative comparison presented as histograms A quantitative comparison is shown in Figure 5.8 and Table 5.1 for field strengths of 3 T, 7 T, and 9.4 T. The calculation of the ground truth unwrapped phase is based on creating a temporal reference and is explained in detail in Section 4.2.4. The histograms in Figure 5.8 show the extent of the unwrapping errors in multiples of 2π with the central and largest bar corresponding to the correctly unwrapped voxels. At 3 T, ROMEO has fewer errors with a low wrap count (scaled logarithmically). The maximum number of wraps was limited in ROMEO, leading to an increase in wrap errors at the edges, however, only the right edge of the accumulated voxels was higher than with other unwrapping methods, while all other wrap counts were lower or equal in ROMEO. Table 5.1 shows that the total number of erroneous voxels is drastically lower than for ROMEO than for PRELUDE and BEST PATH, especially at later

Die approbierte gedruckte Originalversion dieser Dissertation ist an der TU Wien Bibliothek verfügbar.
The approved original version of this doctoral thesis is available in print at TU Wien Bibliothek.
TU Bibliothek Your knowledge hub WIEN

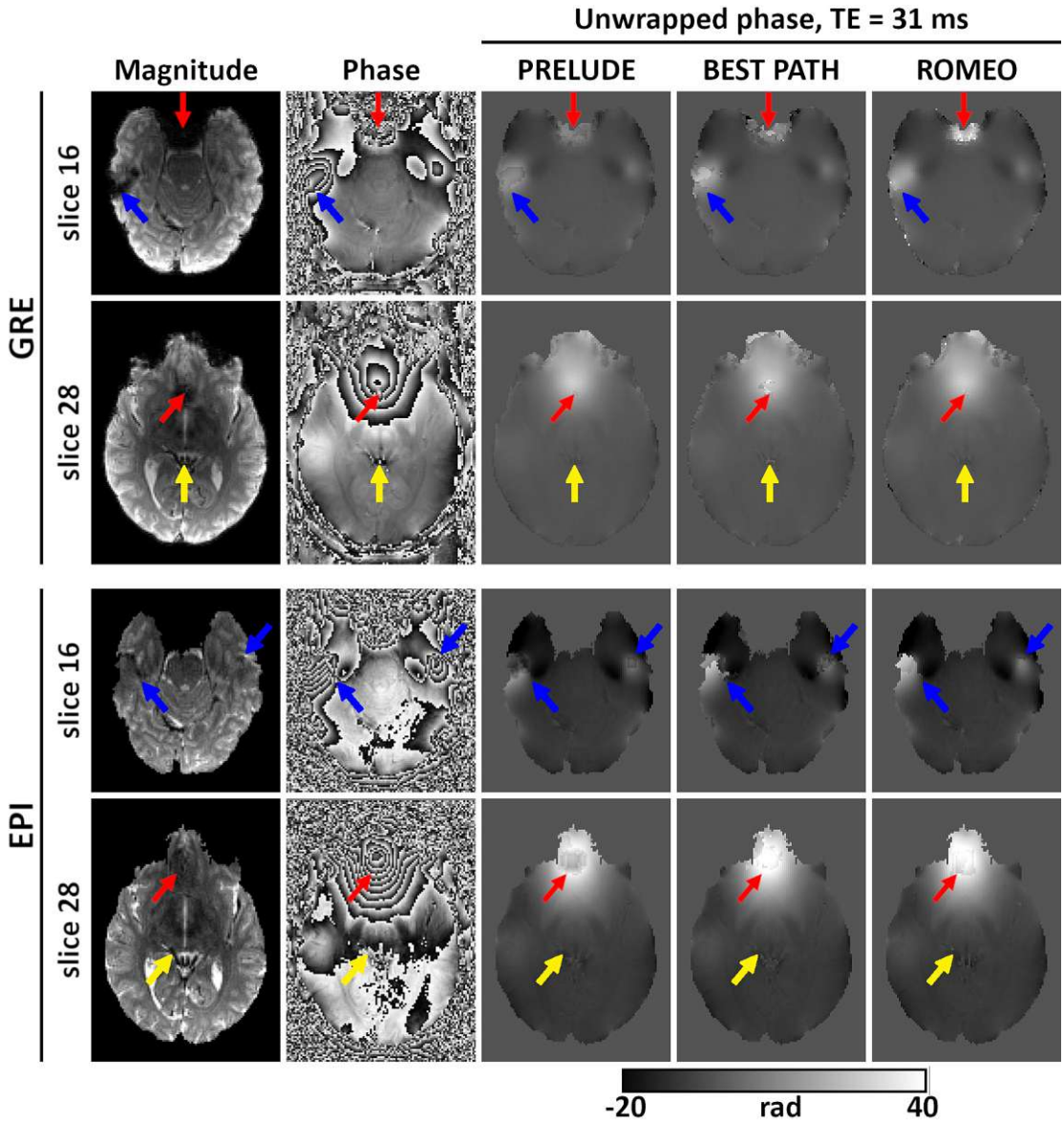

Figure 5.6: Selected unwrapped slices for GRE and EPI scans at 3 T; Both scans had an echo time of 31 ms. Measured magnitude and phase images are shown on the left. The region close to the sinuses (red arrows), open-ended fringe lines (blue arrows) and veins (yellow arrows) are difficult to unwrap and present unwrapping errors for all 3 methods. Overall, the smallest number of non-physiological remaining phase jumps are left after unwrapping with ROMEO.

Die approbierte gedruckte Originalversion dieser Dissertation ist an der TU Wien Bibliothek verfügbar.
The approved original version of this doctoral thesis is available in print at TU Wien Bibliothek.
TU Bibliothek Your knowledge hub WIEN

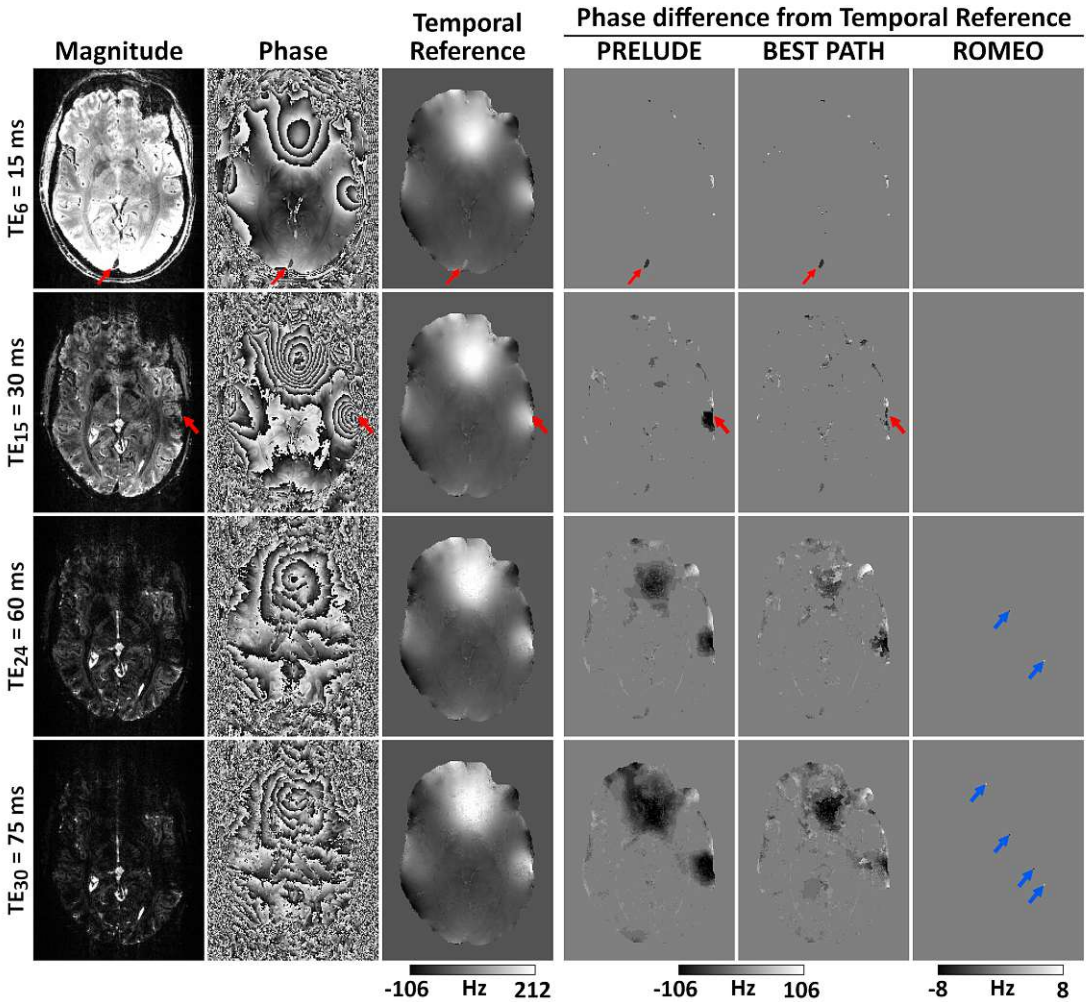

Figure 5.7: Unwrapping evaluation with the temporal reference at 7 T GRE with 31 echoes; At 15 ms, PRELUDE and BEST PATH already had the first unwrapping errors in large veins (red arrow). At larger echo times the number of erroneous voxels grows in PRELUDE and BEST PATH and at 60 and 75 ms a large portion of the image is corrupted. In ROMEO, the first single voxels with different phase were detected at 60 ms (blue arrows). At 75 ms, ROMEO still has only single voxels, which were estimated differently from the temporal reference. Figure from [21].

Die approbierte gedruckte Originalversion dieser Dissertation ist an der TU Wien Bibliothek verfügbar.
The approved original version of this doctoral thesis is available in print at TU Wien Bibliothek.
TU Bibliothek Your knowledge hub WIEN

Table 5.1: Percentage of voxels inside the mask that differed between the unwrapped result and the temporal reference. The error percentage was always lowest for ROMEO and the increase with echo time was negligible. Both PRELUDE and BEST PATH had low errors at short echo times, but they increased sharply and the percentage of unwrapping errors was up to a quarter of the voxels at long echo times.

		Erroneous voxels within the mask [%]		
	TE [ms]	PRELUDE	BEST PATH	ROMEO
3 T GRE	10.0	0.5301	0.6065	0.4168
	21.0	1.738	1.923	0.4172
	31.0	2.973	3.313	0.4174
7 T GRE	5.0	0.2700	0.2906	0.1155
	40.0	5.701	5.399	0.1160
	77.5	22.81	23.39	0.1217
9.4 T GRE	2.8	1.446	1.739	0.8535
	9.8	14.96	14.00	0.8570
	16.8	26.58	24.85	0.8633

echo times. The number of incorrectly estimated voxels is almost constant with echo time in ROMEO, while it increased sharply for the other methods. Similar results are seen for 7 T and 9.4 T field strengths in both Figure 5.8 and Table 5.1, but with an even larger difference between ROMEO and the comparison methods. In particular, at 7 T with a large number of echoes, ROMEO had a very low error rate, while late echoes are very problematic for PRELUDE and BEST PATH.

Die approbierte gedruckte Originalversion dieser Dissertation ist an der TU Wien Bibliothek verfügbar.
The approved original version of this doctoral thesis is available in print at TU Wien Bibliothek.
TU Bibliothek Your knowledge hub WIEN

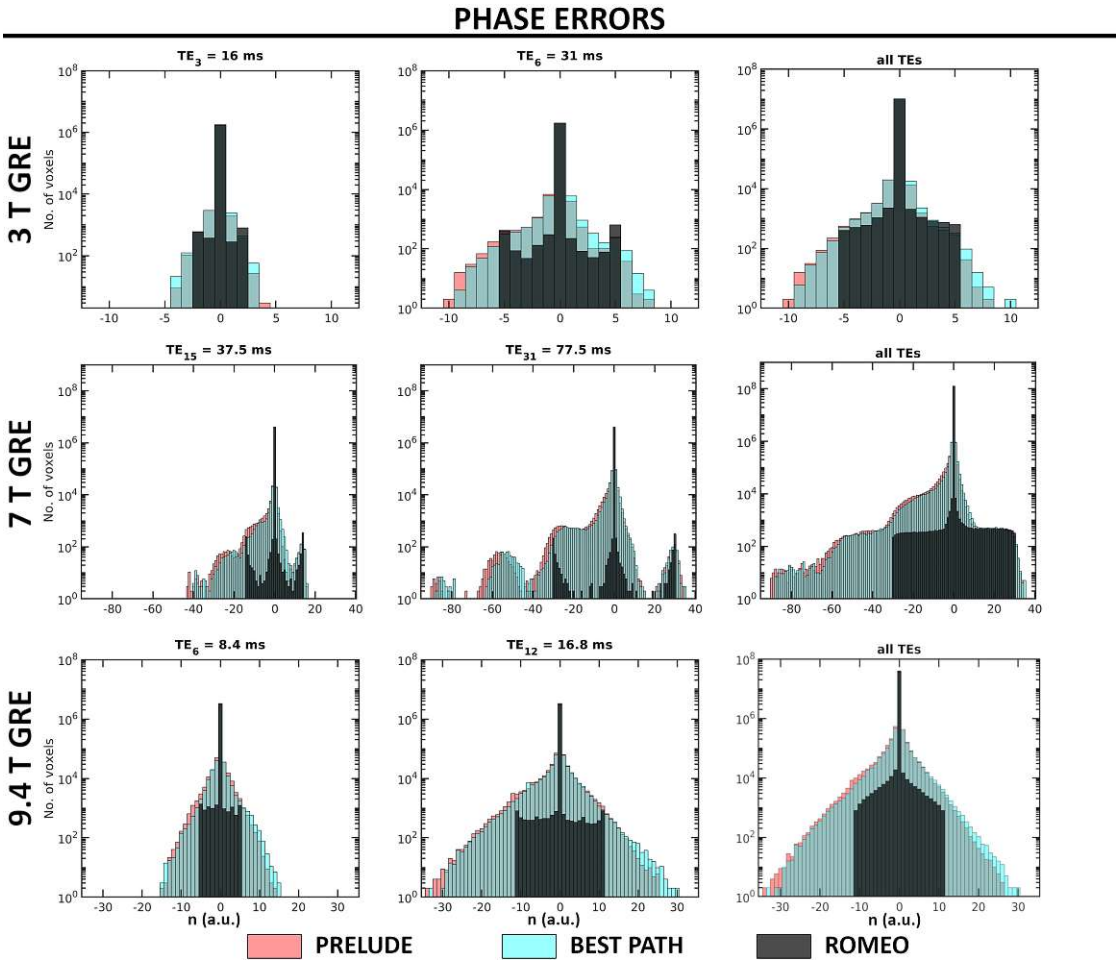

Figure 5.8: Phase unwrapping error histograms for different field strengths and at different echo times; The last column is summed over all echo times excluding the first one. The bins of the histograms correspond to the n in the calculated difference $n2\pi$ from the temporal reference. All histograms are plotted on a logarithmic scale. Figure from [21].

Die approbierte gedruckte Originalversion dieser Dissertation ist an der TU Wien Bibliothek verfügbar.
The approved original version of this doctoral thesis is available in print at TU Wien Bibliothek.
TU Bibliothek Your knowledge hub WIEN

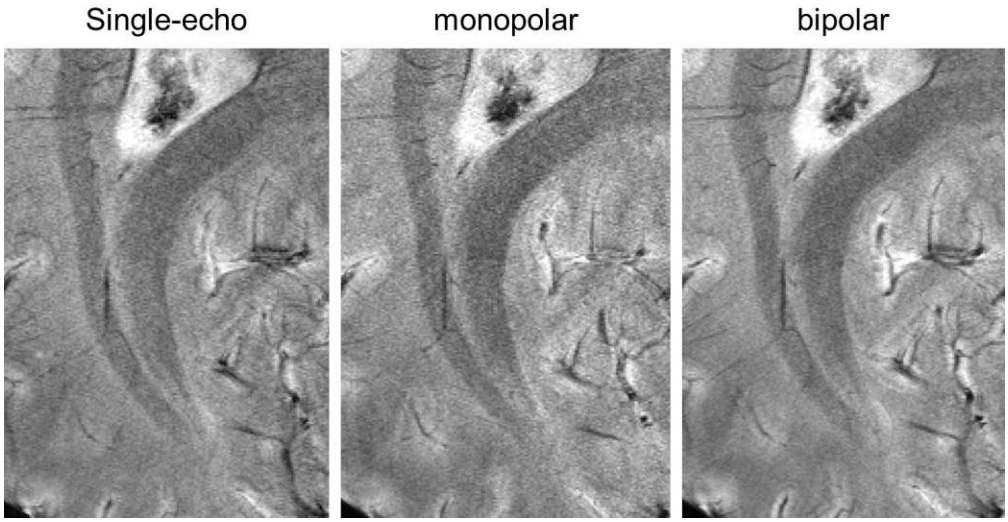

Figure 5.9: Noise comparison between single-echo and SNR-combined monopolar and bipolar magnitude images; to avoid contrast differences, all images have been homogeneity corrected and manually windowed to visually similar contrast levels. Due to possible movement between the acquisitions, the slices might not match exactly.

5.3 CLEAR-SWI

5.3.1 Magnitude Comparison

Comparison of acquisition types Figures 5.9 and 5.10 are visual comparisons of the noise seen with single-echo and multi-echo magnitude images that are used as a basis for SWI. These results can be viewed in relation to SNR simulation in Figure 5.35 and Figure 5.36, which presents the simulated and measured SNR of the same acquisitions. By visual estimation, the noise in Figure 5.9 is highest in monopolar, lower in single-echo and lowest in the bipolar acquisition. This does not match the result expected from the SNR simulation in Figure 5.35, however, as the images are windowed to a small section, the visible noise corresponds to a mixture of CNR and SNR values of the seen tissues. In Figure 5.10, when looking at the first red box, the tissue boundaries between gray and white matter are quite blurry, while they are clearly detectable in the bipolar multi-echo image. The second red box shows the increased visibility and reduced noise in the red nuclei.

Signal dropouts The reduction of signal dropouts in multi-echo scans is shown in Figure 5.11. Red arrows point to severe signal dropouts in the single-echo

Die approbierte gedruckte Originalversion dieser Dissertation ist an der TU Wien Bibliothek verfügbar.
The approved original version of this doctoral thesis is available in print at TU Wien Bibliothek.
TU Bibliothek Your knowledge hub WIEN

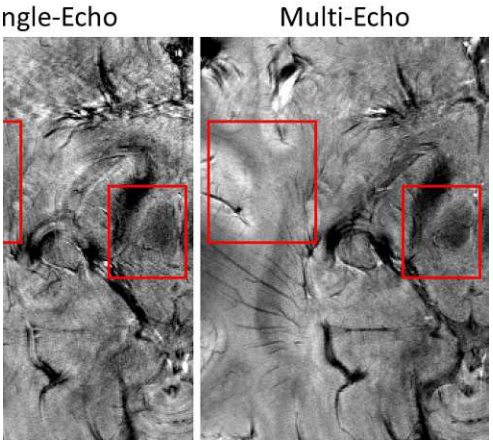

Figure 5.10: Qualitative comparison between homogeneity corrected single-echo and a bipolar multi-echo magnitude; the red boxes show areas were the difference in SNR can be seen by the contours of structures. Due to possible movement between the acquisitions, the slices might not match exactly.

Die approbierte gedruckte Originalversion dieser Dissertation ist an der TU Wien Bibliothek verfügbar.
The approved original version of this doctoral thesis is available in print at TU Wien Bibliothek.
TU Bibliothek Your knowledge hub WIEN

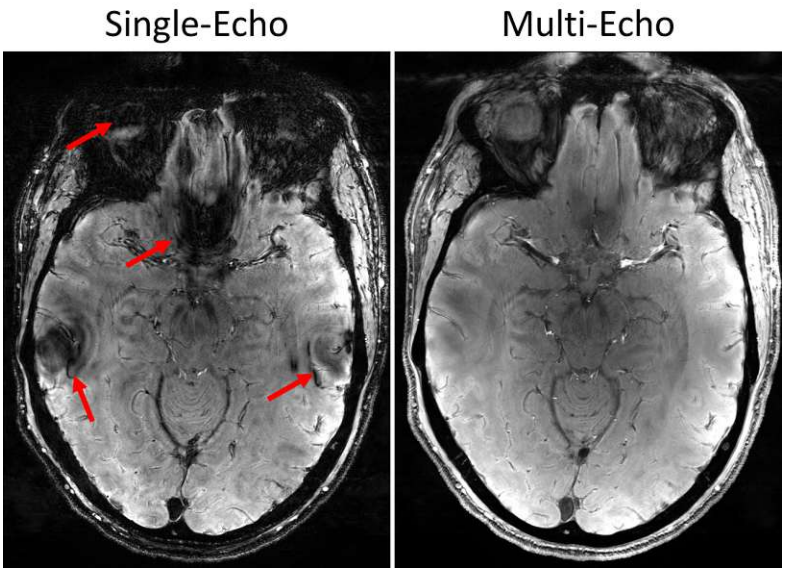

Figure 5.11: Magnitude images from single-echo and SNR-weighted combination of multi-echo; The single-echo magnitude with an echo time of 22.5 ms contains, as is expected, areas with signal dropouts (red arrows). The echo-combined multi-echo magnitude has only slight signal attenuation in these areas, instead of complete signal dropouts.

acquisition. For the multi-echo scan, the SNR-weighted combination weighs early echoes more strongly in places of signal dropout and shows only a slight reduction in signal intensity in these areas.

Contrast comparison and softplus scaling Figure 5.12 compares the different multi-echo combination methods, SNR-weighted, CNR-weighted and unweighted (average) combination. In the top row, the SNR-weighted image has the weakest contrast, CNR-weighted stronger and averaging is in between, which is best seen in the contrast between the red nuclei and substantia nigra and the surrounding tissue. However, all three combination methods have drastically lower contrast compared to the single-echo magnitude.

The second row shows the additional application of the non-linear softplus scaling function (see Section 3.3.3.4), which resulted in a comparable contrast to single-echo. SNR-weighted combination still has the least contrast, but it also has the least signal dropouts (see frontal area and eyes). The contrasts of individual tissues also differs between the combination methods (not shown here) and thus the best combination method depends on the specific needs. For a clinical application, the SNR-weighted softplus magnitude has a good trade-off between low signal

Die approbierte gedruckte Originalversion dieser Dissertation ist an der TU Wien Bibliothek verfügbar.
The approved original version of this doctoral thesis is available in print at TU Wien Bibliothek.
TU Bibliothek Your knowledge hub WIEN

dropouts, which is important close to pathological tissue and high contrast.

5.3.2 Phase Comparison

Homodyne Artefacts The homodyne filtering step in standard single-echo SWI is problematic because it produces wrap artefacts in places where steep phase changes are present. This occurs when the filtering is not sufficient to reduce the phase range to below 2π. In Figure 5.13, a lower brain slice was chosen to demonstrate this problem. In addition to severe distortions in certain areas of the image, however, wrapping artefacts can also be critical by penetrating further into supposedly unaffected areas. This is the case for the bright part of the wrap, where the right red arrow points and for the resulting SWI shown in Figure 5.19. Due to the additional unwrapping step in CLEAR-SWI, the homodyne wrap artefacts were completely avoided (Figure 5.13). In places of strong phase changes, there are still slight phase brightening affects visible with CLEAR-SWI, but these effects pose no risk of misdiagnosis.

Qualitative phase mask comparison A phase masking comparison of standard SWI and CLEAR-SWI with different masking strengths is presented in Figure 5.14. In standard SWI phase masking, 4-10 multiplications are usually chosen to obtain the desired contrast. The background appears noisy already from 4 multiplications, increasing towards higher numbers. The masked phase using the sigmoidal function in CLEAR-SWI appears less noisy and more natural in comparison. It has strong contrast of veins and only at a level parameter of 8-10 does the background phase begin to appear noisy.

High quality of CLEAR-SWI phase mask Figure 5.15 presents the high quality in the CLEAR-SWI phase mask in two selected regions. The first image demonstrates the strong and clear appearance of veins (single slice, no mIP) and also shows small gray matter veins. In the second image, even small veins inside the head of caudate nucleus are visible.

5.3.3 Comparison of Standard SWI and CLEAR-SWI

Figure 5.16 presents a comparison of standard SWI and CLEAR-SWI with three slices from the same acquisition. The top row presents a low slice, where large parts of the image are corrupted from homodyne wraps and signal drop-outs in standard SWI, while CLEAR-SWI has no wrap artefacts and only slightly reduced intensity close to the ear canals instead of signal drop-outs. Additionally, the image homogeneity and the visibility of small veins is greatly improved in CLEAR-SWI. The same general difference can be observed in all three slices that are

Die approbierte gedruckte Originalversion dieser Dissertation ist an der TU Wien Bibliothek verfügbar.
The approved original version of this doctoral thesis is available in print at TU Wien Bibliothek.
TU Bibliothek Your knowledge hub WIEN

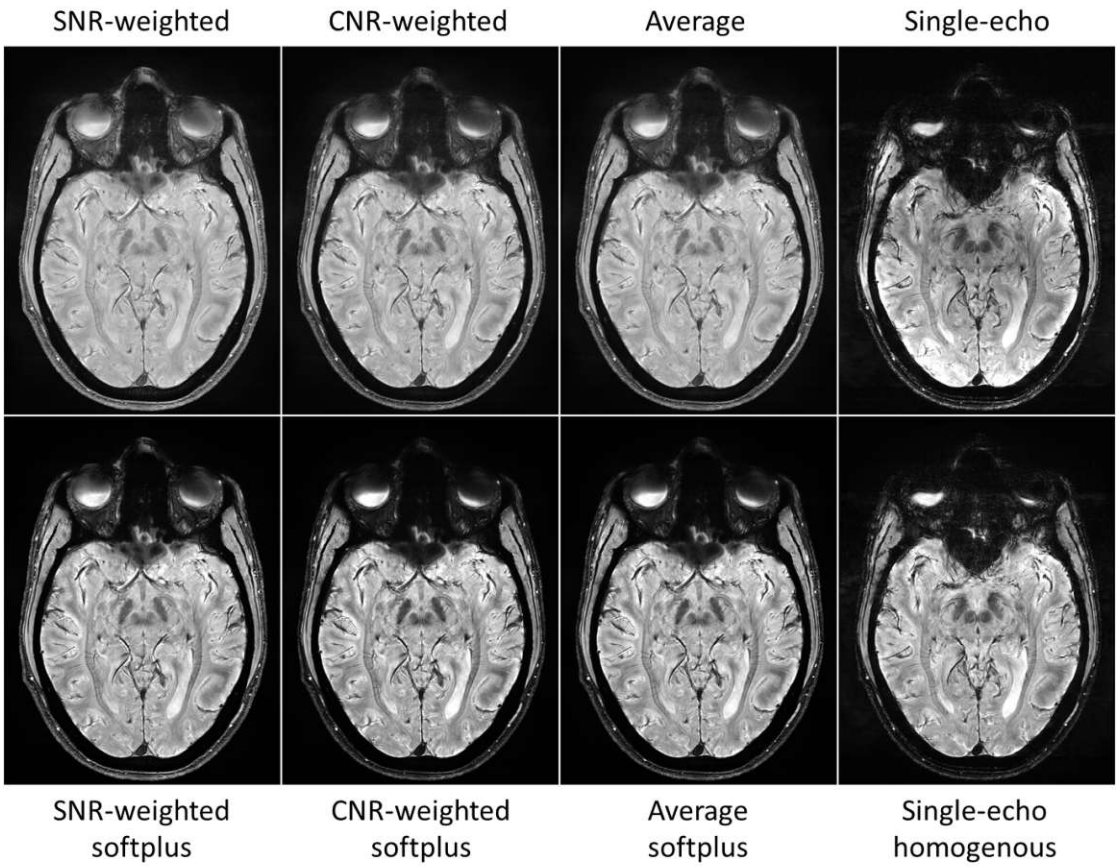

Figure 5.12: Contrast comparison of different multi-echo magnitude combination methods. The top row shows three different combination methods (homogeneity corrected) and as reference the single-echo magnitude. The tissues chosen for CNR-weighted combination were white matter and gray matter. The bottom row shows the same three combination methods with additional softplus scaling applied. The bottom right image shows the CLEAR-SWI homogeneity correction applied to the single-echo magnitude in order to be comparable to the multi-echo images.

Die approbierte gedruckte Originalversion dieser Dissertation ist an der TU Wien Bibliothek verfügbar.
The approved original version of this doctoral thesis is available in print at TU Wien Bibliothek.
TU Bibliothek Your knowledge hub WIEN

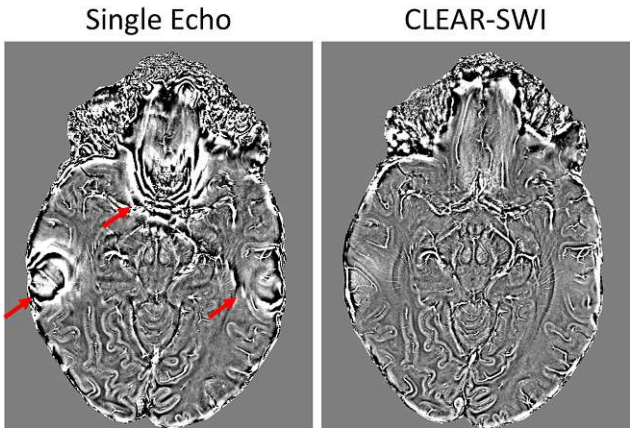

Figure 5.13: High-pass filtered phase from Standard SWI and CLEAR-SWI; The single-echo phase is homodyne filtered and exported on the scanner reconstructor using the standard (Siemens) SWI pipeline. The CLEAR-SWI phase is Laplacian unwrapped and high-pass filtered according to the steps described in 3.3.

presented: reduced artefacts, homogeneous appearance and better vein visibility. The homodyne wrap artefacts are less pronounced in higher slices in standard SWI but some wraps remain at the frontal border of the brain.

Comparison of minimum intensity projections SWI mIPs are commonly used to better visualize the vasculature, as they accumulate the low intensity (i.e. vein) information across multiple slices, which makes following veins easier when viewing individual slices. Figure 5.17 shows a comparison of mIPs of standard SWI and CLEAR-SWI. Standard SWI suffers from detrimental homodyne wrap artefacts in the lower slice, while CLEAR-SWI is not affected and shows veins in these regions in high quality. Standard SWI is additionally affected by intensity variations and appears brighter towards the outside edges of the brain, making it more difficult to visualize veins near the edges of the brain and reducing contrast in the center of the brain. These intensity fluctuations were completely removed in CLEAR-SWI.

Homodyne wrap artefacts in unexpected regions To compare details, a magnification of a small windowed area is shown in Figure 5.18. In CLEAR-SWI, the veins appear better defined and with higher contrast against surrounding

Die approbierte gedruckte Originalversion dieser Dissertation ist an der TU Wien Bibliothek verfügbar.
The approved original version of this doctoral thesis is available in print at TU Wien Bibliothek.
TU Bibliothek Your knowledge hub WIEN

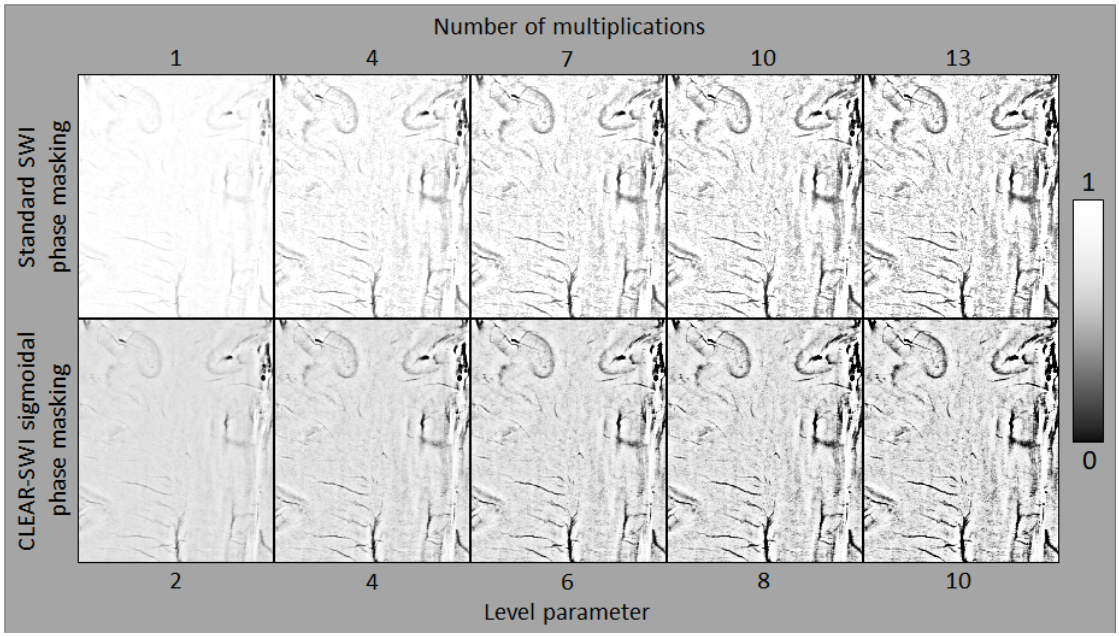

Figure 5.14: Comparison of phase masks obtained with standard SWI and CLEAR-SWI with different phase filtering strength settings; In standard SWI, the number of phase multiplications (power) decides the strength, in CLEAR-SWI, the level parameter in the sigmoidal scaling.

Die approbierte gedruckte Originalversion dieser Dissertation ist an der TU Wien Bibliothek verfügbar.
The approved original version of this doctoral thesis is available in print at TU Wien Bibliothek.
TU WIEN Bibliothek Your knowledge hub

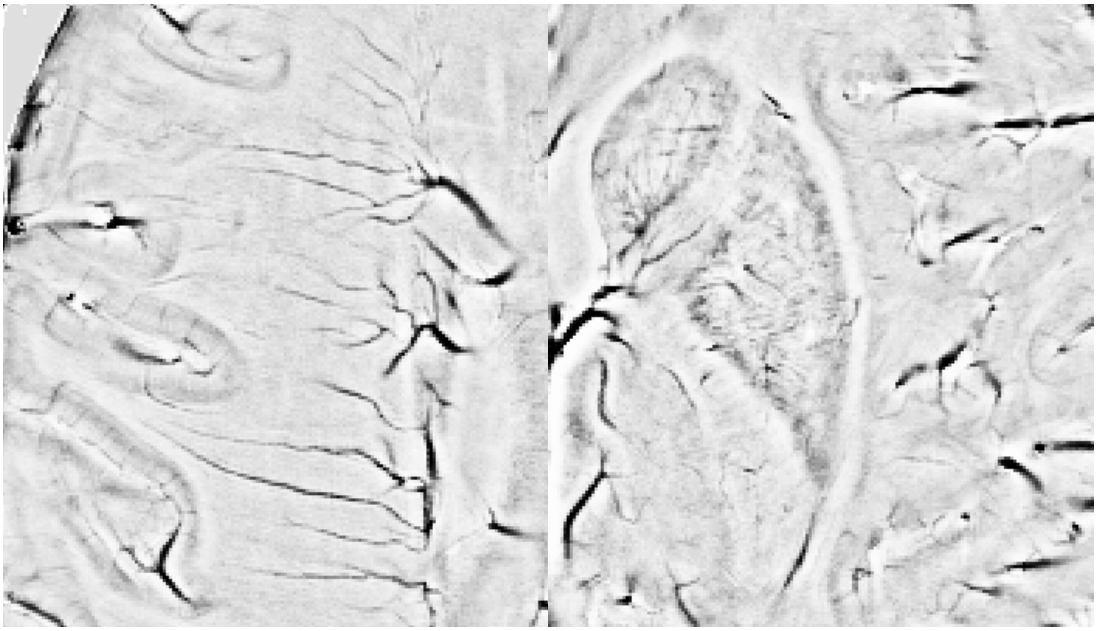

Figure 5.15: Filtered and scaled phase for CLEAR-SWI; Small sections are presented, showing the high quality of veins and small structures in the phase mask.

tissue compared to standard SWI (red box). Two types of artefacts are visible in standard SWI, indicated by blue and red arrows. The blue arrows indicate a large intensity change toward the edge of the brain, resulting in places that are difficult to view. Contrast and brightness can be manually adjusted to these small areas, but visibility is never optimal due to rapid intensity change. The red arrows show a homodyne wrap artefacts that appears without being connected to a larger corrupted area. If the shape of the homodyne artefact resembles pathological phenomena, this can potentially lead to misdiagnosis, as shown in Figure 5.19. The red arrow points to a homodyne wrap artefact in the filtered phase of the standard pipeline. In the standard SWI, this appears as a black dot that can be misdiagnosed as a microbleeding. In CLEAR-SWI, this artefact is not present and nothing special is visible in this region.

Comparison in a multiple sclerosis patient The next two figures show the application of CLEAR-SWI in patients. Figure 5.20 presents a multiple sclerosis case for which a standard clinical SWI and a multi-echo CLEAR-SWI scan were performed with similar acquisition times. The CLEAR-SWI scan has significantly improved quality and allows the detection of additional lesions that are barely visible on standard SWI (Lesion 1). For the multi-echo combination, CNR-weighting

Die approbierte gedruckte Originalversion dieser Dissertation ist an der TU Wien Bibliothek verfügbar.
The approved original version of this doctoral thesis is available in print at TU Wien Bibliothek.
TU Bibliothek Your knowledge hub WIEN

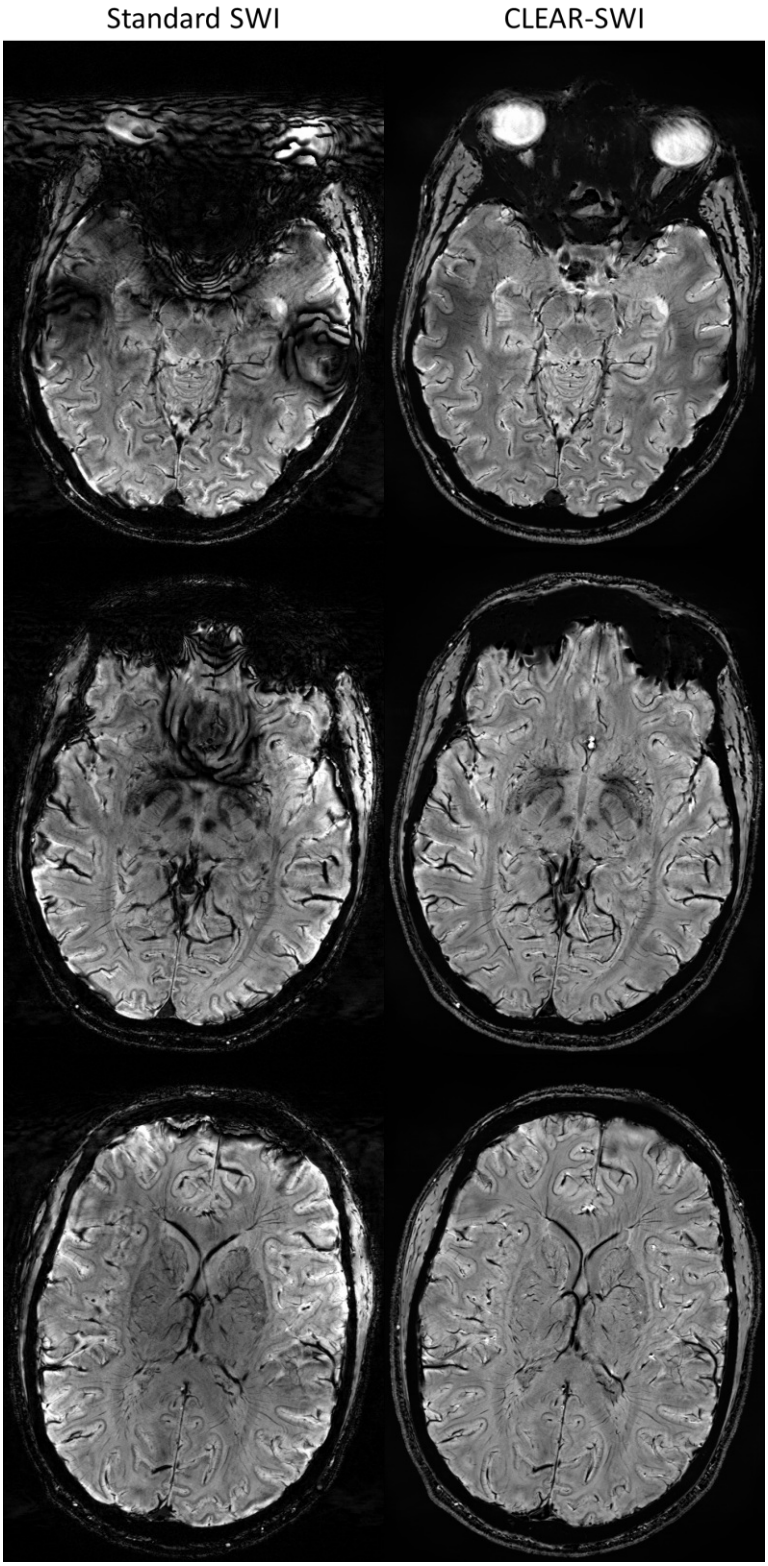

Figure 5.16: Comparison of standard SWI (Dataset NE1) and CLEAR-SWI (Dataset NE6); three different slices are shown, each containing homodyne wrap artefacts in standard SWI, while no severe artefacts are present in CLEAR-SWI.

Die approbierte gedruckte Originalversion dieser Dissertation ist an der TU Wien Bibliothek verfügbar.
The approved original version of this doctoral thesis is available in print at TU Wien Bibliothek.
TU WIEN Bibliothek Your knowledge hub

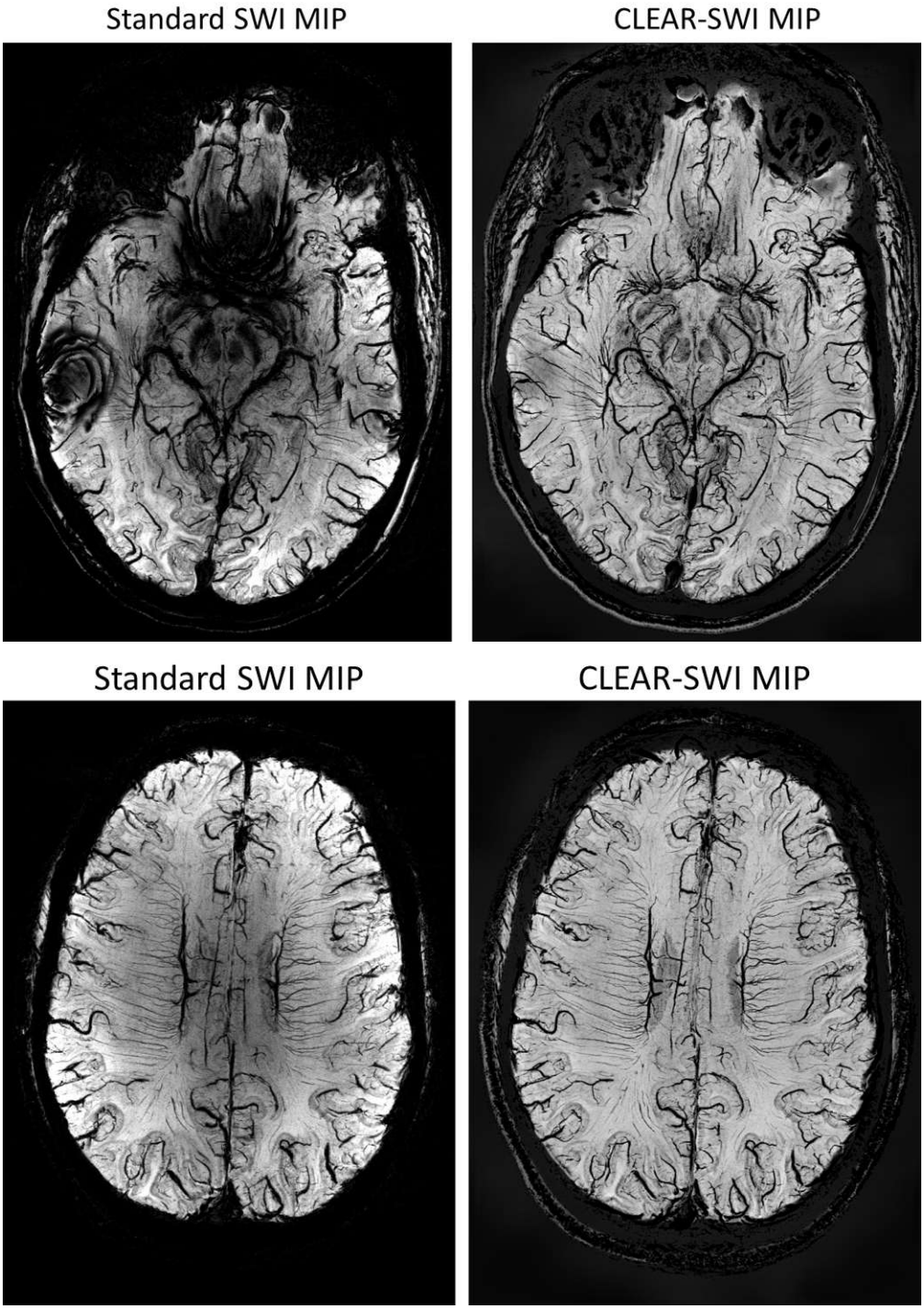

Figure 5.17: Comparison of minimum intensity projections (mIP) of Standard SWI and CLEAR-SWI in a lower slice (top row) and higher slice (bottom row); many wrap-like homodyne filtering artefacts appear in Standard SWI in the lower slice.

Die approbierte gedruckte Originalversion dieser Dissertation ist an der TU Wien Bibliothek verfügbar.
The approved original version of this doctoral thesis is available in print at TU Wien Bibliothek.
TU WIEN Bibliothek Your knowledge hub

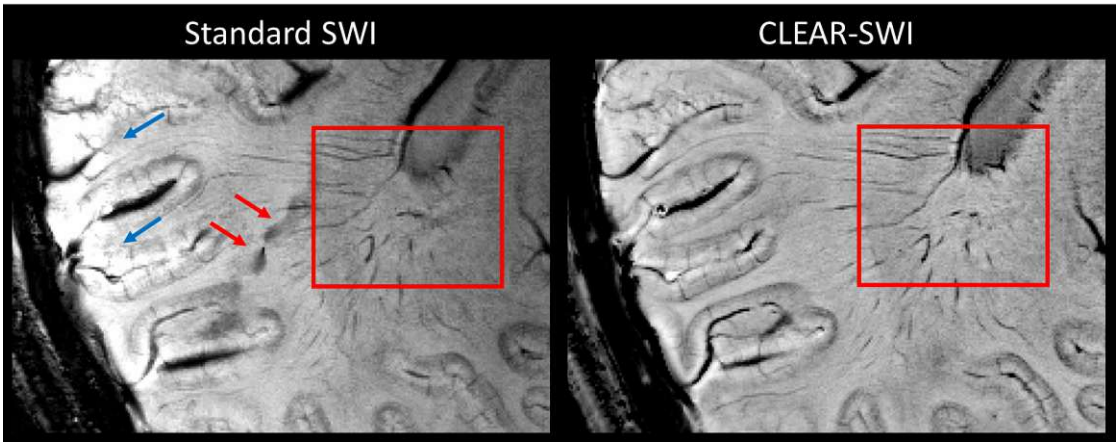

Figure 5.18: Comparison of standard SWI with CLEAR-SWI in a small region; The red box is drawn for comparing the vein quality. The blue arrows point to strong brightening, which hinders image analysis in this region and the red arrows point to homodyne wrap artefacts.

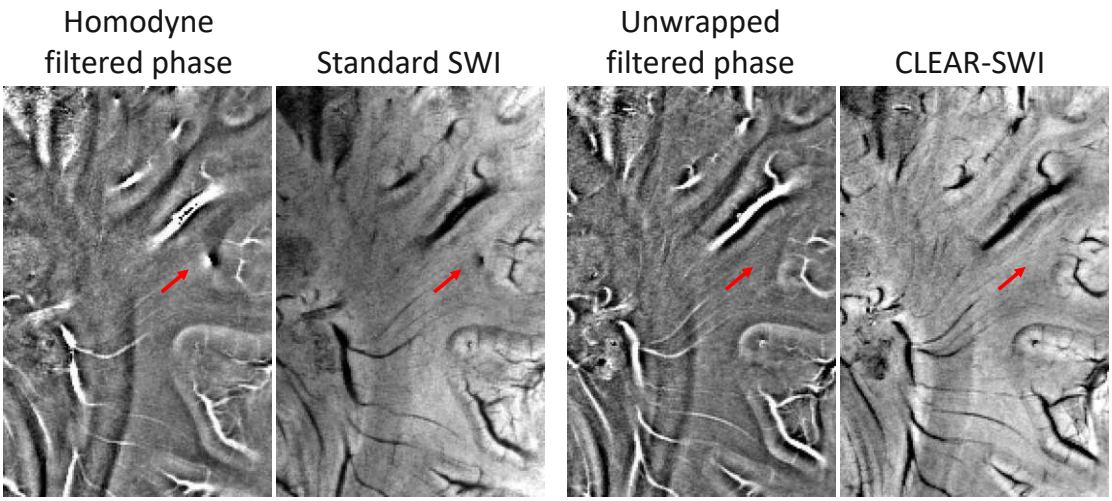

Figure 5.19: Phase artefact appearing as microbleeding in standard SWI; The left two images are the filtered phase and resulting SWI in the standard reconstruction and the right two images the filtered phase and SWI from the CLEAR-SWI pipeline. The red arrow points to the place where the homodyne artefact appears in standard SWI.

Die approbierte gedruckte Originalversion dieser Dissertation ist an der TU Wien Bibliothek verfügbar.
The approved original version of this doctoral thesis is available in print at TU Wien Bibliothek.
TU Bibliothek Your knowledge hub WIEN

was used with measured parameters of the lesion tissue and the iron ring surrounding it. In Lesion 2, it can be seen that this results in a strong lesion contrast with a hyperintense appearance of the tissue within the lesion. Because CLEAR-SWI is based on a multi-echo acquisition, it provides the ability to create M_0 and quantitative T_2^* maps (lower portion of Figure 5.20). Both can additionally aid in the detection and analysis of pathological tissue.

Comparison in tumor patients Four of the 14 tumor cases were selected based on interesting differences between standard SWI and CLEAR-SWI and are shown in Figure 5.21. In Patient A, hypointense homodyne wrap artefacts were present around the tumor and also several centimeters away in standard SWI (red arrows). In CLEAR-SWI, the hypointense tumor region is limited and has a similar shape to the upper half seen in T_2^*. T_2^* contains dephasing information in addition to the tissue constant T_2. Thus the large blue area below the lesion is hypothesized to be not tissue related but due to a strong local phase gradient. In Patient B, the lesion area again appears larger in standard SWI, whereas CLEAR-SWI is able to show the vascularity very close to the tumor. T_2^* may additionally help to characterize the tissue as it shows hyperintense values in the large affected area. Patient C shows image corruption in standard SWI caused by strong phase gradients around the lesion that are not present in CLEAR-SWI. Patient D represents a case where the M_0 map shows additional contrast that is not visible in the other images but could be observed in T_1-weighted FLAIR images (not shown).

Application at 3 T The improvement in quality observed in CLEAR-SWI compared to standard SWI at 7 T was also observed at 3 T (see Figure 5.22). In CLEAR-SWI, the visibility of small veins was increased, which can be seen in the red boxes, where the small veins are easy to detect in CLEAR-SWI and hardly detectable in standard SWI. In the red boxes in the minimum intensity projections, the contrast between veins and surrounding tissues is higher in CLEAR-SWI. The red arrows point to places, where the boundary between white and gray matter is hard to recognize in standard SWI but apparent in CLEAR-SWI. This increase in contrast between white and gray matter can be observed in the whole image. The blue arrows point to the magnitude inhomogeneities that were present in standard SWI, which were corrected in CLEAR-SWI.

Die approbierte gedruckte Originalversion dieser Dissertation ist an der TU Wien Bibliothek verfügbar.
The approved original version of this doctoral thesis is available in print at TU Wien Bibliothek.
TU Bibliothek Your knowledge hub WIEN

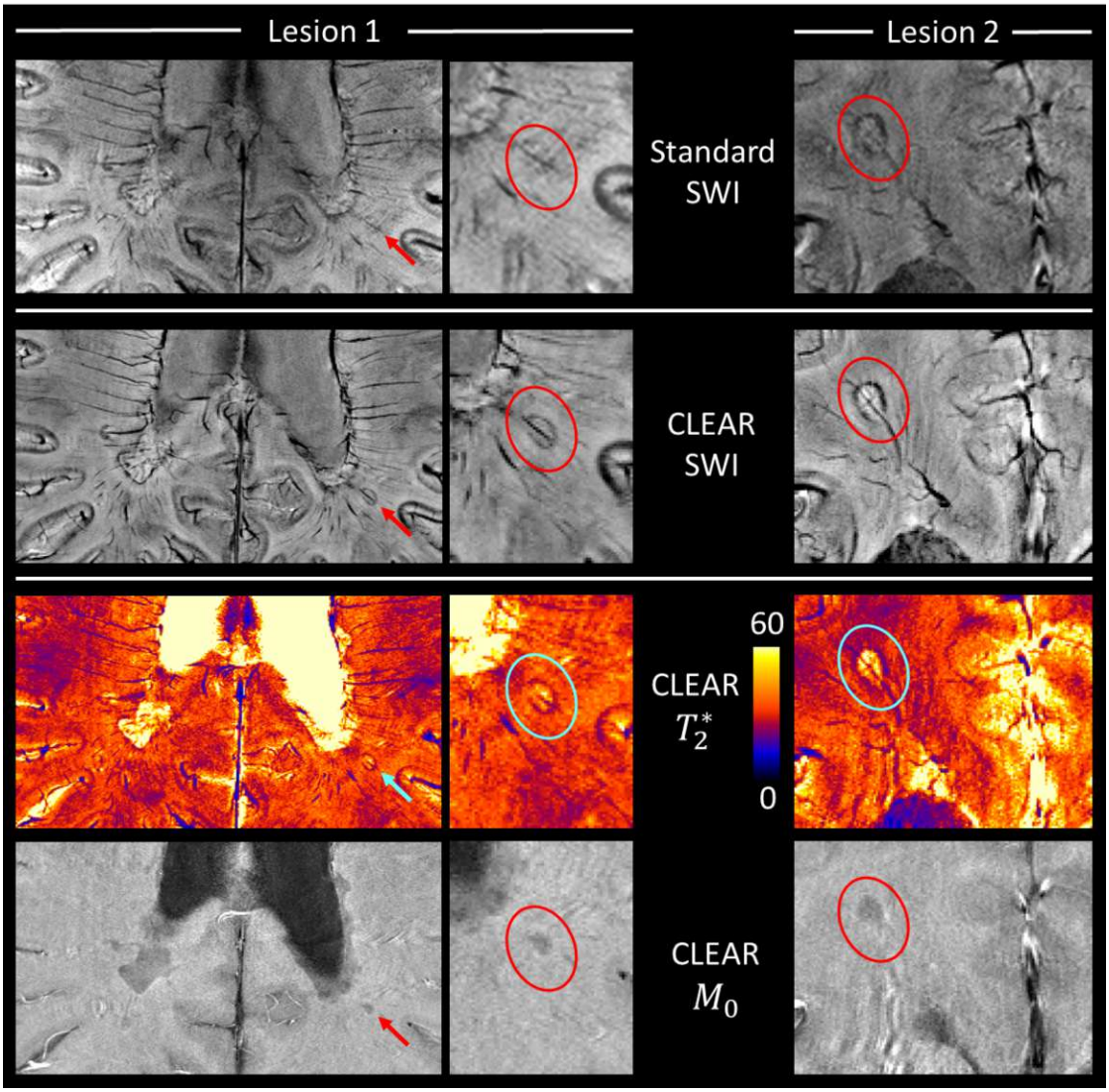

Figure 5.20: Comparison between standard SWI and CLEAR-SWI in a multiple sclerosis patient; also shown is T_2^* and M_0 calculated from the same multi-echo scan used for CLEAR-SWI. The arrow points to Lesion 1, which is also magnified and marked with a red ellipse. The right half shows a second lesion. Although the acquisition time of the clinically used standard SWI sequence and CLEAR-SWI is identical, the change in quality could be partly due to the possibility to choose optimized sequence settings for CLEAR-SWI.

Die approbierte gedruckte Originalversion dieser Dissertation ist an der TU Wien Bibliothek verfügbar.
The approved original version of this doctoral thesis is available in print at TU Wien Bibliothek.
TU Bibliothek Your knowledge hub WIEN

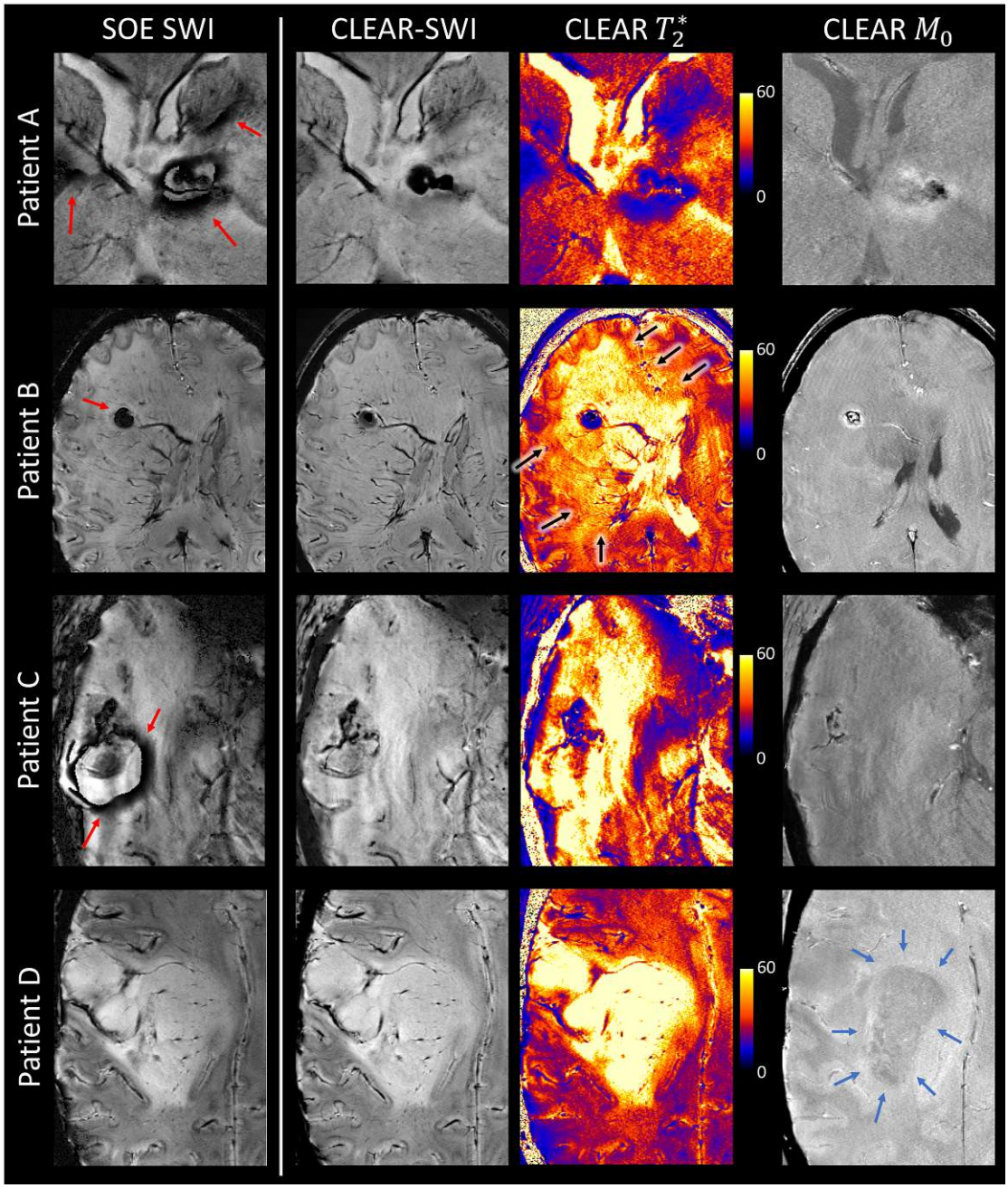

Figure 5.21: CLEAR-SWI versus simulated single-echo SWI (SOE SWI) from the same dataset; The red arrows in SOE SWI point to wrap artefacts. The black arrows in T_2^* and the blue arrows in M_0 point to interesting contrast changes that are especially well visible in the respective image type.

Die approbierte gedruckte Originalversion dieser Dissertation ist an der TU Wien Bibliothek verfügbar.
The approved original version of this doctoral thesis is available in print at TU Wien Bibliothek.
TU WIEN Bibliothek Your knowledge hub

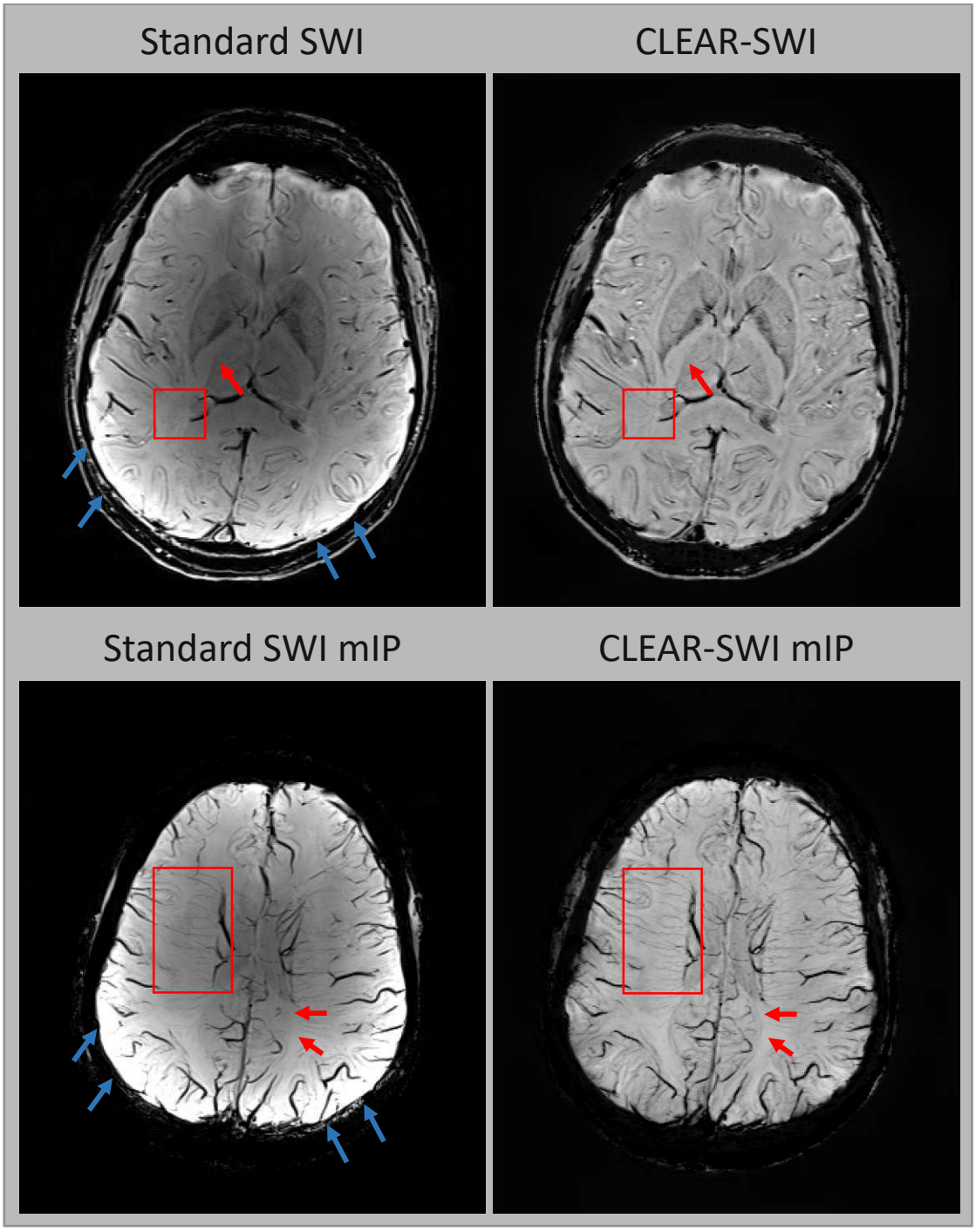

Figure 5.22: Comparison of standard SWI and CLEAR-SWI at 3 T. The top row shows calculated SWI and the bottom row shows minimum intensity projections (mIP) calculated from a stack of SWI slices of a more superior location. CLEAR-SWI shows an improved visualization of veins (red boxes) and additional contrasts between gray and white matter (red arrows). Standard SWI is inhomogeneous at the boundary of the brain (blue arrows).

Die approbierte gedruckte Originalversion dieser Dissertation ist an der TU Wien Bibliothek verfügbar.
The approved original version of this doctoral thesis is available in print at TU Wien Bibliothek.
TU WIEN Bibliothek Your knowledge hub

5.4 Supporting Methods

These supporting methods were required as steps for the presented main methods and their results are presented separately to disentangle the individual aspects and keep the presentation of the main results to the point.

5.4.1 Automatic Masking

As opposed to classical masking algorithms that extract the brain [70], the goal of this masking approach was to remove the background noise and to run robustly without user intervention.

The automatic masking was tested on the 14 gradient echo acquisitions of the tumor dataset. In multi-echo scans, the first echo was chosen to calculate the mask. Otherwise there were no manual choices required for the masking process. One slice for each scan is shown in Figure 3.4.1. There were some cases in which small low-intensity structures inside the brain were removed during masking and in two cases (bottom row; second and fifth image) acquisition artefacts were visible outside of the brain that were not removed in masking. These issues have not been further addressed, as it was of no concern for the application of masking in the methods described later on. The masks were produced automatically without fine tuning to the individual acquisitions, and the method was shown to be robust for a variety of different gradient echo acquisitions.

5.4.2 Sensitivity Estimation and Homogeneity Correction

The sensitivity profile after coil combination was estimated on 7 different subjects. The original combined magnitude for each subject, with a strong sensitivity profile or inhomogeneity artefact is shown in the top row of Figure 5.24 and the estimated sensitivity profiles are shown in the middle row, depicting the inhomogeneity without being affected by large tissue structures, such as the ventricles (columns 4-6). The calculated sensitivity extends outside the brain, and a mask was applied for better visualizing the sensitivity with regard to the original magnitude images.

To verify the estimated sensitivity profile, a homogeneity correction was applied to the magnitude by dividing by the estimated sensitivity, which is shown in the bottom row of Figure 5.24. The inhomogeneities have been completely removed inside the brain and only very small brightening artefacts are visible inside the skull. In all images, the grayscale was automatically adjusted to [0;99%] of the intensity values.

Figure 5.25 shows a homogeneity corrected image in three orthogonal slices. The uncorrected images (left side) suffer from strong inhomogeneity with an increase of signal intensity towards the edges of the brain. The homogeneity cor-

Die approbierte gedruckte Originalversion dieser Dissertation ist an der TU Wien Bibliothek verfügbar.
The approved original version of this doctoral thesis is available in print at TU Wien Bibliothek.
TU Bibliothek Your knowledge hub WIEN

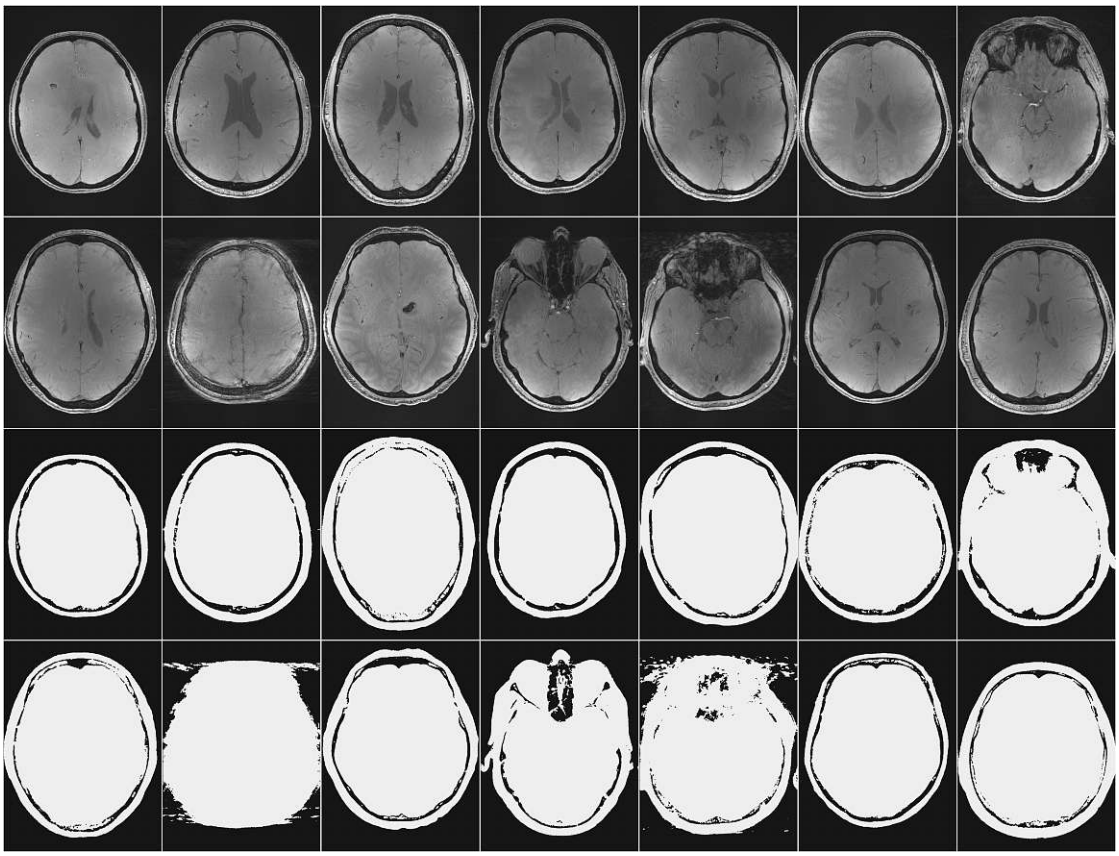

Figure 5.23: Automatic masks for 14 different acquisitions; The original magnitude images are shown in the top two rows and the corresponding masks in the bottom two rows. The masks removed the background noise outside the head and very low intensity voxels inside. The second and fifth mask in the bottom row included some background noise, as there were background artefacts with elevated signal levels.

Die approbierte gedruckte Originalversion dieser Dissertation ist an der TU Wien Bibliothek verfügbar.
The approved original version of this doctoral thesis is available in print at TU Wien Bibliothek.
TU WIEN Bibliothek Your knowledge hub

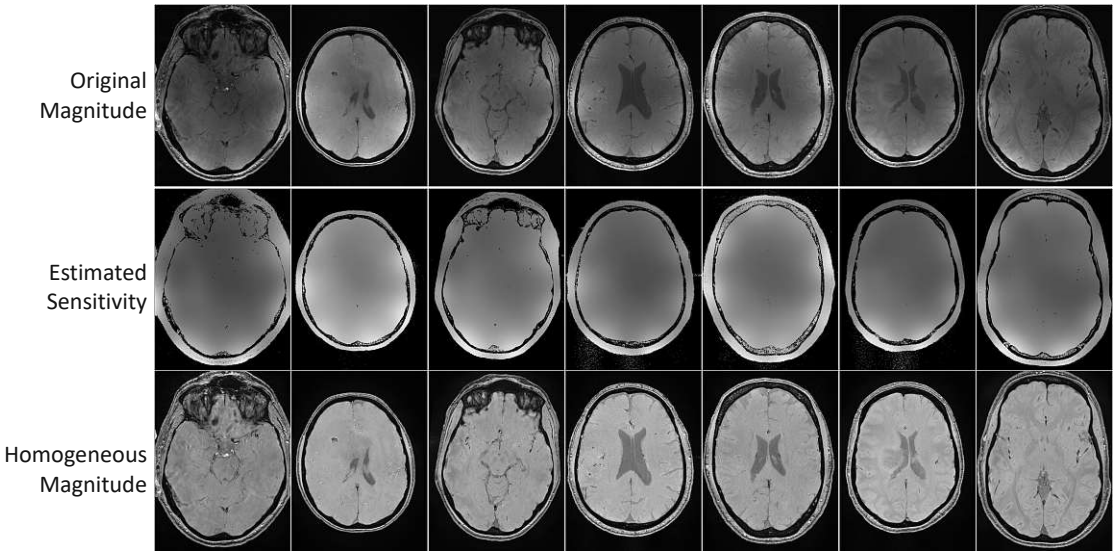

Figure 5.24: Sensitivity estimation and homogeneity correction; 7 datasets from different volunteers are shown and all images are scaled to [0;99%] of intensity values. In the original images in the top row, inhomogeneities are clearly visible and tend to get stronger at the edges of the head towards the individual coils of the RF array. The estimated sensitivity in the middle row closely resembles the inhomogeneity of the original images. The estimated sensitivity is continuous, in principle, and extends to the edge of the images, however, for better viewing, the shown sensitivity was multiplied with an automatic mask. The bottom row shows the homogeneous magnitude after sensitivity correction. The resulting magnitude images are very homogeneous with no visible artefacts and only small inhomogeneities are left in the skull.

Die approbierte gedruckte Originalversion dieser Dissertation ist an der TU Wien Bibliothek verfügbar.
The approved original version of this doctoral thesis is available in print at TU Wien Bibliothek.
TU Bibliothek Your knowledge hub WIEN

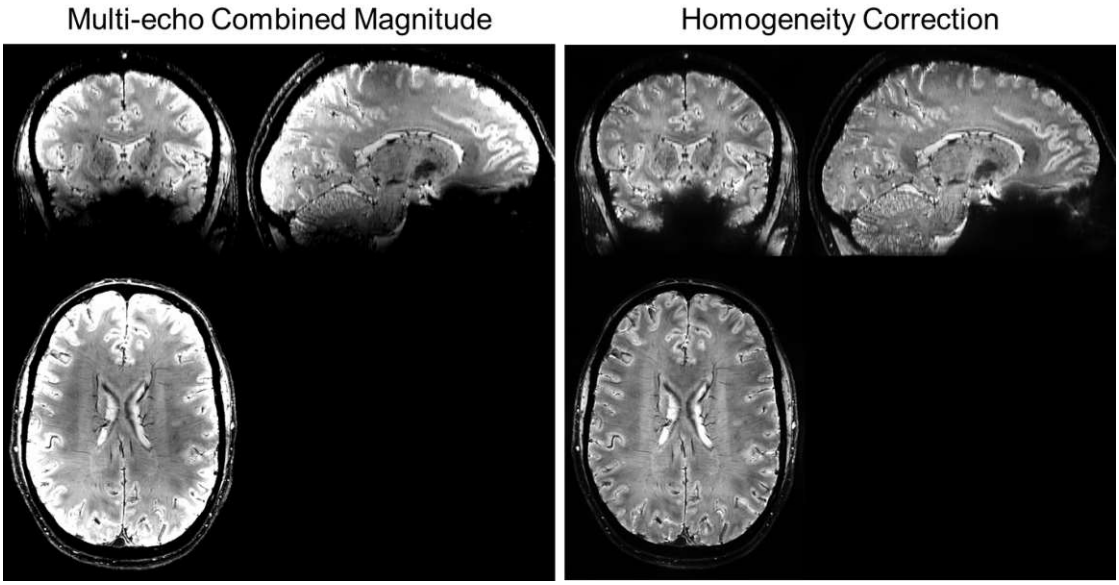

Figure 5.25: Homogeneity correction in 3D view; The combined multi-echo images on the left side are homogeneity corrected and shown on the right side. The images are scaled to similar contrast in the ventricles (top right image, sagittal view).

rection provides similar contrast through the whole brain, even in some areas in very low slices, which are barely visible in the uncorrected image. In the topmost slices in the sagittal view, there is still a small decline in brightness towards the top, which is visible in both uncorrected and corrected images. It was not fully corrected because the change in intensity was too rapid. The signal decline in this region comes together with a change in white matter/gray matter contrast and is probably related to a non-ideal local flip angle, leading to a faster signal decline than would be expected from the standard sensitivity profile.

5.4.3 Fast Gaussian 3D Smoothing

This section first evaluates the general properties of the fast Gaussian smoothing method, then presents smoothing applied to phase values and finally shows results of smoothing images with missing values.

Smoothing evaluation The fast Gaussian smoothing is performed via the iterative application of average filtering separately in each dimension with an 1-dimensional filter (Section 3.4.3). The impulse response (see Section 4.2.1) for different numbers of iterations is compared with true Gaussian smoothing in Figure 4.2.1. With 1 iteration, the impulse response is a square as is expected; with 2

Die approbierte gedruckte Originalversion dieser Dissertation ist an der TU Wien Bibliothek verfügbar.
The approved original version of this doctoral thesis is available in print at TU Wien Bibliothek.
TU Bibliothek WIEN Your knowledge hub

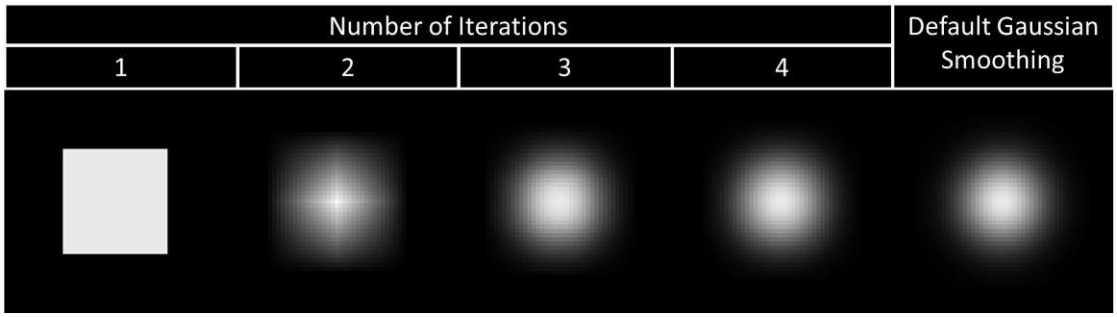

Figure 5.26: Impulse response of the estimated Gaussian smoothing; With more iterations the shape converges toward a Gaussian. Details can be found in Section 4.2.1, Impulse Response.

iterations, the shape is like a pyramid and might introduce visible artefacts if regular patterns or straight edges occur in an image; with 3 iterations, the outcome is smooth with no artefacts but the shape is slightly more rectangular than Default Gaussian Smoothing; with 4 iterations or more (not shown), no differences can be seen between estimated and true Gaussian smoothing. However, the σ of the estimated Gaussian smoothing slightly deviates from the desired σ. This occurs due to the filter size of the average filter being integerized to odd integers. For 3 resp. 4 iterations the filter sizes were chosen to be $13, 13, 15\,\text{px}$ resp. $11, 11, 13, 13\,\text{px}$, which resulted in $\sigma = 6.85\,\text{px}$ resp. $\sigma = 6.95\,\text{px}$ instead of the desired $\sigma = 7\,\text{px}$.

Figure 5.27 shows the deviation to perfect Gaussian smoothing when changing the number of boxes and the size of σ. With a larger number of average filter applications (number of boxes), the smoothing converges towards perfect Gaussian smoothing.

For the application in the context of MRI, speed and smoothing without artefacts is of main concern, while the smoothing does not need to be strictly Gaussian. Considering both results, the impulse response and the deviation from perfect Gaussian smoothing, the optimal number of iterations (number of boxes) was chosen to be 3 in further experiments.

Smoothing phase via complex smoothing Results of complex smoothing of phase values are presented in Figure 5.28 and Figure 5.29 for the same acquisition but different slices. Figure 5.28 shows successful smoothing for three echo times. The high-frequency spatial structures and noise is reduced, while the wrap positions are still identical. Figure 5.29 shows artefacts of spatially smoothing complex images that occur when closely spaced wraps are encountered. These artefacts with open ended fringe lines are the same as seen in homodyne filtering.

Die approbierte gedruckte Originalversion dieser Dissertation ist an der TU Wien Bibliothek verfügbar.
The approved original version of this doctoral thesis is available in print at TU Wien Bibliothek.
TU Bibliothek Your knowledge hub WIEN

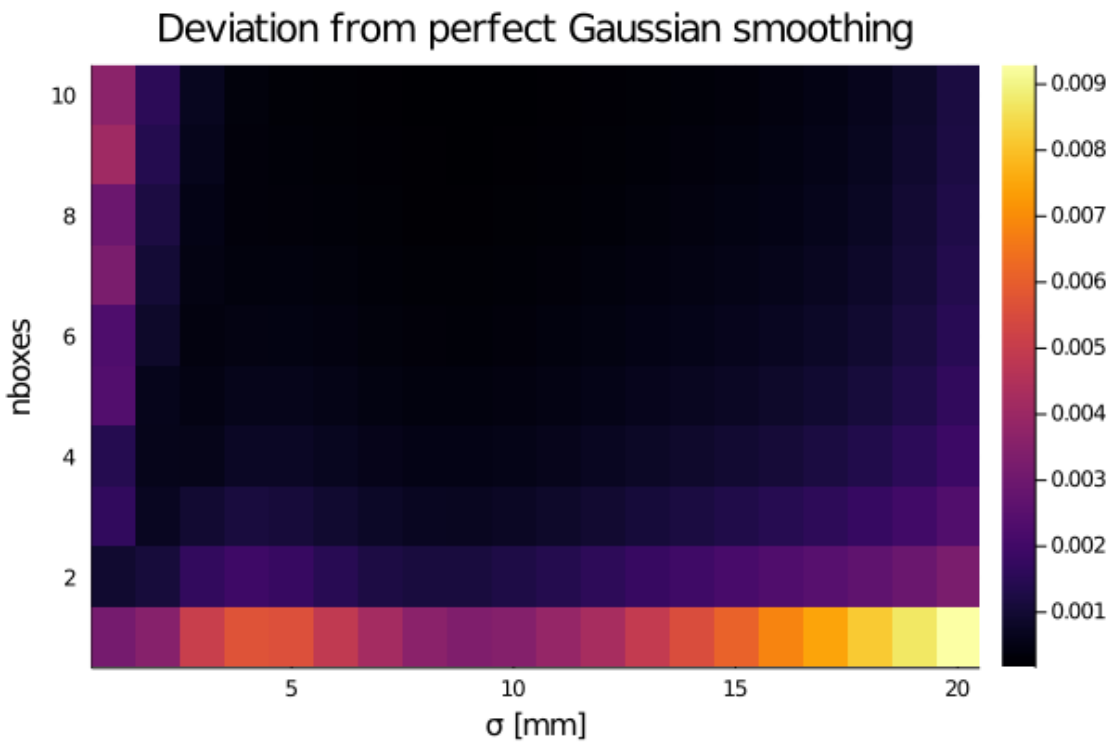

Figure 5.27: Average deviation per voxel from perfect Gaussian smoothing evaluated on a 7 T gradient echo brain image in the range $[0; 1]$; nboxes corresponds to the number of average filter applications that are performed for each dimension. Very small σ sizes (left columns) are problematic with a large number of boxes, as the size of each box is at least 3 voxels and the effective σ is larger than the desired one. Details of calculating the average deviation are given in 4.2.1.

Die approbierte gedruckte Originalversion dieser Dissertation ist an der TU Wien Bibliothek verfügbar.
The approved original version of this doctoral thesis is available in print at TU Wien Bibliothek.
TU Bibliothek Your knowledge hub WIEN

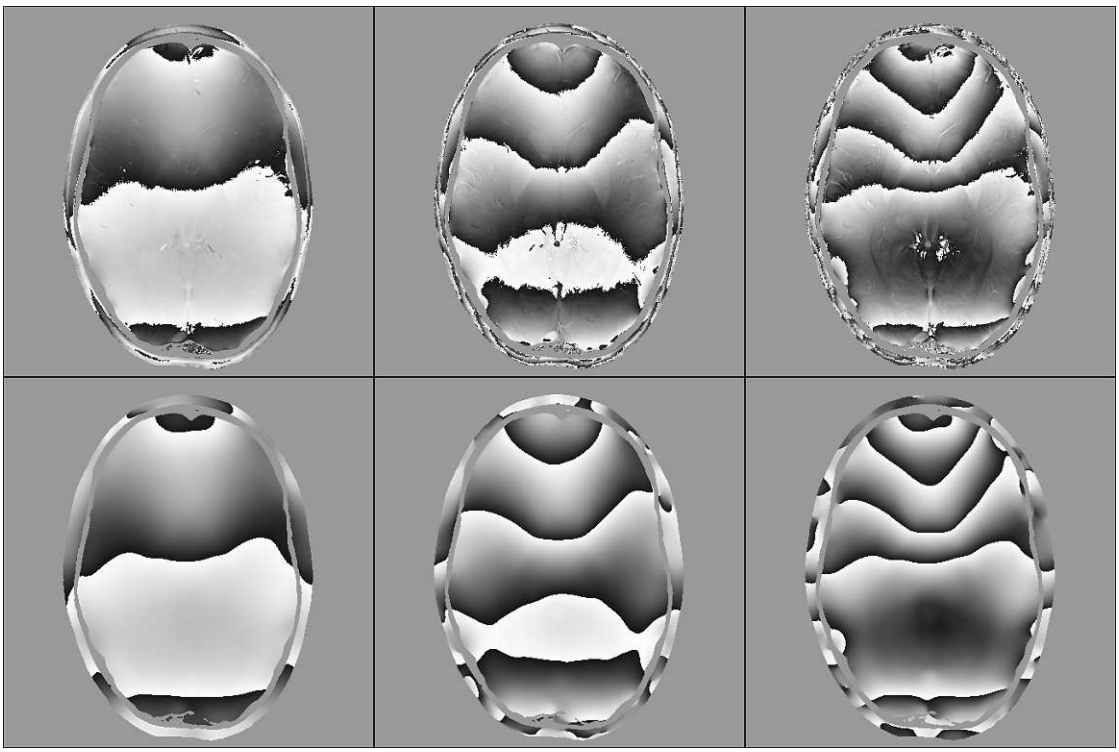

Figure 5.28: Complex smoothing of phase images at 3 different echo times (5 ms (left), 10 ms (middle), and 15 ms (right)); The smoothing was performed in 3D with an isotropic size of $\sigma = 3$ mm. The wrap borders in the smoothed images (bottom row) closely correspond to the locations of the wrap borders in the original phase images (top row).

Die approbierte gedruckte Originalversion dieser Dissertation ist an der TU Wien Bibliothek verfügbar.
The approved original version of this doctoral thesis is available in print at TU Wien Bibliothek.
TU WIEN Bibliothek Your knowledge hub

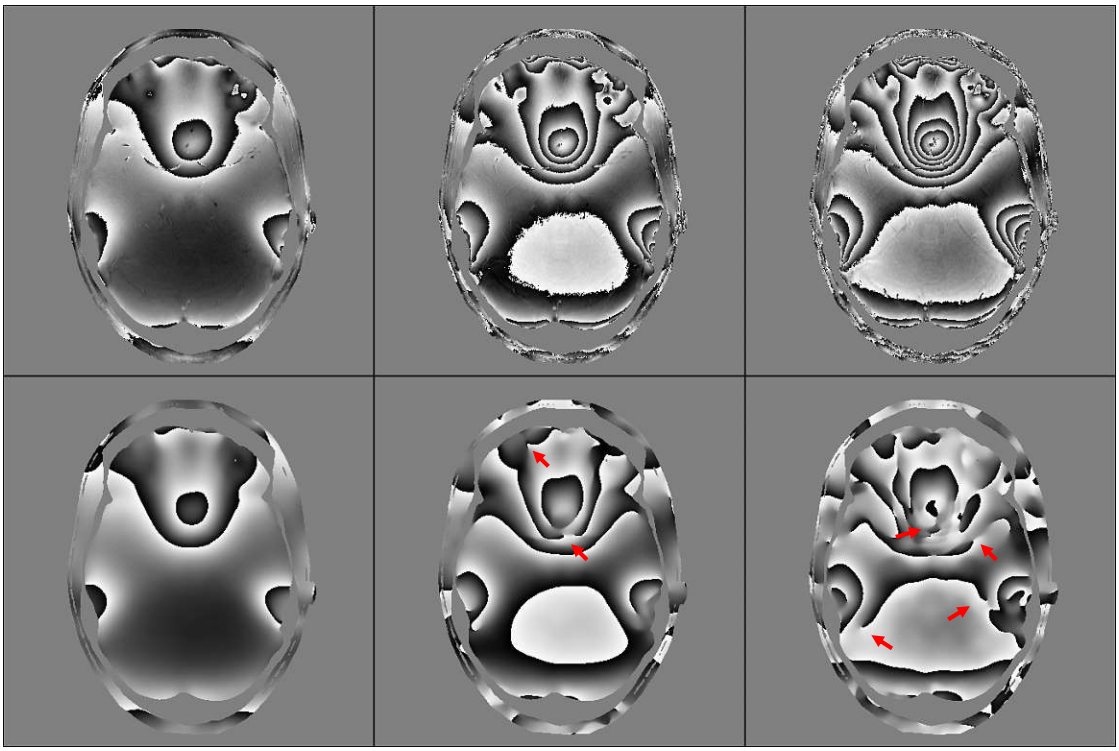

Figure 5.29: Complex smoothing of phase images of a lower slice at 3 different echo times (5 ms (left), 10 ms (middle), and 15 ms (right)); close wraps in the phase image lead to corruption in the smoothed image, which is especially severe for the last echo that contain many closely spaced wraps.

Die approbierte gedruckte Originalversion dieser Dissertation ist an der TU Wien Bibliothek verfügbar.
The approved original version of this doctoral thesis is available in print at TU Wien Bibliothek.
TU WIEN Bibliothek Your knowledge hub

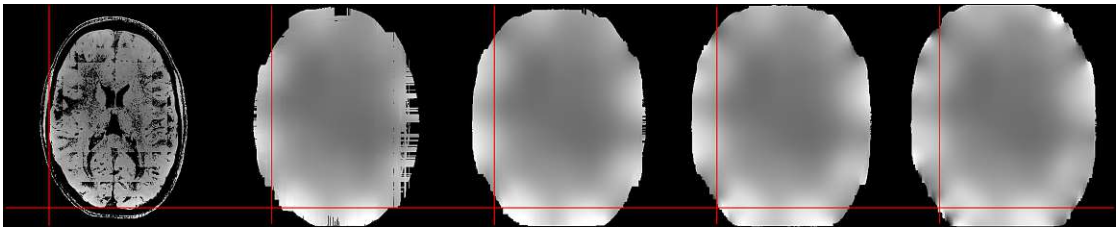

Figure 5.30: Smoothing with a different number of iterations but identical σ; The first image shows the segmented magnitude image with missing values, the next 4 images result from 2,4,6,8 iterations of 3D nangaussian smoothing. An even number of iterations was chosen to avoid large asymmetrical effects, as the direction of the filter is alternated for each iteration. For all four images, no visible problems occur inside the brain (the red lines are shown as reference). With only two iterations, many holes and problematic areas remain close to the brain. With a higher number of iterations (6,8), strong variations occur at the border of the smoothed region.

Smoothing with missing values An example magnitude image with missing values is presented in Figure 5.30. Smoothing with missing values, here called nangaussian smoothing, is performed with a different number of iterations. While for all different number of iterations larger than 2, there are no problems visible inside the brain, the extrapolated area around the brain shows different behavior. With a small number of iterations (2), there are large holes in stripe patterns and even small holes remaining inside the brain. For 8 iterations, the border presents high frequency variations and points to unstable behavior. A number of 4 iterations was deemed optimal.

When comparing with the common division smoothing approach for handling missing values, a different behavior can be observed when encountering regular patterns in the image. Figure 5.31 presents a case in which the magnitude has a regular pattern of missing values (box segmentation step from sensitivity estimation). The division smoothing leads to visible step artefacts stemming from the regular pattern that also translate into the homogeneity corrected image (Figure 5.31, top right). The nangaussian smoothing approach shows no visible artefacts, pointing to an unbiased smoothing regarding to the pattern of the missing values. Note that the step artefacts from box segmentation were caused by the strong inhomogeneity of the magnitude, which is common for high field strength and pronounced in this example due to a slight off center positioning of the head. The exact settings for the comparison method can be found in Section 4.2.1, Comparison with Division Smoothing.

Die approbierte gedruckte Originalversion dieser Dissertation ist an der TU Wien Bibliothek verfügbar.
The approved original version of this doctoral thesis is available in print at TU Wien Bibliothek.
TU WIEN Bibliothek Your knowledge hub

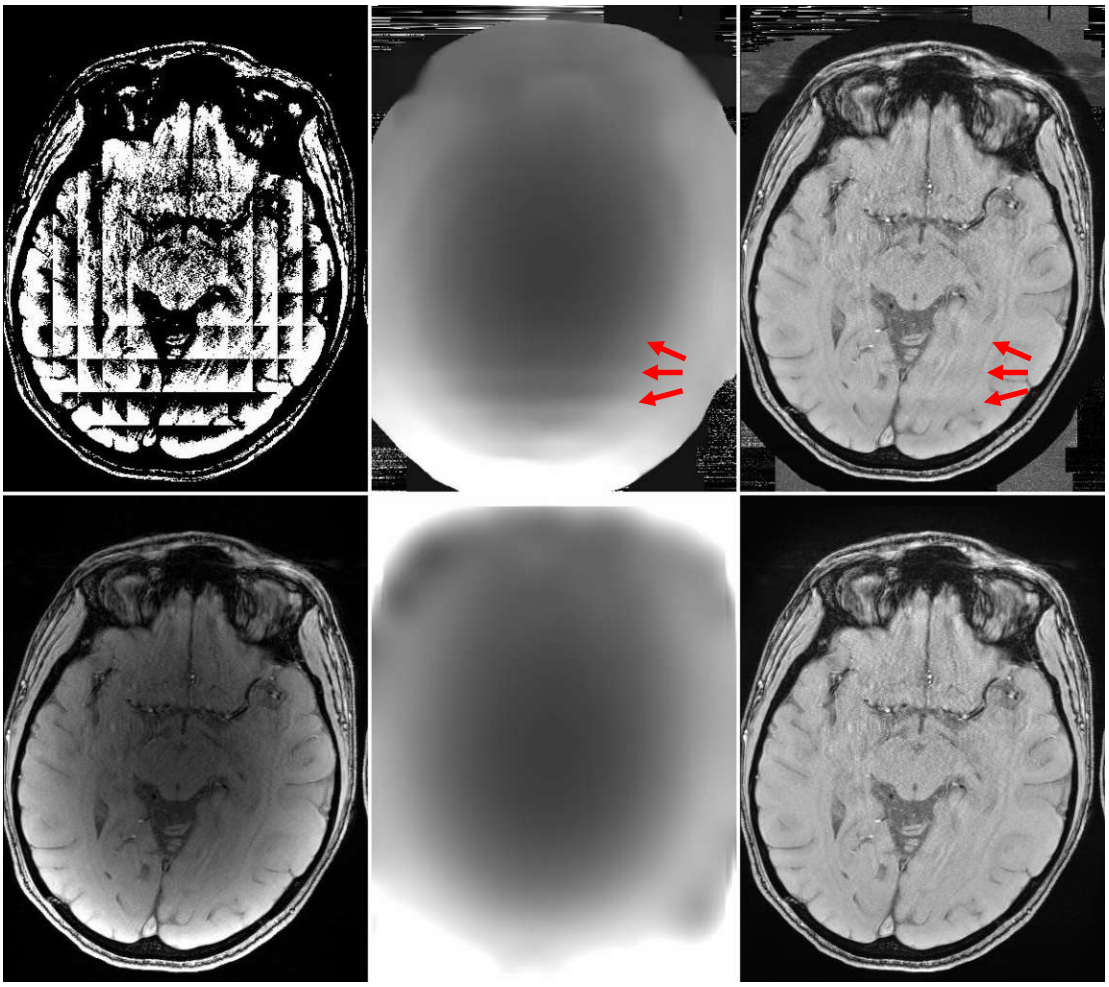

Figure 5.31: Comparison of division smoothing (middle top) with nangaussian smoothing (middle bottom). Masked smoothing was performed with the mask (top left) on the magnitude (bottom left). The mask contained artefacts from box segmentation, which removed too much tissue in a regular pattern. The top right image shows the magnitude divided by the division smoothing image and the bottom right image the magnitude divided by the nangaussian smoothing image. The pattern in the mask causes problems in division smoothing (upper row), leading to step artefacts in the smoothed image (back of the brain) and intensity variations in the homogeneity corrected magnitude. These artefacts were not present for nangaussian smoothing (lower row).

Die approbierte gedruckte Originalversion dieser Dissertation ist an der TU Wien Bibliothek verfügbar.
The approved original version of this doctoral thesis is available in print at TU Wien Bibliothek.
TU WIEN Bibliothek Your knowledge hub

5.4.4 SNR Simulation

The SNR simulations were performed to compare the achievable SNR of 3D multi-echo and single-echo gradient echo acquisitions. The different measurement variables are the TR, the number of echoes, and the polarity - if the echoes were performed with the same polarity of the gradient (monopolar) or with alternating polarity (bipolar). The available time for measurement inside the TR, i.e. the time between the excitation and the spoiler gradient, was exploited to spend the largest possible amount on sampling the signal given the parameter selection (see simulation details in Section 4.2.2). A further restriction was that the echoes were always equally spaced and multiples of the first echo time. If a measurement was not possible for the given restriction and the hardware limits of the gradient system, no data is shown for that TR value. All calculations were normalized to the maximum of the single-echo value.

SNR The calculated SNR depends on the tissue type and was normalized by $\sqrt{T_R}$ – referred to as SNR efficiency – to compare it across a range of different TR values. SNR efficiency values are shown for the three tissue types: white matter (wm), gray matter (gm), and veins (Figure 5.32). In white matter and gray matter the behavior is similar; the single-echo SNR efficiency has its maximum around 25 ms and drops afterwards. With increasing number of echoes in the bipolar case, the maximum of the SNR efficiency increases by about 25% and shifts to longer echo times. The SNR in veins behaves differently and drops rapidly after reaching the maximum, in single-echo at around 12 ms and for more echoes it drops rapidly as well but with increasing echo time. An additional dashed line has been drawn for single-echo, which corresponds to restricting the lowest possible bandwidth to 60 Hz, which is the limitation of the GRE sequence at the 7 T MAGNETOM system. The dashed lines in the multi-echo case represent monopolar acquisitions, which achieve similar SNR efficiency as single-echo, however, at later longer values of TR. In terms of SNR, bipolar acquisitions are superior to monopolar and single-echo if the echo time can be chosen appropriately.

An interesting observation in Figure 5.32 is that the bend in SNR efficiency in the bipolar multi-echo curves is at the same echo time for all tissue types (it is bandwidth and echo spacing related) and is close to the maximum for 5 or more echoes for all tissue types. Resulting from this, the sequence timings to achieve maximum SNR do not depend on the tissue type for equally spaced bipolar multi-echo sequences.

CNR CNR efficiency is defined similarly to SNR efficiency by dividing the CNR by $\sqrt{T_R}$. In the simulation result shown in Figure 5.33, the highest CNR efficiency between white and gray matter is achieved in single-echo, but when limiting the

Die approbierte gedruckte Originalversion dieser Dissertation ist an der TU Wien Bibliothek verfügbar.
The approved original version of this doctoral thesis is available in print at TU Wien Bibliothek.
TU Bibliothek Your knowledge hub WIEN

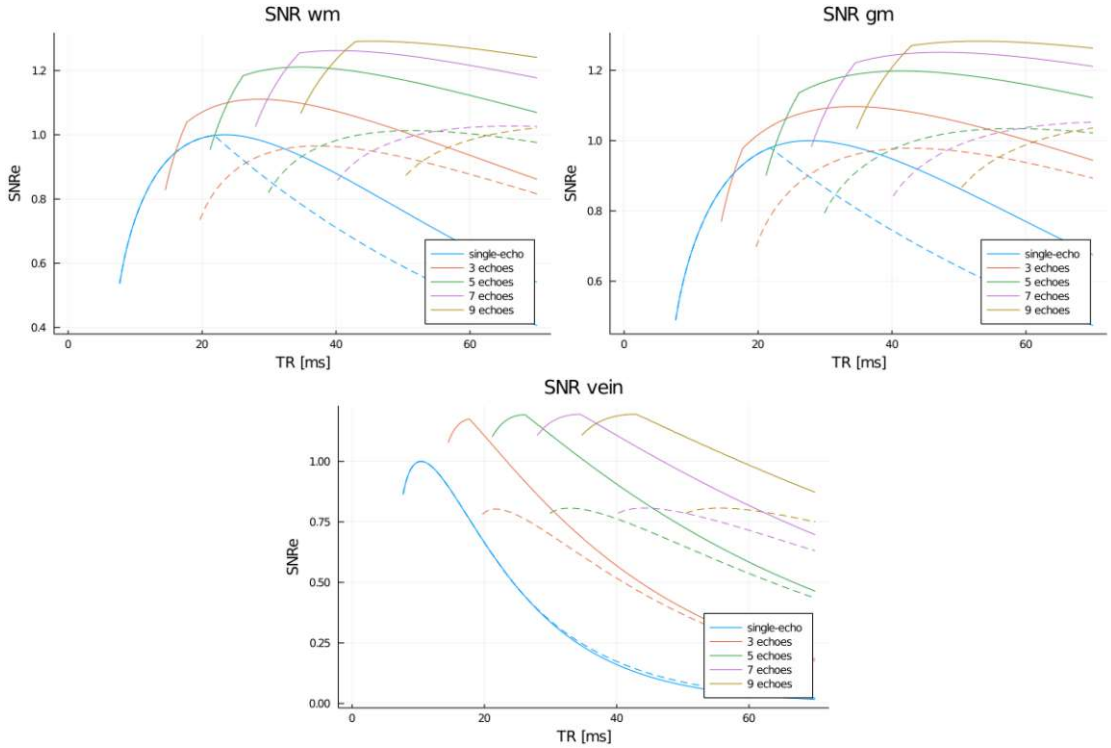

Figure 5.32: Comparison of SNR efficiency for single-echo, monopolar, and bipolar multi-echo scans; For multi-echo, the solid lines correspond to bipolar acquisitions, while the dashed lines correspond to monopolar acquisitions. The blue dashed line is single-echo with the hardware restraint of 60 Hz as lowest allowed bandwidth.

Die approbierte gedruckte Originalversion dieser Dissertation ist an der TU Wien Bibliothek verfügbar.
The approved original version of this doctoral thesis is available in print at TU Wien Bibliothek.
TU Bibliothek Your knowledge hub WIEN

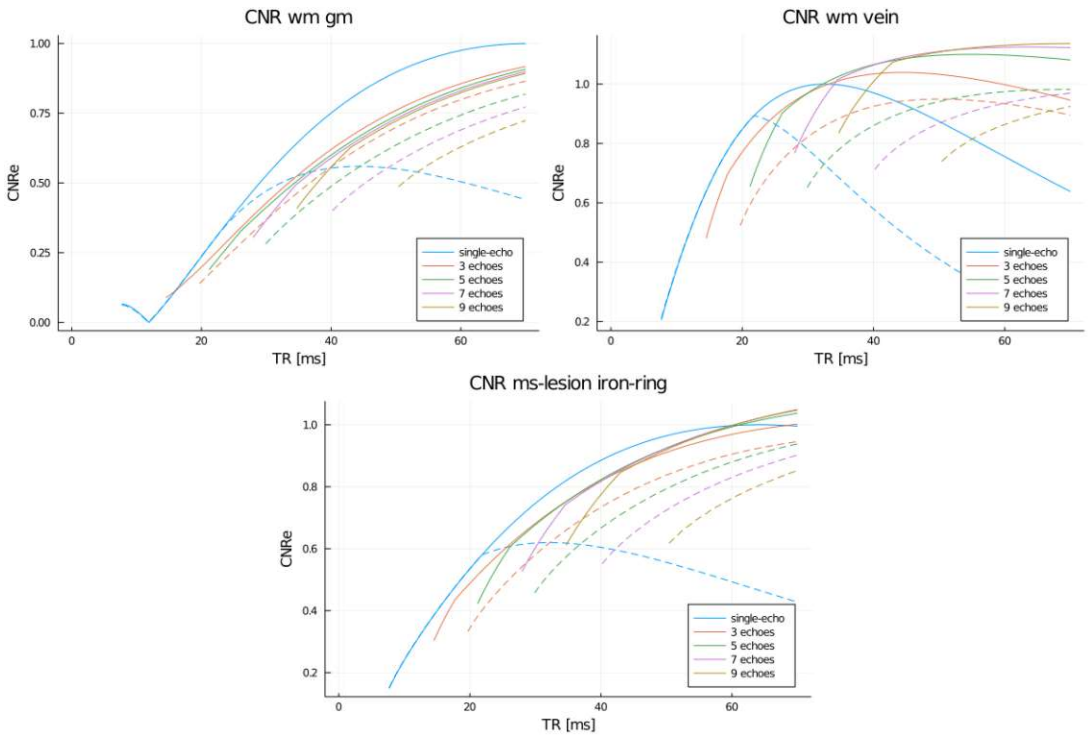

Figure 5.33: Comparison of CNR efficiency for single-echo, monopolar, and bipolar multi-echo scans; For multi-echo, the solid lines correspond to bipolar acquisitions, while the dashed lines correspond to monopolar acquisitions. The blue dashed line is single-echo with the hardware restraint of 60 Hz as lowest allowed bandwidth.

bandwidth to the sequence limit of 60 Hz, the CNR efficiency is only highest up to a TR of about 25 ms. The CNR efficiency between white and gray matter lies close together for all bipolar acquisitions. Single-echo achieves the highest CNR for up to $20 - 25$ ms and for longer TR single-echo suffers from sequence restrictions and bipolar acquisitions achieve higher CNR efficiency.

Phase SNR The simulated SNR efficiency in the phase data is shown in Figure 5.34. The behavior for white matter and gray matter is quite similar, showing that bipolar acquisitions achieve the highest SNR in phase data. Monopolar acquisitions have severely lowered efficiency and single-echo acquisition, when limited by bandwidth restraints, have the lowest phase SNR. For veins, the phase SNR of single-echo scans decreases quickly after a peak at a TR of around 18 ms and bipolar acquisitions are favored, when the number of echoes is chosen accordingly.

Die approbierte gedruckte Originalversion dieser Dissertation ist an der TU Wien Bibliothek verfügbar.
The approved original version of this doctoral thesis is available in print at TU Wien Bibliothek.
TU Bibliothek Your knowledge hub WIEN

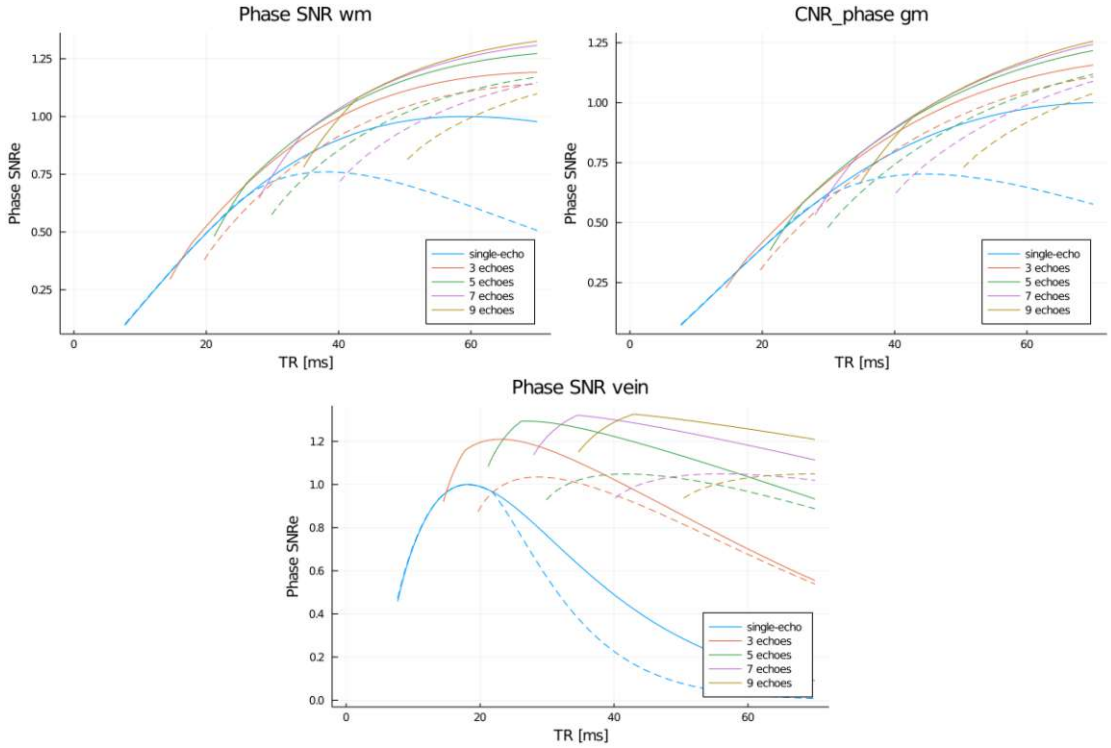

Figure 5.34: Comparison of phase SNR efficiency for single-echo, monopolar, and bipolar multi-echo scans; For multi-echo, the solid lines correspond to bipolar acquisitions, while the dashed lines correspond to monopolar acquisitions. The blue dashed line is single-echo with the hardware restraint of 60 Hz as lowest allowed bandwidth.

Die approbierte gedruckte Originalversion dieser Dissertation ist an der TU Wien Bibliothek verfügbar.
The approved original version of this doctoral thesis is available in print at TU Wien Bibliothek.
TU Bibliothek Your knowledge hub WIEN

Optimal acquisition settings Taking into account all three SNR types and tissues that were presented (with a FOV of 210 mm and 800 pixel in readout direction), the highest SNR for short acquisitions of up to 15 ms is achieved with single-echo acquisitions. For $15 - 20$ ms TR, it depends on the tissue and SNR type, but when veins are of importance bipolar acquisitions should be preferred. For longer echo times, there is a clear advantage of using bipolar acquisitions, and if the number of echoes is adjusted to match the bend in the SNR curves, the SNR values are near to optimal for all tissue types. This can be used to quickly select optimal settings from the presented plots.

SNR of SWI acquisitions The sequence timings from sequences measured for SWI comparisons (Section 4.1.3) were used to simulate the different types of SNR and are shown in Figure 5.35. The symbols represent individual measurement points and the curves represent the simulated optimal timings for all the TRs. For both bipolar acquisitions, the measured sequence is close to the curve, showing that the scan parameters were chosen optimally. For monopolar (green square and green dashed line), the measured sequence is slightly lower than the optimal setting. This is because the optimal bandwidth could not be matched due to the large increment steps available in sequence setup. The first single-echo measurement (TE19.3 BW60) closely matches the corresponding dashed blue line. The second single-echo scan (TE22.5 BW100) has significantly reduced SNR for each type, which is mostly due to the increased bandwidth. When comparing the bipolar NE6 and the single-echo acquisitions, the CNR between white and gray matter is in a similar range, however, the SNR is about twice as high for the bipolar acquisitions and 2-3 times as high for phase SNR in veins.

Comparison with measured SNR Figure 5.36 shows the relative SNR that was estimated between the different acquisitions methods from 150 automatically selected regions (see Section 4.3.1.1). For the multi echo acquisitions, the SNR was estimated on a combined image using root sum of squares combination. The relative SNR was measured from multiple different tissue types but due to the prevalence most were white matter or gray matter. Although the scale is slightly different, the relative SNR behavior closely matches Figure 5.35.

5.4.5 Simulated Single Echo

The two acquisitions NE1 and NE6 from CLEAR-SWI (see Section 4.1.3) were used to evaluate the differences between acquired single-echo data and simulated single-echo data from an acquired multi-echo scan. Ideally, the simulated single echo scan would be identical to the acquired scan in severity and appearance

Die approbierte gedruckte Originalversion dieser Dissertation ist an der TU Wien Bibliothek verfügbar.
The approved original version of this doctoral thesis is available in print at TU Wien Bibliothek.
TU Bibliothek Your knowledge hub WIEN

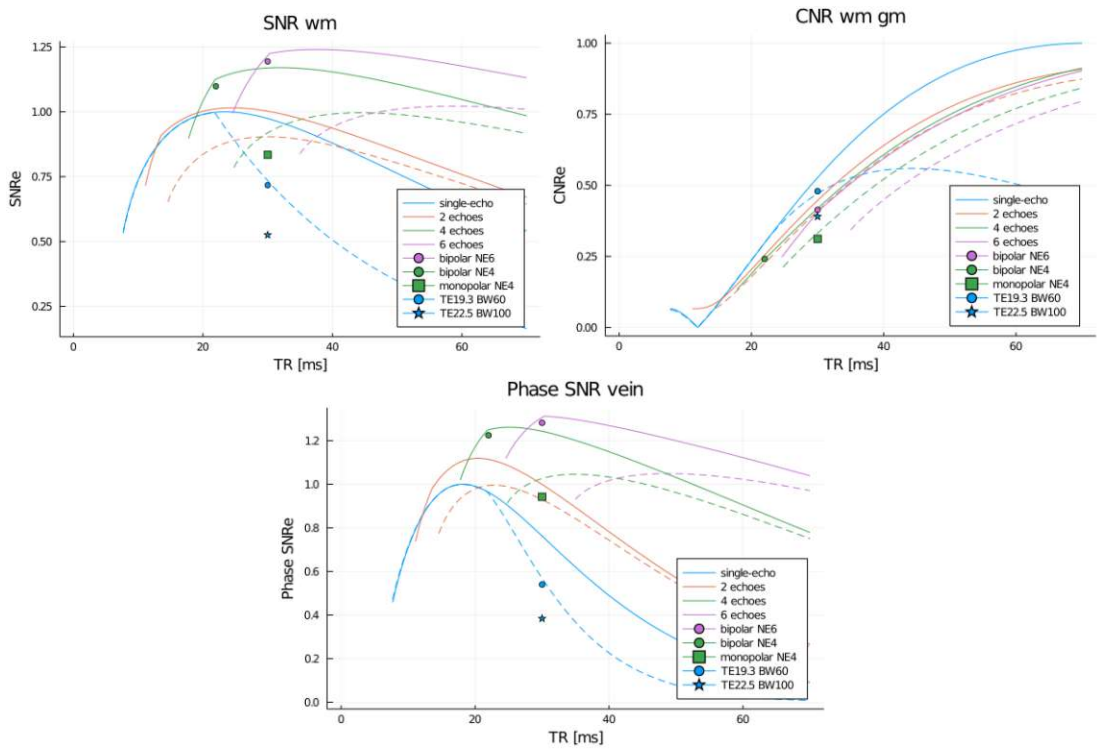

Figure 5.35: Simulated SNR for the performed SWI measurements in comparison with ideal settings. The symbols represent individual measurements performed for the SWI study and the curves represent the simulated measurements with optimal parameters. The main observations are discussed in the corresponding paragraph in the main manuscript.

Die approbierte gedruckte Originalversion dieser Dissertation ist an der TU Wien Bibliothek verfügbar.
The approved original version of this doctoral thesis is available in print at TU Wien Bibliothek.
TU Bibliothek Your knowledge hub WIEN

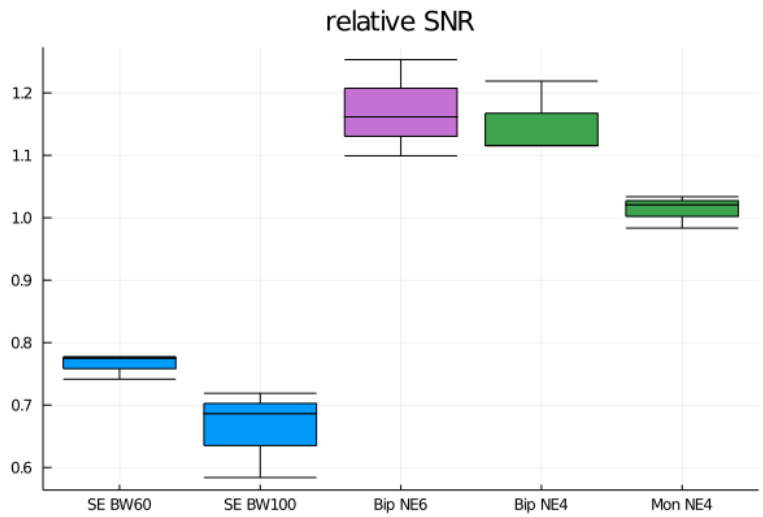

Figure 5.36: Relative SNR estimated from a total of 150 regions in 3 volunteers. The mean SNR of each region over the 5 scans was normalized to 1. The colors are blue - single-echo, purple - 6 echoes and green - 4 echoes. This figure can be viewed in relation with Figure 5.35 and shows similar SNR behavior. The lowest SNR scans are the single echo scans and the highest SNR scans the bipolar scans with similar distances between them.

of artefacts. The top row in Figure 5.37 shows the acquired single-echo data and the bottom row the simulated single-echo data. The blue arrows point to signal dropouts and overbrightening artefacts in the magnitude images, and the appearance of these artefacts is very similar between between the acquired single-echo (top left) and simulated single-echo (bottom left). The middle row presents the homodyne filtered phase, which is provided by the scanner vendor as the phase output of single-echo SWI acquisitions, and which was simulated from the multi-echo data by first calculating the single-echo phase and then performing homodyne filtering. Red arrows point to the major homodyne wrap artefacts, which have similar positioning and severity in both images, however, the appearance is not exactly identical. The right column shows SWI calculated from the magnitude and phase images. The general position and severity of artefacts is similar (red and blue arrows).

A slight difference can be seen in general image quality, with the simulated single-echo (bottom row) having a sharper appearance of tissue interfaces and small structures and reduced noise in the frontal area. However, these differences could be due to movement of the volunteer, as no repeated measurements were performed to evaluate the noise characteristics.

Die approbierte gedruckte Originalversion dieser Dissertation ist an der TU Wien Bibliothek verfügbar.
The approved original version of this doctoral thesis is available in print at TU Wien Bibliothek.
TU Bibliothek Your knowledge hub WIEN

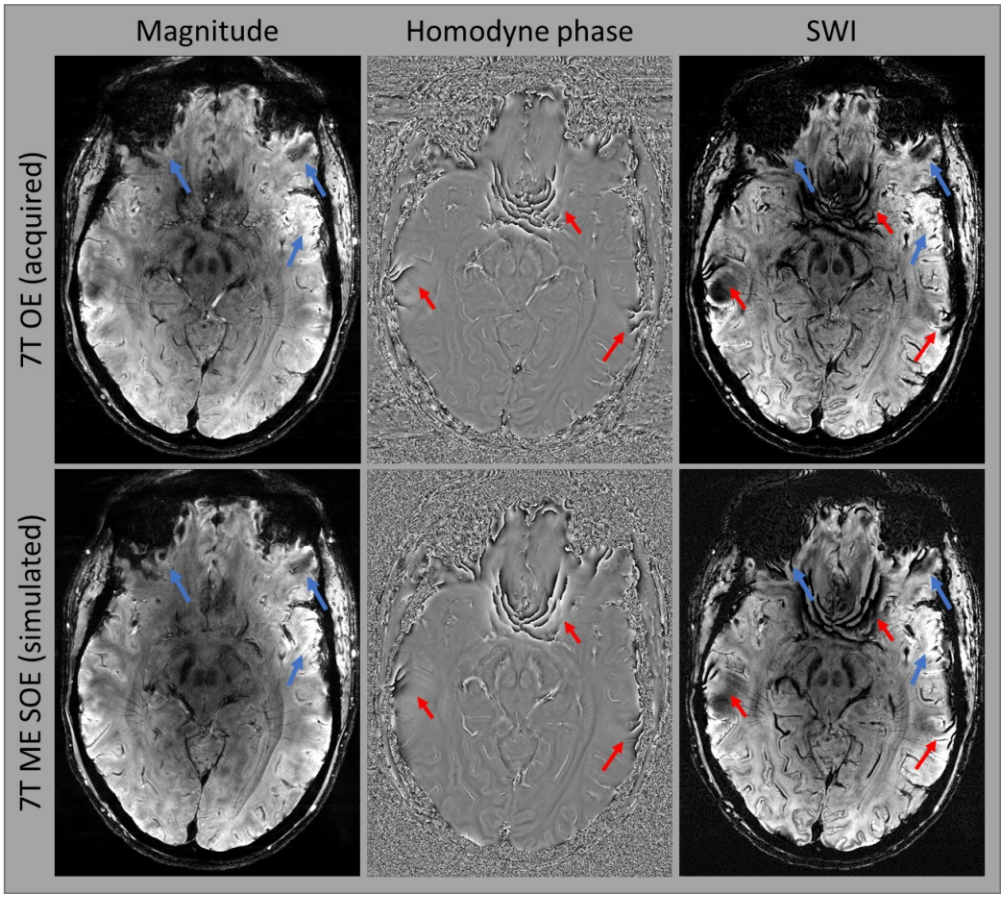

Figure 5.37: Simulated single-echo data from an acquired multi-echo scan; artefacts in the simulated scan (bottom row) resemble those in the single echo scan. Note that the data is from two different measurements and therefore, the slice positioning might not match perfectly.

Die approbierte gedruckte Originalversion dieser Dissertation ist an der TU Wien Bibliothek verfügbar.
The approved original version of this doctoral thesis is available in print at TU Wien Bibliothek.
TU WIEN Bibliothek Your knowledge hub

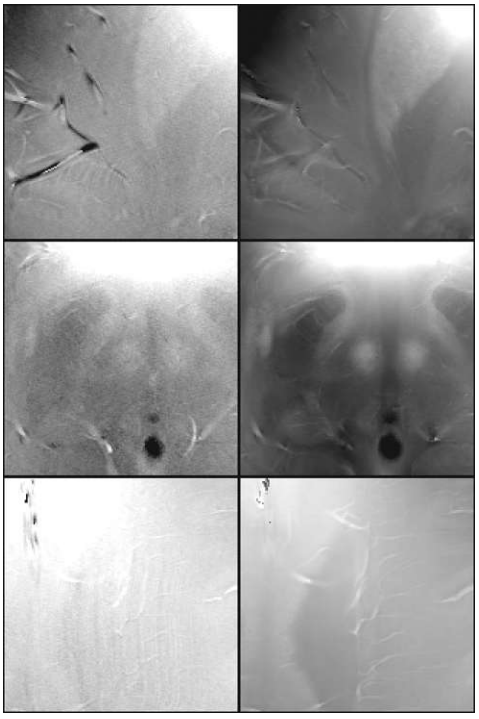

Figure 5.38: Comparison of B_0 maps calculated using the Hermitian inner product (left column) and an improved scheme (Section 3.4.4) incorporating information from all echoes (right column). The range is 0 to 100Hz.

5.4.6 B_0 Calculation

The standard method for B_0 calculation is the Hermitian inner product [71], the angle of which is effectively a phase difference. This difference operation has the advantage that phase offsets are removed and true B_0 is shown. SNR is severely reduced, however. This can be seen in Figure 5.38, where the Hermitian inner product (left column) produces very noisy B_0 maps.

The improved B_0 calculation scheme (Section 3.4.4) utilizes the fact that in ASPIRE combined phase the phase offset is already removed and that after unwrapping, the phase can be combined using noise-optimal weighting factors. This greatly increases the SNR of the phase images (Figure 5.38, right column) and the quality of the depiction of structures like the red nuclei (middle row) and veins (bottom row) are significantly increased. Another aspect is the reduction of artefacts in the improved scheme, as flow artefacts for example are different for different echoes, the effect is reduced after combination (Figure 5.38, black artefacts in veins in top left image). Figure 5.39 presents the similar general appearance of B_0 maps calculated using the Hermitian inner product or all echo information. There is a slight offset towards darker values in the improved scheme, which points to slight non-linear evolution of the phase. Both methods assume that the phase evolves linearly and both are affected by non-linear evolution. It is not quantified which methods provides less biased results.

Die approbierte gedruckte Originalversion dieser Dissertation ist an der TU Wien Bibliothek verfügbar.
The approved original version of this doctoral thesis is available in print at TU Wien Bibliothek.
TU Bibliothek Your knowledge hub WIEN

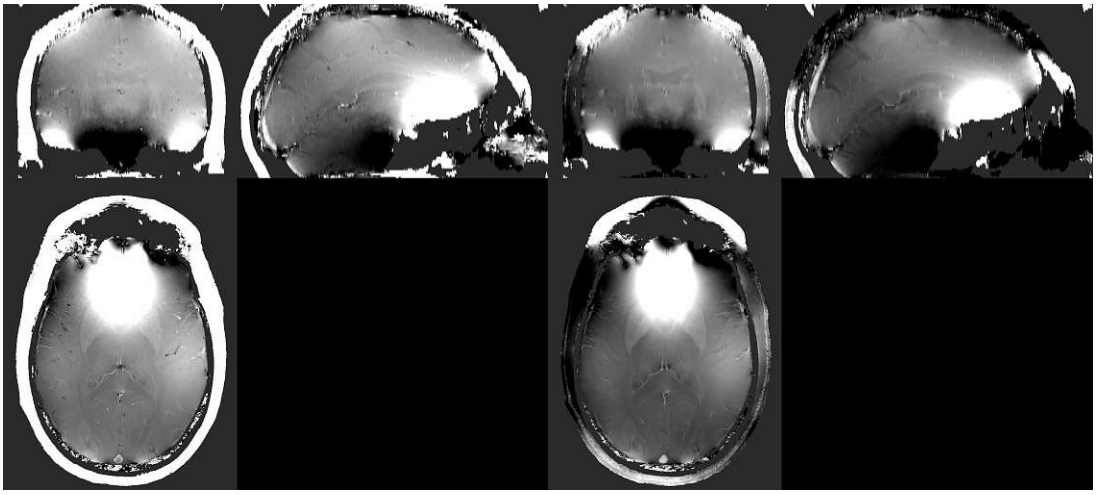

Figure 5.39: Comparison of B_0 maps in triplanar view calculated using the Hermitian inner product (left side) and an improved scheme incorporating the information of all echoes (right side) in triplanar view. The range is -25 to 125Hz

Die approbierte gedruckte Originalversion dieser Dissertation ist an der TU Wien Bibliothek verfügbar.
The approved original version of this doctoral thesis is available in print at TU Wien Bibliothek.
TU WIEN Bibliothek Your knowledge hub

Die approbierte gedruckte Originalversion dieser Dissertation ist an der TU Wien Bibliothek verfügbar.
The approved original version of this doctoral thesis is available in print at TU Wien Bibliothek.

Chapter 6

Discussion

In this thesis, various challenges of imaging susceptibility-based contrast in ultra-high field MRI were discussed and new solutions were presented.

The first problem addressed was the combination of the phase part of complex images from multiple receive coils, which is complicated by the short wavelength of the MR signal at ultra-high field, resulting in signal interference patterns that depend on the individual coil and the object that is measured. The presented solution MCPC-3D-S utilizes the information of multiple echo times to estimate and remove coil-specific phase offset patterns, allowing the combination of the resulting phase-matched images. In a further improvement, ASPIRE, an additional timing constraint to the acquisition leads to a more direct measurement of the phase offset patterns, avoiding the complicated estimation process and leading to a highly robust application.

The next problem that was addressed is phase unwrapping, recovering the "true phase" values from the inherently limited measured phase range of 2π by finding the correct number of multiples of 2π that need to be added to or subtracted from each voxel. The method developed, ROMEO, first creates a map of the connection-quality between neighboring voxels, utilizing the information from the phase, the magnitude and the multi-echo behavior. The unwrapping process is then guided by this quality map, starting with easy to unwrap connections and progressing to the challenging and error prone voxels as last. The resulting unwrapped phase images were shown to be more accurate and less influenced by noisy and corrupted voxels than comparison methods from literature.

The third main topic is the extraction of the susceptibility contrast and its visualization in the context of neuroradiological imaging at ultra-high field. The conventional method of Susceptibility Weighted Imaging suffers from strong artefacts at high field strengths, and to avoid these shortcomings, every step of the algorithm was revisited and replaced with recent solutions from literature and own contributions, resulting in the new processing pipeline called CLEAR-SWI. Em-

Die approbierte gedruckte Originalversion dieser Dissertation ist an der TU Wien Bibliothek verfügbar.
The approved original version of this doctoral thesis is available in print at TU Wien Bibliothek.
TU Bibliothek Your knowledge hub WIEN

phasis was placed on identifying the underlying mechanisms and finding solutions that prevent artefacts while yielding the optimum signal-to-noise ratio.

The discussion comprises subsections for each method, where the findings are compared with findings from literature, the methods are assessed to their generality and the results are put in context to the state of the art. In a final section, the recent impact of the developed methods is presented and the availability of the developed open-source packages is listed.

6.1 Coil Combination

There is a large number of existing methods for coil combination [23], however, the space for phase combination at high field strengths is less explored with no satisfying methods in terms of robustness against artefacts, optimal signal-to-noise ratio and applicability without reference acquisitions or reference coils. The new developments aimed to fill this gap by taking into account the complex nature of the measured signal and the steps that lead to its formation.

The first new method, MCPC-3D-S [42], was based on MCPC-3D [18], but replaces the unwrapping of noisy individual coil images that contain phase singularities with the unwrapping of one combined image with higher SNR and no phase singularities. This greatly improves the robustness and reduces the computation time. The second improvement, ASPIRE [42], incorporates special timing considerations that make it possible to completely avoid unwrapping, resulting in a more robust and faster application. In addition, ASPIRE was applied to knee data, which was not possible with the previous, unwrapping-based methods due to the complexity of the topological structure of the phase created by multiple tissue interfaces with strong susceptibility changes. In previous methods, unwrapping errors lead to severely corrupted phase images, which was completely avoided in ASPIRE, where no phase corruptions could be observed.

Both methods, ASPIRE and MCPC-3D-S, can be used for monopolar and bipolar acquisitions, while bipolar acquisitions require at least 3 echoes and an additional correction step to remove the effect of an odd-even gradient [72]. The trade-off between both developed methods can be seen in the flexibility of choosing the echo times. To avoid unwrapping, ASPIRE requires the first echo time to be equal to the echo spacing between first and second echo. Formulated in a more general way, in the monopolar case, two echoes need to fulfill the condition $(m+1)\,T_{E,j} = mT_{E,k},\ m \in \mathbb{N}$ for two echoes j and k, preferably early echoes where less dephasing is present, while MCPC-3D-S has no echo time restrictions. In the bipolar case, ASPIRE requires the first two echoes to fulfill the above condition and additionally $(T_{E,1}+T_{E,3})/T_{E,2}$ to be an integer, while MCPC-3D-S only requires at least 3 echoes to be acquired. The echo time restrictions for ASPIRE

Die approbierte gedruckte Originalversion dieser Dissertation ist an der TU Wien Bibliothek verfügbar.
The approved original version of this doctoral thesis is available in print at TU Wien Bibliothek.
TU Bibliothek Your knowledge hub WIEN

can generally be fulfilled without degradation of SNR, which was demonstrated in the SNR simulation section. This makes ASPIRE the preferred method and MCPC-3D-S can be used as an alternative if additional echo restrictions have to be fulfilled to be compatible with other methods.

Those phase combination methods can be compared with a range of methods from the literature. Referencing methods require a reference image either acquired in a separate scan (e.g. COMPOSER [73]) or with a different RF coil, referred to as Roemer coil combination [19], both of which lead to a reduction in the quality of phase combination. The disadvantages of using a separate scan are the possibility for motion between the scans, artefacts or differing phase offsets in an often accelerated reference scan and the additional time that is required. Using a reference coil exchanges the phase offsets from the coil array with the phase offsets of the reference coil, however, it adds interference between the coil signals, reducing the signal quality. It works well on low field scanners where volume coils produce a homogeneous image, however, starting at 3 T and getting more severe for higher field strengths, volume coils contain significant phase offsets, and for most ultra-high field (7 T and higher) scanners there are no volume coils available.

The method VRC [50] calculates a virtual reference coil without the need for measuring it, and generally achieves a high combination quality, but arbitrary phase offsets remain in the combined phase and for large objects and ultra-high field strengths, open ended fringe lines start to appear in the virtual reference coil leading to severe corruption of the combined image. Another method that works without an acquired reference is adaptive combine [11], which is implemented as the default algorithm on Siemens scanners. Similarly to VRC, the phase offsets are not fully removed in this method and it is susceptible to open ended fringe lines, which appear more frequently and are more severely than for VRC and can be routinely observed in 7 T brain images. The methods proposed here require a multi-echo acquisition and are based on MCPC-3D [18] and the Hermitian inner product coil combination [17]. Although MCPC-3D in theory yields results of equal combination quality to the proposed methods, it is highly computationally demanding and prone to phase unwrapping artefacts (see the comparison on the knee dataset, Figure 5.2). The Hermitian inner product removes the phase offset completely but is a phase difference method and therefore the SNR is significantly reduced [23].

A limitation of the study presented here is that the improved bipolar correction steps are presented but not evaluated, which is planned to be addressed in future publications. A possible evaluation of the severity of bipolar artefacts can be performed by comparing early echoes that have been scaled to match a late echo time with an acquired late echo [47].

The quality factor of phase matching was shown to be higher and more consis-

Die approbierte gedruckte Originalversion dieser Dissertation ist an der TU Wien Bibliothek verfügbar.
The approved original version of this doctoral thesis is available in print at TU Wien Bibliothek.
TU Bibliothek Your knowledge hub WIEN

tent in ASPIRE and MCPC-3D-S than in the predecessor method MCPC-3D on a brain dataset. Additional comparisons on a more complicated knee dataset showed an even larger improvement of MCPC-3D-S and ASPIRE compared to MCPC-3D, but also some unwrapping problems remained in MCPC-3D, which were resolved only in ASPIRE. Further, the phase offset was completely removed in ASPIRE and MCPC-3D, while the Roemer and VRC methods had large remaining phase offsets. For usage as fieldmaps or for phase-based correction schemes [45], the phase offsets have to be fully removed, which is why usually the Hermitian inner product is used in these cases. The removal of disturbing parts of the phase offsets, called background fields, is a dedicated area of research in quantitative susceptibility mapping [74].

6.2 Phase Unwrapping

Unwrapping of phase images is required whenever the measurements are wrapped into a range of 2π, which occurs in many different fields, e.g. radar technologies [75], interferometric techniques [76] and MRI. Specific to MRI is the fact that additional information is available, such as the magnitude that relates to tissue properties and measurements of multiple echoes, showing different states of the phase evolution.

A new approach to unwrapping, ROMEO, was developed, which incorporates all the available information into connection weights, which are used for finding optimal unwrapping paths through the image. This leads to an increased accuracy compared to BEST PATH [24], which creates a quality map from only a single weight calculated from the spatial phase information around the given voxel. Additionally, the nature of multi-echo acquisitions was taken into account and only one echo is spatially unwrapped, while the remaining echoes are unwrapped using the temporal information in an application of "template-based" unwrapping. The approach of template-based unwrapping is also extended to multi-timepoint data such as functional MRI. This avoids introducing $2\pi n$ phase jumps between neighboring volumes, thus increasing the temporal stability, while significantly speeding up the unwrapping operation, as the weights and quality map are calculated only once for the template volume.

Since it is not possible to measure the "ground truth phase", the underlying property of the phase, directly, phase unwrapping is necessary and this also means that quantitative comparisons of different phase unwrapping algorithms in vivo are very challenging. A temporal reference was calculated by starting with a consensus unwrapped phase of the first echo time and propagating the unwrapped phase to later echo times. The assumption was that phase evolves approximately linearly over time, requiring small echo spacings and the first echo needed to be unwrapped

Die approbierte gedruckte Originalversion dieser Dissertation ist an der TU Wien Bibliothek verfügbar.
The approved original version of this doctoral thesis is available in print at TU Wien Bibliothek.
TU Bibliothek Your knowledge hub WIEN

by all methods without errors, which was only possible with short first echo times that contain very few wraps. With these measures, it was possible to quantitatively evaluate the unwrapping errors of ROMEO, PRELUDE [22] and BEST PATH, showing the percentage of voxels different from the temporal reference (presented in Figure 5.8 and Table 5.1). In contrast to the other methods, the template unwrapping approach taken in ROMEO yielded results that agreed well with this reference phase.

The high unwrapping performance of the newly developed method, ROMEO, was tested on a simulated dataset and a range of datasets acquired at 3 T, 7 T and 9.4 T field strength, and ROMEO showed fewer residual phase wraps than the state of the art methods PRELUDE and BEST PATH in all cases analyzed. On single-echo data, the accuracy of ROMEO was at least comparable and often higher, but the biggest advantage was when ROMEO was applied to multi-echo or multi-timepoint acquisitions, where ROMEO still achieved high unwrapping performance even when the other methods were failing.

For BEST PATH and ROMEO, the unwrapping accuracy was independent of masking, which allows time to be saved that is normally spent on the often fraught problem of mask generation. PRELUDE required a mask for reasonably sized datasets as otherwise the already very long calculation time exceeded tolerable limits, as was shown for the simulated data, for which PRELUDE was not able to produce results in 38 days.

The publication of ROMEO [21] detailed three weights and a fourth one, *phase linearity*, was added in this thesis, improving the performance especially when only a single-echo phase is available. The ROMEO quality maps can be combined and thresholded to produce an object mask, which could be useful in QSM, especially for inhomogeneous images, non-brain regions or pathological cases, where commonly applied methods such as BET [70] do not perform well.

One limitation of the study is that ROMEO has been mainly applied in MRI brain scans, however, the simulated (non-brain) dataset and the significantly improved results compared to state of the art methods point to an applicability in more challenging environments. Due to the flexible selection of weights, ROMEO can be performed with only the phase present and can be applied to problems outside of MRI, however, adding more information (which might also be available outside of MRI) generally results in improved accuracy.

The high accuracy without user intervention and the speed of ROMEO make it feasible to use spatial unwrapping in real time on the MRI reconstruction computer, potentially benefiting large studies with hundreds of phase volumes that require phase-based distortion correction [77] or perform quantitative analysis, extracting information about changes in blood susceptibility in functional QSM [78].

A further improvement of ROMEO to investigate in future is the addition

Die approbierte gedruckte Originalversion dieser Dissertation ist an der TU Wien Bibliothek verfügbar.
The approved original version of this doctoral thesis is available in print at TU Wien Bibliothek.
TU Bibliothek WIEN Your knowledge hub

of Laplacian unwrapping [20] information in the selection of optimal unwrapping paths. This has the potential to combine the benefits of Laplacian unwrapping and ROMEO at the cost of a slight increase in computation time.

6.3 Susceptibility Weighted Imaging

Susceptibility Weighted Imaging [32, 79] is an important tool for diagnosing and characterizing neurological disorders, such as brain tumors [80], vasculature abnormalities [81] and multiple sclerosis [82]. SWI benefits strongly when applied at high field due to the increased resolution and strength of susceptibility effects. However, there are numerous severe problems of SWI at high field: strong phase artefacts, signal dropouts, and inhomogeneous magnitude. Solutions to individual problems are available but are often complicated to apply and a translation into clinics has not taken place.

This thesis presents a new pipeline, called CLEAR-SWI, with the main goal to eliminate high field artefacts but also considering all steps in terms of signal-to-noise ratio and automatic and fast application. This entailed a change to the more efficient bipolar multi-echo acquisition, and ASPIRE coil combination and Laplacian unwrapping were employed together with an optimized high-pass filter to avoid phase artefacts. Further improvements in CLEAR-SWI are the homogeneity correction that estimates the combined transmit and receive fields (B_{1+} and B_{1-} sensitivity), leading to a homogeneous presentation of the resulting image and a softplus scaling function that increases the contrast of the homogeneous magnitude.

CLEAR-SWI was applied to data from 14 Tumor patients at a field strength of 7 T. CLEAR-SWI avoided homodyne artefacts, reduced the severity of signal dropouts, increased the SNR and presented an homogeneous image, all in contrast to the standard SWI processing. This shows the potential for use in clinical imaging, resembling a more robust SWI with reduced artefacts compared to standard SWI, and the additional T_2^* and M_0 maps were provided due to the multi-echo nature of the acquisition.

In an assessment of general applicability, CLEAR-SWI was tested in a pilot study at the lower field strength of 3 T and with a multiple sclerosis patient. It was mainly developed for brain imaging but application to other body parts might be an interesting consideration, as artefacts arising from tissues with heterogeneous susceptibilities are considerably reduced compared to standard SWI. Interesting body parts are liver [83] or kidney[84] due to the challenge of large vessels and heterogeneous surrounding tissue, and cartilage [85], which benefits from high SNR and high field strengths.

Coil combination plays a crucial part in CLEAR-SWI, because it can be a large source of phase artefacts and of reduction in CNR. To perform robust coil

Die approbierte gedruckte Originalversion dieser Dissertation ist an der TU Wien Bibliothek verfügbar.
The approved original version of this doctoral thesis is available in print at TU Wien Bibliothek.
TU Bibliothek Your knowledge hub WIEN

combination with high SNR, the multi-echo coil combination ASPIRE [42] was chosen. Methods from literature are GEPCI [27], which effectively calculates phase differences leading to reduced CNR; homodyne filter and combination [86], which is prone to wrap-like artefacts; the Roemer coil combination that requires a reference coil [19]; the adaptive combine method, which does not perform well at high field strengths [11]; or the VRC method [50], which is currently not robust enough for online application. ASPIRE generated combined phase images with optimal CNR and no singularities, independent of field strength and coil configuration. The requirement for ASPIRE is a simple echo time relation that needs to be fulfilled in acquisition. If this is not possible due to restrictions from other analysis methods, the closely related method MCPC-3D-S [42] is an alternative, which is not subject to the timing restrictions but requires the unwrapping of one 3D volume.

Homodyne phase artefacts are common in high field applications of SWI and pose possibilities for misdiagnosis [49]. A complex region-growing unwrapping has been proposed as a phase processing step before high-pass filtering to avoid these problems [87]. Problems of this approach are the very long computation time for larger matrix sizes, and the difficulty of unwrapping regions with low SNR or fast phase changes, which are commonly present at later echo times or higher field strengths. As an alternative to region-growing unwrapping, Laplacian unwrapping was proposed for SWI [88]. Laplacian unwrapping is also the method of choice for CLEAR-SWI and was demonstrated to provide effective unwrapping even in the inferior brain, close to bone-air interfaces. Laplacian unwrapping is inherently very robust, even in corrupted image regions, but disadvantages are a potential reduction of contrast around strong phase changes (Supporting Material of Reference [21]) and the addition of an arbitrary background field. The arbitrary background field has two disadvantages; it increases the runtime of CLEAR-SWI by requiring the unwrapped phase of each echo to be high-pass filtered before combination, and the unwrapped phase does not correspond to the underlying B_0 field, requiring a separate phase reconstruction if a quantitative susceptibility map is calculated from the same scan. Both problems can be solved when employing ROMEO as unwrapping algorithm but the potential disadvantage is a reduced accuracy in strongly corrupted phase areas, which can already occur for normal veins at late echo times.

To integrate the available phase information from all echoes, CLEAR-SWI uses inverse-variance-weighted combination of the Laplacian-unwrapped and high-pass filtered phase. Similar to the weighted B_0 frequency combination [16], this maximizes the SNR, but also avoids the error-prone and computationally demanding quantitative (region-growing or path-based) unwrapping for B_0 estimation. Another approach is mono-exponential fitting [27], which is inferior in terms of SNR and incurs an excessive computational cost.

Die approbierte gedruckte Originalversion dieser Dissertation ist an der TU Wien Bibliothek verfügbar.
The approved original version of this doctoral thesis is available in print at TU Wien Bibliothek.
TU Bibliothek Your knowledge hub WIEN

The creation of the SWI phase mask in classical SWI is performed by multiplying the magnitude a number of times by the scaled phase [32, 79], resulting in a function of the phase of the degree of the number of multiplication. This function is very steep for small phase values, greatly amplifying the phase noise. In CLEAR-SWI the phase mask was created by a sigmoidal function (tanh), reducing the noise contributions of the phase and thus improving the visibility of small structures, e.g. veins and iron rings. A piecewise-defined cosine function, where all negative phase values were set to 1 and the positive phase part was scaled by the sigmoidal part from 1 to 0 has been applied to a similar effect [16]. In CLEAR-SWI, however, the phase scaling uses the tanh function, which is defined over the whole range and tends to look more natural, as negative phase values still have a slight influence.

The magnitude multi-echo combination of CLEAR-SWI can optimize the SNR or be adapted to specific use cases by optimizing the CNR between two tissue types. To optimize the SNR, the RSOS combination over echoes can be used [9]. It minimizes signal dropouts in areas of high B_0 variation and therefore is suggested option for imaging tissue and veins close to the base of the skull [89]. Another option is to optimize the CNR between specific tissues or regions of interest by using literature values or measured values for tissue relaxation times. This should provide the highest CNR in theory, however, in performed measurements only a small advantage could be detected against RSOS combination, which might not justify the additional complexity. As the contrast in multi-echo combined magnitude appears weaker than in standard single-echo SWI acquisitions with a long echo time, an additional step of softplus scaling after the magnitude combination and homogeneity correction was explored in CLEAR-SWI. This produced a magnitude contrast that was similar in strength to single-echo SWI, but in which images retained the multi-echo advantages of an increased SNR and reduced signal dropouts.

The homogeneity correction that is applied in CLEAR-SWI facilitates the visual assessment by reducing the need to window each region under examination. Alternative methods for correcting homogeneity are either not sufficiently robust, require manual intervention or are computationally demanding [90, 91, 92]. The homogeneity correction (see Chapter 3.4.2, Sensitivity Estimation) robustly removed the strong bias at 3 T and 7 T and was not compromised by the presence of large hypo- or hyper-intense brain tumors.

Other advanced SWI methods, with similar goals of avoiding homodyne phase artefacts and incorporating multi-echo information, have been proposed. One solution first calculates a single-echo SWI from the second echo and replaces corrupted parts with a fitted magnitude and the first echo phase [88]. This solution might solve problems of artefacts, but it is obvious that this approach cannot benefit from

Die approbierte gedruckte Originalversion dieser Dissertation ist an der TU Wien Bibliothek verfügbar.
The approved original version of this doctoral thesis is available in print at TU Wien Bibliothek.
TU Bibliothek Your knowledge hub WIEN

the improved signal-to-noise ratio available from multi-echo acquisitions. The dual echo approach is also restricting the choice of echo times and limits the usability of the acquired data for other reconstruction schemes, such as QSM or T_2^* fitting. The methods GEPCI [27] and the SWI described by Quinn et al. [16] use the multi-echo information fully. The method of Quinn et al. is focused on phase processing, where it proposes weighted echo combination of the phase and introduces a non-linear phase masking function. It was devised for an application at a field strength of 3 T and at 7 T, severe phase artefacts were present. GEPCI is based on voxelwise complex fitting to estimate the underlying tissue parameters and reconstruct a simulated SWI acquisition from it. This process is, however, inferior in terms of SNR, computationally highly demanding, and instabilities arose in the complex fitting step at ultra-high field application (see [44], Appendix E).

Standard SWI processing uses homodyne filtering for phase combination, removing the possibility to use the same measurement for other advanced processing schemes such as QSM. In CLEAR-SWI, the use of ASPIRE coil combination produces combined phase images that are wrapped, scaled B_0 maps. As all essential phase information is still present and no corrupting influences from phase offsets or arbitrary background fields are present, the phase images acquired for SWI can be additionally used for any phase-based method, such as QSM [34], field mapping or distortion correction [71].

In a clinical assessment of brain tumor cases, CLEAR-SWI was able to depict the complex structure of veins, edema and necrotic tissue without artefacts, which assists in determining the type and grade of tumors [80, 93, 94]. In standard SWI, in contrast, the strong phase variations close to the pathologies led to phase artefacts in most and poor signal in some tumor cases. The T_2^* map, which is available with CLEAR-SWI, provided additional information about the state of abnormal tissue surrounding the tumor. The M_0 image, which depends on the proton density and the T_1 constant of the tissue, showed some intensity variation for abnormal tissue and additionally very distinctly showed cerebrospinal fluid. The appearance was similar to T_1-weighted FLAIR images, although the contrast was weaker.

CLEAR-SWI was mainly investigated at a field strength of 7 T, but all it can be identically applied at lower field strengths since the inhomogeneities in the B_0 and B_1 fields are less pronounced at lower field strengths. With higher field strengths, an adaption of the high-pass filtering might be necessary to avoid phase problems. A pilot measurement at 3 Tshowed an improvement in SNR and vein appearance of CLEAR-SWI against standard SWI (Figure 5.22).

Large parts of the CLEAR-SWI pipeline can be applied to single-echo acquisitions, such as magnitude homogeneity correction and non-linear scaling, and phase unwrapping, high-pass filtering and sigmoidal masking. The coil combination in

Die approbierte gedruckte Originalversion dieser Dissertation ist an der TU Wien Bibliothek verfügbar.
The approved original version of this doctoral thesis is available in print at TU Wien Bibliothek.
TU Bibliothek Your knowledge hub WIEN

the single-echo case is more problematic, however, as ASPIRE coil combination requires a multi-echo scan. Possible solutions are the acquisition of a prescan with a very short echo time to perform COMPOSER [73], a dual-echo prescan for ASPIRE phase offset determination [42, 18], or to use the reference-free method VRC [50], which works for brain imaging at 7 T in most cases. A comparison of standard SWI and CLEAR-SWI on single-echo data was performed for the publication (see [44], Appendix F).

In the CLEAR-SWI pipeline, an additional image that might be of interest for exploring the vasculature is the filtered phase alone, as veins are well represented with a natural appearance.

6.4 Supporting Methods

A collection of smaller methods were developed as steps of the main methods: a simple and robust masking scheme that is applied within ROMEO and CLEAR-SWI; sensitivity estimation of the coils (joint B_{1+} and B_{1-} field) for CLEAR-SWI; Gaussian smoothing with the option of weighted and masked smoothing for magnitude and phase applied in ASPIRE and CLEAR-SWI; a signal-to-noise estimation framework applied in CLEAR-SWI for contrast weighting and sequence setup; a simulated single-echo acquisition (from an acquired multi-echo acquisition) for CLEAR-SWI evaluation and compatibility in longitudinal studies; a B_0 calculation approach for multi-echo data.

Although these methods were primarily developed as parts of the main methods, they can be applied as individual methods and this section provides additional considerations for their application.

Masking The automatic masking that is presented is simple and fast and needs no user intervention, as opposed to commonly applied methods, which require manual input of parameters like the BET brain masking tool [70] or the Hybrid Watershed Algorithm [95]. A further difference is that the automatically obtained mask does not remove the skull, which was not required for the methods presented in this study. As the masking approach only identified a threshold, the mask is not always clean, removing some very low intensity voxels inside the brain and keeping some high intensity voxels outside of the object. If these are of concern, an additional morphological filtering step can be applied, *closing* to fill holes without changing the size of the mask, *opening* to remove remaining noise outside the object or *erosion* and *dilation*, if a change in the size of the mask is desired.

Sensitivity Estimation The simplistic idea behind the developed sensitivity estimation is to perform high-pass filtering on the magnitude, which would be

Die approbierte gedruckte Originalversion dieser Dissertation ist an der TU Wien Bibliothek verfügbar.
The approved original version of this doctoral thesis is available in print at TU Wien Bibliothek.
TU Bibliothek Your knowledge hub WIEN

possible in the ideal case of only one tissue present. An application to real data would lead to overbrightening and darkening around darker and brighter tissues, respectively. A first step of tissue segmentation for white matter and then interpolation of the holes is performed to avoid these problems for estimating a bias field. The simple segmentation process only needs to exclude tissues that have strongly different signal. as the inclusion of voxels of similar intensity to white matter has only a minor influence on the resulting bias field. As the segmentation might produce straight borders or regular patterns of holes, the interpolation process needs to be unbiased regarding the shape of the segmentation, which required an investigation and development of a smoothing method for missing values. In general, the sensitivity estimation process described here requires that one tissue type is present over the whole object and that it's intensity can easily be detected. This is the case for white matter in gradient echo and MPRAGE brain scans, but might not be easily applicable for other body parts. Also in very large pathological areas the process might be problematic, however, in the application on 14 tumor datasets for the CLEAR-SWI study no problems could be observed.

Gaussian Smoothing Smoothing of magnitude and phase images is a task often performed in MRI methods and benefits from a fast implementation. Options of weighted smoothing and smoothing with missing values were investigated and a new interpolating and extrapolating approach for missing values that does not cause bias effects was developed.

The smoothing with missing values was applied with simulations and real datasets and showed no bias effect. The extrapolation capability is limited to a few voxels, however, depending on the chosen standard deviation and the number of boxes.

As smoothing is applied to the phase offset of every coil in ASPIRE, a short runtime is crucial. Runtime comparisons have not been performed in a rigorous manner due to several complicating effects, however. The runtime depends on a number of variables, the size of the standard deviation and the number of boxes in the newly developed approach, as well as the kernel size in the traditional approach. In both cases these parameters relate to a trade-off between precision and runtime. An additional consideration is the choice of a reference algorithm for time comparison. The default Julia implementation automatically decides between the application as a spatial filter or an application in the Fourier domain, applies hardware accelerations of vectorized code (simd) and multi-threading. Nevertheless, in simple comparisons for applications of 3D Gaussian smoothing for MRI datasets, the presented boxsmoothing approach was about 2-5x faster than the Julia library version of smoothing with a Gaussian filter. The application with missing values has a negative runtime impact of about a factor of 2.

Die approbierte gedruckte Originalversion dieser Dissertation ist an der TU Wien Bibliothek verfügbar.
The approved original version of this doctoral thesis is available in print at TU Wien Bibliothek.
TU Bibliothek WIEN Your knowledge hub

Signal-to-Noise Ratio Simulation The SNR and CNR simulations present the different achievable values for multiple acquisition types and show that generally bipolar multi-echo acquisitions are superior to monopolar and single-echo acquisitions and that bipolar acquisitions can achieve approximately 50% higher SNR than single-echo sequences for SWI applications. The SNR and CNR simulations were performed for the three tissue types, white matter, gray matter, and veins and were also used to identify the optimal number of echoes and the respective echo times to achieve the highest SNR efficiency.

A surprising aspect of the CNR simulation was that the CNR between white and gray matter was higher with single-echo acquisitions than was achievable with a multi-echo acquisition. The cause can probably be found in Equation 2.54 and is due to an additional attenuation effect for lower T_2^* values that is present for echoes with long acquisition windows, effectively leading to stronger T_2^* contrast under certain conditions. When taking into account a lower limit for the receiver bandwidth of 60 Hz/px, this single-echo advantage is limited to a regime of short repetition times and not of practical importance for SWI.

Simulated Single-Echo A single-echo scan could be successfully simulated from a multi-echo acquisition. The signal dropouts and contrast appearance closely resembled the true single-echo acquisition and for an application of standard SWI, identical homodyne artefacts and SWI appearance was created. The main reason for simulated single-echo was the evaluation of the artefact reduction of CLEAR-SWI, but an additional use case is when a multi-echo acquisition is performed for CLEAR-SWI, for example, and a standard SWI is also needed for compatibility with a longitudinal study.

B_0 Calculation Common approaches to B_0 calculation, such as the Hermitian inner product, require the calculation of phase differences to remove the phase offsets, which significantly lowers the SNR. The approach discussed here uses the fact that phase offsets are already removed in ASPIRE or MCPC-3D-S combined phase, meaning that the individual echoes already represent wrapped B_0 maps. After unwrapping with ROMEO, which is especially suited for this task due to the high temporal stability, they are combined using optimal weighting factors obtained from the magnitude.

This new approach to B_0 combination yields high SNR B_0 maps but one limitation of the presentation in this thesis is the limited evaluation and comparison with methods from literature.

Die approbierte gedruckte Originalversion dieser Dissertation ist an der TU Wien Bibliothek verfügbar.
The approved original version of this doctoral thesis is available in print at TU Wien Bibliothek.
TU Bibliothek Your knowledge hub WIEN

6.5 Impact and Code Availability

Susceptibility-based MRI methods were originally conceived to yield contrast differences in brain images at field strengths up to 3 T. Due to the success of SWI in imaging the vascularity in the brain and detecting iron and calcium deposits, its application has spread to higher field strengths, where increased resolution and contrast can be used and recent methods have started to investigate application to a larger range of body parts. These new applications require robust solutions to handle situations of inhomogeneous B_0 fields, and also to estimate and remove B_1 inhomogeneities even in complex tissues. Another direction of susceptibility imaging is to produce quantitative results, as in QSM, which can identify elevated iron levels or other tissue abnormalities that often accompany neurological disorders.

The methods developed in this thesis primarily target the challenging aspects of phase processing, which directly improves the quality and robustness of current phase-based methods and also contributes to the direction in which susceptibility imaging is heading. ASPIRE makes it possible to acquire phase without singularities and arbitrary background fields in complex environments and at high field strengths, which was previously only possible with phase difference methods with very poor SNR. ROMEO reconstructs the true phase from the measured phase that is wrapped into a 2π range and outperforms the currently used tools in accuracy and speed, while additionally making it possible to unwrap late echoes in a multi-echo sequence, which are highly wrapped but contain valuable contrast. CLEAR-SWI addresses problems arising from ultra-high field strength, complicated topologies such as large tumors and makes it possible to use highly efficient multi-echo sequences. The increased robustness of the individual steps against artefacts in areas of fast phase changes reduces the problems when applying its processing steps to other body parts. The use of a multi-echo sequence and ASPIRE coil combination makes it possible to perform CLEAR-SWI, QSM, T_2^* or a range of other methods on the same acquired dataset, which was not possible with traditional SWI acquisitions. The new methods were all developed with a view towards clinical application, which requires, besides a robust and automatic processing, real-time calculation of large datasets, easing the transitional into clinics.

ASPIRE was implemented in C++ and the vendor's image reconstruction environment ICE to run directly on the scanner reconstruction computer and has seen widespread adoption in the ultra high-field research community, where it is currently applied at 32 of the approximately 90 ultra-high field MRI sites worldwide. The scientific article describing ASPIRE has been cited 44 times since its publication in 2018.

ROMEO was selected as Editor's pick in April 2021[1] and was awarded with

[1] https://onlinelibrary.wiley.com/page/journal/15222594/homepage/editor_s_picks.htm

Die approbierte gedruckte Originalversion dieser Dissertation ist an der TU Wien Bibliothek verfügbar.
The approved original version of this doctoral thesis is available in print at TU Wien Bibliothek.
TU Bibliothek Your knowledge hub WIEN

a highlight article for reproducible research[2] in the journal Magnetic Resonance in Medicine. The quality map generation of ROMEO is in use by the new QSM processing framework QSMxT to produce a phase-based mask [96] and currently, ROMEO is in the process of being integrated into the primary QSM meta-toolbox, SEPIA.

CLEAR-SWI generated interest by the community and the open source code already received 10 stars (starred as favorite) on github[3]. For increasing applicability, it will be distributed together with ASPIRE in the next release to be directly usable on MR scanners.

Code Availability To facilitate easy reproduction and application of the developed methods, effort has been taken to make them publicly available. For most methods, the source code is freely available and for some tools additional compiled versions were generated for easy applicability.

The discussed methods have been partly implemented in Julia, MATLAB and C++. The Julia implementations are available on github, while the MATLAB code is partly made available and the C++ code is not publicly available. Some C++ implementations were directly created as Functors for the Siemens MRI reconstruction framework ICE. Table 6.1 shows which discussed method has been implemented in which language and a footnote with a link to the repository is provided if it is publicly available.

[2]https://blog.ismrm.org/2021/03/26/reproducible-research-insights-with-barbara-dymerska-korbinian-eckstein-and-simon-robinson/

[3]https://github.com/korbinian90/CLEARSWI.jl

Die approbierte gedruckte Originalversion dieser Dissertation ist an der TU Wien Bibliothek verfügbar.
The approved original version of this doctoral thesis is available in print at TU Wien Bibliothek.
TU Bibliothek Your knowledge hub WIEN

Table 6.1: Availability of Code in the different programming languages. CMD stands for command line application.

Tool	Julia	MATLAB	C++	CMD
Automatic Masking	github[4]	implemented		
Sensitivity Estimation	github[4]	implemented		
Gaussian Smoothing	github[4]	github[5]	implemented	
SNR Simulation	github[6]			
Simulated Single Echo	github[7]			
B_0 calculation	github[4]			github[8]
MCPC-3D-S	github[4]	github[5]	ICE	github[8]
ASPIRE		github[5]	ICE	
ROMEO	github[9]		implemented	github[8]
CLEAR-SWI	github[7]	partly github	partly ICE	github[10]

[4]https://github.com/korbinian90/MriResearchTools.jl
[5]https://github.com/korbinian90/ASPIRE
[6]https://github.com/korbinian90/MriResearchTools.jl/tree/clearswi_publication
[7]https://github.com/korbinian90/CLEARSWI.jl
[8]https://github.com/korbinian90/ROMEO
[9]https://github.com/korbinian90/ROMEO.jl
[10]https://github.com/korbinian90/ClearswiApp.jl

Die approbierte gedruckte Originalversion dieser Dissertation ist an der TU Wien Bibliothek verfügbar.
The approved original version of this doctoral thesis is available in print at TU Wien Bibliothek.
TU Bibliothek Your knowledge hub WIEN

Die approbierte gedruckte Originalversion dieser Dissertation ist an der TU Wien Bibliothek verfügbar.
The approved original version of this doctoral thesis is available in print at TU Wien Bibliothek.

Chapter 7

Conclusion

Three topics with the focus on phase imaging at ultra-high field strengths were investigated and new solutions proposed: an improved framework for coil combination with the two methods ASPIRE and MCPC-3D-S, a new phase unwrapping approach, ROMEO, and a reworked pipeline for susceptibility weighted imaging, CLEAR-SWI.

Both coil combination methods ASPIRE and MCPC-3D-S solve the problem of low combination quality and open-ended fringe lines which are common problems at ultra-high fields. They are applicable without reference coils and only require a multi-echo sequence, which is either the sequence itself or a reference acquisition. Both methods successfully removed the phase offsets in the combined phase and achieved high combination quality. ASPIRE additionally requires a simple echo time condition and when satisfied a major part of the calculation can be simplified, significantly reducing the computation time and further increasing the robustness.

The new phase unwrapping method ROMEO is a faster and more accurate alternative to common unwrapping methods such as PRELUDE and BEST-PATH. The possibility to incorporate information from multiple echoes or timepoints in a combination of region growing and template based unwrapping led to its high accuracy and high temporal stability.

The third project involved the complete reworking of every step of the pipeline for Susceptibility Weighted Imaging in the context of clinical ultra-high field imaging, and resulted in the significantly improved method CLEAR-SWI. It employs ASPIRE coil combination, phase unwrapping, a newly developed homogeneity correction approach and other steps to improve contrast and signal-to-noise ratio. Each step from acquisition to the final display of the image was evaluated and improved with recently published methods or own contributions. Severe artefacts that are present in standard SWI, like homodyne wrap artefacts, signal-dropouts and inhomogeneous magnitude were avoided and the signal-to-noise ratio was significantly increased. An additional benefit of CLEAR-SWI was achieved by

Die approbierte gedruckte Originalversion dieser Dissertation ist an der TU Wien Bibliothek verfügbar.
The approved original version of this doctoral thesis is available in print at TU Wien Bibliothek.
TU Bibliothek Your knowledge hub WIEN

replacing the standard single-echo sequence with a multi-echo acquisition from which additional quantitative T_2^* maps and quantitative susceptibility maps can be calculated.

In summary, the developed approaches solve problems arising from inhomogeneous B_0 and B_1 fields at high static magnetic field strength and significantly improve the quality of phase-based diagnostic imaging methods at 7 T.

Die approbierte gedruckte Originalversion dieser Dissertation ist an der TU Wien Bibliothek verfügbar.
The approved original version of this doctoral thesis is available in print at TU Wien Bibliothek.
TU WIEN Bibliothek Your knowledge hub

Bibliography

[1] A. Sadeghi-Tarakameh, L. DelaBarre, R. L. Lagore, A. Torrado-Carvajal, X. Wu, A. Grant, G. Adriany, G. J. Metzger, P.-F. Van de Moortele, K. Ugurbil, E. Atalar, Y. Eryaman, In vivo human head MRI at 10.5T: A radiofrequency safety study and preliminary imaging results, Magnetic Resonance in Medicine 84 (1) (2020) 484–496. doi:10.1002/mrm.28093.

[2] T. Roussel, J. T. Rosenberg, S. C. Grant, L. Frydman, Brain investigations of rodent disease models by chemical exchange saturation transfer at 21.1 T, NMR in biomedicine 31 (11) (2018) e3995. doi:10.1002/nbm.3995.

[3] G. H. Glover, C. E. Hayes, N. J. Pelc, W. A. Edelstein, O. M. Mueller, H. R. Hart, C. J. Hardy, M. O'Donnell, W. D. Barber, Comparison of linear and circular polarization for magnetic resonance imaging, Journal of Magnetic Resonance (1969) 64 (2) (1985) 255–270. doi:10.1016/0022-2364(85)90349-X.

[4] P.-M. Robitaille, L. Berliner, Ultra High Field Magnetic Resonance Imaging, Biological Magnetic Resonance, Springer US, 2006. doi:10.1007/978-0-387-49648-1.

[5] M. V. Vaidya, C. M. Collins, D. K. Sodickson, R. Brown, G. C. Wiggins, R. Lattanzi, Dependence of B1+ and B1- Field Patterns of Surface Coils on the Electrical Properties of the Sample and the MR Operating Frequency, Concepts in magnetic resonance. Part B, Magnetic resonance engineering 46 (1) (2016) 25–40. doi:10.1002/cmr.b.21319.

[6] L. G. Hanson, Is quantum mechanics necessary for understanding magnetic resonance?, Concepts in Magnetic Resonance Part A 32A (5) (2008) 329–340. doi:10.1002/cmr.a.20123.

[7] M. A. Bernstein, K. F. King, X. J. Zhou, Handbook of MRI Pulse Sequences, Elsevier, 2004.

[8] M. Loecher, O. Wieben, k-Space, in: M. A. Syed, S. V. Raman, O. P. Simonetti (Eds.), Basic Principles of Cardiovascular MRI: Physics and Imag-

Die approbierte gedruckte Originalversion dieser Dissertation ist an der TU Wien Bibliothek verfügbar.
The approved original version of this doctoral thesis is available in print at TU Wien Bibliothek.
TU Bibliothek Your knowledge hub WIEN

ing Technique, Springer International Publishing, Cham, 2015, pp. 13–23. doi:10.1007/978-3-319-22141-0_2.

[9] J.-D. Jutras, K. Wachowicz, G. Gilbert, N. De Zanche, SNR efficiency of combined bipolar gradient echoes: Comparison of three-dimensional FLASH, MPRAGE, and multiparameter mapping with VFA-FLASH and MP2RAGE, Magnetic Resonance in Medicine 77 (6) (2017) 2186–2202. doi:10.1002/mrm.26306.

[10] S. Vinitski, R. Griffey, M. Fuka, N. Matwiyoff, R. Prost, Effect of the sampling rate on magnetic resonance imaging, Magnetic Resonance in Medicine 5 (3) (1987) 278–285. doi:10.1002/mrm.1910050309.

[11] D. O. Walsh, A. F. Gmitro, M. W. Marcellin, Adaptive reconstruction of phased array MR imagery, Magnetic Resonance in Medicine 43 (5) (2000) 682–690. doi:10.1002/(sici)1522-2594(200005)43:5<682::aid-mrm10>3.0.co;2-g.

[12] V. Brainovich, U. Sabatini, G. E. Hagberg, Advantages of using multiple-echo image combination and asymmetric triangular phase masking in magnetic resonance venography at 3 T, Magnetic Resonance Imaging 27 (1) (2009) 23–37. doi:10.1016/j.mri.2008.05.006.

[13] B. Wu, W. Li, A. V. Avram, S.-M. Gho, C. Liu, Fast and tissue-optimized mapping of magnetic susceptibility and T2* with multi-echo and multi-shot spirals, NeuroImage 59 (1) (2012) 297–305. doi:10.1016/j.neuroimage.2011.07.019.

[14] G. E. Hagberg, I. Indovina, J. N. Sanes, S. Posse, Real-time quantification of T2* changes using multiecho planar imaging and numerical methods, Magnetic Resonance in Medicine 48 (5) (2002) 877–882. doi:10.1002/mrm.10283.

[15] D. C. Noll, D. G. Nishimura, A. Macovski, Homodyne detection in magnetic resonance imaging, IEEE transactions on medical imaging 10 (2) (1991) 154–163. doi:10.1109/42.79473.

[16] M. Quinn, J. Gati, L. Klassen, A. Lin, J. Bird, S. Leung, R. Menon, Comparison of Multiecho Postprocessing Schemes for SWI with Use of Linear and Nonlinear Mask Functions, American Journal of Neuroradiology 35 (1) (2014) 38–44. doi:10.3174/ajnr.A3584.

[17] M. A. Bernstein, M. Grgic, T. J. Brosnan, N. J. Pelc, Reconstructions of phase contrast, phased array multicoil data, Magnetic Resonance in Medicine 32 (3) (1994) 330–334. doi:10.1002/mrm.1910320308.

Die approbierte gedruckte Originalversion dieser Dissertation ist an der TU Wien Bibliothek verfügbar.
The approved original version of this doctoral thesis is available in print at TU Wien Bibliothek.
TU Bibliothek Your knowledge hub WIEN

[18] S. Robinson, G. Grabner, S. Witoszynskyj, S. Trattnig, Combining phase images from multi-channel RF coils using 3D phase offset maps derived from a dual-echo scan, Magnetic Resonance in Medicine 65 (6) (2011) 1638–1648. doi:10.1002/mrm.22753.

[19] P. B. Roemer, W. A. Edelstein, C. E. Hayes, S. P. Souza, O. M. Mueller, The NMR phased array, Magnetic Resonance in Medicine 16 (2) (1990) 192–225. doi:10.1002/mrm.1910160203.

[20] M. A. Schofield, Y. Zhu, Fast phase unwrapping algorithm for interferometric applications, Optics Letters 28 (14) (2003) 1194–1196. doi:10.1364/OL.28.001194.

[21] B. Dymerska, K. Eckstein, B. Bachrata, B. Siow, S. Trattnig, K. Shmueli, S. D. Robinson, Phase unwrapping with a rapid opensource minimum spanning tree algorithm (ROMEO), Magnetic Resonance in Medicine 85 (4) (2021) 2294–2308. doi:10.1002/mrm.28563.

[22] M. Jenkinson, Fast, automated, N-dimensional phase-unwrapping algorithm, Magnetic Resonance in Medicine 49 (1) (2003) 193–197. doi:10.1002/mrm.10354.

[23] S. D. Robinson, K. Bredies, D. Khabipova, B. Dymerska, J. P. Marques, F. Schweser, An illustrated comparison of processing methods for MR phase imaging and QSM: combining array coil signals and phase unwrapping, NMR in biomedicine 30 (4) (Apr. 2017). doi:10.1002/nbm.3601.

[24] H. S. Abdul-Rahman, M. A. Gdeisat, D. R. Burton, M. J. Lalor, F. Lilley, C. J. Moore, Fast and robust three-dimensional best path phase unwrapping algorithm, Applied Optics 46 (26) (2007) 6623–6635. doi:10.1364/AO.46.006623.

[25] Y. Chen, S. Liu, Y. Kang, E. M. Haacke, A rapid, robust multi-echo phase unwrapping method for quantitative susceptibility mapping (QSM) using strategically acquired gradient echo (STAGE) data acquisition, in: Medical Imaging 2018: Physics of Medical Imaging, Vol. 10573, International Society for Optics and Photonics, 2018, p. 105732U. doi:10.1117/12.2292951.

[26] S. Robinson, H. Schödl, S. Trattnig, A Method for Unwrapping Highly Wrapped Multi-echo Phase Images at Very High Field: UMPIRE, Magnetic resonance in medicine : official journal of the Society of Magnetic Resonance in Medicine / Society of Magnetic Resonance in Medicine 72 (1) (2014) 80–92. doi:10.1002/mrm.24897.

Die approbierte gedruckte Originalversion dieser Dissertation ist an der TU Wien Bibliothek verfügbar.
The approved original version of this doctoral thesis is available in print at TU Wien Bibliothek.
TU Bibliothek Your knowledge hub WIEN

[27] J. Luo, B. D. Jagadeesan, A. H. Cross, D. A. Yablonskiy, Gradient Echo Plural Contrast Imaging — Signal model and derived contrasts: T2*, T1, Phase, SWI, T1f, FST2*and T2*-SWI, NeuroImage 60 (2) (2012) 1073–1082. doi:10.1016/j.neuroimage.2012.01.108.

[28] G. Gilbert, G. Savard, C. Bard, G. Beaudoin, Quantitative comparison between a multiecho sequence and a single-echo sequence for susceptibility-weighted phase imaging, Magnetic Resonance Imaging 30 (5) (2012) 722–730. doi:10.1016/j.mri.2012.02.008.

[29] B. C. Tendler, Investigating the magnetic properties of tissue with MRI phase at 7T, Ph.D., University of Nottingham (2017).

[30] G. P. Arrighini, M. Maestro, R. Moccia, Magnetic Properties of Polyatomic Molecules. I. Magnetic Susceptibility of H2O, NH3, CH4, H2O2, The Journal of Chemical Physics 49 (2) (1968) 882–889, publisher: American Institute of Physics. doi:10.1063/1.1670155.

[31] J. F. Schenck, The role of magnetic susceptibility in magnetic resonance imaging: MRI magnetic compatibility of the first and second kinds, Medical Physics 23 (6) (1996) 815–850, _eprint: https://aapm.onlinelibrary.wiley.com/doi/pdf/10.1118/1.597854. doi:10.1118/1.597854.

[32] E. M. Haacke, Y. Xu, Y.-C. N. Cheng, J. R. Reichenbach, Susceptibility weighted imaging (SWI), Magnetic Resonance in Medicine 52 (3) (2004) 612–618. doi:10.1002/mrm.20198.

[33] J. R. Reichenbach, M. Barth, E. M. Haacke, M. Klarhöfer, W. A. Kaiser, E. Moser, High-resolution MR venography at 3.0 Tesla, Journal of Computer Assisted Tomography 24 (6) (2000) 949–957. doi:10.1097/00004728-200011000-00023.

[34] C. Langkammer, F. Schweser, N. Krebs, A. Deistung, W. Goessler, E. Scheurer, K. Sommer, G. Reishofer, K. Yen, F. Fazekas, S. Ropele, J. R. Reichenbach, Quantitative susceptibility mapping (QSM) as a means to measure brain iron? A post mortem validation study, NeuroImage 62 (3) (2012) 1593–1599. doi:10.1016/j.neuroimage.2012.05.049.

[35] F. Schweser, A. Deistung, B. W. Lehr, J. R. Reichenbach, Quantitative imaging of intrinsic magnetic tissue properties using MRI signal phase: An approach to in vivo brain iron metabolism?, NeuroImage 54 (4) (2011) 2789–2807. doi:10.1016/j.neuroimage.2010.10.070.

Die approbierte gedruckte Originalversion dieser Dissertation ist an der TU Wien Bibliothek verfügbar.
The approved original version of this doctoral thesis is available in print at TU Wien Bibliothek.
TU Bibliothek Your knowledge hub WIEN

[36] T. Liu, P. Spincemaille, L. d. Rochefort, B. Kressler, Y. Wang, Calculation of susceptibility through multiple orientation sampling (COSMOS): A method for conditioning the inverse problem from measured magnetic field map to susceptibility source image in MRI, Magnetic Resonance in Medicine 61 (1) (2009) 196–204. doi:10.1002/mrm.21828.

[37] S. Wharton, A. Schäfer, R. Bowtell, Susceptibility mapping in the human brain using threshold-based k-space division, Magnetic Resonance in Medicine 63 (5) (2010) 1292–1304. doi:10.1002/mrm.22334.

[38] K. Shmueli, J. A. de Zwart, P. van Gelderen, T.-Q. Li, S. J. Dodd, J. H. Duyn, Magnetic Susceptibility Mapping of Brain Tissue In Vivo Using MRI Phase Data, Magnetic resonance in medicine : official journal of the Society of Magnetic Resonance in Medicine / Society of Magnetic Resonance in Medicine 62 (6) (2009) 1510–1522. doi:10.1002/mrm.22135.

[39] L. d. Rochefort, T. Liu, B. Kressler, J. Liu, P. Spincemaille, V. Lebon, J. Wu, Y. Wang, Quantitative susceptibility map reconstruction from MR phase data using bayesian regularization: Validation and application to brain imaging, Magnetic Resonance in Medicine 63 (1) (2010) 194–206. doi:10.1002/mrm.22187.

[40] S. Bollmann, K. G. B. Rasmussen, M. Kristensen, R. G. Blendal, L. R. Østergaard, M. Plocharski, K. O'Brien, C. Langkammer, A. Janke, M. Barth, DeepQSM - using deep learning to solve the dipole inversion for quantitative susceptibility mapping, NeuroImage 195 (2019) 373–383. doi:10.1016/j.neuroimage.2019.03.060.

[41] S. Liu, K. Mok, J. Neelavalli, Y.-C. N. Cheng, J. Tang, Y. Ye, E. M. Haacke, Improved MR venography using quantitative susceptibility-weighted imaging, Journal of magnetic resonance imaging: JMRI 40 (3) (2014) 698–708. doi:10.1002/jmri.24413.

[42] K. Eckstein, B. Dymerska, B. Bachrata, W. Bogner, K. Poljanc, S. Trattnig, S. D. Robinson, Computationally Efficient Combination of Multi-channel Phase Data From Multi-echo Acquisitions (ASPIRE), Magnetic Resonance in Medicine 79 (6) (2018) 2996–3006. doi:10.1002/mrm.26963.

[43] R. C. Prim, Shortest Connection Networks And Some Generalizations, Bell System Technical Journal 36 (6) (1957) 1389–1401. doi:10.1002/j.1538-7305.1957.tb01515.x.

[44] K. Eckstein, B. Bachrata, G. Hangel, G. Widhalm, C. Enzinger, M. Barth, S. Trattnig, S. D. Robinson, Improved susceptibility weighted imaging at

Die approbierte gedruckte Originalversion dieser Dissertation ist an der TU Wien Bibliothek verfügbar.
The approved original version of this doctoral thesis is available in print at TU Wien Bibliothek.
TU Bibliothek Your knowledge hub WIEN

ultra-high field using bipolar multi-echo acquisition and optimized image processing: CLEAR-SWI, NeuroImage (237) (2021) 118157. doi:10.1016/j.neuroimage.2021.118175.

[45] K. Eckstein, S. Trattnig, S. D. Robinson, Correction for Geometric Distortion in Bipolar Gradient Echo Images from B0 Field Variations, in: Proceedings of the 27th Annual Meeting ISMRM, Vol. #4510, Montréal, Québec, Canada, 2019.

[46] B. Tendler, R. Bowtell, Using frequency difference mapping to assess white matter microstructure in the human corpus callosum, in: Proceedings of the 25th Annual Meeting ISMRM, 2016, p. 2849.

[47] K. Eckstein, S. Trattnig, S. D. Robinson, High resolution frequency difference mapping using ASPIRE phase combination, in: Proceedings of the 26th Annual Meeting ISMRM, Vol. #4991, Paris, France, 2018.

[48] S. Wharton, R. Bowtell, Gradient echo based fiber orientation mapping using R2* and frequency difference measurements, NeuroImage 83 (2013) 1011–1023. doi:10.1016/j.neuroimage.2013.07.054.

[49] N. Li, W.-T. Wang, D. L. Pham, J. A. Butman, Artifactual microhemorrhage generated by susceptibility weighted image processing, Journal of Magnetic Resonance Imaging 41 (6) (2015) 1695–1700. doi:10.1002/jmri.24728.

[50] D. L. Parker, A. Payne, N. Todd, J. R. Hadley, Phase reconstruction from multiple coil data using a virtual reference coil, Magnetic Resonance in Medicine 72 (2) (2014) 563–569. doi:10.1002/mrm.24932.

[51] A. Deistung, A. Rauscher, J. Sedlacik, J. Stadler, S. Witoszynskyj, J. R. Reichenbach, Susceptibility weighted imaging at ultra high magnetic field strengths: Theoretical considerations and experimental results, Magnetic Resonance in Medicine 60 (5) (2008) 1155–1168. doi:10.1002/mrm.21754.

[52] S. Liu, S. Buch, Y. Chen, H.-S. Choi, Y. Dai, C. Habib, J. Hu, J.-Y. Jung, Y. Luo, D. Utriainen, M. Wang, D. Wu, S. Xia, E. M. Haacke, Susceptibility-weighted imaging: current status and future directions, NMR in Biomedicine 30 (4) (2017) e3552. doi:10.1002/nbm.3552.

[53] I. Kutskir. Fastest Gaussian Blur (in linear time) [online] (2014). http://blog.ivank.net/fastest-gaussian-blur.html

[54] A. K. Funai, J. A. Fessler, D. T. B. Yeo, V. T. Olafsson, D. C. Noll, Regularized Field Map Estimation in MRI, IEEE Transactions on Medical Imaging 27 (10) (2008) 1484–1494. doi:10.1109/TMI.2008.923956.

Die approbierte gedruckte Originalversion dieser Dissertation ist an der TU Wien Bibliothek verfügbar.
The approved original version of this doctoral thesis is available in print at TU Wien Bibliothek.
TU Bibliothek Your knowledge hub WIEN

[55] B. Kressler, L. de Rochefort, Tian Liu, P. Spincemaille, Quan Jiang, Yi Wang, Nonlinear Regularization for Per Voxel Estimation of Magnetic Susceptibility Distributions From MRI Field Maps, IEEE Transactions on Medical Imaging 29 (2) (2010) 273–281. doi:10.1109/TMI.2009.2023787.

[56] J. M. Bioucas-Dias, G. Valadão, Phase unwrapping via graph cuts, IEEE transactions on image processing: a publication of the IEEE Signal Processing Society 16 (3) (2007) 698–709. doi:10.1109/tip.2006.888351.

[57] P. L. Cardoso, B. Dymerska, B. Bachratá, F. P. Fischmeister, N. Mahr, E. Matt, S. Trattnig, R. Beisteiner, S. D. Robinson, The clinical relevance of distortion correction in presurgical fMRI at 7 T, NeuroImage 168 (2018) 490–498. doi:10.1016/j.neuroimage.2016.12.070.

[58] F. Pittau, M. O. Baud, J. Jorge, L. Xin, F. Grouiller, G. R. Iannotti, M. Seeck, F. Lazeyras, S. Vulliémoz, M. I. Vargas, MP2RAGE and Susceptibility-Weighted Imaging in Lesional Epilepsy at 7T, Journal of Neuroimaging 28 (4) (2018) 365–369. doi:10.1111/jon.12523.

[59] E. Najdenovska, C. Tuleasca, J. Jorge, P. Maeder, J. P. Marques, T. Roine, D. Gallichan, J.-P. Thiran, M. Levivier, M. Bach Cuadra, Comparison of MRI-based automated segmentation methods and functional neurosurgery targeting with direct visualization of the Ventro-intermediate thalamic nucleus at 7T, Scientific Reports 9 (1) (2019) 1119. doi:10.1038/s41598-018-37825-8.

[60] A. M. Peters, M. J. Brookes, F. G. Hoogenraad, P. A. Gowland, S. T. Francis, P. G. Morris, R. Bowtell, T2* measurements in human brain at 1.5, 3 and 7 T, Magnetic Resonance Imaging 25 (6) (2007) 748–753. doi:10.1016/j.mri.2007.02.014.

[61] P. J. Wright, O. E. Mougin, J. J. Totman, A. M. Peters, M. J. Brookes, R. Coxon, P. E. Morris, M. Clemence, S. T. Francis, R. W. Bowtell, P. A. Gowland, Water proton T1 measurements in brain tissue at 7, 3, and 1.5 T using IR-EPI, IR-TSE, and MPRAGE: results and optimization, Magma (New York, N.Y.) 21 (1-2) (2008) 121–130. doi:10.1007/s10334-008-0104-8.

[62] K. T. Bluestein, D. Pitt, M. V. Knopp, P. Schmalbrock, T1 and proton density at 7 T in patients with multiple sclerosis: an initial study, Magnetic Resonance Imaging 30 (1) (2012) 19–25. doi:10.1016/j.mri.2011.07.018.

[63] C. Rorden, M. Brett, Stereotaxic display of brain lesions, Behavioural Neurology 12 (4) (2000) 191–200. doi:10.1155/2000/421719.

[64] P. McCarthy, FSLeyes (2019). doi:10.5281/zenodo.3530921.

Die approbierte gedruckte Originalversion dieser Dissertation ist an der TU Wien Bibliothek verfügbar.
The approved original version of this doctoral thesis is available in print at TU Wien Bibliothek.
TU Bibliothek Your knowledge hub WIEN

[65] R. M. Henkelman, Measurement of signal intensities in the presence of noise in MR images: Technical Reports: Signal intensities in MR image noise, Medical Physics 12 (2) (1985) 232–233. doi:10.1118/1.595711.

[66] C. D. Constantinides, E. Atalar, E. R. McVeigh, Signal-to-Noise Measurements in Magnitude Images from NMR Phased Arrays, Magnetic resonance in medicine : official journal of the Society of Magnetic Resonance in Medicine / Society of Magnetic Resonance in Medicine 38 (5) (1997) 852–857.

[67] S. B. Reeder, B. J. Wintersperger, O. Dietrich, T. Lanz, A. Greiser, M. F. Reiser, G. M. Glazer, S. O. Schoenberg, Practical approaches to the evaluation of signal-to-noise ratio performance with parallel imaging: Application with cardiac imaging and a 32-channel cardiac coil, Magnetic Resonance in Medicine 54 (3) (2005) 748–754. doi:10.1002/mrm.20636.

[68] R. R. Price, L. Axel, T. Morgan, R. Newman, W. Perman, N. Schneiders, M. Selikson, M. Wood, S. R. Thomas, Quality assurance methods and phantoms for magnetic resonance imaging: Report of AAPM nuclear magnetic resonance Task Group No. 1, Medical Physics 17 (2) (1990) 287–295. doi:10.1118/1.596566.

[69] K. Eckstein, Development of a Method for Combining MRI Data from Multiple Receiver Coils, Master's thesis, Vienna University of Technology, Vienna (2016).

[70] S. M. Smith, Fast robust automated brain extraction, Human Brain Mapping 17 (3) (2002) 143–155. doi:10.1002/hbm.10062.

[71] P. Jezzard, R. S. Balaban, Correction for geometric distortion in echo planar images from B0 field variations, Magnetic Resonance in Medicine 34 (1) (1995) 65–73. doi:10.1002/mrm.1910340111.

[72] W. Feng, J. Neelavalli, E. M. Haacke, Catalytic multiecho phase unwrapping scheme (CAMPUS) in multiecho gradient echo imaging: removing phase wraps on a voxel-by-voxel basis, Magnetic Resonance in Medicine 70 (1) (2013) 117–126. doi:10.1002/mrm.24457.

[73] S. D. Robinson, B. Dymerska, W. Bogner, M. Barth, O. Zaric, S. Goluch, G. Grabner, X. Deligianni, O. Bieri, S. Trattnig, Combining phase images from array coils using a short echo time reference scan (COMPOSER), Magnetic Resonance in Medicine 77 (1) (2017) 318–327, _eprint: https://onlinelibrary.wiley.com/doi/pdf/10.1002/mrm.26093. doi:10.1002/mrm.26093.

Die approbierte gedruckte Originalversion dieser Dissertation ist an der TU Wien Bibliothek verfügbar.
The approved original version of this doctoral thesis is available in print at TU Wien Bibliothek.
TU Bibliothek Your knowledge hub WIEN

[74] F. Schweser, S. Robinson, L. de Rochefort, W. Li, K. Bredies, An illustrated comparison of processing methods for phase MRI and QSM: Removal of background field contributions from sources outside the region of interest, NMR in biomedicine 30 (4) (Apr. 2017). doi:10.1002/nbm.3604.

[75] R. Bamler, P. Hartl, Synthetic aperture radar interferometry, Inverse Problems 14 (4) (1998) R1–R54, publisher: IOP Publishing. doi:10.1088/0266-5611/14/4/001.

[76] K. T. Gahagan, D. S. Moore, D. J. Funk, R. L. Rabie, S. J. Buelow, J. W. Nicholson, Measurement of Shock Wave Rise Times in Metal Thin Films, Physical Review Letters 85 (15) (2000) 3205–3208, publisher: American Physical Society. doi:10.1103/PhysRevLett.85.3205.

[77] B. Dymerska, B. A. Poser, W. Bogner, E. Visser, K. Eckstein, P. Cardoso, M. Barth, S. Trattnig, S. D. Robinson, Correcting dynamic distortions in 7T echo planar imaging using a jittered echo time sequence, Magnetic Resonance in Medicine 76 (5) (2016) 1388–1399. doi:10.1002/mrm.26018.

[78] P. S. Özbay, G. Warnock, C. Rossi, F. Kuhn, B. Akin, K. P. Pruessmann, D. Nanz, Probing neuronal activation by functional quantitative susceptibility mapping under a visual paradigm: A group level comparison with BOLD fMRI and PET, NeuroImage 137 (2016) 52–60. doi:10.1016/j.neuroimage.2016.05.013.

[79] J. R. Reichenbach, R. Venkatesan, D. J. Schillinger, D. K. Kido, E. M. Haacke, Small vessels in the human brain: MR venography with deoxyhemoglobin as an intrinsic contrast agent., Radiology 204 (1) (1997) 272–277. doi:10.1148/radiology.204.1.9205259.

[80] G. Grabner, B. Kiesel, A. Wöhrer, M. Millesi, A. Wurzer, S. Göd, A. Mallouhi, E. Knosp, C. Marosi, S. Trattnig, S. Wolfsberger, M. Preusser, G. Widhalm, Local image variance of 7 Tesla SWI is a new technique for preoperative characterization of diffusely infiltrating gliomas: correlation with tumour grade and IDH1 mutational status, European Radiology 27 (4) (2017) 1556–1567. doi:10.1007/s00330-016-4451-y.

[81] K. Santhosh, C. Kesavadas, B. Thomas, A. K. Gupta, K. Thamburaj, T. R. Kapilamoorthy, Susceptibility weighted imaging: a new tool in magnetic resonance imaging of stroke, Clinical Radiology 64 (1) (2009) 74–83. doi:10.1016/j.crad.2008.04.022.

[82] À. Rovira, M. P. Wattjes, M. Tintoré, C. Tur, T. A. Yousry, M. P. Sormani, N. De Stefano, M. Filippi, C. Auger, M. A. Rocca, F. Barkhof, F. Fazekas,

Die approbierte gedruckte Originalversion dieser Dissertation ist an der TU Wien Bibliothek verfügbar.
The approved original version of this doctoral thesis is available in print at TU Wien Bibliothek.
TU Bibliothek Your knowledge hub WIEN

L. Kappos, C. Polman, D. Miller, X. Montalban, MAGNIMS study group, Evidence-based guidelines: MAGNIMS consensus guidelines on the use of MRI in multiple sclerosis-clinical implementation in the diagnostic process, Nature Reviews. Neurology 11 (8) (2015) 471–482. doi:10.1038/nrneurol.2015.106.

[83] V. C. Obmann, C. Marx, A. Berzigotti, N. Mertineit, J. Hrycyk, C. Gräni, L. Ebner, M. Ith, J. T. Heverhagen, A. Christe, A. T. Huber, Liver MRI susceptibility-weighted imaging (SWI) compared to T2* mapping in the presence of steatosis and fibrosis, European Journal of Radiology 118 (2019) 66–74. doi:10.1016/j.ejrad.2019.07.001.

[84] Susceptibility Weighted Imaging (SWI) of the kidney at 3 T – initial results, Zeitschrift für Medizinische Physik 20 (2) (2010) 143–150, publisher: Urban & Fischer. doi:10.1016/j.zemedi.2010.02.004.

[85] M. J. Nissi, F. Toth, J. Zhang, S. Schmitter, M. Benson, C. S. Carlson, J. M. Ellermann, Susceptibility weighted imaging of cartilage canals in porcine epiphyseal growth cartilage ex vivo and in vivo, Magnetic Resonance in Medicine 71 (6) (2014) 2197–2205. doi:10.1002/mrm.24863.

[86] C. Denk, A. Rauscher, Susceptibility weighted imaging with multiple echoes, Journal of Magnetic Resonance Imaging 31 (1) (2010) 185–191. doi:10.1002/jmri.21995.

[87] A. Rauscher, M. Barth, J. R. Reichenbach, R. Stollberger, E. Moser, Automated unwrapping of MR phase images applied to BOLD MR-venography at 3 Tesla, Journal of Magnetic Resonance Imaging 18 (2) (2003) 175–180. doi:10.1002/jmri.10346.

[88] S. S. Oh, S.-H. Oh, Y. Nam, D. Han, R. B. Stafford, J. Hwang, D.-H. Kim, H. Park, J. Lee, An Improved Susceptibility Weighted Imaging Method using Multi-Echo Acquisition, Magnetic resonance in medicine : official journal of the Society of Magnetic Resonance in Medicine / Society of Magnetic Resonance in Medicine 72 (2) (2014) 452–458. doi:10.1002/mrm.24940.

[89] T. F. Barrett, H. A. Dyvorne, F. Padormo, P. S. Pawha, B. N. Delman, R. K. Shrivastava, P. Balchandani, First Application of 7T Magnetic Resonance Imaging in Endoscopic Endonasal Surgery of Skull Base Tumors, World neurosurgery 103 (2017) 600–610. doi:10.1016/j.wneu.2017.03.088.

[90] J. Sled, A. Zijdenbos, A. Evans, A nonparametric method for automatic correction of intensity nonuniformity in MRI data, IEEE Transactions on Medical Imaging 17 (1) (1998) 87–97. doi:10.1109/42.668698.

Die approbierte gedruckte Originalversion dieser Dissertation ist an der TU Wien Bibliothek verfügbar.
The approved original version of this doctoral thesis is available in print at TU Wien Bibliothek.
TU Bibliothek Your knowledge hub WIEN

[91] U. Vovk, F. Pernus, B. Likar, A Review of Methods for Correction of Intensity Inhomogeneity in MRI, IEEE Transactions on Medical Imaging 26 (3) (2007) 405–421. doi:10.1109/TMI.2006.891486.

[92] F. C. Damen, K. Cai, B1- non-uniformity correction of phased-array coils without measuring coil sensitivity, Magnetic Resonance Imaging 51 (2018) 20–28. doi:10.1016/j.mri.2018.04.009.

[93] M. Maeda, S. Itoh, H. Kimura, T. Iwasaki, N. Hayashi, K. Yamamoto, Y. Ishii, T. Kubota, Tumor vascularity in the brain: evaluation with dynamic susceptibility-contrast MR imaging., Radiology 189 (1) (1993) 233–238. doi:10.1148/radiology.189.1.8372199.

[94] X.-c. Wang, H. Zhang, Y. Tan, J.-b. Qin, X.-f. Wu, L. Wang, L. Zhang, Combined value of susceptibility-weighted and perfusion-weighted imaging in assessing WHO grade for brain astrocytomas, Journal of Magnetic Resonance Imaging 39 (6) (2014) 1569–1574. doi:10.1002/jmri.24312.

[95] F. Ségonne, A. M. Dale, E. Busa, M. Glessner, D. Salat, H. K. Hahn, B. Fischl, A hybrid approach to the skull stripping problem in MRI, NeuroImage 22 (3) (2004) 1060–1075. doi:10.1016/j.neuroimage.2004.03.032.

[96] A. W. Stewart, S. D. Robinson, K. O'Brien, J. Jin, G. Widhalm, G. Hangel, A. Walls, J. Goodwin, K. Eckstein, M. Tourell, C. Morgan, A. Narayanan, M. Barth, S. Bollmann, QSMxT: Robust Masking and Artefact Reduction for Quantitative Susceptibility Mapping, Tech. rep., company: Cold Spring Harbor Laboratory Distributor: Cold Spring Harbor Laboratory Label: Cold Spring Harbor Laboratory Section: New Results Type: article (May 2021). doi:10.1101/2021.05.05.442850.

Die approbierte gedruckte Originalversion dieser Dissertation ist an der TU Wien Bibliothek verfügbar.
The approved original version of this doctoral thesis is available in print at TU Wien Bibliothek.
TU Bibliothek Your knowledge hub WIEN